

https://dspace.org/

Hierarchical nitrogen-doped carbon nanotube-carbon nanofiber-based networks for electrochemical capacitors

Mofokeng, Thapelo Prince

2021

https://hdl.handle.net/10539/33089

Downloaded from a DSpace repository. https://dspace.org/

Hierarchical nitrogen-doped carbon nanotube-carbon nanofiber-based networks for electrochemical capacitors



Thapelo Prince Mofokeng (1746729)

A thesis submitted to the Faculty of Science, University of the Witwatersrand, Johannesburg, in fulfilment of the requirements for the degree of Doctor of Philosophy.

Supervisors: Dr. Zikhona N. Tetana and Prof. Kenneth I. Ozoemena

Johannesburg, June 2021

Declaration

I declare that this thesis is my own, unaided work. It is being submitted for the Degree of Doctor of Philosophy at the University of the Witwatersrand, Johannesburg. It has not been submitted before for any degree or examination at any other University.

Signature: …  … Date: ...14 June 2021…

Dedication

This work is dedicated to my family

‘All that I am, and all that I ever will be, it is because of you”

Thank You

Acknowledgements

Although words alone are insufficient to express my gratitude to all those who stood by my side and helped me during my PhD studies, I would like to express my heartfelt gratitude for their efforts.

First and foremost, I would like to express my gratitude to Professor Kenneth I. Ozoemena, my co-supervisor, for developing a unique research and development environment in which I was able to explore various fields of science. I would like to thank Professor Ozoemena for believing in my ideas, allowing me to explore and work on them, and, most importantly, for believing in me. Professor Ozoemena practically taught me everything I know today on materials chemistry and electrochemistry. Without his wise counsel and unwavering encouragement, I would not have been able to make any progress in my study. Professor Ozoemena's approach to science, management and life inspires me greatly, especially in terms of furthering my academic career.

My supervisor; Dr. Zikhona N. Tetana, for her constructive criticism, empathy and motivation. Working with her for the past three years has been a true honour. I owe her a huge debt of gratitude for believing in me and all she has done for me. She did not only provide me with resources but also taught me to become an independent researcher. Her mentorship and advice would be a lifelong asset to me in my future career endeavours.

I would like to express my gratitude to all my collaborative supervisors and mentors. Professor Neil J. Coville, Dr. Manoko S. Maubane-Nkadimeng, Dr. Adewale K. Ipadeola, Dr. Patrick V. Mwonga and Dr. Aderemi B. Haruna for their contributions to my research and support.

My sincere thanks go to the staff members of the Microscopy and Microanalysis Unit at the University of the Witwatersrand for providing the training and assistance with electron microscopy work.

Dr. Funeka P. Nkosi was instrumental in exposing me to the world of supercapacitors and batteries. Thank you for your advice, contributions and help when I needed it. My sincere thanks to Prof. Noshipo Moloto for allowing me to use her laboratory and equipment.

I am also privileged to be a member of the CATMAT research group. It has been a true pleasure to work with all the group members (past and present) and I am grateful for the fruitful conversations and constructive criticism that occurred during seminars and practice talks. Being a member of the research group was a fantastic experience and a great pleasure.

Thanks to my supercapacitor colleagues Bokome Shaku, Sebenzile Shabalala, Thokozani Tsoari and Irfan Habib for their assistance and never-ending discussions.

This research would not have been possible without the financial support of the DSI-NRF Centre of Excellence in Strong Materials and the African Materials Science and Engineering Network (AMSEN), Carnegie–IAS RISE Network grants.

I would also like to express my gratitude to my family for supporting me in all my professional and educational endeavours.

Finally, I would like to thank God for the mercy and grace He has given me. His love has never failed me. I thank Him for this opportunity, and I praise Him for providing me with the strength and determination to complete this degree.

RESEARCH OUTPUTS

1. **Mofokeng, T.P**., Tetana, Z.N. and Ozoemena, K.I., 2020. Defective 3D nitrogen-doped carbon nanotube-carbon fibre networks for high-performance supercapacitor: Transformative role of nitrogen-doping from surface-confined to diffusive kinetics. Carbon, 169, pp.312-326.
2. **Mofokeng, T.P**., Ipadeola, A.K., Tetana, Z.N. and Ozoemena, K.I., 2020. Defect-Engineered Nanostructured Ni/MOF-Derived Carbons for an Efficient Aqueous Battery-Type Energy Storage Device. ACS Omega, 5(32), pp.20461-20472.
3. **Mofokeng, T.P**., Shabalala, S., Haruna, A.B., Tetana, Z.N. and Ozoemena, K.I. Rod-like $Na_{0.44}MnO_2$ as electrode material for aqueous asymmetric capacitors (to submit-2021).
4. **Mofokeng, T.P**., Shabalala, S., Tlhaole, B., Ipadeola, A.K., Haruna, A.B., Linganiso, C.E., Tetana, Z.N. and Ozoemena, K.I. Water-In-Salt" electrolyte-based high-voltage (3.0 V) $Na_{0.44}MnO_2$ asymmetric capacitor (to submit-2021).

CONFERENCES

1. Effect of time on the growth of carbon nanotube on top of carbon fibre networks for high-performance symmetric supercapacitor. Poster presentation at 43rd SACI national convention: Chemistry for a sustainable African economy 2nd to 7th December 2018, CISR – ICC, Pretoria. South Africa.
2. Nitrogen-doped carbon nanotube-carbon fibre networks for high-performance symmetric supercapacitor. Poster presentation at Energy Storage and Industry 4.0: Challenges and Prospects (ENSTIN 2019) 31 July–2 August 2019; KwaMaritane Bush Lodge, Pilanesberg National Park, South Africa.
3. Nitrogen-doped carbon nanotube-carbon fibre networks for high-performance symmetric supercapacitor. Poster presentation at 70th Annual Meeting of the International Society of Electrochemistry 4 - 9 August 2019, Durban, South Africa.
4. Nitrogen-doped carbon nanotube-carbon fibre networks for high-performance symmetric supercapacitor. Oral presentation 10th WITS Cross-Faculty Postgraduate Symposium, September 2019, Johannesburg, South Africa.
5. Nitrogen-doped carbon nanotube-carbon fibre networks for high-performance symmetric supercapacitor. Oral presentation at the 2019 NYRS Symposium, December 2019, Pretoria, South Africa.
6. Defect-Engineered Nanostructured Ni/MOF-Derived Carbons for an Efficient Aqueous Battery-Type Energy Storage. Oral presentation 11th WITS Cross-Faculty Postgraduate Symposium, October 2020, Johannesburg, South Africa.

PROFESSIONAL ORGANIZATIONS

1. Member, South African Chemical Institute.
2. Member, International Society of Electrochemistry.

AWARDS, HONOURS and PRIZES

1. Awarded the prestigious DSI-NRF Centre of Excellence in Strong Materials, 2018-2020.
2. Awarded the African Materials Science and Engineering Network (AMSEN), Carnegie–IAS RISE Network grant, 2021.

Student supervision

1. I supervised two Honours students at the University of the Witwatersrand, Johannesburg, South Africa.

ABSTRACT

In this thesis, various electrode materials were fabricated and investigated as electrode materials for supercapacitor applications.

This research investigated the electrochemical properties of nitrogen-doped carbon nanotubes supported on electrospun carbon nanofiber networks (N-CNT@CF) hybrid material in symmetric and asymmetric capacitors. In addition, the storage kinetics of various energy storage mechanisms were thoroughly investigated. Field-emission scanning electron microscopy (FE-SEM), transmission electron microscopy (TEM), powder X-ray diffraction (P-XRD), Raman spectroscopy, X-ray photoelectron spectroscopy (XPS) and Brunauer-Emmett-Teller (BET) analysis were used to determine morphology, crystallinity, defects, elemental composition and the structural porosity of all the materials synthesized. In addition, electrochemical techniques such as cyclic voltammetry (CV), galvanostatic charge-discharge (GCD), electrochemical impedance spectroscopy (EIS) and cycle stability tests were performed for all materials in aqueous electrolytes using both the three (3) and two (2) electrode configurations.

Firstly, a hierarchical nanostructure of nitrogen-doped CNTs supported on electrospun CNF networks (N-CNT@CF) was synthesized using two simple techniques: electrospinning and chemical vapour deposition (CVD). The N-CNT@CF hybrid structure revealed that uniform N-CNTs were directly grown on the surface of carbon nanofiber networks, resulting in the creation of a hierarchical nanostructure with a high surface area and high porosity. The interactions between N-CNTs and CF networks were discovered to improve the electrical conductivity and electrochemical stability of the material. As a result of the unique hierarchical structure and physicochemical properties, the as-synthesised N-CNT@CF composite material

demonstrated exceptional electrochemical performance with a reversible specific capacitance, outstanding rate capability and long cycling stability. The symmetric device (N-CNT@CF//N-CNT@CF) on the other hand, showed a specific energy density of 5.5 Wh kg^{-1} with a power density of 254 W kg^{-1}. The real-world practical application of N-CNT@CF electrode material was shown by powering an LED bulb.

Secondly, a hybrid supercapacitor device was assembled with N-CNT@CF as the negative electrode and AT-Ni/MOFDC as the positive electrode. The hybrid device designated N-CNT@CF//AT-Ni/MOFDC shows a specific capacity of 10 mAh g^{-1} at 0.5 A g^{-1}. In comparison to the symmetric device (N-CNT@CF//N-CNT@CF), the N-CNT@CF//AT-Ni/MOFDC hybrid capacitor exhibits a higher energy density of about 8 Wh kg^{-1} with a power density of 400 W kg^{-1}, as well as excellent cycling performance (94 % capacity retention after 2,000 cycles).

An asymmetric supercapacitor (ASC) device was also assembled with N-CNT@CF as the negative electrode and $Na_{0.44}MnO_2$ as the positive electrode. The ASC device designated as N-CNT@CF//$Na_{0.44}MnO_2$ shows a high gravimetric and volumetric capacitance of 47 F g^{-1}, 86 F cm^{-3}, respectively. Furthermore, a high energy density of 21 Wh kg^{-1} and a power density of 450 W kg^{-1} were obtained at 0.5 A g^{-1}.

Finally, an asymmetric supercapacitor device operated in a “water-in-salt” electrolyte was developed, using $Na_{0.44}MnO_2$ nanowires and N-rGO as positive and negative electrodes, respectively. The N-rGO//$Na_{0.44}MnO_2$ ASC device was operated in a wide potential between 0 and 3 V in AWIS aqueous electrolyte and exhibits a maximum specific capacitance of 61 F g^{-1}. The energy density of 75.8 Wh kg^{-1} at a power density of 1125 W kg^{-1} was obtained and remains 31 Wh kg^{-1} at a power density of 7500 W kg^{-1}.

Thus, the results obtained from this study show that the unique 3D hierarchical N-CNT@CF networks is a promising electrode material and can be used as an anode material for asymmetric supercapacitors.

Table of contents

DECLARATION……i

DEDICATION……ii

ACKNOWLEDGEMENTS……...……...iii

RESEARCH OUTPUTS……v

CONFERENCES……..…….vi

PROFESSIONAL ORGANIZATIONS…….vii

AWARDS, HONOURS and PRIZES…….vii

ABSTRACT…….....……...…….viii

LIST OF FIGURES……...….xiv

LIST OF TABLES…….....xix

LIST OF SCHEMES……xx

LIST OF ABBREVIATIONS AND SYMBOLS…….……xxi

CHAPTER 1 Introduction 1

1.1 Background and motivation 1

1.1.1 Energy storages systems 3

1.2 Aim and objectives 7

1.2.1 Aim 7

1.2.2 Objectives 7

1.3 Thesis outline 8

1.4 References 10

Literature review 14

2.1 Energy storage systems 14

2.2 Supercapacitors 17

2.3 Energy storage principle in SCs 18

2.4 Energy storage mechanism of SCs 19

2.4.1 Electric double-layer capacitance (EDLC) 19

2.4.2 Pseudocapacitors 23

2.4.2.1 Surface redox pseudocapacitors 23

2.4.2.3 Battery-type Faradaic reaction 26

2.4.3 Hybrid supercapacitors (HSCs) 27
2.4.4 Asymmetric supercapacitor (ASCs) 29
2.5 Differentiating diffusion-controlled processes from a surface-controlled contribution 31
2.6 Electrode material for supercapacitor 33
2.6.2.1 Transition metal oxides 43
2.6.2.2 Conducting polymer 45
2.7 Electrolytes for supercapacitors 49
2.7.1 Aqueous electrolytes 50
2.7.2 Organic electrolytes 51
2.7.3 Ionic liquid electrolytes 52
2.8.1 Electrode fabrication for supercapacitors 53
2.8.2 Electrode testing for supercapacitors 53
2.8.3 Electrochemical techniques 56
2.8.3.1 Cyclic voltammetry 56
2.8.3.2 Galvanostatic charge-discharge (GCD) 58
2.8.3.3 Electrochemical impedance spectroscopy (EIS) 60
2.9 References 65
CHAPTER 3 86
Experimental methods and characterisation techniques 86
3.1 Experimental details 86
3.1.1 Materials 86
3.1.2 Fabrication of electrospun PAN fibres 86
3.1.3 Deposition of the bimetallic catalyst 87
3.1.4 Synthesis of CNTs on top of stabilized PAN fibres 87
3.1.5 Synthesis of Ni-MOF, Ni/MOFDC and AT-Ni/MOFDC 88
3.1.6 Preparation of $Na_{0.44}MnO_2$ 89
3.2 A brief overview of some of the characterization techniques 90
3.2.1 Scanning electron microscopy (SEM) 90
3.2.2 Transmission electron microscopy (TEM) 91
3.2.3 Raman spectroscopy 93
3.2.4 Powder X-Ray diffraction (P-XRD) 94
3.2.5 X-ray photoelectron spectroscopy (XPS) 95
3.2.6 Surface area and porosity analysis 97
3.3 References 99

CHAPTER 4 101
Nitrogen-doped carbon nanotube-carbon fibre networks for high-performance symmetric supercapacitor 101
4.1 Introduction 101
4.2 Experimental 103
4.2.1 Materials and methods 103
4.2.2 Fabrication of electrospun PAN fibres 103
4.2.3 Deposition of the bimetallic catalyst 103
4.2.4 Synthesis of CNTs on top of stabilized PAN fibres 104
4.2.5 Characterization methods 105
4.2.5.1 Material characterization 105
4.2.5.2 Electrochemical characterization 105
4.3 Results and discussion 107
4.3.1 Electrochemical analysis 118
4.3.2 Surface-controlled and diffusion-controlled charge storage contributions 120
4.4 Summary 129
4.5 References 131
CHAPTER 5 141
Nitrogen-doped carbon nanotube-carbon fibre networks as anode materials for nickel-metal organic frameworks-derived carbon hybrid supercapacitors 141
..... 141
5.1 Introduction 141
5.2 Experimental section 143
5.2.1 Materials 143
5.2.2 Synthesis of Ni-MOF, Ni/MOFDC and AT-Ni/MOFDC 143
5.2.3 Characterization 144
5.2.4 Electrochemical characterization 145
5.2.4.1 Fabrication and testing of single electrode materials 145
5.2.4.2 Fabrication of the N-CNT@CF//AT-Ni/MOFDC hybrid device 145
5.3 Results and discussion 146
5.3.1 Physical characterization 146
5.3.2 Electrochemical measurements 153
5.3.2.1 Three-electrode system 153
5.3.2.2 Electrochemical study of hybrid device (N-CNT@CF//AT-Ni/MOFDC) 158
5.4 Summary 163

5.5 References 164
CHAPTER 6 172
Nitrogen-doped carbon nanotube-carbon fibre networks as an anode material for nanowire-like sodium manganese oxide-based asymmetric supercapacitors 172
6.1 Introduction 172
6.2 Experimental section 175
6.2.1 Materials 175
6.2.2 Preparation of $Na_{0.44}MnO_2$ 175
6.2.3 Characterization 176
6.2.4 Electrochemical measurements 177
6.3 Results and discussion 177
6.3.1 Physical characterization 177
6.3.2 Electrochemical measurements 180
6.3.2.1 Three-electrode system 180
6.3.2.2 Asymmetric N-CNTs@CF//$Na_{0.44}MnO_2$ supercapacitor characteristics 190
6.4 Summary 195
6.5 References 197
CHAPTER 7 204
"Water-In-Salt" electrolyte-based high-voltage (3.0 V) $Na_{0.44}MnO_2$ asymmetric capacitor 204
7.1 Introduction 204
7.2 Materials 207
7.2.1 Preparation of graphene oxide (GO) 208
7.2.2 Preparation of N-doped reduced graphene oxide (N-rGO) 208
7.2.3 Electrochemical measurements 208
7.3 Physical characterization 209
7.4 Results and discussion 209
7.4.1 Electrochemical characterization 215
7.4.1.1 N-rGO//$Na_{0.44}MnO_2$ asymmetric supercapacitor characteristics 221
7.5 Summary 227
7.6 References 228
CHAPTER 8 234
Conclusions and recommendations 234
8.1 Conclusions 234
8.2 Recommendations for future work 236

APPENDIX A 238
APPENDIX B 243
APPENDIX C 248
APPENDIX D 250

List of Figures

Figure 2.1: Ragone plot depicting specific energy versus specific power for various energy storage and conversion devices [11]……. 16

Figure 2.2: Schematic of (a) conventional capacitor and (b) supercapacitor [26]……... 17

Figure 2.3: The classification of electrochemical capacitors based on their charge storage mechanism (Adapted from Ref. [27])…….....19

Figure 2.4: Models of the electrical double layer at a positively charged surface: (a) the Helmholtz model, (b) the Gouy–Chapman model and (c) the Stern model [(Adapted from Ref 32)]……21

Figure 2.5: EDLC with porous electrodes in a charged state with equivalent circuit (Adapted from [34])……..22

Figure 2.6: Energy storage mechanisms along with their electrochemical signatures: (a–c) electrical double layer capacitance, (d–f) surface redox capacitance, (g–i) intercalation capacitance and (j–l) faradic battery-type [39]…….....25

Figure 2.7: The fundamental configuration of the HSCs [49]……. 28

Figure 2.8: Electrochemical signatures of typical (a) hybrid and (b) asymmetric supercapacitors [39]……30

Figure 2.9: An illustration of a typical activated carbon structure with strongly disordered macropores (>50 nm), mesopores (2–50 nm) and micropores (less than 2 nm) (Adapted from [64])……..35

Figure 2.10: Schematic illustration of the difference between CNF and CF [79]……38

Figure 2.11: Schematic diagram of electrospinning PAN including basic electrospinning setup, Taylor cone and bending instability……..... 39

Figure 2.12: The 2D hexagonal nanosheets of graphene as a building block of other forms. An illustration of different allotropes of carbon arising from a graphene sheet (Adapted from Ref [99])……41

Figure 2.13: A three-electrode configuration using a battery-type Swagelok cell……...54

Figure 2.14: A two-electrode configuration using a battery-type Swagelok cell……...55

Figure 2.15: A representation of cyclic voltammograms of (a) an ideal capacitor, (b) a capacitor with resistivity and (c) pseudocapacitors [166]……. 58

Figure 2.16: GCD plot of (a) an EDLC (the figure inset illustrates the IR drop) and (b) a redox active pseudocapacitor or faradaic [166]……. 59

Figure 2.17: Phase shift φ in the current I as a response to a sinusoidal perturbation-potential V in a pseudo-linear system (Adapted from Ref [167])……..... 61

Figure 2.18: Nyquist plot with RCT and RΩ [168]……..... 63

Figure 3.1: Schematic representation of an SEM operation [4]…….....91

Figure 3.2: Schematic diagram of a typical TEM [6]……. 93

Figure 3.3: Rayleigh and Raman light scattering by molecules [10]……. 94

Figure 3.4: Schematic diagram of XPS operation [14]…….. 97

Figure 4.1: TEM images of a) Fe-Co@CFs, (b) CNT@CF network CFs (insert show high magnification), (c) N-CNT@CF network (insert show high magnification) and SEM images of (c) CFs, (d) CNT@CF network and (e) N-CNT@CF network……..109

Figure 4.2: P-XRD patterns of (a) CFs, CNTs, CNT@CF network and N-CNT@CF network, and (b, c, d, e) deconvoluted (002) diffraction peak of all materials……111

Figure 4.3: Raman spectra of (a) CFs, (b) CNTs, (c) CNT@CF network and (d) N-CNT@CF network…….....113

Figure 4.4: (a) BET adsorption desorption curve and (b) pore size distribution curve of the CNT@CF network and the N-CNT@CF network……..115

Figure 4.5: XPS survey spectra of CNT@CF network and N-CNT@CF network……116

Figure 4.6: XPS spectra showing deconvoluted C1s, N1s and O1s of CNT@CF and of N-CNT@CF networks…….....117

Figure 4.7: CV curves of (a) CFs, CNTs, CNT@CF and N-CNT@CF at 5 mV s^{-1} scan rates (b) GCD comparison of CFs, CNTs, CNT@CF and N-CNT@CF at 0.5 A g^{-1}; (c) Comparison of specific capacitance of at different current densities, (d) EIS measurements of all electrode materials……..120

Figure 4.8: (a) Log peak current vs log scan rate for CNT@CF, (b) Log peak current vs log scan rate for N-CNT@CF, (c, e) Comparison of the capacitive contribution and the diffusion-controlled contribution fraction for CNT@CF and N-CNTs/CF, and (d, f) histograms of the percentage contributions from 5-100 mV s^{-1}……123

Figure 4.9: CV curves of (a) CFs, CNTs, CNT@CF and N-CNT@CF at 50 mV s^{-1} scan rates (b): CV curves of N-CNT@CF at different scan rates, (c) GCD comparison of CFs, CNTs, CNT@CF and N-CNT@CF at 0.5 A g^{-1}; (d) Comparison of specific capacitance of at different current densities, (e) EIS measurements of CNT@CF and N-CNT@CF electrodes and (f) coulombic efficiency and capacitance retention of N-CNT@CF.....126

Figure 4.10: (a) Ragone plot and (b) image of 1.6 V red LED bulb lit up by N-CNT@CF supercapacitor…….....129

Figure 5.1: (a) Raman spectra of Ni/MOFDC and AT-Ni/MOFDC (the insert show typical deconvoluted Raman signal of carbon) and (b) XRD of the Ni-MOF, Ni/MOFDC and AT-Ni/MOFDC…….148

Figure 5.2: Deconvolved XPS scan of the electrocatalysts (a, b) Ni 2p, (c,d) C 1s and (e, f) O 1s…….150

Figure 5.3: TEM micrograms of (a) Ni/MOFDC, (b) AT-Ni/MOFDC and corresponding nanoparticles size distribution of (c) Ni/MOFDC and (d) AT-Ni/MOFDC……152

Figure 5.4: (a) CV curves, (b) GCD curves, (c) gravimetric specific capacity and (d) Nyquist plots of the Ni/MOFDC and AT-Ni/MOFDC for the three-electrode system……..155

Figure 5.5: (a) Log peak current vs log scan rate for Ni/MOF, (b) Log peak current vs Log scan rate for AT-Ni/MOF, (c) Comparison of the capacitive and diffusion-controlled contributions fraction for the AT-Ni/MOFDC at 5 mV s^{-1} and (d) histograms of the percentage contributions at 5–50 mV s^{-1}……158

Figure 5.6: (a) CV curves of N-CNT@CF and AT-Ni/MOFDC, (b) CV curves of N-CNT@CF//AT-Ni/MOFDC at different scan rates, (c) typical GCD curves of N-CNT@CF//AT-Ni/MOFDC at different current densities and (d) capacity versus current density plot…….....160

Figure 5.7: Electrochemical performance of the N-CNT@CF//AT-Ni/MOFDC hybrid device: (a) typical cycling performance at 5 A g^{-1}, (b) Nyquist plots obtained before and after 2,000 charge-discharge cycles, (c) Bode plots before and after 2,000 cycles of the N-CNT@CF//AT-Ni/MOFDC device and (d) comparative Ragone plot of this work with a symmetric N-CNT@CF//N-CNT@CF.....162

Figure 6.1: (a) SEM image (insert TEM image), (b) corresponding EDS spectrum and (c) EDS EDS mapping images of $Na_{0.44}MnO_2$.....178

Figure 6.2: (a) X-ray diffraction (XRD) pattern of $Na_{0.44}MnO_2$, (b) X-ray photoelectron spectroscopy (XPS) analysis, (b) full scan spectrum of $Na_{0.44}MnO_2$, (c) narrow scan of Na, (d) Mn 2p, (e) O 1s and (f) C 1s……180

Figure 6.3: The CV curves of $Na_{0.44}MnO_2$ in (a) 1M Na_2SO_4, (b) 3M NaOH and (c) 3M KOH medium at scan rate ranging from 5 to 50 mV/s. (d) Specific gravimetric and volumetric capacitance versus scan rate of $Na_{0.44}MnO_2$ under different aqueous electrolytes…….183

Figure 6.4: The GCD curves of $Na_{0.44}MnO_2$ in (a) 1M Na_2SO_4, (b) 3M NaOH and (c) 3M KOH medium at current densities ranging from 0.5 to 5 A g^{-1}, (d) Specific gravimetric and volumetric capacitance versus scan rate of $Na_{0.44}MnO_2$ under different aqueous electrolytes……..185

Figure 6.5: Presents (a) Nyquist plots and (b-d) Bode plots of $Na_{0.44}MnO_2$ in 1M Na_2SO_4, 3M NaOH and 3M KOH. Inset of (a) shows the magnified high-frequency region of Nyquist plots and the electrical circuit used in the fitting of the impedance data……...188

Figure 6.6: (a, c & e) Comparison of the capacitive and diffusion-controlled contributions fraction for $Na_{0.44}MnO_2$ at 20 mVs^{-1} in different electrolytes, (b, d & f) log peak current vs log scan rate for $Na_{0.44}MnO_2$ in different electrolytes……189

Figure 6.7: (a) CV curves of N-CNTs@CF and $Na_{0.44}MnO_2$, (b) CV curves of N-CNTs@CF//$Na_{0.44}MnO_2$ at different scan rates, (c) typical GCD curves of N-CNTs@CF//$Na_{0.44}MnO_2$ at different current densities and (d) capacitance versus current density plot……..192

Figure 6.8: Electrochemical performance of the N-CNTs@CF//$Na_{0.44}MnO_2$ asymmetric device: (a) cycling stability and coulombic efficiency of N-CNTs@CF//$Na_{0.44}MnO_2$ asymmetric device at 5 A g^{-1}, (b) Nyquist plots obtained before and after 5,000 charge-discharge cycles, (c) Bode plots before and after 5,000 cycles of the N-CNTs@CF//$Na_{0.44}MnO_2$ device and (e) comparative Ragone plot of this work with recent literature……..195

Figure 7.1: XRD spectrum of GO and N-rGO…… 211

Figure 7.2: (a) Raman spectrum of GO and N-rGO (b) deconvoluted 2D peaks of GO and (c) deconvoluted 2D peaks of N-rGO. 212

Figure 7.3: (a) XPS survey spectra of the N-rGO, (b) high resolution C1s XPS spectra, (c) high resolution O1s XPS spectra, (d) high resolution N1s XPS spectra. 214

Figure 7.4: TEM images of (a) GO and (b) N-rGO. 215
Figure 7.5: Half-cell electrochemical characterization of $Na_{0.44}MnO_2$ cathode material (a) CV plots of $Na_{0.44}MnO_2$ in different electrolytes collected at scan rates of 40 mV s^{-1}, (b) galvanostatic charging discharging plots collected at the current density of 0.5 A g^{-1}, (c) EIS measurements of $Na_{0.44}MnO_2$ electrode in different electrolytes (insert Randle circuit) and (d) variation of specific capacitance as a function of current density. 217
Figure 7.6: Half-cell electrochemical characterization of N-rGO anode material (a) CV plots of N-rGO in different electrolytes collected at scan rates of 40 mV s^{-1}, (b) galvanostatic charging discharging plots collected at the current density of 0.5 A g^{-1}, (c) EIS measurements of N-rGO electrode in different electrolytes and (d) variation of specific capacitance as a function of current density. 220
Figure 7.7: Electrochemical properties of the assembled ASC N-rGO//$Na_{0.44}MnO_2$ with AWIS as electrolyte (a) CV plots of negative electrode prepared using nitrogen-doped graphene oxide and positive electrode prepared using $Na_{0.44}MnO_2$ at a scan rate of 40 mV s^{-1} in AWIS electrolyte, (b) CV plots of ASC cell recorded at different scan rates, (c) GCD plots recorded at different current densities and (d) specific capacitance of at different current densities. 223
Figure 7.8: (a) Coulombic efficiency and capacity retention for 1,900 GCD cycles carried out at a current density of 5 A g^{-1}, (b) EIS measurement before and after 1,900 cycles, (c) Bode plots before and after 1,900 cycles of the N-rGO//$Na_{0.44}MnO_2$ device and (d) Ragone plot of the supercapacitor (energy density *vs*. power density). 226

List of Tables

Table 4.1: Surface parameters and elemental composition of hybrid materials…….114

Table 4.2: Comparison of capacitance of the present N-CNT@CF hybrid network with previously reported carbon composites electrode materials using 6 M KOH electrolyte.125

Table 4.3: EIS parameters for the electrode materials for two-electrode systems……...128

Table 5.1: Brunauer-Emmett-Teller (BET) analysis of the as-prepared Ni-MOF and the composites……..153

Table 5.2: EIS parameters for the electrode materials for three-electrode systems……157

Table 5.3: EIS parameters for N-CNT@CF//AT-Ni/MOFDC hybrid device before and after the 2,000th cycle……...161

Table 6.1: Brunauer-Emmett-Teller (BET) analysis of the as-prepared $Na_{0.44}MnO_2$.....180

Table 6.2: EIS fitting results of $Na_{0.44}MnO_2$ in three electrolytes……..187

Table 6.3: EIS parameters for N-CNTs@CF// $Na_{0.44}MnO_2$ asymmetric cell before and after the 5,000th cycle……...194

Table 7.1: Crystallographic parameters for GO and N-rGO……. 210

Table 7.2: Raman parameters for GO and N-rGO.....213

Table 7.3: EIS fitting results of $Na_{0.44}MnO_2$ in WIS and AWIS electrolytes.....217

Table 7.4: EIS fitting results of N-rGO in WIS and AWIS electrolytes.....219

Table 7.5: EIS parameters for N-rGO//$Na_{0.44}MnO_2$ asymmetric cell before and after the 1,900th cycles. 225

List of Schemes

Scheme 3.1: Fabrication of N-CNF@CF network by electrospinning and CVD method……...……..88

Scheme 3.3: Schematic illustrations of the synthesis of the Ni-MOF, Ni/MOFDC and AT-Ni/MOFDC…….89

Scheme 3.4: Schematic illustrations of the synthesis of the $Na_{0.44}MnO_2$.....90

LIST OF ABBREVIATIONS AND SYMBOLS

ACN	Acetonitrile
A	Area
A	Ampere
Å	Ångström
AC	Alternating current
Ag	Silver
Al	Aluminium
Ar	Argon
AT-Ni/MOFDC	Acid-treated nickel metal organic framework derived carbon
AWIS	Acetonitrile-water-in-salt
BE	Binding energy
BET	Brunauer-Emmet-Teller
BJH	Barret-Joyner-Halenda model
C	Carbon
C	Coulomb
C	Capacitance
C_{elec}	Electrode capacitance

C_1	Capacitance of electrode 1
C_2	Capacitance of electrode 2
C_{sp}	Specific capacitance
$C_{th,g}$	Theoretical specific capacitance
$C_{th,sp}$	Theoretical specific capacity
CB	Carbon black
CCD	Charge-coupled-device
CD	Charge-discharge
CE	Counter electrode
CF	Carbon fibre
CNFs	Carbon nanofibers
CNTs	Carbon nanotubes
Co	Cobalt
CPE	Constant phase element
CPE_{sf}	Constant phase element of the surface film
CPE*dl*	Constant phase element of the double layer capacitance
CV	Cyclic voltammetry
CVD	Chemical vapour deposition
d	Distance

E	Energy
E_{sp}	Energy density
EC	Electrochemical capacitor
EDLC	Electrical double layer capacitor
EDS	Energy dispersive X-ray spectroscopy
EDX	Energy dispersive X-ray spectroscopy
EEC	Electric equivalent circuit
EIS	Electrochemical impedance spectroscopy
EMD	Electrolytic manganese dioxide
ESR	Equivalent series resistance
eV	Electron-volt
F	Farad
F	Faraday's constant (9.64853×10^4 C)
f	Frequency
FEG-SEM	Field emission gun scanning electron microscope
g	Gram
h	Hour
Hz	Hertz
I	Current

I_t	Current response signal at time
IHP	Inner Helmholtz plane
JCPDS	Joint committee on powder diffraction standards
K^+	Potassium ions
KCl	Potassium chloride
KOH	Potassium hydroxide
kg	Kilogram
kV	Kilovolt
LED	Light emitting diode
Li	Lithium
LIB	Lithium-ion battery
m	Meter
m	Active material mass
mA	Milliampere
min	Minute
MOF	Metal organic framework
MnO_2	Manganese Dioxide
MWCNT	Multiwalled carbon nanotube
ms	Microsecond

mV	Millivolt
M*w*	Molecular weight
NaOH	Sodium hydroxide
$Na_{0.44}MnO_2$	Sodium manganese oxide
NMP	N-Methyl-2-pyrrolidone
Na_2SO_4	Sodium sulphate
n	Integer
N	Nitrogen
Ni	Nickel
nm	Nanometre
N-CNT@CF	Nitrogen-doped carbon nanotube-carbon fibre
O	Oxygen
P_{max}	Maximum power
P_{sp}	Power density
PVDF	Polyvinylidene fluoride
PXRD	Powder X-ray diffraction
q^+	Charge on positive electrode
q^-	Charge on negative electrode
R	Resistance

R_{ct}	Charge transfer resistance
R_f	Surface film resistance
R_s	Ohmic resistance of the solution
RE	Reference electrode
Redox	Reduction-oxidation
S	Mass, volume or geometric area
s	Second
S_{elec}	Mass, volume or area of an electrode
SEI	Solid electrolyte interphase
SEM	Scanning electron microscopy
SWCNT	Single-walled carbon nanotube
SSA	Specific surface area
T	Temperature
t	Time
t_d	Discharge time
TEA	Trimethylamine
TEM	Transmission electron microscopy
TMA	Trimeric acid
V	Volt

V	Voltage
vs	Versus
WIS	Water-in-salt
W	Watt
W kg^{-1}	Watt per kilogram
Wh kg^{-1}	Watt hour per kilogram
W_z	Warburg impedance
WE	Working electrode
XPS	X-ray photoelectron spectroscopy
XRD	X-ray diffraction
Z	Impedance
Z’	Resistance – the real part of the complex impedance
Z”	Reactance – the imaginary part of the complex impedance
Δt	Time window
ΔV	Voltage window
ΔV_{iRdrop}	Voltage drop
ΔV_{max}	Maximum voltage region
ε_0	Permittivity of free space
ε_r	Relative permittivity / dielectric constant

η	Coulombic efficiency
θ	Diffraction angle
λ	Wavelength
μm	Micro-meter
ν	Scan rate
φ	Phase shift angle
Ω	Ohm
ω	Angular frequency
1D	One-dimensional
2D	Two-dimensional
3D	Three-dimensional
º	Degree
ºC	Degree Celsius
%	Percent

CHAPTER 1

Introduction

In this chapter, the background and motivation for the study are briefly described. The chapter also includes the aim and objectives of the study, as well as the thesis outline.

1.1 Background and motivation

One of the biggest challenges facing humankind and planet earth in the modern era is, without a doubt, climate change. The anthropogenic signs and impacts of climate change are obvious for all mankind to see and experience. Climate change is believed to result from the ever-increasing human population and their reliance on burning fossil fuels for the production of energy. To date, fossil fuels play a dominant role in global energy systems, however, due to their high demands they are starting to deplete in some parts of the world [1]. Besides limited fossil fuel reserves, burning fossil fuels give rise to environmental pollution (air and water contamination and greenhouse gas emissions) which deteriorate the health and wellbeing of society's ecosystem [2].

Collateral to the above-mentioned problems, the migration to the fourth industrial revolution (4IR) also adds pressure on the energy sector to accelerate the sustainable production of renewable energy. The need to utilize environmentally clean energy resources and develop their technologies is a serious global goal. For the past two decades, different types of renewable energy production such as wind, solar, hydropower and ocean energy have been intensively investigated [3-5]. These energy resources are sustainable and environmentally friendly, however, they are intermitted in nature and depend on geographic conditions [6].

In South Africa, over 80 % of electricity produced by the national power utility company, the electricity supply commission (Eskom) is from coal-fired power plants [7]. Eskom has been struggling with mismanagement, debts and failing power plants for the past few years. As a result of these challenges, South Africans have been experiencing disrupted power supply (load-shedding) for certain hours in a day due to the inability of the power grid to cope with the high demand of energy at a given time. These power cuts do not only affect the living condition of ordinary South Africans but are also associated with a decline in industrialization and slow economic growth. The uncertainty of the supply of electricity has large economic implications since the industrial sector is the main economic contributor to South Africa's gross domestic product (GDP) [8].

Therefore, to avoid situations like load-shedding and uncertainty in the supply of electricity, the global energy landscape is changing rapidly towards the use of environmentally friendly and sustainable energy technologies. This is not different from the energy sector in South Africa, which has also started to join the world with the introduction of new technologies, including the use of roof-top solar photovoltaics and solar geysers. This paradigm shift towards the use of renewable energy can greatly reduce the demand for the supply of electricity faced by Eskom. South Africa is one of the most geographically privileged nations in the world, benefitting from high wind speeds in coastal areas and high solar irradiance in places like Northern Cape and Limpopo province. This places the country at an advantage to generate more electricity from renewable energy systems (RES). In addition, the generation of electricity from RES will not only help in diversifying the energy supply but also minimize the use of fossil fuels and hence reduce greenhouse gas emissions.

Nevertheless, due to the intermitted nature of renewable energy, a lot of concerns arise based on the feasibility of an uninterrupted autonomous supply of electricity from technologies such

as solar panels and wind turbines [9]. For example, the electricity produced from solar panels is more powerful in midday as compared to the evening and early hours of the morning where usually the demand is higher (peak-hours). Also, the sun does not shine all day and night, and the wind does not flow at high speeds based on our demands. In addition, the batteries currently used to store solar energy have low capacity. Consequently, solar and wind power alone or independently, are not yet sufficient solutions to deal with the increasing demand for energy [10]. Under this situation, the evolution of the next generation of large-scale energy storage systems is necessary to further improve or widen the utilization of renewable technologies. Supercapacitors and rechargeable batteries are examples of energy storage systems that use an electrochemical mechanism to store electricity. When these devices are coupled with renewable energy technologies, it is anticipated that the reliability and sustainability of solar and wind energy would be improved.

1.1.1 Energy storages systems

One of the main purposes of energy storage systems is to provide alternative energy when the primary source is inadequate. As mentioned earlier, the current stage of renewable energy systems faces challenges due to their significant fluctuations in electricity generation, especially during high power demands. In addition, when these technologies supply electricity off-grid (not connected to the power grid), storage devices are essential to maintain a constant power supply. Thus, when considering reliable and sustainable use of renewable energy technologies, electrochemical capacitors (ECs) and batteries take a centre stage for highly efficient energy storage and management.

There are different electrochemical storage devices used for different applications based on the specific power and energy required. Batteries are electrochemical energy storage devices that are famous because of their superior energy density characteristic. However, their low power

density and safety concerns (explosions and use of toxic chemicals) turn to limit their widespread application. On the other hand, electrochemical capacitors (ECs), also referred to as supercapacitors (SCs), have been widely investigated as advanced energy storage devices for decades ever since they were found to potentially complement batteries [11]. The energy storage in SCs arises from either an electrochemical double-layer or reversible redox reaction at the electrode/electrolyte interface. SCs are known for their high energy density compared with conventional capacitors and high-power density compared with batteries. Also, the electrode materials utilized in SCs remain relatively unchanged during charge/discharge cycles, which gives SCs excellent long cycle stability as compared to batteries. Therefore, SCs can deliver a considerable amount of energy within a short space of time (high power density) and can operate within a wide temperature range [12]. These characteristics make SCs have a wide potential application such as in portable electronics, electric vehicles, and energy harvesting systems like solar panels and wind turbines [11-14].

Based on their storage mechanisms, supercapacitors can be classified into three types: (i) electrochemical double-layer capacitors (EDLCs), (ii) pseudocapacitors and (iii) hybrid capacitors. The EDLCs physically store charges at the electrode/electrolyte interface by adsorption and desorption of electrolyte ions. Pseudocapacitors, on the other hand, use a redox reaction (Faradaic) a few nanometres from the electrode surface to store charges [16]. The hybrid capacitors use both the EDLCs and pseudocapacitance/battery-type storage mechanism. The electrode materials for the EDLCs are generally made of carbon, while those of pseudocapacitors are made of transition metal oxides or conductive polymers. Different kinds of electrolytes such as aqueous and organic are normally used in SCs.

The performance of the SCs device is mainly determined by the electrode material, electrolyte, and cell configuration. However, most of the investigations have been done on electrode

materials. The common electrode materials are carbon-based materials [17], metal oxides [18], and polymers [19]. Among these electrode materials, carbon-based materials have received the most attention because of their desirable properties such as low cost, high specific surface area, high conductivity and chemical stability, making them the model electrode material for SCs.

Different types of carbon materials such as activated carbon, carbon nanotubes (CNTs), carbon nanofibers (CNFs), carbon spheres (CSs) and graphene were used before as electrode materials for SCs [17]. However, even though these materials show promising electrochemical performance, they suffer from low energy density, which turns to limit their widespread application for SCs. Thus, scientists and engineers have looked at different ways to improve the energy density of carbon materials. This led to the development of new synthesis methods which enables functionalization and the fabrication of different carbon morphologies that can improve the energy storage properties of carbonaceous materials.

In recent years, a lot of efforts have been done to develop carbon-based composite/hybrid electrodes for SCs. Different kinds of composites such as carbon nanotube/carbon nanofibers (CNTs/CNFs) [20], graphene/CNTs [21] and MnO_2@CNFs [22] have been used as electrodes for supercapacitors. These composite materials have been reported to have enhanced physiochemical and electrochemical properties compared to their components [23]. The enhanced properties are attributed to the synergy among the individual components which turn to make the composites to be multifunctional materials.

Furthermore, it has been stated that heteroatom doping of carbon materials with nitrogen or boron improves the electrochemical properties of carbon electrodes [24]. Heteroatoms can alter the electronic properties of carbonaceous materials and increase charge carrier density, causing surface redox reactions. In addition, the electronic conductivity, surface wettability and

capacitance of heteroatom-doped carbon are enhanced by these changes in the carbon matrix [25, 26].

The essence of charge storage in Faradaic materials is controlled by redox reactions on the surface of the material. The Faradaic electrochemical processes arise both on the surface and in the bulk near the surface of the electrode [27]. As a result, Faradaic materials play a critical role in providing high specific capacity and energy at the same time, which is an advantage in energy storage devices [28]. Pseudocapacitors are very much different from EDLCs in their nature of charge storage, in that they are governed by a chain of Faradaic reactions and store energy through fast redox reaction [29]. The reversible redox reaction at the surface of the electrode material, contributes more storage charge than EDLC materials, resulting in a higher capacitance.

Hybrid device, on the contrary, use both the properties of the EDLCs and the pseudocapacitive/battery-type electrode materials in a two-electrode system. Thus, since the hybrid device uses a configuration with a Faradaic electrode and a non-Faradaic electrode, the hybrid device can overcome the energy density constraint of traditional EDLCs, resulting in higher energy density [30].

Ni-based materials have attracted more attention as battery-type electrode materials, due to their well-defined redox nature, high theoretical specific capacity and good chemical compatibility in alkaline medium [31]. However, Ni-based materials have some drawbacks, such as low electrical conductivity, low-rate performance and short lifespan, which make them difficult to use in high-performance SCs [32]. The most effective way to crack this bottleneck is to use Ni-based materials as hybrid electrodes with electrical double-layer capacitor materials, which is known to improve electrical conductivity, energy density and cycle stability. However, because of the poor binding force between Ni-based materials and carbon-

based materials, as well as the lack of active sites in Ni-based materials, charge separation is often slow, reducing the synergistic effect between Ni metal and carbon species [33].

Na-ion capacitors (NICs), on the other hand, have attracted a lot of research attention due to their high energy density [34]. The NICs are usually assembled by a Faradaic sodium-intercalation positive electrode (such as $NaMnO_2$) with a non-Faradaic capacitive negative electrode (typically a carbonaceous material) in an aqueous electrolyte. The Faradaic sodium-intercalation materials deliver high energy, while the non-Faradaic capacitive material provides high power density and excellent cycling stability. The trade-off between the power density and energy density of the NICs provides an opportunity to effectively improve energy density. The majority of NICs, on the other hand, have low power densities and poor cycling stability [35]. As a result, enhancing cycling life and rate capability without losing energy density remains a significant challenge in the development of high energy density capacitors. This exciting path could be realized if electrode materials and electrolytes are properly chosen.

The electrode materials used in this study were composite materials made up of carbon and transition-metal oxides, which were combined in an asymmetric system to improve the energy density and cyclic stability of hybrid supercapacitors.

1.2 Aim and objectives

1.2.1 Aim

This research was aimed at synthesizing and characterizing 3D hierarchical nitrogen-doped carbon nanotube grown on top of carbon nanofiber (N-CNT@CF), nickel-based metal-organic frameworks derived carbon (Ni/MOFDC) and sodium manganese oxide ($Na_{0.44}MnO_2$) as enhanced electrodes for supercapacitor application.

1.2.2 Objectives

The research objectives are as follows:

- To synthesize polyacrylonitrile (PAN) nanofibers fibres using the electrospinning technique.
- To grow nitrogen-doped carbon nanotubes (N-CNTs) on top of carbon nanofibers.
- To synthesize nickel-starved metal-organic framework derived carbon (AT/Ni-MOFDC).
- To synthesize sodium manganese oxide ($Na_{0.44}MnO_2$).
- To study the structure, morphology and composition of the synthesized materials.
- To investigate the electrochemical properties and performance of the N-CNT@CF hybrid for symmetric supercapacitor in an aqueous electrolyte.
- To investigate the electrochemical properties and performance of the N-CNT@CF //AT/Ni-MOFDC for asymmetric supercapacitor in an aqueous electrolyte.
- To investigate the electrochemical properties and performance of the N-CNT@CF //$Na_{0.44}MnO_2$ in asymmetric capacitors in different electrolytes.
- To investigate the electrochemical properties and performance of the N-rGO //$Na_{0.44}MnO_2$ in asymmetric capacitors using "water-in-salt" electrolytes.

1.3 Thesis outline

The following are the chapters that make up this thesis:

Chapter 1: Is the introductory chapter giving the research background, the motivation for the study and the aim and objectives of the study.

Chapter 2: Details the literature review that gives the background and core principles of energy storage devices and particularly symmetric and asymmetric supercapacitors. Materials for electrodes are also reviewed.

Chapter 3: Presents the experimental methods which include material fabrication and characterization techniques used in the study.

Chapter 4: Provides the results and discussion of N-CNT@CF//N-CNT@CF symmetric supercapacitor.

Chapter 5: Provides the results and discussion of the N-CNT@CF//AT/Ni-MOFDC hybrid supercapacitor work.

Chapter 6: Provides the results and discussion of the N-CNT@CF//$Na_{0.44}MnO_2$ asymmetric supercapacitors.

Chapter 7: Provides the electrochemical results and discussion of the N-rGO//$Na_{0.44}MnO_2$ asymmetric supercapacitor using water-in-salt electrolytes.

Chapter 8: Provides the concluding remarks and recommendations for future work.

1.4 References

[1] Johnsson, F., Kjärstad, J. and Rootzén, J., 2019. The threat to climate change mitigation posed by the abundance of fossil fuels. *Climate Policy*, **19**, pp.258-274.

[2] Zhong, C., Deng, Y., Hu, W., Qiao, J., Zhang, L. and Zhang, J., 2015. A review of electrolyte materials and compositions for electrochemical supercapacitors. *Chemical Society Reviews*, **44**, pp.7484-7539.

[3] Rosales-Asensio, E., Borge-Diez, D., Blanes-Peiró, J.J., Pérez-Hoyos, A. and Comenar-Santos, A., 2019. Review of wind energy technology and associated market and economic conditions in Spain. *Renewable and Sustainable Energy Reviews*, **101**, pp.415-427.

[4] Mekhilef, S., Saidur, R. and Safari, A., 2011. A review on solar energy use in industries. *Renewable and Sustainable Energy Reviews*, **15**, pp.1777-1790.

[5] Chu, S. and Majumdar, A., 2012. Opportunities and challenges for a sustainable energy future. *Nature*, **488**, pp.294-303.

[6] Georgeson, L., Maslin, M. and Poessinouw, M., 2016. Clean up energy innovation. *Nature News*, **538**, p.27.

[7] Yoro, K.O. and Sekoai, P.T., 2016. The potential of CO_2 capture and storage technology in South Africa's coal-fired thermal power plants. *Environments*, **3**, p.24.

[8] Ateba, B.B., Prinsloo, J.J. and Gawlik, R., 2019. The significance of electricity supply sustainability to industrial growth in South Africa. *Energy Reports*, **5**, pp.1324-1338.

[9] De Groot, R.A.F., Van der Veen, V.G. and Sebitosi, A.B., 2013. Comparing solar PV (photovoltaic) with coal-fired electricity production in the centralized network of South Africa. *Energy*, **55**, pp.823-837.

[10] Kim, H., Park, K.Y., Hong, J. and Kang, K., 2014. All-graphene-battery: bridging the gap between supercapacitors and lithium ion batteries. *Scientific Reports*, **4**, pp.1-8.

[11] Kim, B.K., Sy, S., Yu, A. and Zhang, J., 2015. Electrochemical supercapacitors for energy storage and conversion. *Handbook of Clean Energy Systems*, pp.1-25.

[12] Hung, K., Masarapu, C., Ko, T. and Wei, B., 2009. Wide-temperature range operation supercapacitors from nanostructured activated carbon fabric. *Journal of Power Sources*, **193**, pp.944-949.

[13] Cao, X., Yin, Z. and Zhang, H., 2014. Three-dimensional graphene materials: preparation, structures and application in supercapacitors. *Energy & Environmental Science*, **7**, pp.1850-1865.

[14] Libich, J., Máca, J., Vondrák, J., Čech, O. and Sedlaříková, M., 2018. Supercapacitors: Properties and applications. *Journal of Energy Storage*, **17**, pp.224-227.

[15] Rosas-Laverde, N.M., Pruna, A. and Busquets-Mataix, D., 2020. Improving electrochemical properties of polypyrrole coatings by graphene oxide and carbon nanotubes. *Nanomaterials*, **10**, p.507.

[16] Zhu, S., Li, L., Liu, J., Wang, H., Wang, T., Zhang, Y., Zhang, L., Ruoff, R.S. and Dong, F., 2018. Structural directed growth of ultrathin parallel birnessite on β-MnO_2 for high-performance asymmetric supercapacitors. *ACS Nano*, **12**, pp.1033-1042.

[17] Dubey, R. and Guruviah, V., 2019. Review of carbon-based electrode materials for supercapacitor energy storage. *Ionics*, **25**, pp.1419-1445.

[18] An, C., Zhang, Y., Guo, H. and Wang, Y., 2019. Metal oxide-based supercapacitors: progress and prospectives. *Nanoscale Advances*, **1**, pp.4644-4658.

[19] Meng, Q., Cai, K., Chen, Y. and Chen, L., 2017. Research progress on conducting polymer based supercapacitor electrode materials. *Nano Energy*, **36**, pp.268-285.

[20] Qiu, Y., Li, G., Hou, Y., Pan, Z., Li, H., Li, W., Liu, M., Ye, F., Yang, X. and Zhang, Y., 2015. Vertically aligned carbon nanotubes on carbon nanofibers: A hierarchical three-dimensional carbon nanostructure for high-energy flexible supercapacitors. *Chemistry of*

Materials, **27**, pp.1194-1200.

[21] Díez, N., Botas, C., Mysyk, R., Goikolea, E., Rojo, T. and Carriazo, D., 2018. Highly packed graphene–CNT films as electrodes for aqueous supercapacitors with high volumetric performance. *Journal of Materials Chemistry A*, **6**, pp.3667-3673.

[22] Wu, D., Xie, X., Zhang, Y., Zhang, D., Du, W., Zhang, X. and Wang, B., 2020. MnO_2/carbon composites for supercapacitor: Synthesis and electrochemical performance. *Frontiers in Materials*, **7**, p.2.

[23] Alali, K.T., Liu, J., Liu, Q., Li, R., Aljebawi, K. and Wang, J., 2019. Grown carbon nanotubes on electrospun carbon nanofibers as a 3D carbon nanomaterial for high energy storage performance. *ChemistrySelect*, **4**, pp.5437-5458.

[24] Abbas, Q., Raza, R., Shabbir, I. and Olabi, A.G., 2019. Heteroatom doped high porosity carbon nanomaterials as electrodes for energy storage in electrochemical capacitors: A review. *Journal of Science: Advanced Materials and Devices*, **4**, pp.341-352.

[25] Jiang, L., Yang, S., Song, W., Zhao, J., Lu, Z., Zhai, Q. and Wang, J., 2020. A simple and green preparation method of nitrogen-doped carbon nanocages for supercapacitor application. *ChemNanoMat*, **6**, pp.308-315.

[26] Wu, J., Pan, Z., Zhang, Y., Wang, B. and Peng, H., 2018. The recent progress of nitrogen-doped carbon nanomaterials for electrochemical batteries. *Journal of Materials Chemistry A*, **6**, pp.12932-12944.

[27] Wang, G., Zhang, L. and Zhang, J., 2012. A review of electrode materials for electrochemical supercapacitors. *Chemical Society Reviews*, **41**, pp.797-828.

[28] Peng, X., Peng, L., Wu, C. and Xie, Y., 2014. Two dimensional nanomaterials for flexible supercapacitors. *Chemical Society Reviews*, **43**, pp.3303-3323.

[29] Li, H., Wang, B., He, X., Xiao, J., Zhang, H., Liu, Q., Liu, J., Wang, J., Liu, L. and Wang, P., 2015. Composite of hierarchical interpenetrating 3D hollow carbon skeleton

from lotus pollen and hexagonal MnO_2 nanosheets for high-performance supercapacitors. *Journal of Materials Chemistry A*, **3**, pp.9754-9762.

[30] Naoi, K., 2010. 'Nanohybrid capacitor': The next generation electrochemical capacitors. *Fuel Cells*, **10**, pp.825-833.

[31] Zhang, Z., Huo, H., Gao, J., Yu, Z., Ran, F., Guo, L., Lou, S., Mu, T., Yin, X., Wang, Q. and Yin, G., 2019. Ni-MOF derived NiO/C nanospheres grown in situ on reduced graphene oxide towards high performance hybrid supercapacitor. *Journal of Alloys and Compounds*, **801**, pp.158-165.

[32] Salunkhe, R.R., Kaneti, Y.V. and Yamauchi, Y., 2017. Metal–organic framework-derived nanoporous metal oxides toward supercapacitor applications: progress and prospects. *ACS Nano*, **11**, pp.5293-5308.

[33] Liu, Z., Chen, Z. and Yu, F., 2018. Microencapsulated phase change material modified by graphene oxide with different degrees of oxidation for solar energy storage. *Solar Energy Materials and Solar Cells*, **174**, pp.453-459.

[34] Wang, F., Wang, X., Chang, Z., Wu, X., Liu, X., Fu, L., Zhu, Y., Wu, Y. and Huang, W., 2015. A quasi-solid-state sodium-ion capacitor with high energy density. *Advanced Materials*, **27**, pp.6962-6968.

[35] Ajuria, J., Redondo, E., Arnaiz, M., Mysyk, R., Rojo, T. and Goikolea, E., 2017. Lithium and sodium ion capacitors with high energy and power densities based on carbons from recycled olive pits. *Journal of Power Sources*, **359**, pp.17-26.

CHAPTER 2

Literature review

2.1 Energy storage systems

Since the discovery of electricity, a lot of research work has been done to look for effective methods to store energy and release it when required [1, 2]. This is even more important nowadays due to the vast utilization of intermitted renewable energy-based technologies such as solar and wind power. Energy storage systems in renewable energy are mainly used to store electricity during periods of relatively high production and low demand, then release it back to the electric power grid during periods of lower production or higher demand [3, 4]. In most cases, energy storage may provide economic, reliable and environmental benefits. However, this depends on the extent to which it is deployed. Energy storage could help the utility grid operate more efficiently, reduce the likelihood of blackouts (load-shedding) during peak demand and allow for more renewable resources to be built and utilised. They are four main categories of energy storage: (i) mechanical energy storage, (ii) thermal energy storage, (iii) chemical energy storage and (iv) electrochemical energy storage. This thesis will only focus on different types of electrochemical energy storage devices.

Energy storage and release in an electrochemical device occur in two fundamentally different ways: (i) *via* the Faradaic process where oxidation and reduction reactions take place between the electrolyte and electrode material and (ii) through non-Faradaic electrostatic interactions [5]. In a Faradaic reaction, chemical potential energy is stored and released through redox reactions of electrochemically active species, while in a non-Faradaic interaction, the energy is

stored electrostatically. Lithium-ion batteries (LIBs), lead-acid batteries and capacitors are the three most popular electrochemical storage devices used in our society. High-energy-density batteries and high-power-density capacitors are currently being considered to meet rising energy demands [6]. Capacitors are categorized into three groups: (i) electrostatic capacitors, (ii) electrolytic capacitors and (iii) electrochemical capacitors [7].

Electrochemical capacitors (ECs), also referred to as ultracapacitors or supercapacitors, are devices that store energy and are currently being researched in a variety of academic and industrial laboratories since they can be used as complementary charge storage devices to traditional batteries in a variety of applications requiring peak power pulses [8]. A supercapacitor is a type of energy storage device that possesses higher energy density than conventional capacitors. Also, supercapacitors often have capacitances that are several orders of magnitude greater than conventional capacitors [9]. This device can store ten to one hundred times more energy per unit volume/mass compared to the conventional capacitor, accept and release charge much faster than batteries and withstand far more charge and discharge cycles than rechargeable batteries [10]. The Ragone plot (**Figure 2.1**) depicts comparisons within the energy storage systems.

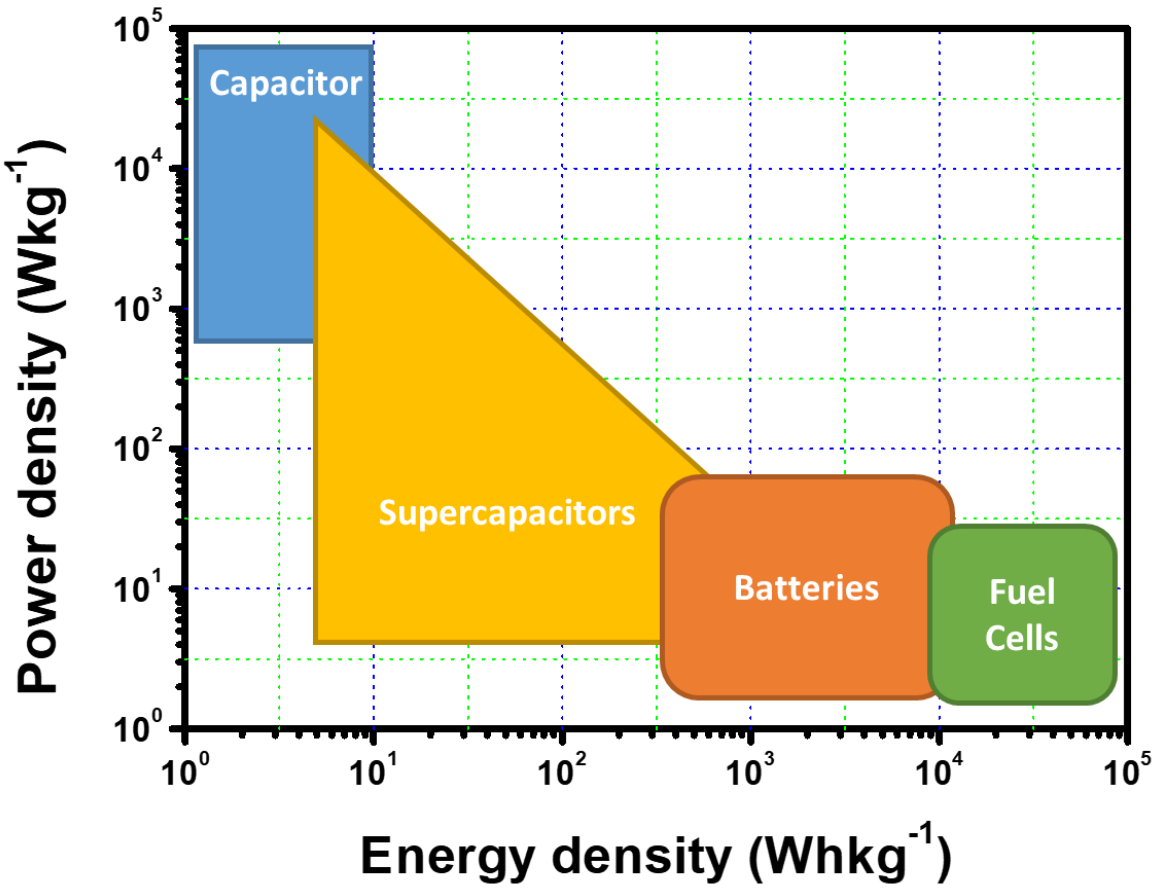


Figure 2.1: Ragone plot depicting specific energy versus specific power for various energy storage and conversion devices [11].

As it can be seen from the Ragone plot, batteries generally have higher energy densities than supercapacitors but suffer from low power density. Supercapacitors have superior electrochemical properties compared to secondary batteries, such as high-power density, long cycling performance [12]. Furthermore, supercapacitors have excellent reversibility and stability over a wide temperature range [13-15], while during the charge-discharge process, battery materials experience irreversible phase shifts, thereby dramatically reducing their life cycle [16, 17]. Therefore, when a high-power density system with rapid charging and discharging is needed, supercapacitors are an attractive energy storage device.

2.2 Supercapacitors

Supercapacitors (SCs) are energy storage devices that work similarly to conventional capacitors. However, unlike conventional capacitors, which store charge by accumulating it at the two electrodes, SCs uses a slightly different mechanism. SCs store energy using two different surface phenomena: “electrochemical double-layer (EDL)” and “surface redox reactions”. The former is based on non-Faradaic charge separation at the double-layer (e.g., electrode/electrolyte interface), while the latter is based on fast Faradaic redox reactions of electroactive materials at the interface [18, 19]. SCs operate by passing a voltage between two electrodes (cells) merged between an ion-permeable separator that prevents electrical contact (short-circuiting) while allowing electrolyte ions to pass between the electrode and the electrolyte solution, whereas, in a conventional capacitor, the electrodes are separated by an insulating layer that holds the charges apart when a voltage is applied, as illustrated in **Figure 2.2** [20, 21]. Unlike conventional capacitors, SCs use porous materials, such as carbonaceous materials like carbon nanotubes (CNTs) [22], carbon nanofibers (CNFs) [23], graphene [24] and activated carbon [25]. This enables a large amount of charge to be stored, resulting in incredibly high capacitance that is higher than conventional capacitors.

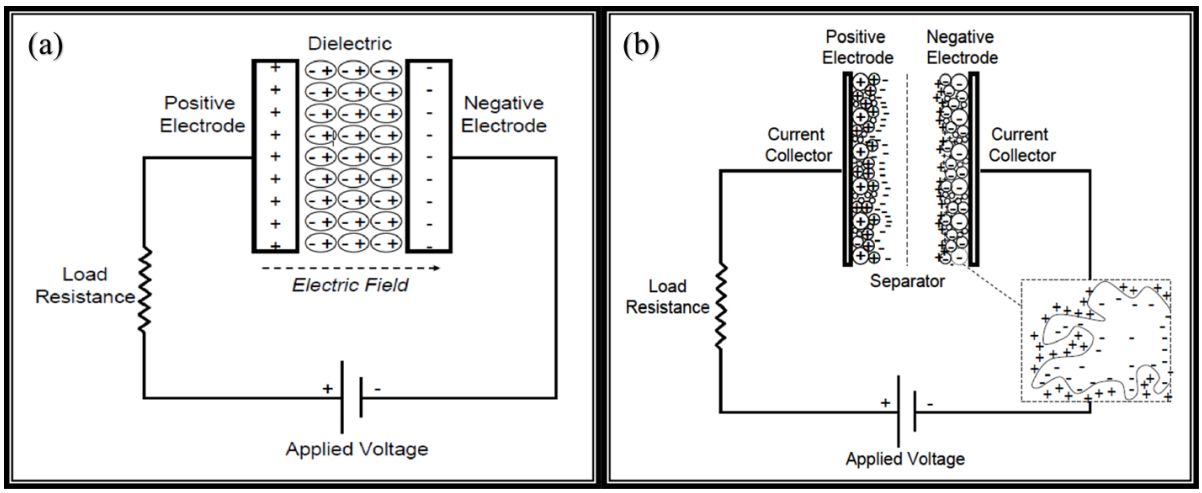


Figure 2.2: Schematic of (a) conventional capacitor and (b) supercapacitor [26].

2.3 Energy storage principle in SCs

Based on their energy storage mechanism, SCs are classified into three categories:

i. Electric double-layer capacitors (EDLCs) arising from the build-up of charges at the electrolyte/electrode interface.
ii. Pseudocapacitors is related to the storage from fast redox reactions.
iii. Hybrid capacitors combine the individual characteristics of both EDLC and pseudocapacitors and can be arranged in various architectures to form different subgroups.

The performance of SCs is largely controlled by the energy storage mechanism, the materials used for electrodes, the type of electrolyte and device assembly. **Figure 2.3** displays a flow chart that portrays each of these supercapacitor groups in terms of charge storage mechanism.

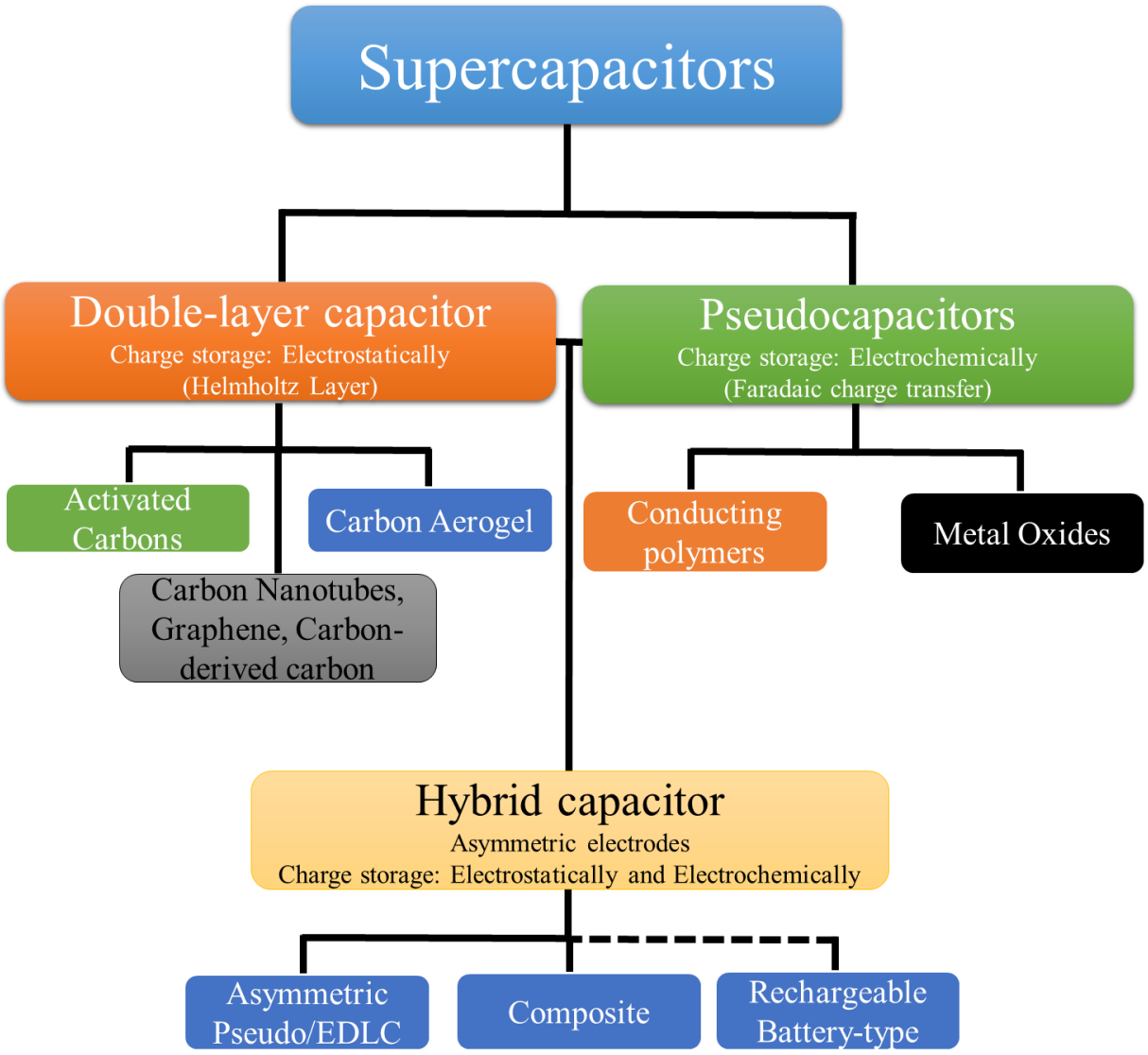


Figure 2.3: The classification of supercapacitors based on their charge storage mechanism (Adapted from Ref. [27]).

2.4 Energy storage mechanism of SCs

2.4.1 Electric double-layer capacitance (EDLC)

When potential is applied across the EDLCs device, accumulation and release of electrostatic charge occur *via* a withdrawal or deposition of electrons in the anode or cathode [28]. The positive or negatively charged surface is balanced by an accumulation of oppositely charged ions from the electrolyte forming a double-layer of positive-negative charges (and vice-versa)

that ideally remains electrostatic having no electron transfers between the layers throughout the process. The concept of EDLC was discovered by von Helmholtz in the 19th century and is well known as the "Helmholtz double layer" model [29, 30].

According to the Helmholtz double-layer model, two layers with different charges condense between the electrode and electrolyte separated by an atomic distance, as shown in **Figure 2.4a**. With two planar electrodes separated by a small gap, this arrangement is identical to traditional dielectric capacitors [31]. The capacitance estimation for the EDLC is generally calculated using equation 2.1:

$$C = \frac{\varepsilon_r \varepsilon_o A}{d} \tag{2.1}$$

where ε_r denotes the electrolyte permittivity, ε_o denotes the dielectric constant or permittivity of vacuum, A denotes the surface area of the active material and *d* is the thickness of the electric double-layer.

After Helmholtz proposed the double-layer model, Gouy and Chapman modified the model (see **Figure 2.4b**) by using a diffusion layer in the electrolyte to account for the continuous distribution of electrolyte ions (both cations and anions) induced by thermal motion [32].

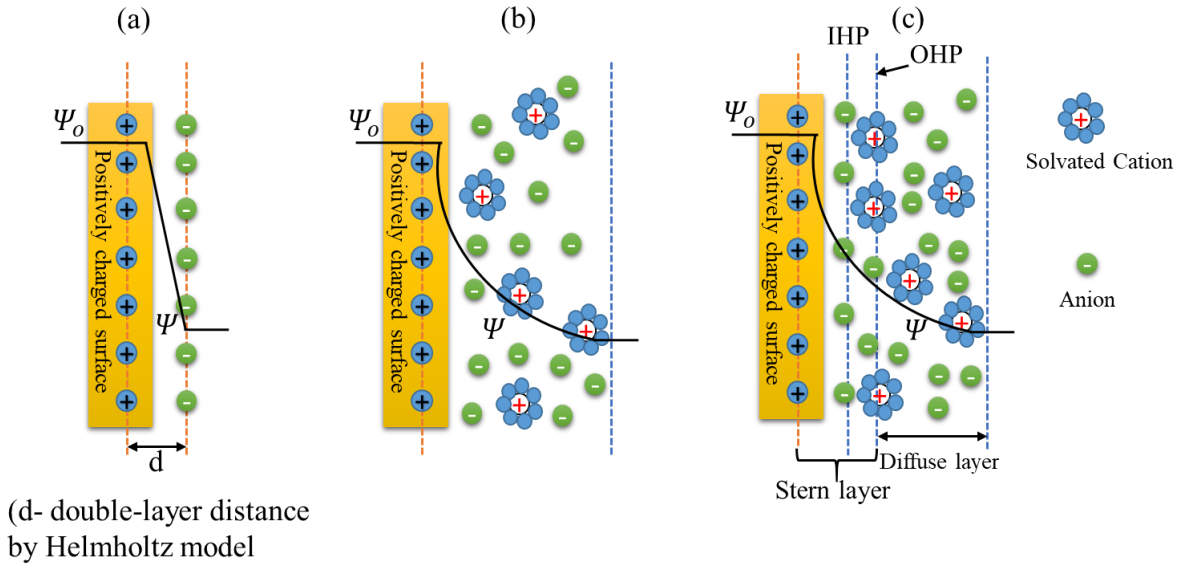


Figure 2.4: Models of the electrical double layer at a positively charged surface: (a) the Helmholtz model, (b) the Gouy–Chapman model and (c) the Stern model (Adapted from Ref [32]).

Stern later merged the Helmholtz and Gouy-Chapman models because the Helmholtz and Gouy-Chapman models did not account for a variety of important factors. The Helmholtz model omitted the diffusion of the ions within the electrolyte, together with the relationship between the electrolyte dipole moment and the active material. Two ionic transport areas are involved in the Stern model: the diffuse layer and the inner layer (Stern layer or compact layer) as shown in **Figure 2.4c** [33]. Adsorbed ions make up the compact layer. These adsorbed ions are grouped into two types: (i) the inner Helmholtz plane (IHP) and (ii) the outer Helmholtz plane (OHP) [32]. Consequently, the overall capacitance in the EDLC can be thought of as the sum of these two regions: (i) the Stern type of compact double layer capacitance (C_H) and (ii) the diffusion region capacitance (C_{Diff}) and is expressed as in equation 2.2 [32].

$$\frac{1}{C_S} = \frac{1}{C_H} + \frac{1}{C_{Diff}} \qquad (2.2)$$

In an EDLC device, the electrochemical performance of the active material is controlled by the electric field across the electrode, the electrolyte ions, the solvent used to dissolve the

electrolyte ions and the chemical affinity between the electrode material and the electrolyte ions. The EDLC electrode is usually made of porous materials like CNTs, CNFs, graphene, and activated carbon, hence, the charge storage behaviour on the inner surface is more complicated than on the outer surface. The porosity, electrolyte resistance and the wettability of the electrode surface by the electrolyte all influence the EDLC behaviour. The EDLCs are similar to batteries in construction, however, the difference is that in EDLCs both the cathode and anode are porous materials such as activated carbons (ACs) coated on a current collector and placed between an ion-permeable separator. The charges at the electrodes are polarized when voltage is applied, with an equivalent number of oppositely charged electrolyte ions at the surface of the electrode material, as illustrated in **Figure 2.5**.

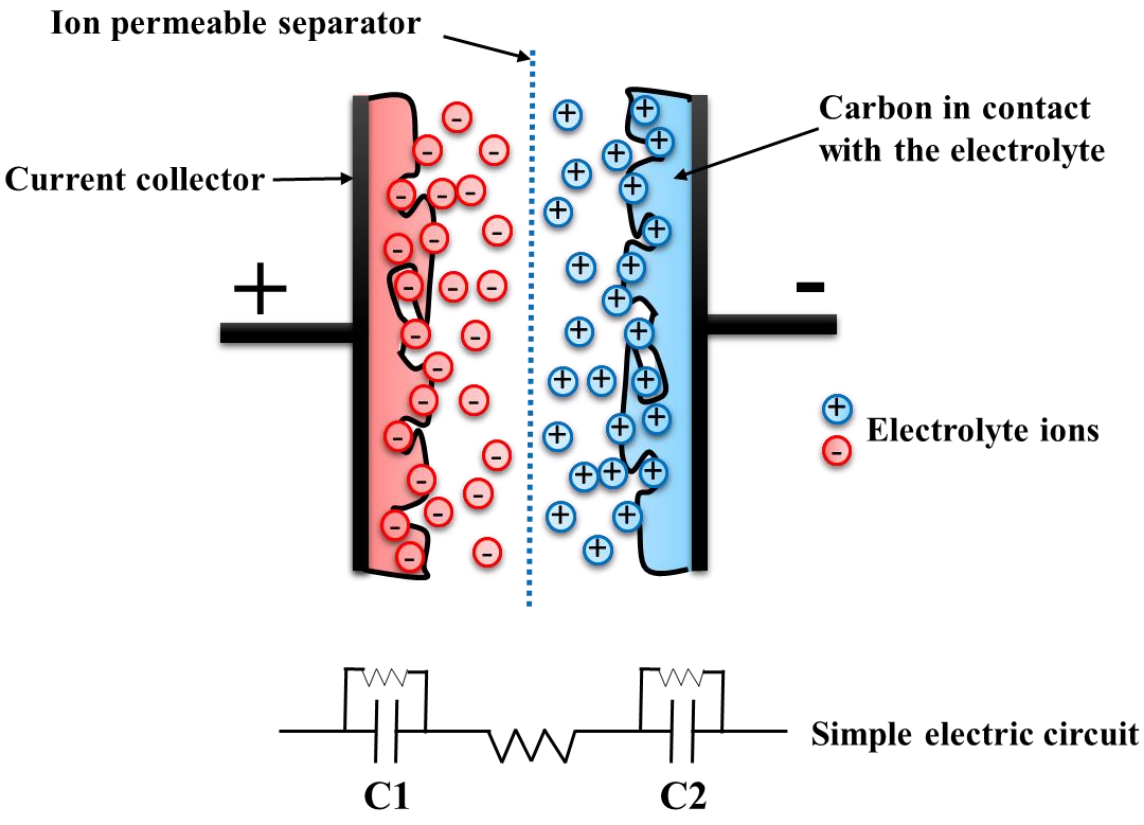


Figure 2.5: EDLC with porous electrodes in a charged state with equivalent circuit (Adapted from [34]).

2.4.2 Pseudocapacitors

The term “pseudocapacitance” was first defined by Conway to describe materials with electrochemical signatures (i.e., cyclic voltammetry (CV) and galvanostatic charge-discharge (GCD)) that are similar to those of EDLC capacitors, but with a different charge storage mechanism [35]. On the other hand, pseudocapacitive reactions are Faradaic, storing electrical energy at or near the electrode surface through quick and reversible redox reactions. Since charge storage involves redox reactions, the electrode material reacts similarly to a battery. However, the electrochemical response shows quasi-rectangular CVs and close to linear GCD curves, which are similar to the EDLCs, suggesting surface redox reactions not constrained by solid-state diffusion [36, 37]. Materials undergoing such redox reactions include several metal oxides, such as RuO_2, MnO_2 and Co_3O_4 and conducting polymers (CP) [38]. There are two key charge storage mechanisms in pseudocapacitive materials: (i) surface redox pseudocapacitance and (ii) intercalation pseudocapacitance, which are both described in the subsequent sections.

2.4.2.1 Surface redox pseudocapacitors

The charge-storage process in pseudocapacitors results from charge transfer near the surface of the electrode. As shown in **Figure 2.6d–f,** the CV and GCD profiles for surface-redox pseudocapacitors are similar to those of EDLCs (**Figure 2.6a–c**), implying that charge storage and the entire potential window are linearly related [39]. But this does not suggest that pseudocapacitors only store charges using the double layer mechanism. Surface redox pseudocapacitive materials store charges using both faradaic and non-faradaic mechanisms [39]. The materials that show this kind of electrochemistry signature are referred to as intrinsic pseudocapacitive materials. RuO_2 and MnO_2 are the most studied intrinsic pseudocapacitive materials. These materials can store charge in two ways: (i) through Faradaic electron transfer by accessing two or more redox states of metal centres (e.g., Mn(III) and Mn(IV)) and (ii) by

non-Faradaic charge storage in the electrochemical double layer present at the surface of these materials [35]. Using MnO_2 as an example**, Figure 2.6(e, f)** depicts the electrochemical response of redox pseudocapacitors. MnO_2 stores charges in the +4 and +3 oxidation states of manganese by surface redox reactions as shown in equation 2.3 [40].

$$MnO_2 + x\ A^+ + xe^- \leftrightarrow A_xMnO_2 \quad (2.3)$$

The symbol "A" in the above reaction system represents an alkali metal cation (e.g., Li^+, Na^+or K^+)

The two distinct mechanisms (EDLC and pseudocapacitance) are induced by separate physical processes and electrode materials. Therefore, the relationship between potential and charges accumulated at the electrode/electrolyte interface or within the inner surface of the electrode material can be explained by their electrochemical characteristics [39]. As a result, without these electrochemical characteristics, the materials cannot be labelled as pseudocapacitive.

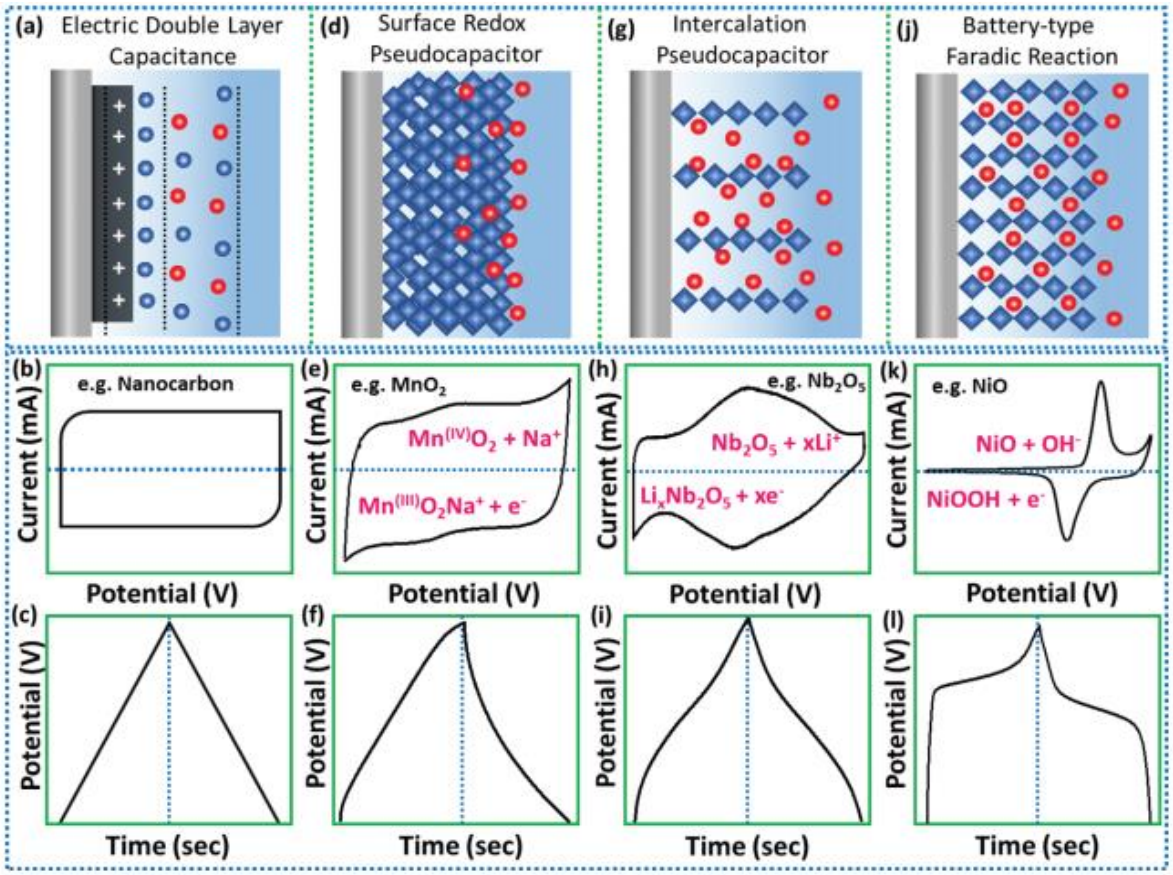


Figure 2.6: Energy storage mechanisms along with their electrochemical signatures: (a–c) electrical double layer capacitance, (d–f) surface redox capacitance, (g–i) intercalation capacitance and (j–l) faradic battery-type [39].

2.4.2.2 Intercalation pseudocapacitors

As shown in **Figure 2.6g-i**, the intercalation pseudocapacitor process involves the incorporation of an electrolyte ion into the bulk lattice of the redox-active material with a Faradaic charge transfer. During insertion, several electrons are transferred to the host to preserve the electrical neutrality of the electrode [40]. Furthermore, the current is normally proportional to scan rate and peak potentials do not change significantly with scan rate. Another key characteristic is that phase transformations of the materials does not occur during intercalation. Equation 2.4 describes the general reaction mechanism of intercalation pseudocapacitors:

$$MA_y + x\ Li^+ + xe^- \leftrightarrow Li_xMA_y \quad (2.4)$$

In the above reaction mechanism, the symbol MA_y represents metal oxide such as TiO_3. In comparison to EDLCs, the charge storage mechanism for the intercalation pseudocapacitance is not confined to the surface, allowing for the reversible faradic electrochemical reactions to take place in the bulk of the materials, as shown in **Figure 2.6g-i** [39, 41].

2.4.2.3 Battery-type Faradaic reaction

One of the hottest debated topics in electrochemistry is the difference between pseudocapacitive and batteries-type electrodes [35, 39, 42]. This is due to the misunderstanding of battery-type electrodes being reported as pseudocapacitor [43]. It is advised that when analysing electrochemical data on a new nanomaterial, the first question a researcher can ask is whether the material is battery-like or capacitor-like. When it comes to redox reactions, traditional battery-type electrode materials vary from capacitor-like electrode materials in that phase changes of electrode materials occurs during the electrochemical process. Therefore, battery-type electrodes clearly show separate oxidative and reductive peaks from their CVs (see **Figure 2.6k**) or constant-current charge/discharge curves with obvious plateaus (**Figure 2.6i**). The typical battery materials include $Ni(OH)_2$ and other common metals such as Co, Cu and Cd as well as their oxide/hydroxide. Unlike capacitive charge storage, charge storage by battery-type electrodes follows a nonlinear relationship with the applied potential, making reported capacitance for the above-mentioned electrode materials unambiguously incorrect. Since the "average capacitance (F)" is not directly proportional to the potential window, it is important to measure the capacity (mAh g^{-1}) or specific charge (C g^{-1}) from the CV and GCD profiles of battery-type electrodes. Therefore, equations 2.5 and 2.6 can be used to measure the practical, specific capacity from both CV and GCD curves:

$$\text{Specific capacity } (mAg^{-1}) = \frac{\int i(V)\, dV\ (AV)}{m\ (g) \times \nu\ (Vs^{-1}) \times 3.6} \quad (2.5)$$

$$\text{Specific capacity } (mAg^{-1}) = \frac{\int i(A)\, dt\ (s)}{m\ (g) \times 3.6} \quad (2.6)$$

where the integration of current over voltage window divide by 2 gives the total voltammetric charge in A V (ampere volts); ν is scan rate, m is the active mass of the electrode and t is the discharge time.

2.4.3 Hybrid supercapacitors (HSCs)

It is critical to design and fabricate electrochemical energy storage systems with high energy and power densities as well as long cycling life. As a part of one of these systems, hybrid supercapacitors (HSCs) are energy storage devices made up of battery-type and capacitive electrodes that combine the benefits of both batteries and electric double-layer capacitors, making them promising advanced energy storage devices for commercial use. This novel energy storage system has the potential to generate higher energy density (than EDLCs) and higher power density (than batteries) to fill in the gaps in the Ragone plots between EDLCs and batteries, as well as to meet the forever growing energy demands resulting from the growth of intelligent and smart devices [44, 45]. Additionally, this combination of battery-type and capacitive electrodes has higher working potential and yields higher capacitance which is two to three times more than that of conventional capacitors as well as EDLC and pseudocapacitors.

Figure 2.7 depicts the basic configuration of HSCs. During the electrochemical reaction, the battery-type electrode stores energy *via* Faradaic charge transfer, while the other electrode balances charges *via* electro-sorption of guest electrolyte ions onto the active surface of the material (e.g., active carbon). From the same device, two distinct electrochemical processes corresponding to Faradaic and non-Faradaic reactions occur simultaneously. The former

electrode, which has well-separated redox peaks is used as an energy output source, while the latter has no Faradaic charge transfer and the charge storage can only occur at the surface in the form of a double-layer, that is responsible for power output. Therefore, the electrochemical response from (CV and GCD) of a HSCs with battery-type cathode and capacitive (EDLC or pseudocapacitive) anode electrode deviate from an ideal battery characteristic, exhibiting more capacitance-like behaviour, as shown in **Figure 2.8a**. Although the high capacity and wide working voltage of HSC increase their energy storage capacity, the battery-type electrode inherently slows charge kinetics due to phase transformation, resulting in, shorter cycle life and poor rate performance [46]. Different strategies have been suggested to address these concerns, including the development of nanomaterials and the use of conductive additives like graphene, CNTs and AC [47, 48].

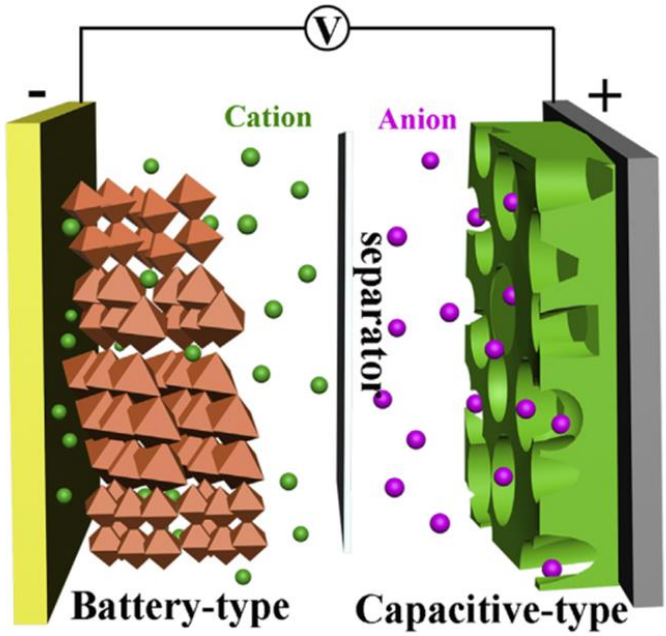


Figure 2.7: The fundamental configuration of the HSCs [49].

2.4.4 Asymmetric supercapacitor (ASCs)

Apart from battery-type positive electrodes, pseudocapacitive materials are promising electrode that can deliver similar power density to EDLCs. ASCs are capacitors that have both high capacitance and a high energy density. The ASCs have attracted a lot of attention because of their proclivity for merging the properties of their constituents (EDLC and pseudocapacitors). The storage mechanism of the ASCs is made up of a combination of these two storage mechanisms. The asymmetric device can provide a high working voltage, high energy density and long cycling stability since half of a hybrid device acts as an EDLC and the other half as a pseudocapacitor [50]. To avoid confusion with hybrid supercapacitors, when both EDLC and pseudocapacitive electrodes or (one EDLC/one pseudocapacitive) are used in a two-electrode system (e.g., activated carbon/MnO_2) (**Figure 2.8b**), the term "asymmetric" should be used.

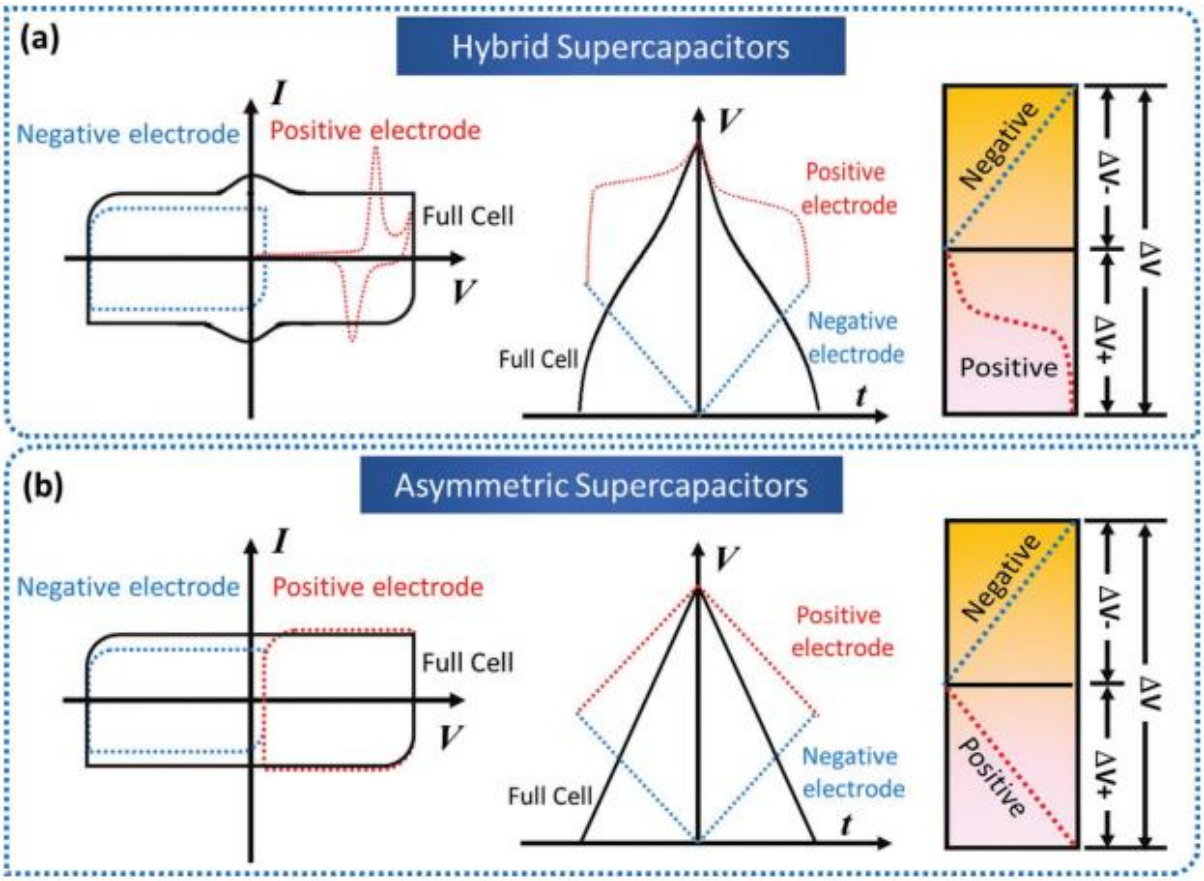


Figure 2.8: Electrochemical signatures of typical (a) hybrid and (b) asymmetric supercapacitors [39].

To achieve the optimum working voltage for the SCs cell, both ASCs and HSCs combine the potential windows of the cathode and anode electrodes. Therefore, to achieve the highest cell voltage and energy density, charge balancing ($q^+ = q^-$) should be performed on both electrodes. The ideal mass ratio between cathode and anode electrode materials can be determined using equation 2.7.

$$\frac{m^+}{m^+} = \frac{C^- \times V^-}{C^+ \times V^+} \tag{2.7}$$

where m^+, m^-, C^+, C^-, ΔV^+, and ΔV^- are the masses, capacitance and the potential window for the cathode and anode materials, respectively. Furthermore, specific energy and power density,

are calculated using equations 2.8 and 2.9, respectively describe the performance metrics of ASCs and HSCs.

$$E\ (Wh\ kg^{-1}) = \frac{0.5 \times C \times V^2}{3.6} \quad (2.8)$$

$$P\ (W\ kg^{-1}) = \frac{E \times 3600}{t} \quad (2.9)$$

where C is capacitance in (F g^{-1}), V is the voltage window in (V) and t is discharge time in (s). Moreover, the electrochemical kinetics of battery-type, pseudocapacitive, and EDLC electrodes differ and can be distinguished using the Trasatti and Dunn differentiation techniques, which will be discussed in the subsequent section.

2.5 Differentiating diffusion-controlled processes from a surface-controlled contribution

Electrochemical energy storage arises from either capacitive, pseudocapacitive, or battery-like processes. Materials with advanced charge-storage capabilities that are engineered to deliver high capacity at a high rate often exhibit a multiplicity of such mechanisms, which complicates the understanding of their charge-storage behaviour [51]. Thus, several electrochemical techniques have been developed to determine the contribution of different charge storage mechanisms involved in an electrochemical capacitor, such as through the electrical double layer and diffusion-limited processes. The charge storage mechanism of electrode material can be categorised as follows: (i) capacitive (EDLC process), (ii) faradic reactions (pseudocapacitive/battery-type) and (iii) mixed processes (EDLC and pseudocapacitive). Simple CV measurements at different scanning rates are enough to distinguish the energy storage mechanism of electrode materials. Based on the fundamentals of cyclic voltammetry,

the current (i/A) is related to the scan rate (v/V s^{-1}) *via* the power-law as shown in equation 2.10 and 2.11 [52].

$$i = av^b \tag{2.10}$$

$$log\, j = b\, log\, v + log\, a \tag{2.11}$$

where *j* stands for current density, *a* and *b* stand for adjustable parameters that can be found by plotting log *j* against log *v*. An adsorption-controlled, pure capacitive process is the dominant energy storage mechanism when $b = 1$; when $b = 0.5$, the storage mechanism is a diffusion-controlled; and when $b > 0.5$ but less than 1.0, the storage mechanism with both EDLC and pseudocapacitive processes.

The power-law equation can be sub-divided into capacitive and faradic current responses using the same voltammetric principle in equations 2.12 and 2.13, respectively.

- EDLC (surface-controlled) current response:

$$i \propto v \;, \Rightarrow\; i = k_1 v \tag{2.12}$$

- Pseudocapacitive (diffusion-controlled) current response:

$$i \propto v^{1/2} \;, \Rightarrow\; i = k_2 v^{1/2} \tag{2.13}$$

Equations 2.14 and 2.15 can be used to calculate the total current response at a given potential (V).

$$i = k_1 v + k_2 v^{1/2} \tag{2.14}$$

$$\Rightarrow\; i/v^{1/2} = k_1 v^{1/2} + k_2 \tag{2.15}$$

where k_1 and k_2 are constants that describe the capacitive and Faradaic current contributions, respectively. Therefore, by plotting $i/v^{1/2}$ against $v^{1/2}$, the values of k_1 and k_2 can be obtained. The capacitive current contributions can be plotted and distinguished from the faradic contributions by measuring the k_1 value at various voltages and scan rates.

2.6 Electrode material for supercapacitor

The role played by active electrode materials in supercapacitors is crucial; therefore, developing advanced electrode materials that can meet the necessary energy demand is of paramount importance. High surface area together with high conductivity are one of the most important parameters for improving the charge storage of electrode materials [53]. However, collateral to the high surface area, pore size distribution and structural defects, also influence the charge storage properties. For instance, a large surface area aids in the formation of an electrical double layer, while a uniform pore size distribution regulates the electrolyte ions pathway in the inner core of the electrode material [54, 55]. As a result, the electrochemically active surface area may be used to explain the behaviour of an electrode material. In general, carbon materials, conducting polymers and transition metal oxides/hydroxides are the most used electrode materials in supercapacitor.

2.6.1 Electrodes materials for EDLCs

Carbon-based materials for energy storage remain at the forefront of nanoscience and nanotechnology, due to their diverse physical and chemical properties, such as electrical transport, chemical reactivity, optical, and thermal properties [56]. In addition, carbon materials have also been extensively investigated in supercapacitor applications at both the laboratory and industrial scales due to their low cost, non-toxicity and ease of availability.

Activated carbon, carbon nanotubes, carbon nanofibers and reduced graphene oxide are the commonly used EDLC electrode materials in supercapacitors.

2.6.1.1 Activated carbons (AC)

Activated carbons (AC) are attracting a lot of interest in supercapacitors due to their large specific surface area (SSA), pore structures and regulated channels, excellent chemical stability and low cost [57]. Generally, activation refers to the process of increasing surface area and porosity from carbonised organic precursors and the resulting category of materials is known as activated carbons. ACs made from corn [58], tree bark [59], coconut shell [60] and other materials have been stated to have excellent electrochemical properties for EDLC electrode materials, with some even outperforming commercial AC. Aside from the precursor materials, the carbonization and activation processes play an important role in the properties of AC [61]. Activated carbon can be prepared by either a physical activation (CO_2/steam) or a chemical activation process (KOH, K_2CO_3, H_3PO_4 and $ZnCl_2$) at different temperatures.

The pores created during the activation process aid in the storage of charges in electrochemical device applications. The evaluation of the size of the pores has shown that the development of smaller pores relative to the electrolyte ions may result in poor charge storage. This is because high microporosity networks increase electrolyte ions diffusion resistance, resulting in poor adsorption of electrolyte ions, mainly for fast scan rates. During fast scan rates, the adsorption of ions into micropores is low due to the inability of the material to keep up with the quick charging and discharging rate, causing poor rate performance [62]. Likewise, the large sizes of pores relative to the electrolyte ions can also lead to poor entrapment of electrolyte ions which can also be a limitation to the specific capacitance and the maximum specific power. As a result, to provide the required pores for efficient charge transport and storage, an ideal pore size distribution is required. Wide pore sizes, such as macropores (> 50 nm) and mesopores (2-

50 nm), are better for ions buffering and diffusion, whereas micropores (less than 2 nm) help with charge adsorption and storage [63].

The diffusion phenomenon within the pores of activated carbons could be explained by three mechanisms: (a) adsorbate molecule transportation to the external AC surface, (b) adsorbate molecule diffusion from macropores to mesopores and micropores and (c) adsorbate molecule adherence to the pore surface through weak van der Waals interactions. **Figure 2.9** depicts a simplified representation of these processes. The size of the molecules and the pore structure of the ACs play a major role in the diffusion process.

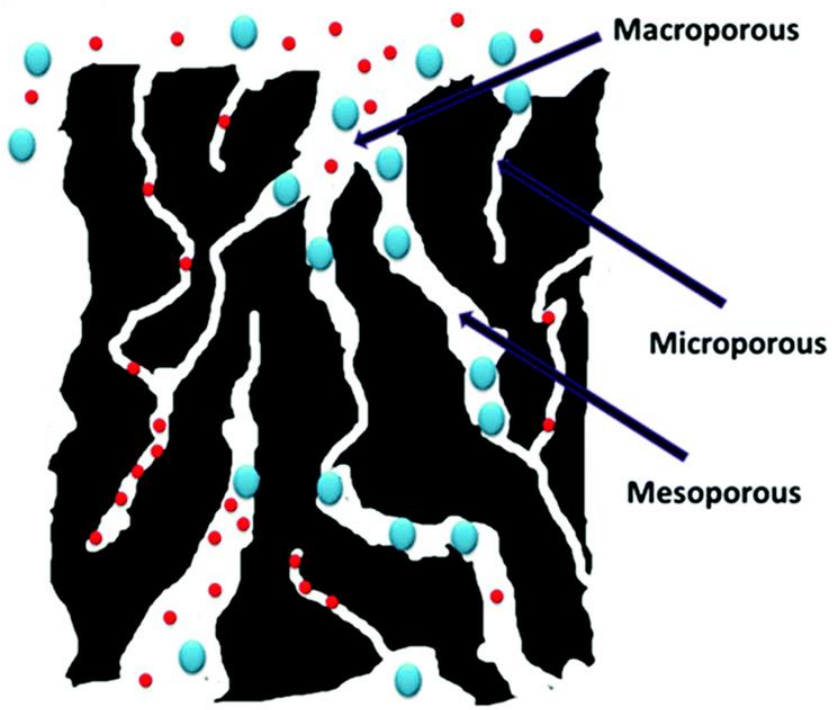


Figure 2.9: An illustration of a typical activated carbon structure with strongly disordered macropores (>50 nm), mesopores (2–50 nm) and micropores (less than 2 nm) (Adapted from [64]).

2.6.1.2 Carbon nanotubes (CNTs)

Single-walled carbon nanotubes (SWCNTs) and multiwall carbon nanotubes (MWCNTs) are the two common types of carbon nanotubes that have excellent electrical conductivity, thermal

stability and a special tubular porous structure. SWCNTs present a single graphene sheet wrapped into a cylindrical tube while MWCNTs show several arrays of nanotubes that are concentrically nested. There are one-dimensional materials with a mesoporous texture (i.e., the pore size distribution is between 2 – 50 nm) which promotes easy ion-diffusion when used in electrochemical devices [65]. Due to their unique tubular and mesoporous structure that allows easy charge mobility and large accessibility to electrolyte ions, CNTs can deliver relatively high capacitances when compared to AC [66]. Furthermore, during charge/discharge reactions, CNTs have a lower contact resistance, resulting in high energy and power densities [67].

In general, chemical vapour deposition (CVD) is a widely used and well-established method for producing CNTs. In addition, producing CNTs using CVD requires the use of a decomposable carbon source and a catalyst (typically metal or mixed metals). One of the major advantages of this method is the wide range of support materials available for CNTs synthesis. Also, it is widely acknowledged that support plays a critical role in nanotube preparation due to the interaction between the catalyst particles and the support material. The most frequently used catalyst supports are silica (SiO_2) [68], alumina (Al_2O_3) [69], calcium carbonate ($CaCO_3$) [70] and magnesia (MgO) [71].

For CVD methods, the three most important requirements are the carbon feedstock, a metal that acts as a catalyst in the growth stage and an adequate energy source (thermal or plasma). In general, transition metals, such as iron, nickel and cobalt are used as catalysts. Different hydrocarbons such as ethanol and acetylene are usually used as carbon sources. For instance, Durrer *et al.* [72] used a Ferritin-based Fe catalyst to research the growth of individual SWCNTs by the CVD method. According to the findings, atomic force microscope (AFM) imaging revealed that the Ferritin concentration in the adsorption solution can regulate the density of SWCNTs on the surface, which is critical for SWCNT integration and avoiding

SWCNT bundle formation. Using acetylene/ammonia mixture and Fe/Co as a catalyst, Hofmann and colleagues investigated the impact of catalyst film thickness on the growth of carbon nanostructures by plasma-enhanced chemical vapour deposition (PECVD). For a catalyst thickness below 3 nm, a transition from large diameter bamboo-shaped CNF to small diameter MWCNT was discovered. Furthermore, it was believed that the choice and dilution of hydrocarbons has a distinct influence on carbon nanostructures [73].

Even though CNTs have a large surface area (> 1000 m^2/g), much work has been done to boost their surface area, porosity and performance by activating or doping them with elements such as nitrogen, boron and sulphur. Tetana *et al.* [74] prepared high-quality N-MWCNTs over a Fe-Co/$CaCO_3$ catalyst in the temperature range 700 – 850 °C using acetonitrile as a nitrogen source and acetylene as a carbon source. The yield, size, quality, morphology and thermal stability of N-MWCNTs were studied in relation to growth temperature and CH_3CN vaporization temperature. The CNTs that were produced were mostly bamboo-shaped and multi-walled. In addition, at higher temperatures (800 – 850 °C), a mixture of N-MWCNTs and carbon spheres (CSs) was also observed. The best conditions for the synthesis of high-quality N-MWCNTs in good yields were found to be 800 °C and room temperature CH_3CN vaporization, as these yield pure N-MWCNTs in good yields. The problem can also be solved with composite materials made by doping CNTs into AC. Dolah *et al.* [75] made CNT electrode materials from oil palm fruit bunch fibres, CNTs and KOH, which were activated by CO_2 gas and performed well for supercapacitors despite having a low surface area of 400 m^2/g. Although preparing CNTs from biomass can greatly reduce costs, there are several drawbacks, including high energy consumption and a lengthy process. As a result, it is crucial to develop new preparation methods for the use of CNTs in supercapacitor application.

2.6.1.3 Carbon nanofibers (CNFs)

Carbon nanofiber (CNF) is one of the most important members of carbon fibres, which has been investigated in both fundamental scientific research and practical applications. CNFs are promising materials in a variety of fields, including electrical devices, battery and supercapacitor electrode materials and sensors [76-78]. The electrical conductivity of CNFs is often the priority needed to be considered in these applications [79]. There are some distinctions between traditional carbon fibres (CFs) and carbon nanofibers (CNFs). First is their size, which is also the most noticeable. CNFs have diameters of 50–200 nm, while conventional CFs have diameters of several micrometres [80]. The disparity between CNF and traditional CF is schematically shown in **Figure 2.10**.

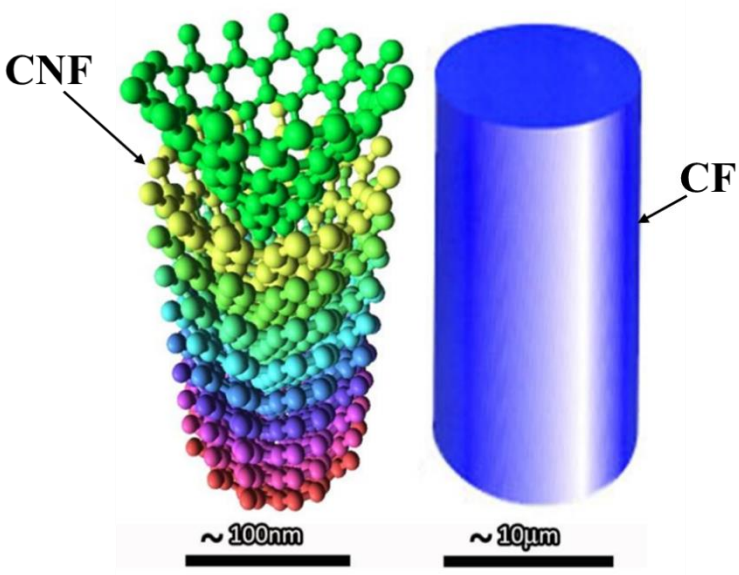


Figure 2.10: Schematic illustration of the difference between CNF and CF [79].

The CNFs are promising materials that can be synthesized with different morphologies, diameters and lengths. CNFs can be produced using two techniques: (i) vapour growth and (ii) electrospinning. Synthesis of carbon fibres from vapour growth was explored from the 1970s and 1980s [81, 82]. Carbon fibres can be produced by catalytic decomposition of hydrocarbons in the presence of metal particles (catalysts), however, the mass-production prove to be

difficult. In contrast, electrospinning, which involves the spinning of polymeric precursor fibres and subsequent thermal treatment, has become the most widely used technique. Although any material with a carbon backbone can be used as a carbon fibre precursor, polyacrylonitrile (PAN), cellulose and pitch are the most used polymeric precursors [83].

Due to excellent mechanical properties and high carbon yield, PAN has been the most widely used precursors among the above mentioned three precursors [84, 85]. Electrospinning of PAN, unlike conventional fibre spinning techniques, is powered by electrical force rather than mechanical force. When the voltage is applied, the droplet of PAN solution at the tip of the spinneret deforms from its original shape [86, 87]. As the applied electrical potential reaches a critical value, the PAN solution overcomes its surface tension, and a jet of solution ejects from the tip of the spinneret in a form of a Taylor cone and electrospinning begins. Furthermore, the jet then takes a 3D bending and twisting, becoming thinner as the loop circumference increases, as shown in **Figure 2.11**.

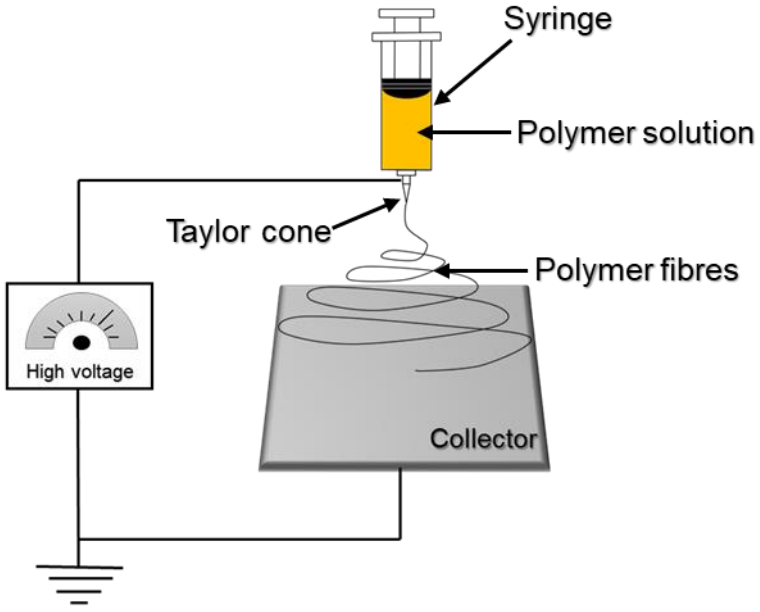


Figure 2.11: Schematic diagram of electrospinning PAN including basic electrospinning setup, Taylor cone and bending instability.

In comparison to CNTs, electrospun PAN carbon nanofibers have similar characteristics as 1D carbon nanostructures and are also cheap and relatively simple to incorporate into applications [83]. In addition, the CNFs mat made from electrospun PAN has an interconnected nanofiber network structure that contributes to its ease of handling. This allows for the removal of polymer binders and conductive fillers from electrodes, resulting in improved electrochemical performance [88]. Despite this, electrospun PAN CNF mats are unable to solve any of the drawbacks of conventional carbon nanofiber mats. In recent years, researchers have focused on increasing the specific surface area of CNFs made from electrospun PAN and designing hierarchical composite nanostructures to address a comprehensive improvement in electrochemical performance [83].

2.6.1.4 Graphene

Due to its unique physicochemical properties (physical, chemical and electrochemical), graphene is an emerging material of interest with interesting properties significant to the scientific and technical industries [89]. Graphene is a single atomic thick two-dimensional (2-D) material composed of sp^2 hybridized carbons bonded in a hexagonal lattice [90]. It is a single-atom-thick carbon allotrope that acts as the structural base for all other carbon allotropes: (1) 0D fullerenes, which are made by wrapping graphene sheets into a sphere (Bucky ball), (2) 1D CNTs, which are made by rolling graphene sheets into a cylindrical shape and (3) 3D graphite, which is made by piling multiple layers of individual graphene sheets stuck together by van der Waals bonds as shown in **Figure 2.12** [91].

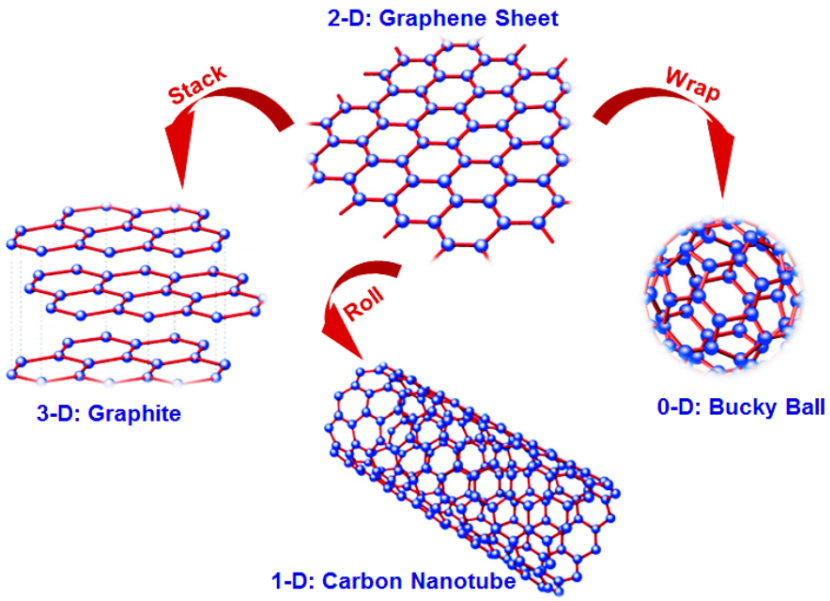


Figure 2.12: The 2D hexagonal nanosheets of graphene as a building block of other forms. An illustration of different allotropes of carbon arising from a graphene sheet (Adapted from Ref [99]).

Several graphene synthesis methods have been widely proposed in the literature, the first of which monolayer graphene has a single graphitic layer, while bilayer and trilayer graphene have two or three layers. Graphene is well known for its extraordinary electrical and thermal conductivity, high charge carrier density, high mobility and excellent mechanical properties [92, 93]. These properties make graphene suitable for many applications including and not limited to supercapacitors [94], batteries [95], fuel cells [96], sensors [97] and electronics [98].

Several graphene synthesis methods have been widely proposed in the literature, the first of which was introduced by Novoselov *et al.* [100] in 2004 and included the use of a basic mechanical exfoliation technique known as the scotch-tape process. This preparation method is still widely used in many laboratories to produce a few layers of graphene to study their fundamental properties [101]. However, this approach does not allow for large-scale production [101]. To address the yield problem associated with the exfoliation method, graphene has also been synthesized using the chemical vapour deposition (CVD) process using

gaseous hydrocarbon sources and growth templates such as ruthenium (Ru), nickel (Ni) and copper (Cu) [102]. The CVD method is currently considered to be the most effective way to produce a large single-layer graphene sheet [101]. This method has demonstrated the synthesis of large-area, high-quality graphene; however, when comparing the properties of graphene made from the CVD method and graphene made using the exfoliation method, the exfoliation method produces better graphene [103, 104].

Reina *et al.* [105], for example, used an ambient-pressure chemical vapour deposition (APCVD) process on polycrystalline Ni films to prepare wide-area films (cm^2) with 1 to 12 layers. The graphene layer had good electrical and optical properties. Similarly, Qin *et al.* [106] used the CVD growth method to successfully synthesize a large-area graphene film on Cu substrates. In copper, the graphene film growth had a low carbon solubility and in nickel, it had a low carbon saturation. Unfortunately, graphene materials have two major drawbacks: re-stacking of sheets, which reduces the usable surface for reactions and low density due to the material's 2-D structure [107]. These issues are caused by the π-π bond interaction between adjacent graphene sheets, which decreases the 2-D material's unique surface area. As a result, supercapacitors using pure graphene as electrode materials may have low real capacitance values. To overcome these drawbacks, other materials have been integrated into the graphene framework to form composite materials with EDLC and faradaic materials for improving supercapacitor surface reactivity [108-110].

2.6.2 Metal oxide pseudocapacitors

Faradaic materials started to play a crucial role in supercapacitors ever since Brian Evan Conway conducted a large number of experiments using ruthenium oxide (RuO_2) as electrode materials in 1971 [7]. RuO_2 is one of the most researched metal oxides due to its low equivalent series resistance (ESR) and high specific capacitance. However, its high cost in comparison to

other transition metal oxides has prompted researchers to look at other options [111]. To achieve similar electrochemical performance, transition metal oxides/hydroxide and polymers are usually used.

2.6.2.1 Transition metal oxides

2.6.2.1.1 Ruthenium oxide (RuO_2)

RuO_2 was the first transition metal oxide tested for use in supercapacitors and its high theoretical capacitance makes it one of the most promising electrode materials. (~ 2000 F g^{-1}) [112], high cycle capability, high electric conductivity, wide potential window and good electrochemical reversibility [113]. The pseudocapacitive characteristics of RuO_2 in an acidic medium follow fast and reversible faradaic reaction, based on equation 2.16, where $0 \leq x \geq 2$.

$$RuO_2 + xH^+ + xe^- \leftrightarrow RuO_{2-x}(OH)_x \quad (2.16)$$

In an acidic medium, oxidation states transition from (II) to (IV). But, in an alkaline medium, the oxidation states switch from (II) to (III). For example, charging carbon/Ru composite oxidizes RuO_2 to RuO_4^{2-}, RuO^{4-} and RuO_4, while during discharge, these high valence states are reduced back to RuO_2 [114]. It is well known that $RuO_2 \cdot nH_2O$ is a strong proton conductor and that in an acidic medium, the reaction of RuO_2 necessitates the addition and extraction of H^+ according to equation 2.16 [115]. As a result of the combined water in hydrous RuO_2, H^+ diffusion in the electrode is accelerated. The hydrous Ru oxides have much higher capacitance than the anhydrous type, with values of 861 F g^{-1} and 900 F g^{-1}, respectively [116]. Furthermore, the capacitance decreases from 720 F g^{-1} to 19.2 F g^{-1} as water decreases from $RuO_2 \cdot 0.5H_2O$ to $RuO_2 \cdot 0.03H_2O$ [117].

Ruthenium (Ru) is one of the members of the platinum group of metals (PGMs) and its high cost has hindered it from being used commercially. However, its excellent electrochemical

properties do not prevent research on its potential applications. Although several studies have focused on other potential transition metal oxides, RuO_2 reports have also been published at the same time [118]. Ruthenium oxide has various forms such as nanoneedles [119], nano-porous films [120] and nanoparticles [121]. Hu *et al.* [122] used a template method to make a $RuO_2 \cdot xH_2O$ nanotubular array with a capacitance of around 1300 F g^{-1}. Remarkably, hydrous RuO_2 prepared using the sol-gel method showed a specific capacitance of 390 F g^{-1}. Similarly, chemically prepared RuO_2 exhibits the lowest capacitance value of 50 F g^{-1} [120].

Despite its numerous advantages, RuO_2 is still unsuitable for industrial use in supercapacitors due to its high cost and limited availability. To lower the expenses, different approaches have been suggested such as combining RuO_2 with other low-cost metal oxides like MnO_2, TiO_2, SnO and Co_3O_4 [123-126] to form composites or coating RuO_2 on cheaper substrates to form composites [127, 128]. Microwave-assisted hydrothermal synthesis yielded a $RuO_2 \cdot nH_2O/TiO_2$ nanocomposite with a maximum specific capacitance of 992 F g^{-1} and a high-power density of 400 kW k g^{-1}[129]. The TiO_2 crystallites are formed before the nucleation of $RuO_2 \cdot nH_2O$ in this composite, which enhances the exposure and operational efficiency of $RuO_2 \cdot nH_2O$. The specific capacitance of $RuO_2 \cdot nH_2O$/MWCNTs/Ti electrodes in H_2SO_4 can reach up to 1652 F g^{-1}, thanks to the porous structure, which enables quick and reversible redox reactions to take place on the electrode/electrolyte interface [130]. The conductivity of RuO_2 is enhanced by the conductive substrates, resulting in a shorter ion transfer distance.

2.6.2.1.2 Manganese oxide (MnO_2)

Due to low cost, vast abundance, low toxicity and high theoretical capacitance (1370 F g^{-1}), MnO_2 has been synthesized in various forms as a replacement for RuO_2. MnO_2 comes in a variety of polymorphs, each with its crystallographic structure (α, β, γ, δ and λ). At the interlayer spacing, birnessite-type MnO_2 has crystalline layered structures, with layers of edge-

sharing MnO_6 octahedral to hold water molecules or other cations. The layered structure of δ-MnO_2 permits intercalation of ions within the interlayer pathway, while the 2D morphology promotes surface-dependent electrochemical reactions, which are ideal for energy storage applications, such as supercapacitors [131]. Two mechanisms have been suggested to describe the charge storage behaviour of MnO_2 (equations 2.17 and 2.18). Equation 2.17 display the insertion of electrolyte cations ($C^+ = H^+$, Li^+, Na^+ and K^+) into the bulk MnO_2:

$$MnO_2 + C^+ + e^- \leftrightarrow MnOOC \quad (2.17)$$

The second is based on electrolyte cation surface adsorption on the MnO_2 electrode as shown in equation 2.18.

$$(MnO_2)_{surface} + C^+ + e^- \leftrightarrow (MnOOC)_{surface} \quad (2.18)$$

Intercalation of the electrolyte ions into MnO_2 causes the variation in the valance state of the material rendering lattice expansion and reduction of Mn^{4+} to Mn^{3+}. Interfacial reaction, for instance, causes a transition in manganese oxidation states (Mn^{4+} to Mn^{3+}), while the electrolyte cations help preserve the charge balance of MnO_2. Despite MnO_2 having a high capacitance, the real-world usage is constrained by the low conductivity as compared to RuO_2.

Nevertheless, hybridization of MnO_2 with other materials such as carbo-based materials or conducting polymers to form composites that can create more surface defects and charge carriers are also viable methods for improving electrical conductivity and charge storage performance [132]. Examples of such composites include OLC/MnO_2 [133], MnO_2/graphene [134], MnO_2/CNT [135], MnO_2/PANI/CNTs [136], MnO_2/carbon nanofibers [137].

2.6.2.2 Conducting polymer

The other Faradaic-type supercapacitor materials are conducting polymers with a high concentration of π-conjugated polymeric chains [138]. This offers fast charge-discharge

kinetics, suitable surface morphology, fast doping and un-doping processes which yields unique properties, such as large surface areas and shortened pathways for charge/mass transport [139]. Conducting polymers are employed in supercapacitors because of their relatively high capacitance, conductivity and low equivalent series resistance. In addition, conducting polymers have redox storage capability and provide a large surface area, making them ideal for high capacitance supercapacitors. These compounds can be doped with metallic conductivity, which is a useful property for supercapacitor electrode materials. They are reported to be superior to other carbon materials, including activated carbons, in some respects [140]. Polypyrrole, polyaniline (PANI) and poly-(3, 4-ethylenedioxythiophene) (PEDOT) are some of the most widely used conducting polymers, with particular capacitances equivalent to metal oxides like ruthenium oxide [141-143]. One of the challenges faced by conductive polymers is the lack of effective n-type doped (negatively charged). Another problem is the insufficient mechanical stability during charge-discharge cycles due to mechanical stress [138].

2.6.3 Battery-type materials

For the past two decades, nickel-based materials have been employed in Ni–Zn, Ni–Cd, and Ni–metal hydride batteries. Even though Ni-based materials have pure battery-like characteristics (i.e., storing charges through Faradaic processes), a lot of reports have misinterpreted Ni-based materials as pseudocapacitive electrodes in supercapacitors and asymmetric devices [131, 144]. However, when considering the fundamental concept of capacitance [7], the term pseudocapacitance [35] can only be applied to materials that have the electrochemical signatures of capacitive-type electrodes, i.e., linear charge accumulation dependencies within certain ranges of applied potentials and the linear (mirror-like) galvanostatic charge-discharge responses [145]. With this concept in mind, nickel oxide

(charged/discharged through a Faradaic mechanism) should be considered as high-power battery material rather than pseudocapacitive materials.

Regardless of this confusion, Ni-based battery electrodes, in conjunction with a suitable capacitive-negative electrode, may be useful as positive electrodes in HSCs operating in alkaline electrolytes. Ni-based materials like $Ni(OH)_2$ and NiO are being used as cathode electrodes in HSCs. $Ni(OH)_2$ is being extensively explored because of its low cost, well-defined electrochemical redox activity and high theoretical capacitance (1041 C g^{-1}, 290 mAh g^{-1}), to name a few. Furthermore, different phases (α & β) which correspond to the γ- and β-NiOOH after oxidation and a hexagonal-layered structure make it attractive for supercapacitors. The hydroxyl deficient phase α-$Ni(OH)_2$ has interlayered H_2O molecules, while β-$Ni(OH)_2$ has a brucite structure without H_2O molecules. As a result, the α-$Ni(OH)_2$/γ-NiOOH pair has a higher capacitance than the β-$Ni(OH)_2$/β-NiOOH [39]. Charges are stored in $Ni(OH)_2$ by the deprotonation/protonation reaction, which is expressed in equation 2.19.

$$Ni(OH)_2 + OH^- \leftrightarrow NiOOH + H_2O + e^- \quad (2.19)$$

Previous research has indicated that the hydrous $Ni(OH)_2$ positive-electrode material has the potential to have a specific capacitance of up to 1000 F g^{-1}. However, the low rate capability and the poor cycling stability limit its practical applications.

Due to low cost, environmental friendliness and high theoretical capacity (1292 C g^{-1}, 359 mAh g^{-1}), Nickel oxide (NiO) is a promising positive electrode for HSCs. However, the change in oxidation states of NiO and the energy storage process are debatable. Nevertheless, two major theories are normally used to justify the storage processes: one take account of the mechanism occurring between NiO and NiOOH (equation. 2.20 and 2.21); while the second one considers that in an alkaline electrolyte, NiO transforms to $Ni(OH)_2$ and the reactions occurs between $Ni(OH)_2$ and NiOOH as shown in equations 2.22 and 2.23.

$$Ni(OH)_2 + OH^- \leftrightarrow NiOOH + H_2O + e^- \quad (2.20)$$

$$Ni(OH)_2 + H_2O \leftrightarrow NiOOH + H^+ + e^- \quad (2.21)$$

or

$$Ni(OH)_2 \leftrightarrow NiOOH + H^+ + e^- \quad (2.22)$$

$$Ni(OH)_2 + OH^- \leftrightarrow NiOOH + H_2O + e^- \quad (2.23)$$

However, as a result of the significant volume shift during the charging and discharging of Ni-based material, the electrochemical response is normally poor. Thus, to alleviate such drawbacks the electric conductivity and surface area of NiO can be effectively increased by combining it with carbonaceous materials, metals, or conducting polymers [146, 147]. For example, HSCs with Ni/NiO as the positive electrode and CNT-COOH as the negative electrode delivered a high energy and power density of 61.3 Wh kg^{-1} and 900 W kg^{-1} respectively. Moreover, the device demonstrated excellent durability with 92.8 % capacitance retention over 10,000 cycles, demonstrating that the unique structure of the Ni/NiO composite will prevent the structure from collapsing due to volume expansion during cycling. In another study, Ramesh *et al.* [148] used a heat-treatment reduction process in the presence of cetyl ammonium bromide (CtAB) and urea to make a hybrid composite of nickel hydroxide nanoparticles decorated with nitrogen-doped multi-walled carbon nanotubes (N-MWCNT). The fabricated $Ni(OH)_2$@N-MWCNT hybrid composite showed a maximum specific capacitance of 350 F g^{-1} at 0.5A g^{-1}, an energy density of 43.75 W kg^{-1} and a power density of 1500W kg^{-1} with excellent capacity retention after 5000 cycles.

Another technique is to combine NiO with conducting polymers (CPs), to increases electrical conductivity, pseudocapacitance and stability. For example, Yang *et al.* [149] created a fibre-shaped HSC with NiO/$Ni(OH)_2$ nanoflowers encapsulated in a 3D unified poly(3,4-

ethylenedioxythiophene (PEDOT) on contra wires as the positive electrode and mesoporous carbon (CMK3) as the negative electrode. At 0.4 mA cm^{-2} current density, the HSC cell provided an aerial capacitance of 31.6 mF cm^{-2} (3.16 F cm^{-3}), which was sustained to 15.9 mF cm^{-2} (or 1.59 F cm^{-3}) at a high current density of 8 mA cm^{-2}, demonstrating outstanding electrochemical performance. The HSC device also had a stable cycling performance over 1400 cycles with an energy density of 0.011 mWh cm^{-2} at a power density of 0.33 mW cm^{-2}.

2.7 Electrolytes for supercapacitors

The electrolyte, which provides ionic conductivity and hence enables charge compensation on each electrode in a cell, is one of the most critical components of supercapacitors [150]. The electrolyte in supercapacitors not only influences EDL formation or the reversible redox process for charge storage in pseudocapacitors, but it also influences the amount of charge stored and the cycling performance. In addition, the electrolyte composition, together with ionic size, ions concentration, ion-solvent interaction, electrolyte-electrode interactions and the potential window, all influence charge storage, energy/power densities and cycle-life [150]. The electrochemical stable potential window (ESPW) of the electrolyte, for example, influences both energy and power densities by explicitly defining the operating cell voltage (i.e. equation 2.8 & 2.9). The ionic conductivity of an electrolyte, on the other hand, has a direct effect on the equivalent series resistance (ESR) of a supercapacitor, which has a substantial impact on the power density [151]. Also, the cycle life of a supercapacitor device can be affected by interactions between the ion and the solvent, as well as the electrolyte and the electrode material.

To date, various types of electrolytes have been developed and tested in electrode materials. Aqueous electrolytes, solid and/or quasi-solid-state electrolytes and redox-active electrolytes are the three groups of electrolytes. However, for this review, we will only look at liquid

electrolytes. Liquid electrolytes are generally classified into three subclasses: aqueous electrode, ionic liquids and organic electrolytes.

2.7.1 Aqueous electrolytes

Aqueous electrolytes have been widely explored in research and development over the past three decades. This is mostly because aqueous electrolytes are inexpensive and can be easily handled in the laboratory without the use of special equipment, significantly simplifying the fabrication and assembly processes. Additionally, aqueous electrolytes are greatly used in supercapacitors because of their low viscosity, low cost and easy preparation as compared to ionic liquid/organic electrolytes that need a dry room with a low H_2O content (< 1.0 ppm) [152]. Aqueous electrolytes have up to one order of magnitude higher ionic conductivity than organic electrolytes and ionic liquid. For example, Lewandowski and colleagues [153] compared the performance of activated carbon cloth in three different types of electrolytes: (i) aqueous (H_2SO_4 and KOH), (ii) organic and (iii) ionic liquids. According to their findings, aqueous electrolytes have a higher conductivity and lower series resistance than organic electrolytes and ionic liquids. Potassium hydroxide (KOH) and sulfuric acid (H_2SO_4) are the most commonly used aqueous electrolytes in supercapacitors due to their high ionic conductivity (up to 1 S cm^{-1}) and low cost [154]. However, the restriction of water electrolysis at 1.23 V is a downside of the aqueous electrolyte. This lowers the working potential and as a result, affect both the specific energy and power of aqueous-based supercapacitors [155].

With the advancement of supercapacitors, hybrid capacitors have been proposed as a way to avoid this problem by combining or adding the possible windows of two separate electrode materials. The combination of the potential windows gains an increase in the cell voltage and high specific capacitance which results in a high specific energy device. For instance, Zheng *et al.* [156] reported interpenetrating CNTs with vanadium pentoxide (V_2O_5) nanowires to

obtain a nanocomposite synthesized *via* a simple in-situ hydrothermal process. In the study, an asymmetric supercapacitor was assembled using the V_2O_5/CNTs nanocomposite electrode (with 33 wt% CNTs) as the negative electrode and MnO_2/carbon composite as the positive electrode in 1 M Na_2SO_4. The asymmetric device based on these nanocomposites delivered specific energy of 16 W h kg^{-1} with an associated specific power of 75 W kg^{-1} at 0.64 mA cm^{-2} in a 1.6 V cell voltage [156]. Deng *et al.* [157] synthesized graphene/VO_2 (RG/VO_2) hybrid material using a hydrothermal technique and constructed an asymmetric system in 0.5 M K_2SO_4 with a graphene/VO_2 (RG/VO_2) composite as a cathode electrode and reduced graphene (RG) as an anode electrode. The ASC device was operated within 1.7 V and at 0.25 A g^{-1}, where the RG/VO_2/RG hybrid system provided 22.8 Wh kg^{-1} of specific energy and 425 W kg^{-1} of specific power [157]. As a result, the hybrid capacitor can increase the aqueous electrolyte's voltage.

2.7.2 Organic electrolytes

Even though academic research has concentrated on aqueous electrolyte-based supercapacitors, organic-based electrolytes supercapacitors are currently dominating the commercial market due to their high operating potential window, which is usually in the range of 2.5 to 2.8 V. The increased operating cell voltage significantly boost both the energy and power densities. Furthermore, using organic electrolytes allows the use of less expensive materials for existing collectors and packages (e.g., Aluminium foil). However, the electrical conductivity and specific capacitance of the organic electrolyte are lower (~100 mS cm^{-1}) than that of aqueous electrolytes and can affect the ESR and charge transfer resistance (R_{CT}) [150]. Tetraalkylammonium cations, such as tetramethylammonium (Me_4N^+) and tetraethylammonium (Et_4N^+), with tetrafluoroborate (BF^{4-}) or hexafluorophosphate (PF^{6-}) anions dissolved in acetonitrile (ACN) or propylene carbonate (PC) solvents are commonly

used in supercapacitors. ACN has a higher conductivity than aqueous electrolytes due to its low viscosity, but its high volatility and toxicity pose a safety risk as compared to aqueous electrolytes. Despite having a higher viscosity than acetonitrile, propylene carbonate has lower conductivity than acetonitrile mixtures.

However, there are a few other things to take note of when using organic electrolytes for supercapacitors. For instance, organic electrolytes have a higher cost, a smaller specific capacitance, lower conductivity and safety issues related to flammability, volatility and toxicity as compared to supercapacitors using aqueous electrolytes. Furthermore, organic electrolyte requires complex purification and assembly processes in a strictly controlled environment to eradicate any residual impurities (e.g., water) that can cause severe performance degradation and serious self-discharge issues [7].

2.7.3 Ionic liquid electrolytes

Ionic liquids are non-flammable, non-volatile and have low vapour pressure which makes them work at high electrochemical potential (e.g., 6V) [158]. At room temperature, some ionic liquids (their salts) melt, forming a mixture of cations and anions. Nonetheless, ionic liquids are expensive, viscous and are poor conductors of electricity [159]. High viscosity limits the fast mobility of the electrolyte ions and reduce the electrolyte access to the inner core of the electrode surface [160]. It has been reported that the addition of propylene carbonate or acetonitrile can improve the conductivity of ionic liquids. Examples of ionic liquids comprise of quaternary ammonium salts (tetraalkylammonium $[R_4N]^+$) and cyclic amines (pyrrolidinium, aromatic pyridinium, and saturated piperidinium) to name a few [161].

2.8 Fabrication, testing and evaluation of supercapacitor electrodes and devices.

2.8.1 Electrode fabrication for supercapacitors

The selection of electrochemically active electrode materials is considered to be key to designing high-performance SCs. Therefore, having selected the right material, the electrode preparation methodology also constitutes an important step to offering a good interaction between the active material and electrolyte while retaining its original properties (i.e., the electrical conductivity, structure and morphology). Generally, in SCs, the electrodes are prepared from a mixture of an active material with or without a conductive additive and a binding material. The conductive additive (such as carbon acetylene black (CB)) is used to improve the conductivity of the electrode materials without affecting the electrochemical storage capacity, while the binder (such as polytetrafluoroethylene (PTFE) or polyvinylidene fluoride (PVDF)) is used to prevent the active material on the electrode from dissolving when submerged in the electrolyte. These materials are usually dissolved in N-methyl-2-pyrrolidone (NMP) solvent to form a paste. The resulting paste is then coated on a substrate that is conductive to electricity flow such as carbon paper or nickel foam.

2.8.2 Electrode testing for supercapacitors

To assess the electrochemical characteristics and behaviour of materials for SCs and batteries, several techniques are employed as described below in this section. Electrochemical measurements for SCs electrodes are usually performed with three-electrode and two-electrode system. A three-electrode system, as depicted in **Figure 2.13**, is utilised to investigate the electrochemical properties of single electrode material. In this type of a system, a working electrode, typically made of the active material, reference electrode, counter electrode and a chosen electrolyte make up the electrochemical cell. The reference electrode acts as the

reference point for voltage control and the current does not pass through it in a three-electrode system. The counter electrode, on the other hand, is made of chemically inert and highly conductive material such as glassy carbon, nickel foam and platinum mesh. The current required at the working electrode is generated by the counter electrode, by altering the potential of the electrolyte in an electrochemical set-up. Lastly, the nature of the electrolytes used for a specific measurement influences the choice of counter and reference electrodes [162]. For example, in acidic and neutral electrolytes, platinum and glassy carbon are used as a counter electrode, while a saturated calomel electrode (SCE) or silver/silver chloride electrode (Ag/AgCl) is used as the reference electrode. However, in an alkaline medium, mercury/mercury oxide (Hg/HgO) is the best choice as a reference electrode [163].

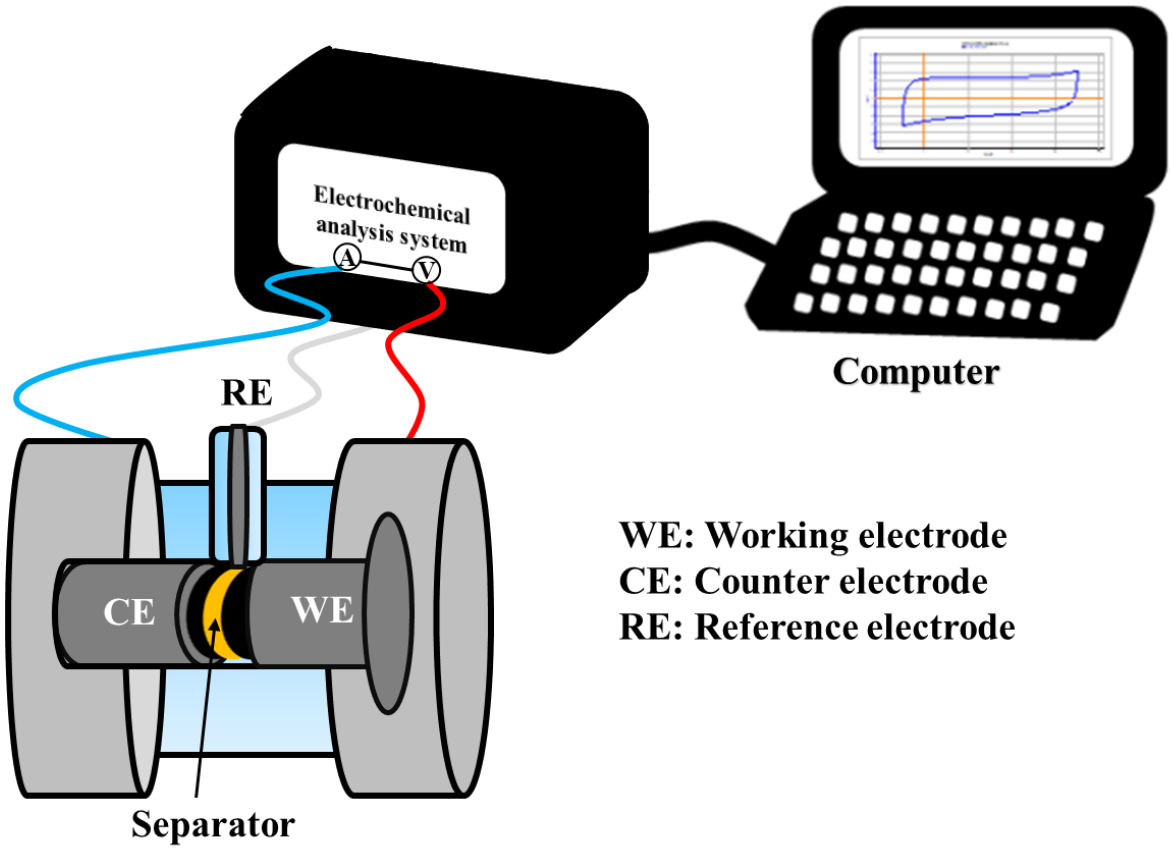


Figure 2.13: A three-electrode configuration using a battery-type Swagelok cell.

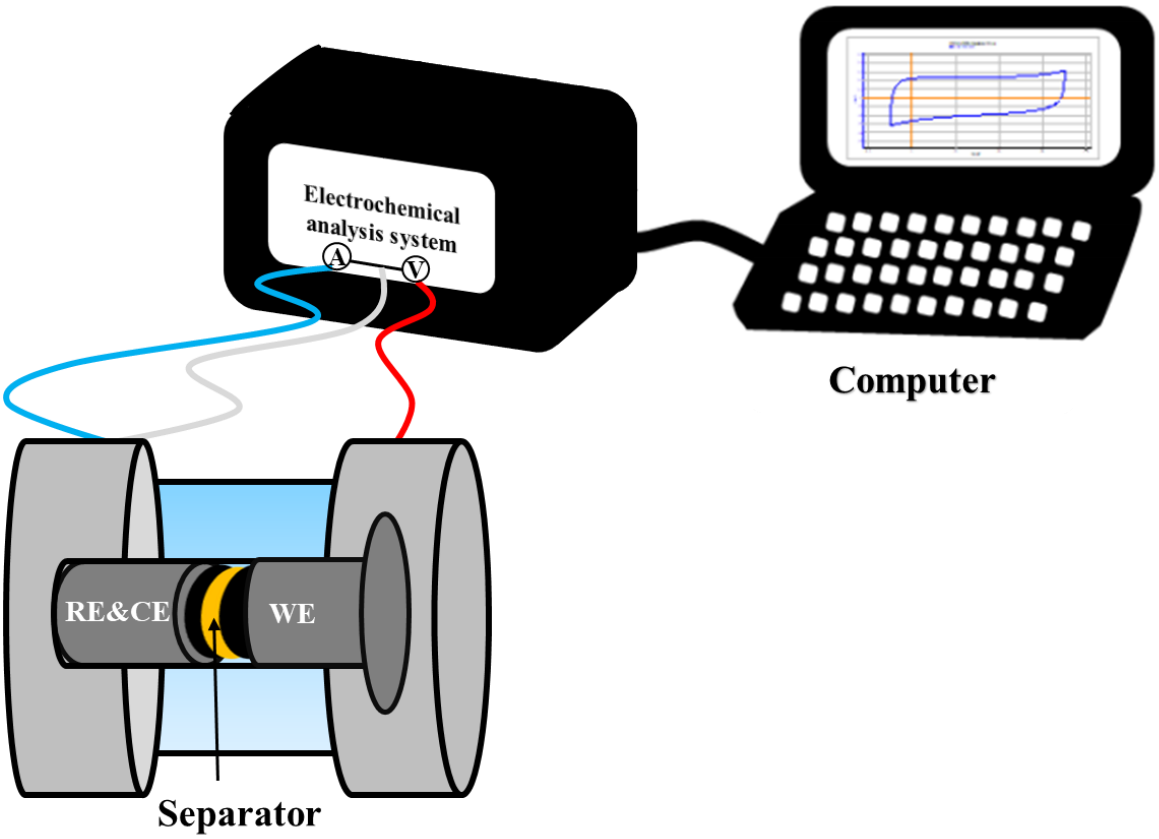


Figure 2.14: A two-electrode configuration using a battery-type Swagelok cell.

Figure 2.14 depicts the two-electrode system of a supercapacitor. The two-electrode system (full-cell) is characterized by a positive and negative electrode with a separator in-between them and an electrolyte. The two working electrodes in the two-electrode configuration can be similar (symmetric) or dissimilar (asymmetric). Two-electrode measurements can be used to calculate the energy density, power densities and longer cycle life/durability [164]. In theory, the specific capacitance (F g^{-1}) of a full-cell is equivalent to 1/4 of the capacitance calculated from a half-cell [164]. Because of the theoretical factor of 1/4, the equivalent specific capacitance and effective mass of a two-electrode device are automatically converted to those of a three-electrode system. Despite this, due to size variations in the solvated cations and anions, as well as potential differences between the positively charged and negatively charged

electrodes during the charge/discharge test, the exact capacitance calculated for one of the electrodes in a full cell is not the same as that of a half-cell electrode [165].

2.8.3 Electrochemical techniques

2.8.3.1 Cyclic voltammetry

Cyclic voltammetry (CV) is a popular technique for obtaining qualitative data on the kinetics of reactions and processes occurring at the electrode/electrolyte interphase in electrochemical systems. In this technique, the potential of a working electrode is changed linearly from one potential to another and then back again at a given scan rate and the resulting current is measured. In a voltammogram diagram, the current is plotted against the voltage for each scan rate. The kinetics of physical and chemical reactions occurring within the voltage range determines the shape of the CV curve. According to the IUPAC convention, the upper half of the curve represents oxidation, and the lower half represents reduction. This technique offers knowledge on redox reaction thermodynamics, electron-transfer reaction kinetics and charge separation. CV can be used to determine the potential windows (operating voltage) of the materials and also determine the specific capacitance of the material by integrating the area under the CV curve, following equations 2.24 and 2.25:

$$C_{sp} = \frac{\Delta Q}{m \times \Delta V} = \frac{\int_0^{2V_{0/\nu}} |i|\ dt}{m \times 2V_0} \tag{2.24}$$

To convert the current response of the CV to specific capacitance equation 2.25 is used:

$$C_{sp}\left[\frac{F}{g}\right] = \frac{I[mA]}{\nu\left[{}^{mV}/_{s}\right] \times m\ [g]} \tag{2.25}$$

For three-electrode systems, equation 2.26 is used for the calculation of specific capacitance, C_{sp} (F g^{-1}, F cm^{-3} and F cm^{-2} for gravimetric, volumetric and areal capacitances, respectively).

$$C_{sp} = \frac{C}{S} \tag{2.26}$$

where S represents the active mass (g) or the volume (cm^3) or the area (cm^2) of the electrode. In a two-electrode system, where both the working and counter electrodes are identical, equation 2.27 is used to calculate the specific capacitance, C_{sp} per electrode (F g^{-1}, F cm^{-3} and F cm^{-2} for gravimetric, volumetric and geometric specific capacitances, respectively).

$$C_{sp} = \frac{4C}{S} \tag{2.27}$$

where S is the mass (g) or the volume (cm^3) or the geometric area (cm^2) of the active material of both electrodes.

In ideal EDLCs, the charge is stored electrostatically, and the current is independent of the potential, resulting in rectangular-shaped voltammograms, as shown in **Figure 2.15a**. For a double-layer capacitor that is affected by resistive losses, the current is dependent on the voltage applied, therefore the curve on the voltammogram will be similar to a parallelogram, as shown in **Figure 2.15b**. On the other hand, electrodes with kinetically slow faradic processes exhibit distinctive peaks and the electrical charge stored in the capacitor is strongly dependent on the potential, as illustrated in **Figure 2.15c** [166].

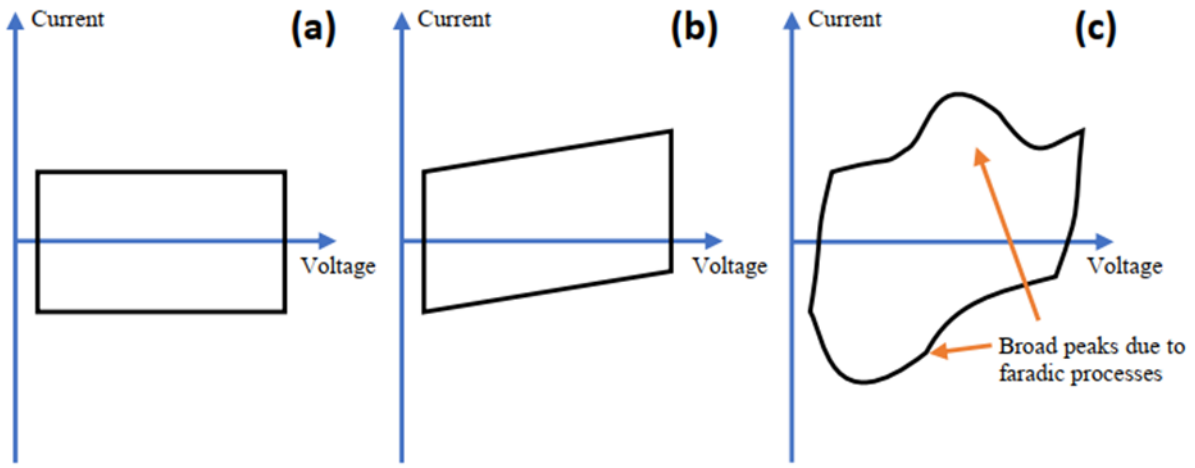


Figure 2.15: A representation of cyclic voltammograms of (a) an ideal capacitor, (b) a capacitor with resistivity and (c) pseudocapacitors [166].

2.8.3.2 Galvanostatic charge-discharge (GCD)

The galvanostatic charge-discharge (GCD) or Chronopotientiometry (CP) test is obtained by monitoring the voltage for an applied current between the working and counter electrodes as a function of time. The GCD curves are usually used to determine the specific capacitance or capacity, specific energy and power, rate capability and cycling stability of materials. The GCD plot is obtained by measuring the generated voltage (V) as a function of discharge time (s). The voltage limit is retained throughout the procedure. The applied current increases with time and is reversed after attaining the set potential. The potential increases to reach the maximum potential, with a current reversal occurring to decrease the potential to the lower present value. **Figure 2.16** shows a typical GCD curve for EDLC and pseudocapacitive electrode materials. The GCD curve for EDLC material shown in **Figure 2.16a** indicates a linear or triangular charge-discharge behaviour with a constant IR drop (responsible for the negative resistive ohmic loss associated with the active material resistance). Also, the specific capacitance remains unchanged over the entire potential range. The GCD plot of a faradaic material shown in **Figure 2.16b** is completely different as compared to that EDLC curve. For faradaic, the

curve displays a non-linear plot due to the presence of redox reactions occurring during the charge and discharge test.

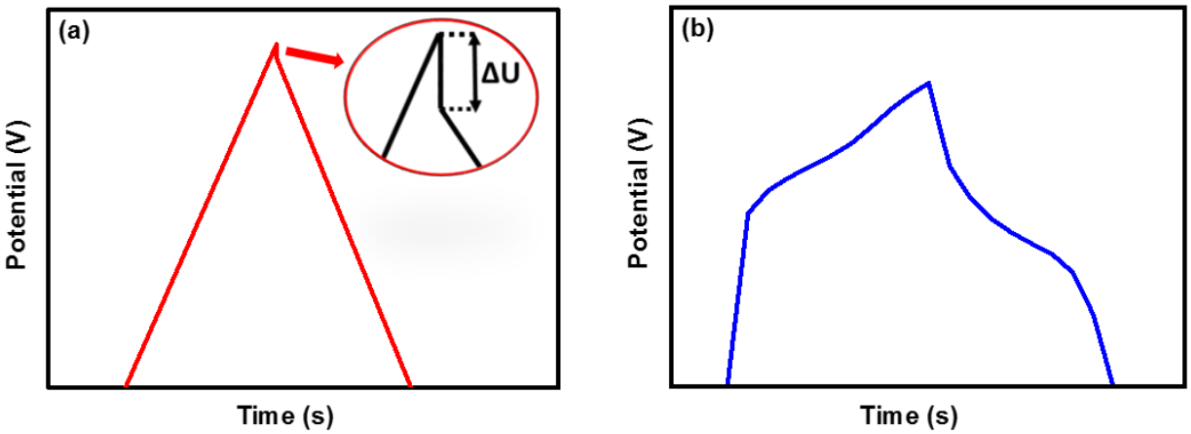


Figure 2.16: GCD plot of (a) an EDLC (the figure inset illustrates the IR drop) and (b) a redox active pseudocapacitor or faradaic [166].

The discharge part of the GCD curves is used to measure the characteristics of the SC electrodes, such as specific capacitance, energy density, power density and maximum power density. The capacitance, C (F) of a supercapacitor is given by the well-established equation 2.28.

$$C = \frac{I\Delta t}{\Delta V} \tag{2.28}$$

where I (A) represent is current, ΔV (V) represent the discharge voltage window without the IR drop, Δt (s) represent the discharge time. The energy density, power density and maximum power density for SCs are calculated from GCD results. Gravimetric energy density, E_{sp} (Wh kg^{-1}) and power density, P_{sp} (W kg^{-1}) are calculated by equations 2.29 and 2.30.

$$E_{sp} = \frac{CV^2}{2m} \times \frac{1000}{3600} \tag{2.29}$$

$$P_{sp} = \frac{E_{sp} \times 3600}{\Delta t} \quad (2.30)$$

where ΔV (V) is the maximum voltage region applied, m (kg) is the mass of the active material in both electrodes and Δt (s) is the discharge time. The maximum power is calculated using equation 2.31.

$$P_{max} = \frac{\Delta V^2 \times 1000}{4m \times ESR} \quad (2.31)$$

where ΔV is the maximum potential window applied, m (kg) in the mass of active material in both electrodes and ESR is the equivalent series resistance of the system, determined from voltage drop at the beginning of the discharge curve from GCD curves and can be calculated using equation 2.32.

$$ESR = \frac{\Delta V_{iRdrop}}{2I} \quad (2.32)$$

Lastly, coulombic efficiency η (%) and capacity retention (%) for SCs is calculated by equations 2.33 and 2.34.

$$\eta\,(\%) = \frac{t_d}{t_c} \times 100\% \quad (2.33)$$

where t_d is the discharge time and t_c charging time.

$$\text{Capacity retention} = \frac{C_{p,\,final}}{C_{p,\,2}} \times 100\% \quad (2.34)$$

where C_p the initial capacitance and C_{p2} is the final capacitance.

2.8.3.3 Electrochemical impedance spectroscopy (EIS)

Electrochemical impedance spectroscopy (EIS) is a powerful and important technique used to evaluate electrochemical behaviour and to establish a hypothesis using equivalent circuit

models of electrode material. This technique is commonly used to determine bulk conductivity, but it can also be used to obtain details about charged particles motion and investigate interfaces. The ability of a circuit to resist the flow of an electrical current is known as impedance and it is a more complicated parameter than a simple resistance.

In a supercapacitor device, the relationship between current and voltage is highly nonlinear. However, pseudo linearity can be assumed when only a small portion of the *I-V* curve is considered. The impedance (*Z*) can be calculated by applying a low-amplitude alternating excitation potential, *E* and calculating the phase shift, φ, in the obtained current, as shown in **Figure 2.17**. This phase change is determined by the impedance to current electron flow induced by electrode kinetics, the electrolyte, diffusion and chemical reactions in the cell [167].

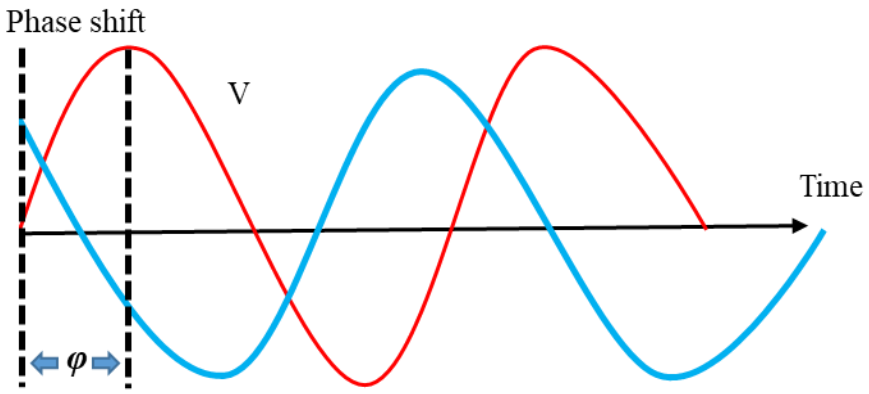


Figure 2.17: Phase shift φ in the current *I* as a response to a sinusoidal perturbation-potential V in a pseudo-linear system (Adapted from Ref [167]).

The impedance Z (Ω) is expressed mathematically as a complex number comprising of real resistance (Z') and imaginary reactance (Z"). The resistance is the real part of the complex number and is a property of the system that is independent of the incident alternating current (AC). The reactance of the imaginary part is frequency-dependent and appears in capacitors and conductors when an incident AC frequency is applied. The excitation potential V (V) can

be expressed as a function of time as in equation 2.35, while the response signal I (A) can be expressed similarly, but with a phase shift φ (rad) as in equation 2.36 [167].

$$V_t = V_o \sin\omega t \quad (2.35)$$

$$I_t = I_o \sin(\omega t - \phi) \quad (2.36)$$

where V_t (V) is the potential difference at time t (s), V_0 (V) is the amplitude of the potential signal at t = 0, I_t (A) is the current response signal at time t, I_0 (A) is the amplitude of the current signal at t = 0 and ω (rad·s^{-1}) is the angular frequency, where $\omega = 2\pi f$ and f (Hz) is the frequency.

The EIS variance is calculated by plotting the imaginary component of impedance – Im (Z) (or Z") as a function of the real part Re (Z) (or Z'), which is usually expressed in terms of the Nyquist plot. EIS is often used to calculate the specific capacitance of three and two electrode configurations by examining charge transfer (R_{ct}) and total resistances at the electrolyte-electrode-current collector interface (i.e., ESR). Generally, the EIS curve constitutes two different parts: a semi-circular loop at high frequency (> 10^4 Hz) and a linear part at low frequency due to the different electrochemical phenomena occurring during the electrochemical measurement as shown in **Figure 2.18**.

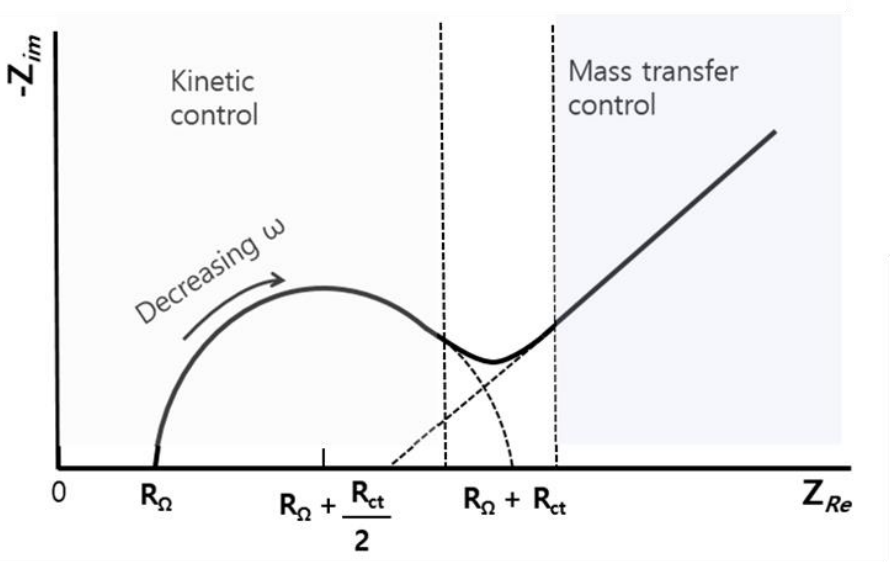


Figure 2.18: Nyquist plot with R_{ct} and RΩ [168].

On the other hand, EIS data can be plotted in a different format for data analysis purposes. One such plot format is the Bode plot, which plots both the impedance magnitude $|Z(\omega)|$and phase shift φ (ω) versus log *f*. In this plot, the material's electrical response is divided into three distinct regions. At low frequency, charge transfer and/or diffusion-controlled reactions may cause electrical relaxation. At intermediate frequencies, relaxations are associated with long-range ion migration/conduction within the bulk of the electrolyte. At high frequencies (short times), electrical relaxations are associated with short-range ion migrations.

In addition, EIS data can be fitted to an Electric Equivalent Circuit (EEC), which represents the various components of the device (e.g., resistors, capacitors and inductors) and their values can be evaluated. Some of these possible components are: (i) The solution resistance which is affected by the solution's ionic concentration, type of ions, temperature and the area where the conductance occurs; (ii) The double-layer capacitance on the interface between the electrode and the electrolyte. The resistance depends on the ionic concentration, type of ions, temperature, electrode surface layer roughness, content and more; (iii) polarization resistance controlled by the diffusion and kinetics of reactants on the electrode-electrolyte interface; (iv)

charge transfer resistance formed by a single kinetically controlled electrochemical reaction that depends on the reaction kinetics, reactants and products' concentration, etc.; (v) diffusion, creating an impedance called Warburg impedance, which depends on the frequency. On a Nyquist plot, the Warburg impedance appears as a line with a 45 ^{o} slope; (vi) the constant phase element (CPE) is a component that was invented to represents a capacitor that does not behave ideally and therefore is treated as empirical. This impedance element can be attributed to the non-uniform current distribution, surface roughness or other factors. The impedance of this component is calculated using equation 2.36 [169].

$$Z_{CPE} = \frac{1}{[Q(j2\pi f)^{n}]} \tag{2.36}$$

where *Q* is a frequency-independent constant that relates to the interface and n is derived from the slope of log $Z(\omega)$ plotted versus log *f* (with values $-1 \leq n \geq 1$). When $n > 0.5$ but <1, the CPE is an equivalent element to a capacitor and when $n = 0$ it resembles a resistor. For $n = 0.5$ the CPE impedance resembles the Warburg impedance and n = -1 resembles an inductor [170].

2.9 References

[1] Lewis, N.S., 2007. Toward cost-effective solar energy use. *Science*, **315**, pp.798-801.

[2] Ibrahim, H., Ilinca, A. and Perron, J., 2008. Energy storage systems—Characteristics and comparisons. *Renewable and Sustainable Energy Reviews*, **12**, pp.1221-1250.

[3] Yang, Z., Liu, J., Baskaran, S., Imhoff, C.H. and Holladay, J.D., 2010. Enabling renewable energy and the future grid with advanced electricity storage. *JOM*, **62**, pp.14-23.

[4] Alotto, P., Guarnieri, M. and Moro, F., 2014. Redox flow batteries for the storage of renewable energy: A review. *Renewable and Sustainable Energy Reviews*, **29**, pp.325-335.

[5] Iro, Z.S., Subramani, C. and Dash, S.S., 2016. A brief review on electrode materials for supercapacitor. *International Journal of Electrochemical Science*, **11**, pp.10628-10643.

[6] Choi, C., Ashby, D.S., Butts, D.M., DeBlock, R.H., Wei, Q., Lau, J. and Dunn, B., 2020. Achieving high energy density and high power density with pseudocapacitive materials. *Nature Reviews Materials*, **5**, pp.5-19.

[7] Conway, B.E., 2013. Electrochemical supercapacitors: scientific fundamentals and technological applications. *Springer Science & Business Media*.

[8] Burke, A., 2000. Ultracapacitors: why, how, and where is the technology. *Journal of Power Sources*, **91**, pp.37-50.

[9] Xiong, T., Lee, W.S.V., Huang, X. and Xue, J.M., 2017. Mn_3O_4/reduced graphene oxide based supercapacitor with ultra-long cycling performance. *Journal of Materials Chemistry A*, **5**, pp.12762-12768.

[10] Noori, A., El-Kady, M.F., Rahmanifar, M.S., Kaner, R.B. and Mousavi, M.F., 2019. Towards establishing standard performance metrics for batteries, supercapacitors and beyond. *Chemical Society Reviews*, **48**, pp.1272-1341.

[11] Kötz, R. and Carlen, M.J.E.A., 2000. Principles and applications of electrochemical capacitors. *Electrochimica Acta*, **45**, pp.2483-2498.

[12] Gao, H., Xiang, J. and Cao, Y., 2017. Hierarchically porous $CoFe_2O_4$ nanosheets supported on Ni foam with excellent electrochemical properties for asymmetric supercapacitors. *Applied Surface Science*, **413**, pp.351-359.

[13] Hung, K., Masarapu, C., Ko, T. and Wei, B., 2009. Wide-temperature range operation supercapacitors from nanostructured activated carbon fabric. *Journal of Power Sources*, **193**, pp.944-949.

[14] Gupta, R.K., Candler, J., Palchoudhury, S., Ramasamy, K. and Gupta, B.K., 2015. Flexible and high-performance supercapacitors based on $NiCo_2O_4$ for wide temperature range applications. *Scientific Reports*, **5**, pp.1-11.

[15] Dagousset, L., Pognon, G., Nguyen, G.T., Vidal, F., Jus, S. and Aubert, P.H., 2017. Electrochemical characterisations and ageing of ionic liquid/γ-butyrolactone mixtures as electrolytes for supercapacitor applications over a wide temperature range. *Journal of Power Sources*, **359**, pp.242-249.

[16] Wang, L., Wang, J., Zhang, X., Ren, Y., Zuo, P., Yin, G. and Wang, J., 2017. Unravelling the origin of irreversible capacity loss in $NaNiO_2$ for high voltage sodium ion batteries. *Nano Energy*, **34**, pp.215-223.

[17] Cao, X., Li, H., Qiao, Y., Li, X., Jia, M., Cabana, J. and Zhou, H., 2020. Stabilizing reversible oxygen redox chemistry in layered oxides for sodium-ion batteries. *Advanced Energy Materials*, **10**, p.1903785.

[18] Inagaki, M., Konno, H. and Tanaike, O., 2010. Carbon materials for electrochemical capacitors. *Journal of Power Sources*, **195**, pp.7880-7903.

[19] Dupont, M.F. and Donne, S.W., 2016. Faradaic and non-faradaic contributions to the power and energy characteristics of electrolytic manganese dioxide for electrochemical capacitors. *Journal of the Electrochemical Society*, **163**, p.A888.

[20] Sarjeant, W.J., Zirnheld, J., MacDougall, F.W., Bowers, J.S., Clark, N., Clelland, I.W., Price, R.A., Hudis, M., Kohlberg, I., McDuff, G. and McNab, I., 1999. Handbook of low and high dielectric constant materials and their applications. *Academic Press*, UK, **2**, pp.423-491.

[21] Tahalyani, J., Akhtar, M.J., Cherusseri, J. and Kar, K.K., 2020. Characteristics of capacitor: fundamental aspects. In handbook of nanocomposite supercapacitor materials I. Springer, Cham. pp. 1-51.

[22] Obreja, V.V., 2008. On the performance of supercapacitors with electrodes based on carbon nanotubes and carbon activated material—A review. *Physica E: Low-dimensional Systems and Nanostructures*, **40**, pp.2596-2605.

[23] Barranco, V., Lillo-Rodenas, M.A., Linares-Solano, A., Oya, A., Pico, F., Ibañez, J., Agullo-Rueda, F., Amarilla, J.M. and Rojo, J.M., 2010. Amorphous carbon nanofibers and their activated carbon nanofibers as supercapacitor electrodes. *The Journal of Physical Chemistry C*, **114**, pp.10302-10307.

[24] Chee, W.K., Lim, H.N., Zainal, Z., Huang, N.M., Harrison, I. and Andou, Y., 2016. Flexible graphene-based supercapacitors: a review. *The Journal of Physical Chemistry C*, **120**, pp.4153-4172.

[25] Zhi, M., Yang, F., Meng, F., Li, M., Manivannan, A. and Wu, N., 2014. Effects of pore structure on performance of an activated-carbon supercapacitor electrode recycled from scrap waste tires. *ACS Sustainable Chemistry & Engineering*, **2**, pp.1592-1598.

[26] Halper, M.S. and Ellenbogen, J.C., 2006. Supercapacitors: A brief overview. *The MITRE Corporation*, McLean, Virginia, USA, pp.1-34.

[27] Simon, P. and Gogotsi, Y., 2010. Materials for electrochemical capacitors. Nanoscience and technology: *A Collection of Reviews from Nature Journals*, pp.320-329.

[28] Faraji, S. and Ani, F.N., 2015. The development supercapacitor from activated carbon by electroless plating—*A review*. *Renewable and Sustainable Energy Reviews*, **42**, pp.823-834.

[29] Grahame, D.C., 1947. The electrical double layer and the theory of electro-capillarity. *Chemical Reviews*, **41**, pp.441-501.

[30] Wang, H. and Pilon, L., 2011. Accurate simulations of electric double layer capacitance of ultra-microelectrodes. *The Journal of Physical Chemistry C*, **115**, pp.16711-16719.

[31] Burt, R., Birkett, G. and Zhao, X.S., 2014. A review of molecular modelling of electric double layer capacitors. *Physical Chemistry Chemical Physics*, **16**, pp.6519-6538.

[32] Zhang, L.L. and Zhao, X.S., 2009. Carbon-based materials as supercapacitor electrodes. *Chemical Society Reviews*, **38**, pp.2520-2531.

[33] Oldham, K.B., 2008. A Gouy–Chapman–Stern model of the double layer at a (metal)/(ionic liquid) interface. *Journal of Electroanalytical Chemistry*, **613**, pp.131-138.

[34] Pandolfo, A.G. and Hollenkamp, A.F., 2006. Carbon properties and their role in supercapacitors. *Journal of Power Sources*, **157**, pp.11-27.

[35] Brousse, T., Bélanger, D. and Long, J.W., 2015. To be or not to be pseudocapacitive?. *Journal of The Electrochemical Society*, **162**, p.A5185.

[36] Salanne, M., Rotenberg, B., Naoi, K., Kaneko, K., Taberna, P.L., Grey, C.P., Dunn, B. and Simon, P., 2016. Efficient storage mechanisms for building better supercapacitors. *Nature Energy*, **1**, pp.1-10.

[37] Augustyn, V., Simon, P. and Dunn, B., 2014. Pseudocapacitive oxide materials for high-rate electrochemical energy storage. *Energy & Environmental Science*, **7**, pp.1597-1614.

[38] Jiang, Y. and Liu, J., 2019. Definitions of pseudocapacitive materials: A brief review. *Energy & Environmental Materials*, **2**, pp.30-37.

[39] Chodankar, N.R., Pham, H.D., Nanjundan, A.K., Fernando, J.F., Jayaramulu, K., Golberg, D., Han, Y.K. and Dubal, D.P., 2020. True meaning of pseudocapacitors and their performance metrics: asymmetric versus hybrid supercapacitors. *Small*, **16**, p.2002806.

[40] Choi, C., Ashby, D.S., Butts, D.M., DeBlock, R.H., Wei, Q., Lau, J. and Dunn, B., 2020. Achieving high energy density and high power density with pseudocapacitive materials. *Nature Reviews Materials*, **5**, pp.5-19.

[41] Wang, Y., Song, Y. and Xia, Y., 2016. Electrochemical capacitors: mechanism, materials, systems, characterization and applications. *Chemical Society Reviews*, **45**, pp.5925-5950.

[42] Gogotsi, Y. and Penner, R.M., 2018. Energy storage in nanomaterials–capacitive, pseudocapacitive, or battery-like? *ACS Nano*, **12**, 2081–2083.

[43] Brisse, A.L., Stevens, P., Toussaint, G., Crosnier, O. and Brousse, T., 2018. Ni $(OH)_2$ and NiO based composites: battery type electrode materials for hybrid supercapacitor devices. *Materials*, **11**, p.1178.

[44] Dubal, D.P., Ayyad, O., Ruiz, V. and Gomez-Romero, P., 2015. Hybrid energy storage: the merging of battery and supercapacitor chemistries. *Chemical Society Reviews*, **44**, pp.1777-1790.

[45] Zuo, W., Li, R., Zhou, C., Li, Y., Xia, J. and Liu, J., 2017. Battery-supercapacitor hybrid devices: recent progress and future prospects. *Advanced Science*, **4**, p.1600539.

[46] Jin, Y., Li, S., Kushima, A., Zheng, X., Sun, Y., Xie, J., Sun, J., Xue, W., Zhou, G., Wu, J. and Shi, F., 2017. Self-healing SEI enables full-cell cycling of a silicon-majority anode with a coulombic efficiency exceeding 99.9%. *Energy & Environmental Science*, **10**, pp.580-592.

[47] Liu, Y., Zhang, N., Yu, C., Jiao, L. and Chen, J., 2016. $MnFe_2O_4$@ C nanofibers as high-performance anode for sodium-ion batteries. *Nano Letters*, **16**, pp.3321-3328.

[48] Xu, Q., Sun, J.K., Li, G., Li, J.Y., Yin, Y.X. and Guo, Y.G., 2017. Facile synthesis of a SiO x/asphalt membrane for high performance lithium-ion battery anodes. *Chemical Communications*, **53**, pp.12080-12083.

[49] Liu, H., Liu, X., Wang, S., Liu, H.K. and Li, L., 2020. Transition metal based battery-type electrodes in hybrid supercapacitors: A review. *Energy Storage Materials*, **28**, pp.122-145.

[50] Muzaffar, A., Ahamed, M.B., Deshmukh, K. and Thirumalai, J., 2019. A review on recent advances in hybrid supercapacitors: Design, fabrication and applications. *Renewable and Sustainable Energy Reviews*, **101**, pp.123-145.

[51] Ko, J.S., Lai, C.H., Long, J.W., Rolison, D.R., Dunn, B. and Nelson Weker, J., 2020. Differentiating double-layer, psuedocapacitance, and battery-like mechanisms by analyzing

impedance measurements in three dimensions. *ACS Applied Materials & Interfaces*, **12**, pp.14071-14078.

[52] Shao, H., Lin, Z., Xu, K., Taberna, P.L. and Simon, P., 2019. Electrochemical study of pseudocapacitive behavior of $Ti_3C_2T_x$ MXene material in aqueous electrolytes. *Energy Storage Materials*, **18**, pp.456-461.

[53] Heimböckel, R., Hoffmann, F. and Fröba, M., 2019. Insights into the influence of the pore size and surface area of activated carbons on the energy storage of electric double layer capacitors with a new potentially universally applicable capacitor model. *Physical Chemistry Chemical Physics*, **21**, pp.3122-3133.

[54] Zhao, J., Lai, H., Lyu, Z., Jiang, Y., Xie, K., Wang, X., Wu, Q., Yang, L., Jin, Z., Ma, Y. and Liu, J., 2015. Hydrophilic hierarchical nitrogen-doped carbon nanocages for ultrahigh supercapacitive performance. *Advanced Materials*, **27**, pp.3541-3545.

[55] Lee, D.Y., An, G.H. and Ahn, H.J., 2017. High-surface-area tofu based activated porous carbon for electrical double-layer capacitors. *Journal of Industrial and Engineering Chemistry*, **52**, pp.121-127.

[56] Yang, Q., Lu, Z., Liu, J., Lei, X., Chang, Z., Luo, L. and Sun, X., 2013. Metal oxide and hydroxide nanoarrays: Hydrothermal synthesis and applications as supercapacitors and nanocatalysts. *Progress in Natural Science: Materials International*, **23**, pp.351-366.

[57] Wei, T., Wei, X., Gao, Y. and Li, H., 2015. Large scale production of biomass-derived nitrogen-doped porous carbon materials for supercapacitors. *Electrochimica Acta*, **169**, pp.186-194.

[58] Wang, D., Min, Y. and Yu, Y., 2015. Facile synthesis of wheat bran-derived honeycomb-like hierarchical carbon for advanced symmetric supercapacitor applications. *Journal of Solid State Electrochemistry*, **19**, pp.577-584.

[59] Momodu, D., Madito, M., Barzegar, F., Bello, A., Khaleed, A., Olaniyan, O., Dangbegnon, J. and Manyala, N., 2017. Activated carbon derived from tree bark biomass with promising material properties for supercapacitors. *Journal of Solid State Electrochemistry*, **21**, pp.859-872.

[60] Mi, J., Wang, X.R., Fan, R.J., Qu, W.H. and Li, W.C., 2012. Coconut-shell-based porous carbons with a tunable micro/mesopore ratio for high-performance supercapacitors. *Energy & Fuels*, **26**, pp.5321-5329.

[61] Wang, G., Zhang, L. and Zhang, J., 2012. A review of electrode materials for electrochemical supercapacitors. *Chemical Society Reviews*, **41**, pps.797-828.

[62] Zhang, Y., Fan, W., Lu, H. and Liu, T., 2018. Highly porous polyimide-derived carbon aerogel as advanced three-dimensional framework of electrode materials for high-performance supercapacitors. *Electrochimica Acta*, **283**, pp.1763-1772.

[63] Hu, C., 2008. Fluid coke derived activated carbon as electrode material for electrochemical double layer capacitor. Li, J., Wang, N., Tian, J., Qian, W. and Chu, W., 2018. Cross-coupled macro-mesoporous carbon network toward record high energy-power density supercapacitor at 4 V. *Advanced Functional Materials*, **28**, p.1806153.

[64] Li, R., Zhang, L. and Wang, P., 2015. Rational design of nanomaterials for water treatment. *Nanoscale*, **7**, pp.17167-17194.

[65] Vangari, M., Pryor, T. and Jiang, L., 2013. Supercapacitors: review of materials and fabrication methods. *Journal of Energy Engineering*, **139**, pp.72-79.

[66] Fisher, R.A., Watt, M.R. and Ready, W.J., 2013. Functionalized carbon nanotube supercapacitor electrodes: a review on pseudocapacitive materials. *ECS Journal of Solid State Science and Technology*, **2**, p.M3170.

[67] Saghafi, M., Mahboubi, F., Mohajerzadeh, S. and Holze, R., 2014. Preparation of vertically aligned carbon nanotubes and their electrochemical performance in supercapacitors. *Synthetic Metals*, **195**, pp.252-259.

[68] Honda, S., Baek, Y.G., Lee, K.Y., Ikuno, T., Kuzuoka, T., Ryu, J.T., Ohkura, S., Katayama, M., Aoki, K., Hirao, T. and Oura, K., 2004. Synthesis of randomly oriented carbon nanotubes on SiO_2 substrates by thermal chemical vapor deposition toward field electron emitters. *Thin Solid Films*, **464**, pp.290-294.

[69] Makris, T.D., Giorgi, L., Giorgi, R., Lisi, N. and Salernitano, E., 2005. CNT growth on alumina supported nickel catalyst by thermal CVD. *Diamond and Related Materials*, **14**, pp.815-819.

[70] Li, Z., Dervishi, E., Xu, Y., Saini, V., Mahmood, M., Oshin, O.D., Biris, A.R. and Biris, A.S., 2009. Carbon nanotube growth on calcium carbonate supported molybdenum-transition bimetal catalysts. *Catalysis Letters*, **131**, pp.356-363.

[71] Bahrami, B., Khodadadi, A., Mortazavi, Y. and Esmaieli, M., 2011. Short time synthesis of high quality carbon nanotubes with high rates by CVD of methane on continuously emerged iron nanoparticles. *Applied Surface Science*, **257**, pp.9710-9716.

[72] Durrer, L., Helbling, T., Zenger, C., Jungen, A., Stampfer, C. and Hierold, C., 2008. SWNT growth by CVD on Ferritin-based iron catalyst nanoparticles towards CNT sensors. *Sensors and Actuators B: Chemical*, **132**, pp.485-490.

[73] Hofmann, S., Cantoro, M., Kleinsorge, B., Casiraghi, C., Parvez, A., Robertson, J. and Ducati, C., 2005. Effects of catalyst film thickness on plasma-enhanced carbon nanotube growth. *Journal of Applied Physics*, **98**, p.034308.

[74] Tetana, Z.N., Mhlanga, S.D., Bepete, G., Krause, R.W.M. and Coville, N.J., 2012. The synthesis of nitrogen-doped multiwalled carbon nanotubes using Fe-Co/$CaCO_3$ catalyst. *South African Journal of Chemistry*, **65**, pp.39-49.

[75] Dolah, B.N.M., Deraman, M., Othman, M.A.R., Farma, R., Taer, E., Basri, N.H., Talib, I.A., Omar, R. and Nor, N.S.M., 2014. A method to produce binderless supercapacitor electrode monoliths from biomass carbon and carbon nanotubes. *Materials Research Bulletin*, **60**, pp.10-19.

[76] Xu, Y., Zhang, C., Zhou, M., Fu, Q., Zhao, C., Wu, M. and Lei, Y., 2018. Highly nitrogen doped carbon nanofibers with superior rate capability and cyclability for potassium ion batteries. *Nature Communications*, **9**, pp.1-11.

[77] Chen, L.F., Zhang, X.D., Liang, H.W., Kong, M., Guan, Q.F., Chen, P., Wu, Z.Y. and Yu, S.H., 2012. Synthesis of nitrogen-doped porous carbon nanofibers as an efficient electrode material for supercapacitors. *ACS Nano*, **6**, pp.7092-7102.

[78] Li, W., Zhang, L.S., Wang, Q., Yu, Y., Chen, Z., Cao, C.Y. and Song, W.G., 2012. Low-cost synthesis of graphitic carbon nanofibers as excellent room temperature sensors for explosive gases. *Journal of Materials Chemistry*, **22**, pp.15342-15347.

[79] Feng, L., Xie, N. and Zhong, J., 2014. Carbon nanofibers and their composites: a review of synthesizing, properties and applications. *Materials*, **7**, pp.3919-3945.

[80] Endo, M., Kim, Y.A., Hayashi, T., Fukai, Y., Oshida, K., Terrones, M., Yanagisawa, T., Higaki, S. and Dresselhaus, M.S., 2002. Structural characterization of cup-stacked-type nanofibers with an entirely hollow core. *Applied Physics Letters*, **80**, pp.1267-1269.

[81] Rodriguez, N.M., 1993. A review of catalytically grown carbon nanofibers. *Journal of Materials Research*, **8**, pp.3233-3250.

[82] Tibbetts, G.G., Lake, M.L., Strong, K.L. and Rice, B.P., 2007. A review of the fabrication and properties of vapor-grown carbon nanofiber/polymer composites. *Composites Science and Technology*, **67**, pp.1709-1718.

[83] Zhang, L., Aboagye, A., Kelkar, A., Lai, C. and Fong, H., 2014. A review: carbon nanofibers from electrospun polyacrylonitrile and their applications. *Journal of Materials Science*, **49**, pp.463-480.

[84] Rahaman, M.S.A., Ismail, A.F. and Mustafa, A., 2007. A review of heat treatment on polyacrylonitrile fiber. *Polymer Degradation and Stability*, **92**, pp.1421-1432.

[85] Nie, H.L., Ma, Z.H., Fan, Z.X., Branford-White, C.J., Ning, X., Zhu, L.M. and Han, J., 2009. Polyacrylonitrile fibers efficiently loaded with tamoxifen citrate using wet-spinning from co-dissolving solution. *International Journal of Pharmaceutics*, **373**, pp.4-9.

[86] Yarin, A.L., Koombhongse, S. and Reneker, D.H., 2001. Taylor cone and jetting from liquid droplets in electrospinning of nanofibers. *Journal of Applied Physics*, **90**, pp.4836-4846.

[87] Yarin, A.L., Koombhongse, S. and Reneker, D.H., 2001. Bending instability in electrospinning of nanofibers. *Journal of Applied Physics*, **89**, pp.3018-3026.

[88] Jin, J., Shi, Z.Q. and Wang, C.Y., 2014. Electrochemical performance of electrospun carbon nanofibers as free-standing and binder-free anodes for sodium-ion and lithium-ion batteries. *Electrochimica Acta*, **141**, pp.302-310.

[89] Yi, M. and Shen, Z., 2015. A review on mechanical exfoliation for the scalable production of graphene. *Journal of Materials Chemistry A*, **3**, pp.11700-11715.

[90] Liao, L., Peng, H. and Liu, Z., 2014. Chemistry makes graphene beyond graphene. *Journal of the American Chemical Society*, **136**, pp.12194-12200.

[91] Adetayo, A. and Runsewe, D., 2019. Synthesis and fabrication of graphene and graphene oxide: a review. *Open Journal of Composite Materials*, **9**, p.207.

[92] Zakaria, M.R., Kudus, M.H.A., Akil, H.M. and Thirmizir, M.Z.M., 2017. Comparative study of graphene nanoparticle and multiwall carbon nanotube filled epoxy nanocomposites based on mechanical, thermal and dielectric properties. *Composites Part B: Engineering*, **119**, pp.57-66.

[93] Lemine, A.S., Zagho, M.M., Altahtamouni, T.M. and Bensalah, N., 2018. Graphene a promising electrode material for supercapacitors—A review. *International Journal of Energy Research*, **42**, pp.4284-4300.

[94] Tan, Y.B. and Lee, J.M., 2013. Graphene for supercapacitor applications. *Journal of Materials Chemistry A*, **1**, pp.14814-14843.

[95] El-Kady, M.F., Shao, Y. and Kaner, R.B., 2016. Graphene for batteries, supercapacitors and beyond. *Nature Reviews Materials*, **1**, pp.1-14.

[96] Choi, H.J., Jung, S.M., Seo, J.M., Chang, D.W., Dai, L. and Baek, J.B., 2012. Graphene for energy conversion and storage in fuel cells and supercapacitors. *Nano Energy*, **1**, pp.534-551.

[97] Justino, C.I., Gomes, A.R., Freitas, A.C., Duarte, A.C. and Rocha-Santos, T.A., 2017. Graphene based sensors and biosensors. *TrAC Trends in Analytical Chemistry*, **91**, pp.53-66.

[98] Yun, Y.J., Ju, J., Lee, J.H., Moon, S.H., Park, S.J., Kim, Y.H., Hong, W.G., Ha, D.H., Jang, H., Lee, G.H. and Chung, H.M., 2017. Highly elastic graphene-based electronics toward electronic skin. *Advanced Functional Materials*, **27**, p.1701513.

[99] Das, S., Sudhagar, P., Kang, Y.S. and Choi, W., 2015. Synthesis and Characterization of Graphene. Carbon Nanomaterials for Advanced Energy Systems: Advances in Materials Synthesis and Device Applications, pp.85-131.

[100] Novoselov, K.S., Geim, A.K., Morozov, S.V., Jiang, D., Zhang, Y., Dubonos, S.V., Grigorieva, I.V. and Firsov, A.A., 2004. Electric field effect in atomically thin carbon films. *Science*, **306**, pp.666-669.

[101] Chen, J., Duan, M. and Chen, G., 2012. Continuous mechanical exfoliation of graphene sheets via three-roll mill. *Journal of Materials Chemistry*, **22**, pp.19625-19628.

[102] Li, X., Magnuson, C.W., Venugopal, A., Tromp, R.M., Hannon, J.B., Vogel, E.M., Colombo, L. and Ruoff, R.S., 2011. Large-area graphene single crystals grown by low-pressure chemical vapor deposition of methane on copper. *Journal of the American Chemical Society*, **133**, pp.2816-2819.

[103] Bae, S., Kim, H., Lee, Y., Xu, X., Park, J.S., Zheng, Y., Balakrishnan, J., Lei, T., Kim, H.R., Song, Y.I. and Kim, Y.J., 2010. Roll-to-roll production of 30-inch graphene films for transparent electrodes. *Nature Nanotechnology*, **5**, p.574.

[104] Kobayashi, T., Bando, M., Kimura, N., Shimizu, K., Kadono, K., Umezu, N., Miyahara, K., Hayazaki, S., Nagai, S., Mizuguchi, Y. and Murakami, Y., 2013. Production of a 100-m-long high-quality graphene transparent conductive film by roll-to-roll chemical vapor deposition and transfer process. *Applied Physics Letters*, **102**, p.023112.

[105] Reina, A., Jia, X., Ho, J., Nezich, D., Son, H., Bulovic, V., Dresselhaus, M.S. and Kong, J., 2009. Large area, few-layer graphene films on arbitrary substrates by chemical vapor deposition. *Nano Letters*, **9**, pp.30-35.

[106] Li, X., Cai, W., An, J., Kim, S., Nah, J., Yang, D., Piner, R., Velamakanni, A., Jung, I., Tutuc, E. and Banerjee, S.K., 2009. Large-area synthesis of high-quality and uniform graphene films on copper foils. *Science*, **324**, pp.1312-1314.

[107] Patil, A.J., Vickery, J.L., Scott, T.B. and Mann, S., 2009. Aqueous stabilization and self-assembly of graphene sheets into layered bio-nanocomposites using DNA. *Advanced Materials*, **21**, pp.3159-3164.

[108] Chen, Y., Zhang, Y., Geng, D., Li, R., Hong, H., Chen, J. and Sun, X., 2011. One-pot synthesis of MnO_2/graphene/carbon nanotube hybrid by chemical method. *Carbon*, **49**, pp.4434-4442.

[109] Sun, X., Sun, H., Li, H. and Peng, H., 2013. Developing polymer composite materials: carbon nanotubes or graphene?. *Advanced Materials*, **25**, pp.5153-5176.

[110] Kai, W., Liwei, L., Wen, X., Shengzhe, Z., Yong, L., Hongwei, Z. and Zongqiang, S., 2017. Electrodeposition synthesis of PANI/MnO_2/graphene composite materials and its electrochemical performance. *International Journal of Electrochemical Science*, **12**, pp.8306-8314.

[111] Najib, S. and Erdem, E., 2019. Current progress achieved in novel materials for supercapacitor electrodes: mini review. *Nanoscale Advances*, **1**, pp.2817-2827.

[112] Yan, J., Wang, Q., Wei, T. and Fan, Z., 2014. Recent advances in design and fabrication of electrochemical supercapacitors with high energy densities. *Advanced Energy Materials*, **4**, p.1300816.

[113] Miller, E.E., Hua, Y. and Tezel, F.H., 2018. Materials for energy storage: Review of electrode materials and methods of increasing capacitance for supercapacitors. *Journal of Energy Storage*, **20**, pp.30-40.

[114] Su, Y.F., Feng, W.U., Bao, L.Y. and Yang, Z.H., 2007. RuO_2/activated carbon composites as a positive electrode in an alkaline electrochemical capacitor. *New Carbon Materials*, **22**, pp.53-57.

[115] Swider, K.E., Merzbacher, C.I., Hagans, P.L. and Rolison, D.R., 1997. Synthesis of ruthenium dioxide−titanium dioxide aerogels: redistribution of electrical properties on the nanoscale. *Chemistry of Materials*, **9**, pp.1248-1255.

[116] Zhang, J., Ma, J., Zhang, L.L., Guo, P., Jiang, J. and Zhao, X.S., 2010. Template synthesis of tubular ruthenium oxides for supercapacitor applications. *The Journal of Physical Chemistry C*, **114**, pp.13608-13613.

[117] Zheng, J.P., Cygan, P.J. and Jow, T.R., 1995. Hydrous ruthenium oxide as an electrode material for electrochemical capacitors. *Journal of the Electrochemical Society*, **142**, p.2699.

[118] Chan, P.Y. and Majid, S.R., 2017. Metal oxide-based electrode materials for supercapacitor applications. *Advanced Materials and their Applications-Micro to Nano Scale*, p.13.

[119] Subhramannia, M., Balan, B.K., Sathe, B.R., Mulla, I.S. and Pillai, V.K., 2007. Template-assisted synthesis of ruthenium oxide nanoneedles: Electrical and electrochemical properties. *The Journal of Physical Chemistry C*, **111**, pp.16593-16600.

[120] Patake, V.D. and Lokhande, C.D., 2008. Chemical synthesis of nano-porous ruthenium oxide (RuO_2) thin films for supercapacitor application. *Applied Surface Science*, **254**, pp.2820-2824.

[121] Devadas, A., Baranton, S., Napporn, T.W. and Coutanceau, C., 2011. Tailoring of RuO_2 nanoparticles by microwave assisted "Instant method" for energy storage applications. *Journal of Power Sources*, **196**, pp.4044-4053.

[122] Hu, C.C., Chang, K.H., Lin, M.C. and Wu, Y.T., 2006. Design and tailoring of the nanotubular arrayed architecture of hydrous RuO2 for next generation supercapacitors. *Nano Letters*, **6**, pp.2690-2695.

[123] Jianming, L. and Xiaomei, C., 2015. RuO_2/MnO_2 composite materials for high-performance supercapacitor electrodes. *Journal of Semiconductors*, **36**, p.083006.

[124] . Xu, J., Wang, Q., Wang, X., Xiang, Q., Liang, B., Chen, D. and Shen, G., 2013. Flexible asymmetric supercapacitors based upon Co_9S_8 nanorod//Co_3O_4@ RuO_2 nanosheet arrays on carbon cloth. *ACS Nano*, **7**, pp.5453-5462

[125] Xie, Y. and Yao, C., 2020. Electrochemical performance of RuO_2-TiO_2 nanotube hybrid electrode material. *Materials Research Express*, **6**, p.125550.

[126] Pusawale, S.N., Deshmukh, P.R., Gunjakar, J.L. and Lokhande, C.D., 2013. SnO_2–RuO_2 composite films by chemical deposition for supercapacitor application. *Materials Chemistry and Physics*, **139**, pp.416-422.

[127] Warren, R., Sammoura, F., Kozinda, A. and Lin, L., 2014, January. ALD ruthenium oxide-carbon nanotube electrodes for supercapacitor applications. In 2014 IEEE 27th International Conference on Micro Electro Mechanical Systems (MEMS) (pp. 167-170). IEEE.

[128] Majumdar, D., Maiyalagan, T. and Jiang, Z., 2019. Recent progress in ruthenium oxide-based composites for supercapacitor applications. *ChemElectroChem*, **6**, pp.4343-4372.

[129] Hu, C.C., Yang, Y.L. and Lee, T.C., 2010. Microwave-Assisted Hydrothermal Synthesis of $RuO_2 \cdot xH_2O$–TiO_2 Nanocomposites for High Power Supercapacitors. *Electrochemical and Solid State Letters*, **13**, p.A173.

[130] Hsieh, T.F., Chuang, C.C., Chen, W.J., Huang, J.H., Chen, W.T. and Shu, C.M., 2012. Hydrous ruthenium dioxide/multi-walled carbon-nanotube/titanium electrodes for supercapacitors. *Carbon*, **50**, pp.1740-1747.

[131] Shi, F., Li, L., Wang, X.L., Gu, C.D. and Tu, J.P., 2014. Metal oxide/hydroxide-based materials for supercapacitors. *RSC Advances*, **4**, pp.41910-41921.

[132] Tan, H.T., Sun, W., Wang, L. and Yan, Q., 2016. 2D transition metal oxides/hydroxides for energy-storage applications. *ChemNanoMat*, **2**, pp.562-577.

[133] Makgopa, K., Ejikeme, P.M., Jafta, C.J., Raju, K., Zeiger, M., Presser, V. and Ozoemena, K.I., 2015. A high-rate aqueous symmetric pseudocapacitor based on highly graphitized onion-like carbon/birnessite-type manganese oxide nanohybrids. *Journal of Materials Chemistry A*, **3**, pp.3480-3490.

[134] Peng, L., Peng, X., Liu, B., Wu, C., Xie, Y. and Yu, G., 2013. Ultrathin two-dimensional MnO2/graphene hybrid nanostructures for high-performance, flexible planar supercapacitors. *Nano Letters*, **13**, pp.2151-2157.

[135] Choi, C., Sim, H.J., Spinks, G.M., Lepró, X., Baughman, R.H. and Kim, S.J., 2016. Elastomeric and dynamic MnO_2/CNT core–shell structure coiled yarn supercapacitor. *Advanced Energy Materials*, **6**, p.1502119.

[136] Liu, W., Wang, S., Wu, Q., Huan, L., Zhang, X., Yao, C. and Chen, M., 2016. Fabrication of ternary hierarchical nanofibers MnO_2/PANI/CNT and theirs application in electrochemical supercapacitors. *Chemical Engineering Science*, **156**, pp.178-185.

[137] Wang, J.G., Yang, Y., Huang, Z.H. and Kang, F., 2013. Effect of temperature on the pseudo-capacitive behavior of freestanding MnO_2@ carbon nanofibers composites electrodes in mild electrolyte. *Journal of Power Sources*, **224**, pp.86-92.

[138] Shi, Y., Peng, L., Ding, Y., Zhao, Y. and Yu, G., 2015. Nanostructured conductive polymers for advanced energy storage. *Chemical Society Reviews*, **44**, pp.6684-6696.

[139] Snook, G.A., Kao, P. and Best, A.S., 2011. Conducting-polymer-based supercapacitor devices and electrodes. *Journal of Power Sources*, **196**, pp.1-12.

[140] Frackowiak, E., Khomenko, V., Jurewicz, K., Lota, K. and Béguin, F., 2006. Supercapacitors based on conducting polymers/nanotubes composites. *Journal of Power Sources*, **153**, pp.413-418.

[141] Huang, Y., Li, H., Wang, Z., Zhu, M., Pei, Z., Xue, Q., Huang, Y. and Zhi, C., 2016. Nanostructured polypyrrole as a flexible electrode material of supercapacitor. *Nano Energy*, **22**, pp.422-438.

[142] Eftekhari, A., Li, L. and Yang, Y., 2017. Polyaniline supercapacitors. *Journal of Power Sources*, **347**, pp.86-107.

[143] D'Arcy, J.M., El-Kady, M.F., Khine, P.P., Zhang, L., Lee, S.H., Davis, N.R., Liu, D.S., Yeung, M.T., Kim, S.Y., Turner, C.L. and Lech, A.T., 2014. Vapor-phase polymerization of nanofibrillar poly (3, 4-ethylenedioxythiophene) for supercapacitors. *ACS Nano*, **8**, pp.1500-1510.

[144] Vijayakumar, S., Nagamuthu, S. and Muralidharan, G., 2013. Supercapacitor studies on NiO nanoflakes synthesized through a microwave route. *ACS Applied Materials & Interfaces*, **5**, pp.2188-2196.

[145] Bagheri, N., Aghaei, A., Vlachopoulos, N., Skunik-Nuckowska, M., Kulesza, P.J., Häggman, L., Boschloo, G. and Hagfeldt, A., 2016. Physicochemical identity and charge storage properties of battery-type nickel oxide material and its composites with activated carbon. *Electrochimica Acta*, **194**, pp.480-488.

[146] Dubal, D.P., Gund, G.S., Lokhande, C.D. and Holze, R., 2013. Decoration of spongelike $Ni(OH)_2$ nanoparticles onto MWCNTs using an easily manipulated chemical protocol for supercapacitors. *ACS Applied Materials & Interfaces*, **5**, pp.2446-2454

[147] Gund, G.S., Dubal, D.P., Shinde, S.S. and Lokhande, C.D., 2014. Architectured morphologies of chemically prepared NiO/MWCNTs nanohybrid thin films for high performance supercapacitors. *ACS Applied Materials & Interfaces*, **6**, pp.3176-3188.

[148] Ramesh, S., Karuppasamy, K., Yadav, H.M., Lee, J.J., Kim, H.S., Kim, H.S. and Kim, J.H., 2019. $Ni(OH)_2$-decorated nitrogen doped MWCNT nanosheets as an efficient electrode for high performance supercapacitors. *Scientific Reports*, **9**, pp.1-10.

[149] Yang, H., Xu, H., Li, M., Zhang, L., Huang, Y. and Hu, X., 2016. Assembly of $NiO/Ni(OH)_2$/PEDOT nanocomposites on contra wires for fiber-shaped flexible asymmetric supercapacitors. *ACS Applied Materials & Interfaces*, **8**, pp.1774-1779.

[150] Zhong, C., Deng, Y., Hu, W., Qiao, J., Zhang, L. and Zhang, J., 2015. A review of electrolyte materials and compositions for electrochemical supercapacitors. *Chemical Society Reviews*, **44**, pp.7484-7539.

[151] Lust, E., Jänes, A. and Arulepp, M., 2004. Influence of electrolyte characteristics on the electrochemical parameters of electrical double layer capacitors. *Journal of Solid State Electrochemistry*, **8**, pp.488-496.

[152] Lokhande, C.D., Dubal, D.P. and Joo, O.S., 2011. Metal oxide thin film based supercapacitors. *Current Applied Physics*, **11**, pp.255-270.

[153] Lewandowski, A., Olejniczak, A., Galinski, M. and Stepniak, I., 2010. Performance of carbon–carbon supercapacitors based on organic, aqueous and ionic liquid electrolytes. *Journal of Power Sources*, **195**, pp.5814-5819.

[154] Lokhande, C.D., Dubal, D.P. and Joo, O.S., 2011. Metal oxide thin film based supercapacitors. *Current Applied Physics*, **11**, pp.255-270.

[155] Fic, K., Lota, G., Meller, M. and Frackowiak, E., 2012. Novel insight into neutral medium as electrolyte for high-voltage supercapacitors. *Energy & Environmental Science*, **5**, pp.5842-5850.

[156] Chen, Z., Qin, Y., Weng, D., Xiao, Q., Peng, Y., Wang, X., Li, H., Wei, F. and Lu, Y., 2009. Design and synthesis of hierarchical nanowire composites for electrochemical energy storage. *Advanced Functional Materials*, **19**, pp.3420-3426.

[157] Deng, L., Zhang, G., Kang, L., Lei, Z., Liu, C. and Liu, Z.H., 2013. Graphene/VO_2 hybrid material for high performance electrochemical capacitor. *Electrochimica Acta*, **112**, pp.448-457.

[158] Sato, T., Masuda, G. and Takagi, K., 2004. Electrochemical properties of novel ionic liquids for electric double layer capacitor applications. *Electrochimica Acta*, **49**, pp.3603-3611.

[159] Angell, C.A., Ansari, Y. and Zhao, Z., 2012. Ionic Liquids: Past, present and future. *Faraday Discussions*, **154**, pp.9-27.

[160] Galiński, M., Lewandowski, A. and Stępniak, I., 2006. Ionic liquids as electrolytes. *Electrochimica Acta*, **51**, pp.5567-5580.

[161] Lewandowski, A. and Świderska-Mocek, A., 2009. Ionic liquids as electrolytes for Li-ion batteries—An overview of electrochemical studies. *Journal of Power Sources*, **194**, pp.601-609.

[162] Inagaki, M., Konno, H. and Tanaike, O., 2010. Carbon materials for electrochemical capacitors. *Journal of Power Sources*, **195**, pp.7880-7903.

[163] Weingarth, D., Foelske-Schmitz, A., Wokaun, A. and Kötz, R., 2013. PTFE bound activated carbon-a quasi reference electrode for ionic liquids and its application. *ECS Transactions*, **50**, p.111.

[164] Stoller, M.D. and Ruoff, R.S., 2010. Best practice methods for determining an electrode material's performance for ultracapacitors. *Energy & Environmental Science*, **3**, pp.1294-1301.

[165] Shivakumara, S., Kishore, B., Penki, T.R. and Munichandraiah, N., 2014. Symmetric supercapacitor based on partially exfoliated and reduced graphite oxide in neutral aqueous electrolyte. *Solid State Communications*, **199**, pp.26-32.

[166] Frackowiak, E. and Beguin, F., 2001. Carbon materials for the electrochemical storage of energy in capacitors. *Carbon*, **39**, pp.937-950.

[167] Zia, A.I. and Mukhopadhyay, S.C., 2016. Impedance spectroscopy and experimental setup. In Electrochemical Sensing: Carcinogens in Beverages. Springer, Cham. pp. 21-37.

[168] Joe, J., Yang, H., Bae, C. and Shin, H., 2019. Metal chalcogenides on silicon photocathodes for efficient water splitting: A mini overview. *Catalysts*, **9**, p.149.

[169] Jorcin, J.B., Orazem, M.E., Pébère, N. and Tribollet, B., 2006. CPE analysis by local electrochemical impedance spectroscopy. *Electrochimica Acta*, **51**, pp.1473-1479.

[170] Lu, M., 2013. Supercapacitors: materials, systems, and applications. John Wiley & Sons.

CHAPTER 3

Experimental methods and characterisation techniques

This chapter describes the experimental methods, as well as a brief description of some of the characterization techniques used.

3.1 Experimental details

3.1.1 Materials

Polyacrylonitrile (PAN) polymer (M= 150000), iron nitrate nonahydrate ($Fe(NO_3)_3 \cdot 9H_2O$, 98 %), cobalt nitrate hexahydride ($Co(NO_3)_2 \cdot 6H_2O$, 98 %), nickel nitrate hexahydrate ($Ni(NO_3)_2 \cdot 6H_2O$, 98 %), N, N-dimethylformamide (DMF, 99.8 %), triethylamine (TEA, $N(CH_2CH_3)_3$, ≥ 99.5 %), ethylene glycol (EG, $C_2H_6O_2$, 99.8 %), potassium permanganate ($KMnO_4$, ≥ 99.5 %), sodium sulphate (Na_2SO_4, ≥ 99 %) and manganese sulfate ($MnSO_4 \cdot H_2O$, ≥ 99 %), acetonitrile (99,8 %), urea (99 %), potassium hydroxide (KOH) pellets 85%, were all purchased from Sigma Aldrich (South Africa). Ethanol (C_2H_6O, 99 %), quarts boat, quart tube, pure nitrogen (N_2) was supplied by Afrox (South Africa), Millipore water (resistivity value of 18.2 MΩ cm was collected from the Milli-Q water system), 3.0 M hydrochloric acid (HCl), carbon paper. All the chemicals were used exactly as received.

3.1.2 Fabrication of electrospun PAN fibres

The LINARI Nano-Tech electrospinning set-up was used for the fabrication of nanofibers. To begin, a polymer solution was made by dissolving 10% PAN in DMF and stirred for 24 hours at room temperature. A high direct current (DC) voltage of 9 kV was used, the distance between

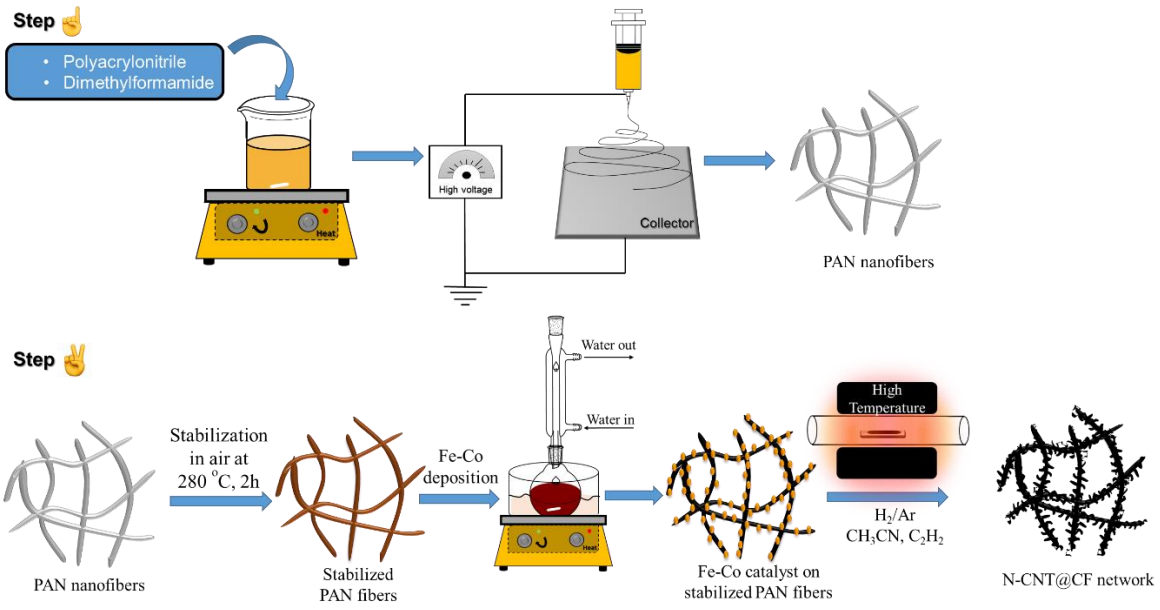
the spinneret and the collector was kept at 15 cm and the flow rate was kept constant at 500 μL h^{-1}. The electrospun fibres were deposited on a metal collector plate covered in aluminium foil for 10 hours. After collecting, the dense fibre mat was stabilized at 280 °C under air for 2 hours in a tube furnace.

3.1.3 Deposition of the bimetallic catalyst

A bimetallic catalyst Fe-Co deposited on stabilized PAN fibres was synthesized by the co-precipitation method using urea as the precipitating agent. A ratio of 1:1 (Fe/Co precursors) was used, and the total metal loading was kept at 10 wt. %. Typically, the metal nitrate precursors and urea (1.5 moles urea per mole of metal) were dissolved in deionised water (50 mL) and then added to the stabilized PAN fibres, which were dispersed previously in deionised water (100 mL) at 90 °C. The hydrolysis of urea was allowed to proceed for 12 hrs with stirring, followed by centrifugation and drying at 70 °C under vacuum.

3.1.4 Synthesis of CNTs on top of stabilized PAN fibres

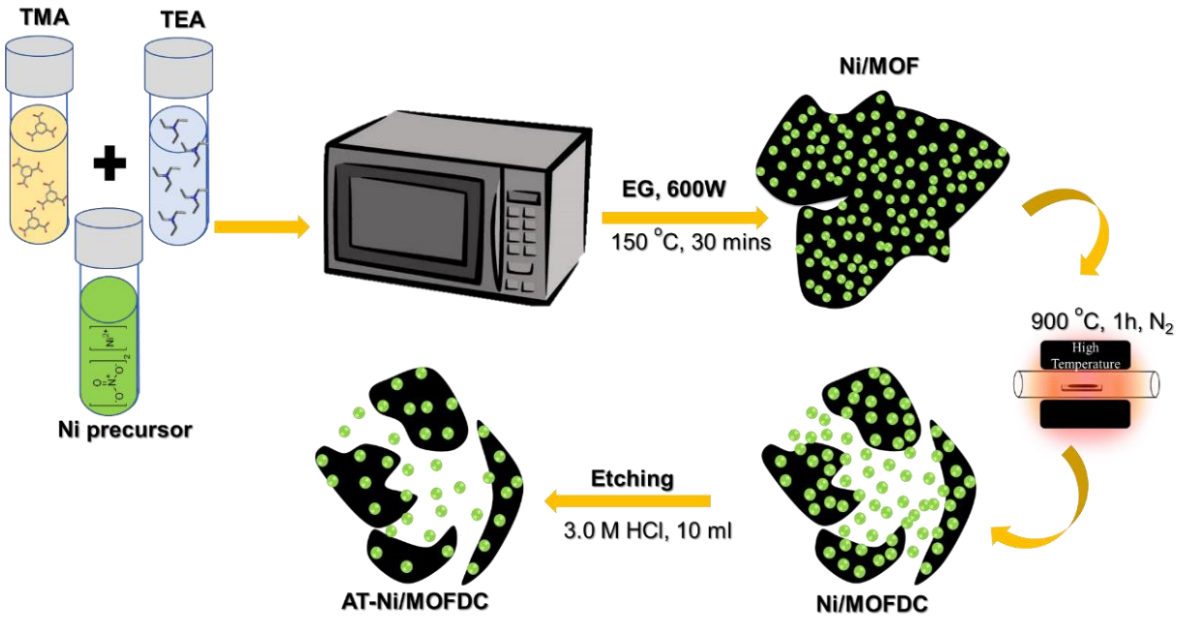
Prior to the synthesis of CNTs, Fe-Co deposited PAN fibres were annealed at 500 °C for 1 hour at a heating rate of 5 °C min^{-1} in an atmosphere of H_2 and Ar to enable the reduction of iron and cobalt precursors to iron and cobalt nanoparticles. CNTs were then grown for 10 minutes at 800 °C using C_2H_2 gas as a source of carbon (50 sccm), H_2 as a reducing agent (35 sccm) and Ar as a carrier gas (500 sccm). For the synthesis of N-CNT@CF, the same procedure was used, but C_2H_2 (50 sccm) was bubbled through CH_3CN solution, which was used as a source of nitrogen. The catalyst in all materials was leached using hot concentrated nitric acid. **Scheme 3.1** illustrate a diagram for the fabrication of the N-CNT@CF hybrid as an example.



Scheme 3.1: Fabrication of N-CNF@CF network by electrospinning and CVD method.

3.1.5 Synthesis of Ni-MOF, Ni/MOFDC and AT-Ni/MOFDC

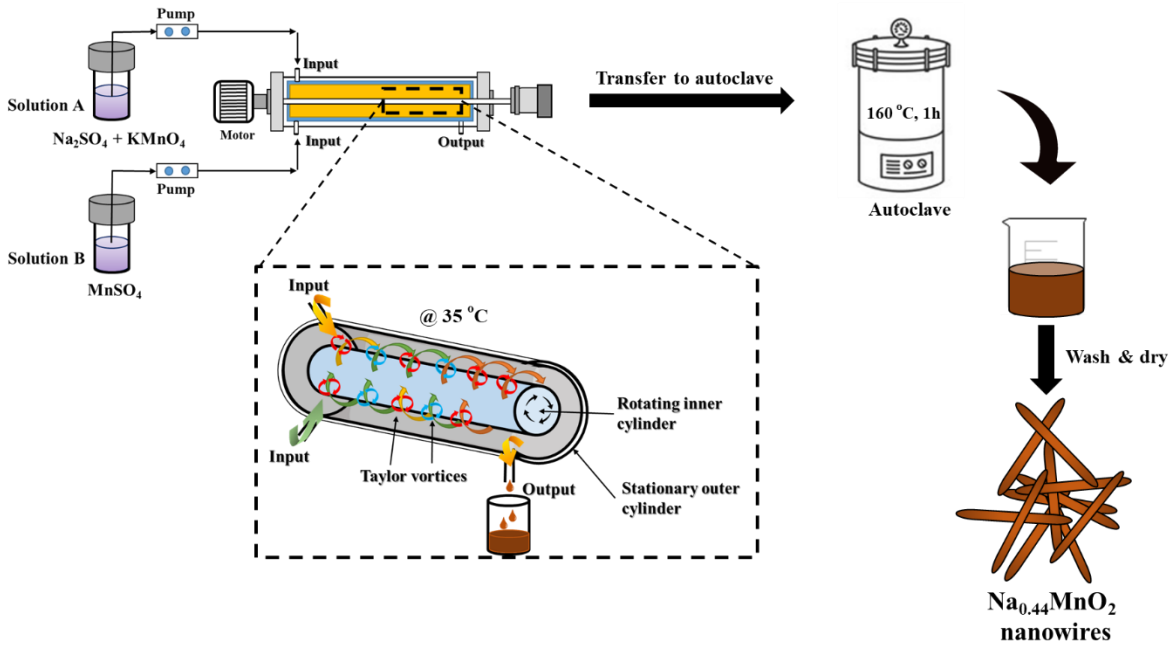
Nickel-based metal-organic framework (Ni-MOF) was synthesized using a microwave-assisted solvothermal method [1], with minor modifications. Typically, 1.6811 g (8.0 mmol) of TMA, 10 mL (1.2 mol) of TEA and 1.1632 g (4.0 mmol) of $Ni(NO_3)_2.6H_2O$, were dissolved in 50 mL (0.9 mol) of EG in a beaker. The mixture was ultrasonicated for 1 hour to ensure homogeneity. The mixture was then microwave irradiated (MW) for 30 minutes at 600 W and 150 °C before cooling to ambient temperature. A deep green Ni-MOF crystal was collected, centrifuged three times using ethanol to remove impurities and then dried for 12 hours in a vacuum oven at 80 °C. The Ni-MOF powder was poured into a quartz boat, placed in a quartz tube and annealed in an electric furnace for 3 hours at 900 °C under N_2 flow at a rate of 5 °C min^{-1}, resulting in nickel nanoparticles supported MOF-derived carbon (Ni/MOFDC). The Ni/MOFDC was split into two parts: one was chemically etched with 3.0 M HCl (10 mL), yielding AT-Ni/MOFDC and the other was not (i.e., Ni/MOFDC).



Scheme 3.2: Schematic illustrations of the synthesis of the Ni-MOF, Ni/MOFDC and AT-Ni/MOFDC.

3.1.6 Preparation of $Na_{0.44}MnO_2$

The two-step synthetic techniques: Couette-Taylor flow reactor and hydrothermal method were used to synthesize the sodium manganese oxide material [2]. The stoichiometric ratios of $KMnO_4$, Na_2SO_4 and $MnSO_4$ were first calculated. Typically, 0.1054 g of $KMnO_4$ was dissolved in ultrapure water (30 mL), followed by the addition of Na_2SO_4 to the above solution A. The Na_2SO_4 and $KMnO_4$ concentration ratio was 15:1. Subsequently, 0.1690 g of $MnSO_4$ was dissolved in distilled water (20 mL) to form solution B. Solutions A and B were then fed into the Laminar Continuous Taylor Flow Reactor (LCTR). In the LCTR, the two solutions were subjected to Taylor-Couette flow, which allows for vigorous homogeneous micro and macro mixing at 35 °C, resulting in a faster reaction, dense and uniform product particle. The resultant dark brown solution was then poured into a 60 mL Teflon-lined autoclave and kept for 1 hour at 160 °C. After the autoclave had naturally cooled to room temperature, the product was filtered out, washed five times with deionized water/ethanol and dried at 80 °C for 12 hours (see **Scheme 3.3**).



Scheme 3.3: Schematic illustrations of the synthesis of the $Na_{0.44}MnO_2$.

3.2 A brief overview of some of the characterization techniques

3.2.1 Scanning electron microscopy (SEM)

In the field of material science and engineering, scanning electron microscopy (SEM) is a fast and easy technique for the analysis of materials. The SEM can provide high-resolution analysis and a wide range of analytical modes, each of which provides unique details about the surface features of the material [3].

The major parts of the SEM, as presented in **Figure 3.1**, are an electron gun, an electron lens system, electron-beam deflection coils, various electron detectors, display and recording devices. A directed electron beam of high-energy electrons is used in SEM to produce a range of signals at the surface of solid materials. To produce different types of signals, secondary electrons, back-scattered electrons, characteristic X-ray, light cathode luminescence and specimen current are used in the process. The secondary electron is used for imaging information about the depth and morphology at the material surface. The signals result from

interactions of the electron beam with atoms at or near the surface of the material. These signals that are derived reveal information about the sample such as morphology, thickness, porosity and orientation of the microscopic materials that make up bulk material.

The surfaces of all the materials in this thesis were electrically conductive, so they were coated with gold/palladium alloy and carbon materials using a carbon sputter coating method to avoid the accumulation of electrostatic charge on the surface.

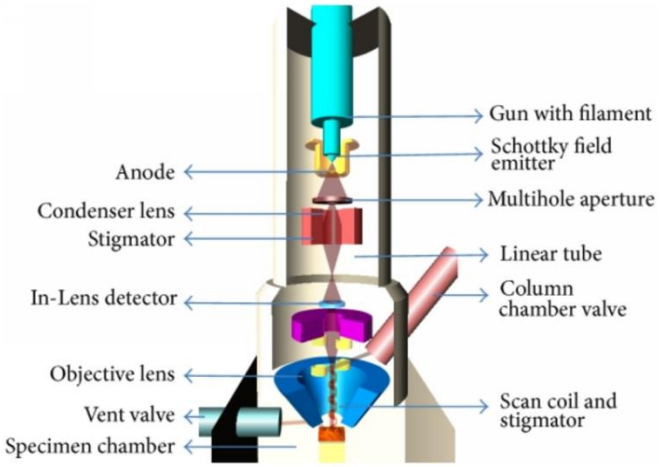


Figure 3.1: Schematic representation of an SEM operation [4].

The microstructures, morphology and the elemental composition of the samples were observed using scanning electron microscope (SEM) coupled with energy-dispersive X-ray (EDX) analysis using (FEI Nova Nanolab 600) instrument.

3.2.2 Transmission electron microscopy (TEM)

Transmission electron microscopy (TEM) is an imaging technique that involves transmitting a focused high-energy electron beam through a thin sample. The electrons interact with the sample atoms and the transmitted image is then magnified and focused onto an imaging device, such as a fluorescent screen. As shown in **Figure 3.2**, TEM consists of an electron source, a condenser system, an objective lens and a projector system. For elemental studies, many TEM

instruments have an X-ray detector and/or an energy loss spectrometer. The electron gun is composed of a cathode and an accelerating system. A thermal cathode, a Schottky emitter or a cold field emission cathode may all be used as cathodes. The electrons are released at high temperatures from tungsten or LaB_6 in the thermal cathode. In a Schottky emitter, a strong electrostatic field is applied to the tip, lowering the emission barrier. The quantum mechanical tunnel effect is used in the cold field emission cathode to capture electrons using a stronger electrostatic field at a sharp tip. To prevent the tip from being destroyed by atoms in the chamber, this form of cathode requires an ultra-high vacuum. The electrons are then accelerated towards the anode by a device. Majority of transmission electron microscopes work at 100–300 kV. Electrons are transferred onto the specimen by a condenser system, which employs two to five electron lenses. These lenses allow you to monitor the size of the illuminated area on the sample as well as the illumination angle. The electrons are then transmitted through the sample, concentrated, and magnified and a picture is formed [5].

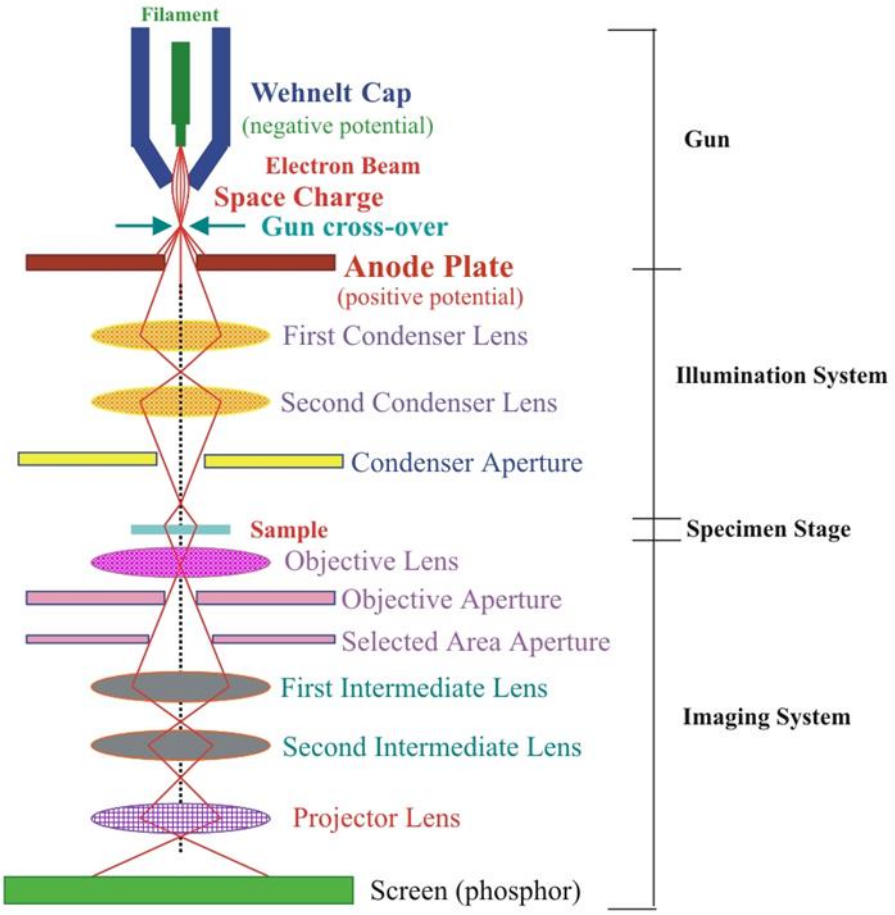


Figure 3.2: Schematic diagram of a typical TEM [6].

TEM analysis was performed on an FEI Tecnai T12 Spirit electron microscope operating at an accelerating voltage of 120 kV. Sample preparation for TEM measurement was achieved by dispersing the powdered samples in ethanol followed by ultra-sonication for 3 minutes. The suspension was then added dropwise to carbon-coated Cu grids before measurement.

3.2.3 Raman spectroscopy

Raman spectroscopy is a technique used to study the molecular vibration, rotational and other low-frequency modes in materials. In this context, the Raman spectroscopic has been considered as a potential and a very promising instrumental technique applied in materials and biological fluids [7]. This technique can also be used to get a better understanding of the

chemical composition of materials. Raman spectroscopy runs on inelastic scattering of monochromatic light, which is typically produced by a laser operating in the visible, near-infrared or near-ultraviolet ranges, as shown in **Figure 3.3** [8].

In this process, the molecule is irradiated by electromagnetic radiation which interacts with the bonds or electron cloud of the molecule and emits a scattered light. The Raman Effect occurs when light from the laser interacts with molecules, phonons, or other excitations in a material, causing the intensity of the laser photons to change in relation to the energy or frequency of the original monochromatic light [9]. The energy or frequency changes in a material provide details on the vibrational modes. In this thesis, Raman spectroscopy (Jobin-Yvon T6400) with a 532 nm laser wavelength and spectral acquisition time of 120 s was used to characterize the materials.

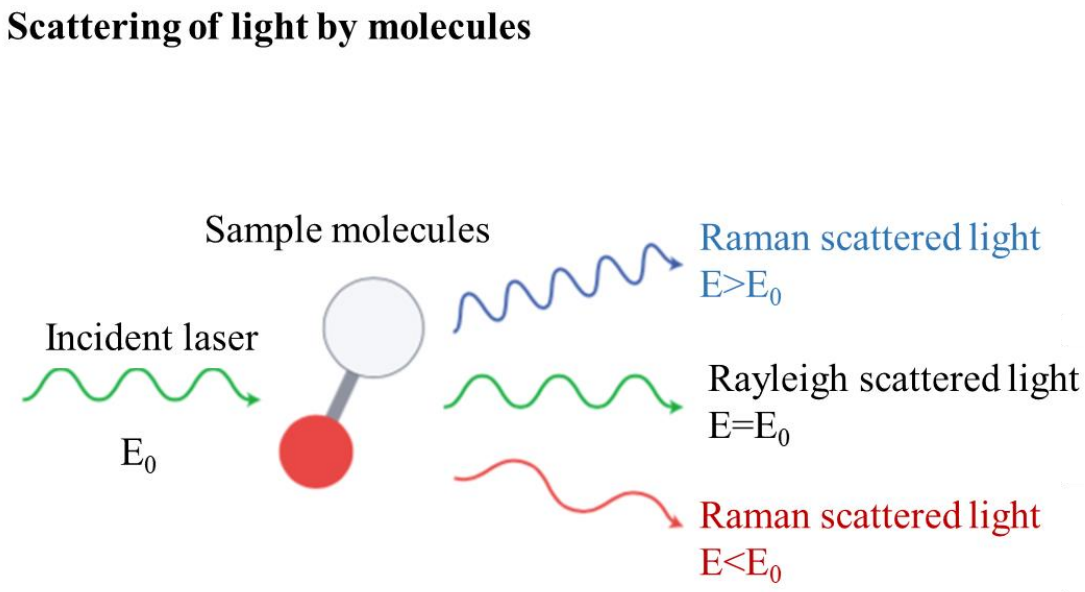


Figure 3.3: Rayleigh and Raman light scattering by molecules [10].

3.2.4 Powder X-Ray diffraction (P-XRD)

Powder X-ray diffraction (PXRD) is used to characterize large crystallized materials or powder metals, ceramic minerals, pharmaceutical compounds, organometallic complexes and metallo-

organic materials. It enables fast analysis of powders containing several components without the need for extensive sample preparation. It is used to uniquely identify phases of bulk crystalline materials by comparing their unique X-ray signature to a huge database that practically contains XRD fingerprints of every phase of every known material.

X-ray diffraction is a non-destructive and flexible analytical technique. The X-ray diffraction peaks are generated by the constructive interaction of monochromatic X-ray beams scattered by each set of lattice planes. When these waves reach the sample, the sample atoms diffract them, producing spots at particular angles on the detector plate. By measuring the angle where these spots occur, the spacing between the atoms can be determined using Bragg's law [11] given in equation 3.1.

$$n\lambda = 2d\sin\theta \tag{3.1}$$

where n is an integer value (1,2,3...), λ is the wavelength of the incident x-ray, d is the spacing between the diffracting planes and θ is the incident angle. The angle between the projection of the X-ray source and the detector is 2θ. The XRD pattern of all the as-prepared materials was characterized using a Bruker D2 phaser equipped with Cu-Kα radiation (λ= 1.5405 Å), with an operating voltage of 30 kV and a current of 10 Ma.

3.2.5 X-ray photoelectron spectroscopy (XPS)

X-ray photoelectron spectroscopy (XPS) is commonly considered an important and key technique for surface characterization. Generally, XPS is the most quantitative, the most readily interpretable and the most informative about chemical and electronic information. XPS method provides a total elemental analysis, except for hydrogen and helium. Without the need for further sample preparation, the materials are usually analysed as obtained.

XPS spectra are obtained when a material is bombarded with X-ray photons that interact with core electrons present around the nucleus of the atoms in the sample. The electrons that escape the sample, are emitted at specific kinetic energy as shown in **Figure 3.4**. This kinetic energy depends on the photoelectron energy and the binding energy required to remove the electron. As this binding energy depends on the atom type, the orbital in which it is situated and its bonding neighbours, it can be plotted and analysed and the type of atom, chemical state and abundance can be determined [12].

The XPS spectrum can provide a variety of levels of spectral interpretation, including simple elemental analysis, comprehensive considerations of chemical shifts and chemical bonding nature in the surface region and various loss or relaxation structures that provide additional details on the chemical nature of the surface. This interpretation becomes progressively more challenging as one goes to more complex surfaces, such as multi-component and multi-phase materials [13].

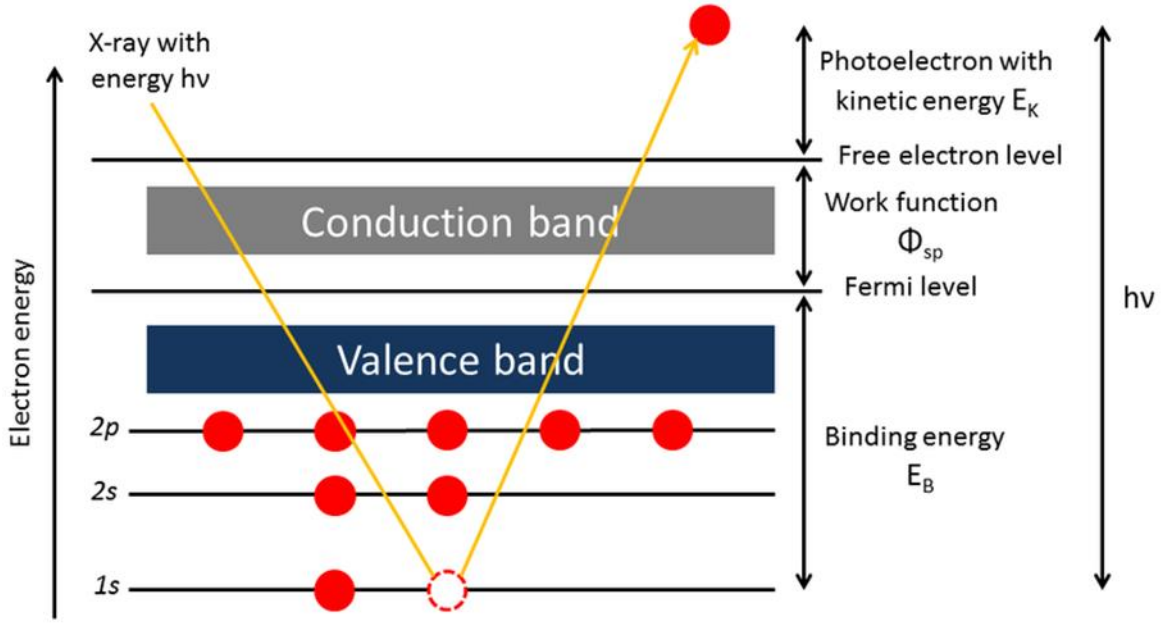


Figure 3.4: Schematic diagram of XPS operation [14].

X-ray photoelectron spectroscopy (XPS) measurements of all material in this work were studied using ESCAlab 250Xi XPS with a monochromatic Al kα radiation source (1486.7eV)). Survey spectra were taken at pass energy of 100 eV and high-resolution pass energy of 20 eV. The instrument used is located in NMISA, Building 5, CSIR Campus, Pretoria, South Africa.

3.2.6 Surface area and porosity analysis

Specific surface area (SSA) and porosity can be measured by a gas adsorption method. The Brunauer-Emmet-Teller (BET) technique most commonly used, named after the three who first published the theory [15], is based on the concept that inert gas is physically adsorbed on the surface of a solid without reacting, in a single monolayer. This applies to liquid nitrogen (N_2) which has a boiling temperature of -196 ºC. Nitrogen gas is most commonly used as it is inert, and the molecule is small therefore tracing the surface roughness best and enable entering small pores. The sample is weighed and pre-treated by heating and flowing an inert gas to remove any adsorbed water or other contaminants. The sample is then cooled, and the inert measuring gas allowed to adsorb on the surface. The amount of adsorbed gas is measured and is

proportional to the area it adsorbed on, allowing the sample surface area to be calculated. The SSA and porosity of all materials synthesized in this thesis were measured using an ASAP 2000 Micrometrics TriStar Surface Area and Porosity Analyser.

3.3 References

[1] Ipadeola, A.K., Barik, R., Ray, S.C. and Ozoemena, K.I., 2019. Bimetallic Pd/SnO_2 nanoparticles on metal organic framework (MOF)-derived carbon as electrocatalysts for ethanol oxidation. *Electrocatalysis*, **10**, pp.366-380.

[2] Feng, M., Du, Q., Su, L., Zhang, G., Wang, G., Ma, Z., Gao, W., Qin, X. and Shao, G., 2017. Manganese oxide electrode with excellent electrochemical performance for sodium ion batteries by pre-intercalation of K and Na ions. *Scientific Reports*, **7**, pp.1-8.

[3] Orloff, J. ed., 2017. Handbook of charged particle optics. CRC press.

[4] Jusman, Y., Ng, S.C. and Abu Osman, N.A., 2014. Investigation of CPD and HMDS sample preparation techniques for cervical cells in developing computer-aided screening system based on FE-SEM/EDX. The Scientific World Journal, 2014.

[5] Bhushan, B. ed., 2012. Encyclopedia of nanotechnology (No. 544.1). Dordrecht, Netherlands: Springer.

[6] Ghimire, H., 2015. Quantitative Study of Nano to Submicron Scales Intracellular Structural Disorder Using Electron and Confocal Microscopies: Application to Cancer Detection (Doctoral dissertation, University of Memphis).

[7] Moreira, L.M., Silveira Jr, L., Santos, F.V., Lyon, J.P., Rocha, R., Zângaro, R.A., Villaverde, A.B. and Pacheco, M.T., 2008. Raman spectroscopy: A powerful technique for biochemical analysis and diagnosis. *Spectroscopy*, **22**, pp.1-19.

[8] Rubim, J.C., Sousa, M.H., Silva, J.C. and Tourinho, F.A., 2001. Raman spectroscopy as a powerful technique in the characterization of ferrofluids. *Brazilian Journal of Physics*, **31**, pp.402-408.

[9] Tseng, Y.C., Cheng, Y.C., Lee, Y.C., Ma, D.L., Yu, B.Y., Lin, B.C. and Chen, H.L., 2016. Using Visible Laser-Based Raman Spectroscopy to Identify the Surface Polarity of Silicon Carbide. *The Journal of Physical Chemistry C*, **120**, pp.18228-18234.

[10] Anon.'Basics of Raman scattering | Nanophoton', Nano photon, Raman, Raman spectroscopy. [Online]. Available: https://www.nanophoton.net/lecture-room/raman-spectroscopy/lesson-1-1. [Accessed: 08-April-2021]

[11] Pope, C.G., 1997. X-ray diffraction and the Bragg equation. *Journal of Chemical Education*, **74**, p.129.

[12] Claesson, P., van der Wal, A. and Fogden, A., 2007. New techniques for optimization of particulate cleaning.

[13] Ghosh, S., Bomma, S., Prasanna, V.L., Srivani, P. and Bhanji, D., 2013. New Analytical Methods in Nanotechnology-A Review. *Asian Journal of Research in Pharmaceutical Sciences*, **3**, pp.31-41.

[14] Vandenbroucke, A., 2015. Abatement of volatile organic compounds by combined use of non-thermal plasma and heterogeneous catalysis (Doctoral dissertation, Ghent University).

[15] Brunauer, S., Emmett, P.H. and Teller, E., 1938. Adsorption of gases in multimolecular layers. *Journal of the American Chemical Society*, **60**, pp.309-319.

CHAPTER 4

Nitrogen-doped carbon nanotube-carbon fibre networks for high-performance symmetric supercapacitor[1]

4.1 Introduction

Supercapacitors have received a great deal of recognition both in academia and industry over the last two decades as one of the most efficient energy storage devices for high power applications [1, 2]. In addition, as opposed to batteries, supercapacitors have a long cycle life and can run at a variety of temperatures [3-5]. Supercapacitors are best suited for technical and engineering applications that involve the fast release of energy, like uninterrupted power systems (UPS), electric vehicles (especially the "stop-start" mechanism), power machinery such as forklifts and smart grids, etc.

Supercapacitors made completely of carbon-based materials are known as electric double-layer capacitors (EDLCs). Carbon-based materials are recognized for possessing desirable properties that enable an electric double layer (EDL) storage mechanism. These properties include low cost, high specific surface area, high conductivity and chemical stability. Over the past decade, different synthetic methods have been used to fabricate advanced carbon-based electrode materials. This includes designing one-dimensional (1D) nanostructured such as carbon nanotubes (CNTs) and carbon nanofibers (CNFs) [6, 7], creating surface defects and improving

[1]A substantial part of this chapter has been published in a peer-reviewed journal: **Mofokeng, T.P**., Tetana, Z.N. and Ozoemena, K.I., 2020. Defective 3D nitrogen-doped carbon nanotube-carbon fibre networks for high-performance supercapacitor: Transformative role of nitrogen-doping from surface-confined to diffusive kinetics. Carbon, 169, pp.312-326.

porosity [8] and changing the carbon matrix by doping with other elements such as boron and nitrogen [9-11].

When it comes to improving porosity, the pore size distribution, as well as the surface area, have a major impact on the electrochemical performance of the material. In addition, the conductivity of the material is also important for improving the electrochemical performance of the electrode material [12]. However, it should be noted that capacitance is not always proportional to the surface area of the electrode material; instead, uniform pore size distribution has a major impact on the electrochemical performance of the electrode material. The formation of an EDL is aided by a high specific surface area, while the adsorption/desorption pathways of the electrolyte ions are determined by a uniform pore size distribution [13]. As a result of the electrolyte ions migrating through the inner part of the porous electrode material, the capacitance of material with micropores would substantially be increasing [14]. But, a material with high microporosity, on the other hand, increases electrolyte ion diffusion resistance, leading to unfavourable ion adsorption at the electrode/electrolyte interface, particularly at high scan rates and current densities. Ion diffusion into micropores is low at high scan rates/current densities due to the inability of the electrode material to keep up with the fast charging and discharging rate, resulting in poor rate efficiency [15]. Mesopores, on the other hand, can accelerate electrolyte ions for better charge propagation, whilst macropores can operate as electrolyte ion reservoirs, shortening electrolyte ions propagation distances. In this regard, synthesizing hierarchical porous carbon materials that possess uniform pore distribution will enhance the electrochemical performance of carbon-based electrodes.

Furthermore, doping carbon-based materials with heteroatoms like nitrogen can change its electrical structure and enhance charge carrier density, leading to surface redox reactions. These alterations in the carbon matrix can enhance the electrical conductivity, surface

wettability and capacitance of heteroatom-doped carbon [16, 17]. As a result, heteroatom-doped carbon materials with a hierarchical 3D porous structure are attractive electrode materials for improving or expanding supercapacitor application [18].

4.2 Experimental

4.2.1 Materials and methods

Polyacrylonitrile (PAN) polymer (M =150000), N, N-dimethyl formamide (DMF) 99.8 %, iron nitrate nonahydrate ($Fe(NO_3)_3{\cdot}9H_2O$, 98 %), cobalt nitrate hexahydride ($Co(NO_3)_2{\cdot}6H_2O$, 98 %), urea (99 %), acetonitrile (99.8 %) and potassium hydroxide (KOH) pellets 85 % were purchased from Sigma- Aldrich (SA). All the chemicals were used exactly as they were received.

4.2.2 Fabrication of electrospun PAN fibres

The LINARI Nano-Tech electrospinning set-up was used for the fabrication of nanofibers. To begin, a polymer solution was made by dissolving 10% PAN in DMF and stirred for 24 hours at room temperature. A high direct current (DC) voltage of 9 kV was used, the distance between the spinneret and the collector was kept at 15 cm and the flow rate was kept constant at 500 μL h^{-1}. The electrospun fibres were deposited on a metal collector plate covered in aluminium foil for 10 hours. After collecting, the dense fibre mat was stabilized at 280 °C under air for 2 hours in a tube furnace.

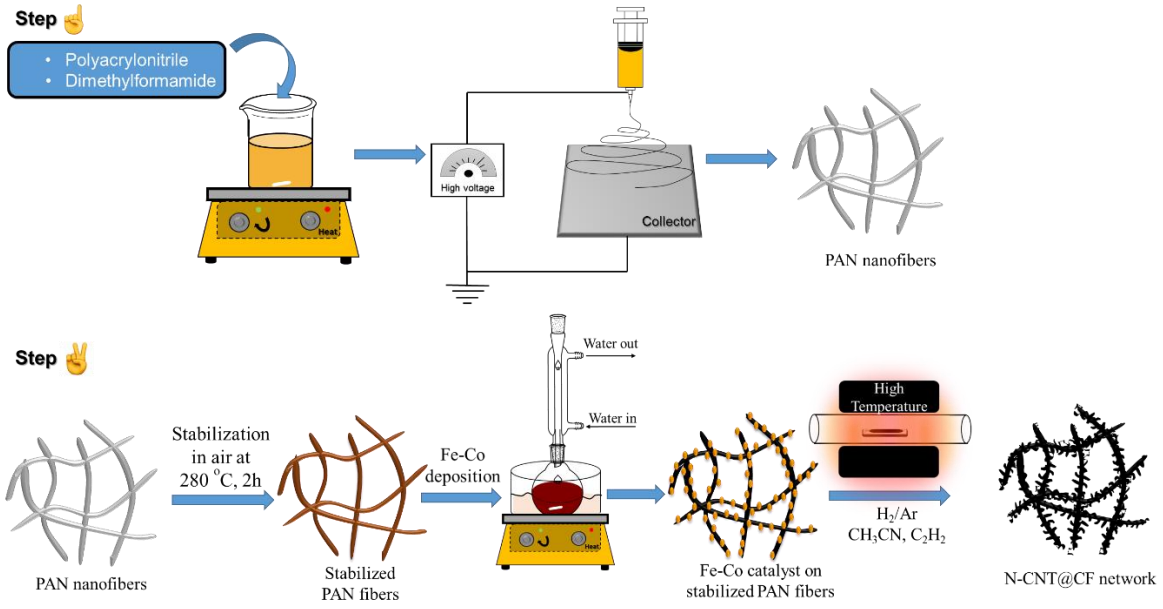
4.2.3 Deposition of the bimetallic catalyst

The bimetallic catalyst Fe-Co deposited on stabilized PAN fibres was synthesized by the co-precipitation method using urea as the precipitating agent. A ratio of 1:1 (Fe/Co precursors) was used and the total metal loading was kept at 10 wt. %. Typically, the metal nitrate precursors and urea (1.5 moles urea per mole of metal) were dissolved in deionised water (50

mL) and then added to the stabilized PAN fibres, which were dispersed previously in deionised water (100 mL) at 90 °C. The hydrolysis of urea was allowed to proceed for 12 h with stirring, followed by centrifugation and drying at 70 °C under vacuum.

4.2.4 Synthesis of CNTs on top of stabilized PAN fibres

Prior to the synthesis of CNTs, Fe-Co deposited PAN fibres were annealed at 500 °C for 1 hour at a heating rate of 5 °C min^{-1}. CNTs were then grown for 10 minutes at 800 °C using C_2H_2 gas as a source of carbon (50 sccm), H_2 as a reducing agent (35 sccm) for Fe and Co precursors and Ar as a carrier gas (500 sccm). For the synthesis of N-CNT@CF, the same procedure was used, but C_2H_2 (50 sccm) was bubbled through CH_3CN solution, which was used as a source of nitrogen. **Scheme 3.1** illustrate a diagram for the fabrication of the N-CNT@CF hybrid as an example.



Scheme 4.1: Fabrication of N-CNT@CF network by electrospinning and CVD method.

4.2.5 Characterization methods

4.2.5.1 Material characterization

The microstructures, morphology and the elemental composition of the samples were observed using scanning electron microscopy (SEM) coupled with energy-dispersive X-ray spectroscopy (EDX) analysis using (FEI Nova Nanolab 600) instrument. TEM analysis was performed on an FEI Tecnai T12 Spirit electron microscope operating at an accelerating voltage of 120 kV. Sample preparation for TEM measurement was achieved by dispersing the powdered samples in ethanol followed by ultra-sonication for 3 minutes. The suspension was then added dropwise to carbon-coated Cu grids prior to measurement. Structural features were further analysed using Raman spectroscopy (Jobin-Yvon T6400) and X-ray diffraction (XRD) using a Bruker D2 phaser equipped with Cu-Kα radiation (λ= 1.5405 Å), with an operating voltage of 30kV and current of 10 mA. BET surface areas of the samples (~ 200 mg for each sample) were obtained through N_2 adsorption using an ASAP 2000 Micrometrics TriStar Surface Area and Porosity Analyser.

4.2.5.2 Electrochemical characterization

All electrochemical characteristics were first determined in a three-electrode system (half-cell) and then a two-electrode system (full-cell). For the preparation of working electrodes, the active materials were crushed and dispersed in ethanol before being sonicated for 20 minutes to make a paste. The paste was spread onto a circular carbon paper disk (A= 1.131) and dried at 60 °C in an oven for 8 hours to guarantee full evaporation of the solvent. The electrodes were typically loaded with 1.0-1.2 mg of mass. The counter electrode was a circular nickel foam disk (A=1.131) and the silver wire was used as a reference electrode. The SP300 Potentiostat (Bio-logic Science equipment operating on EC-Lab software) was used to perform cyclic voltammetry (CV), galvanostatic charge-discharge (GCD) and electrochemical impedance

spectroscopy (EIS) in a 6 M KOH electrolyte. Equations (4.1-4.6) [19] were used to determine specific capacitance (C_s), energy density (E_s), power density (P_s) and maximum power density based on the discharge time from GCD curves. Equation 4.1 was used to calculate the capacitance, C (F):

$$C = \frac{I \times \Delta t}{\Delta V} \quad (4.1)$$

where I (A) is the current, Δt (s) discharge time, m (g) mass of the active electrode material and ΔV is the potential window.

Specific capacitance, C_s (F g^{-1}) for three-electrode system/half-cell was calculated based on equation 4.2.

$$C_s = \frac{C}{m} \text{ (half-cell)} \quad (4.2)$$

where m (g) is the mass of the active electrode material.

For a symmetric two-electrode device, m (g) represents the total mass of the active material from both the counter and working electrode and the specific capacitance can be estimated using equation 4.3.

$$C_s = \frac{4C}{m} \text{ (full-cell)} \quad (4.3)$$

The energy density, E_s (Wh kg^{-1}) was calculated using equation (4.4).

$$E_s = \frac{C \times (\Delta V)^2}{2m} \times \frac{1000}{3600} \quad (4.4)$$

where C is capacitance, ΔV is the potential window and m (kg) is the mass of active material in both electrodes. The power density, P_s (W kg^{-1}) was calculated based on equation 4.5.

$$P_s = \frac{E_s \times 3600}{\Delta t} \quad (4.5)$$

The maximum power density, P_{max} (W kg^{-1}) was evaluated using equation 4.6.

$$P_{max} = \frac{\Delta V_{max}^2 \times 1000}{4m \times ESR} \quad (4.6)$$

where ΔV_{max} is the maximum potential window applied, m (kg) in the mass of active material in both electrodes and ESR is the equivalent series resistance of the system, determined from voltage drop at the beginning of the discharge curve from GCD curves and can be calculated based on equation 4.7.

$$ESR = \frac{\Delta V_{i\,Rdrop}}{2I} \quad (4.7)$$

where ΔV_{iRdrop} (V) is the voltage drop between two points at beginning of the discharge curve.

4.3 Results and discussion

Figure 4.1 depicts TEM and SEM pictures of the morphology of materials at various phases of fabrication. **Figure 4.1a** shows the Fe-Co catalyst deposition on the surface of stabilized PAN fibres following a 1 h reduction operation at 500 °C in an Ar and H_2 environment. After the catalyst was reduced, Fe and Co precursors were entirely reduced to Fe-Co nanoparticles. In addition, the catalyst was evenly coated on the surface of nanofibers, where it was used as an active catalyst for the formation of multiwalled carbon nanotubes (MWCNTs). One of the key factors in regulating CNTs growth in terms of diameter and length is the uniform catalyst deposition on top of nanofibers and the size of the nanoparticles, which have a significant impact on the porosity and surface area of hybrid materials [20, 21]. **Figure 4.1(b & c)** shows TEM images of the CNT@CF and N-CNT@CF networks. Both hybrid materials exhibited a unique hierarchical structure with a high density of MWCNTs that were linked uniformly on

top of the CF network. The black dot-like particles observed encapsulated at the tip of the CNTs validate the tip-growth process [22, 23]. In the inset of **Figure 4.1(b & c)**, high magnification photographs of the CNT@CF network and the N-CNT@CF network can also be observed. The outer shells (multiwall) and interior (hollow part) diameters of CNTs for both hybrid materials were measured using ImageJ 1.46r software. The CNTs in the CNT@CF network had outer diameter of 9.8 and inner diameter of 10.1 nm, whereas the N-CNT@CF network had outer diameter of 6.2 and inner diameter of 18.8 nm. The small outer diameter of the N-CNT@CF network could indicate few multiwalled carbon nanotubes and a high degree of graphitization, whereas the larger inner diameter could indicate better porosity due to the wider diameter of the tubes. However, other characterization techniques such Raman spectroscopy and BET analysis, are needed to back up the statements made above.

SEM was used to characterize the pristine CFs and their associated hybrid materials. **Figure 4.1d** shows pristine CFs with ultra-long 1D fibres and a smooth surface, with an average diameter of 700 nm and lengths of several hundreds of millimetres. CNTs and N-doped CNTs were uniformly grown on the surface of the CFs network, as illustrated in **Figure 4.1(e & f)**. The entanglement of CNTs on CFs provides a three-dimensional structure that can store the electrolyte and enhance ion transport into the active sites of the material, enhancing capacitance and rate performance [24].

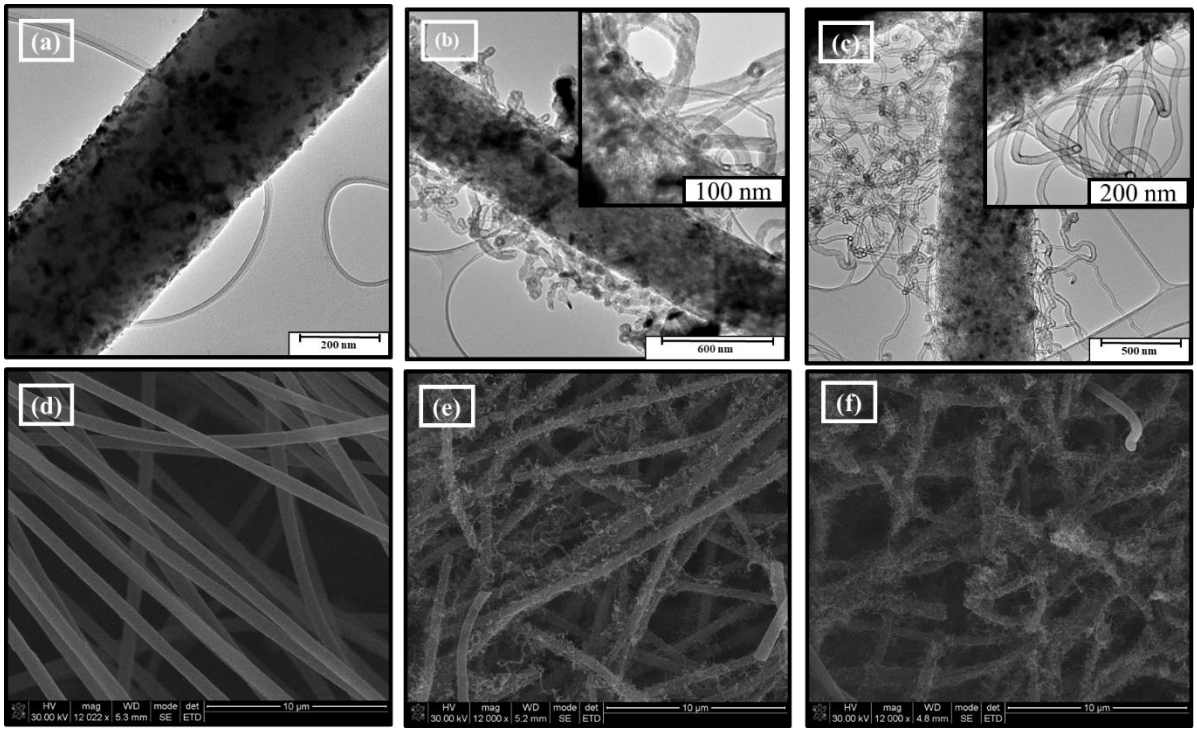


Figure 4.1: TEM images of (a) Fe-Co@CFs, (b) CNT@CF network CFs (insert show high magnification), (c) N-CNT@CF network (insert show high magnification) and SEM images of (c) CFs, (d) CNT@CF network and (e) N-CNT@CF network**.**

XRD is a valuable tool for determining the crystallinity of nanomaterials. The XRD patterns of reference CFs and CNTs, as well as the CNT@CF and N-CNT@CF networks, are shown in **Figure 4.2a**. The diffraction pattern of reference CFs shows a broad diffraction peak centred at 2θ = 25° and a small diffraction peak at 2θ = 43.2°, which was assigned to the (002) and (101) diffraction patterns of disordered carbon structure [24, 26]. On the other hand, the reference CNTs and CNT@CF networks exhibit four narrow peaks at 2 = 25° and 43.2°, which correspond to the (002) and (101) graphitic planes of carbon, respectively, while the other two peaks around 2 = 54.5° and 78.2° are due to the Fe-Co catalyst that remained after acid treatment on the materials. Only a sharp (002) peak was observed for the N-CNT@CF network.

Furthermore, both materials had an asymmetric (002) peak, with the hybrid materials moving to higher 2θ positions. As a result, a detailed investigation of the (002) was required to detect structural variations between the reference materials and the hybrids. The peak profiles of the

CNTs, CNT@CF, and N-CNT@CF networks were deconvoluted and fitted using the Voigt spectral line, while the CFs were fitted using the Gaussian spectral line, as described by Singh *et al*. [27]. The (002) peak of the reference CFs sample is shown in **Figure 4.2b**. Two additional peaks were discovered in the deconvoluted diffraction pattern, namely γ and π peaks. The γ peak is attributed to the presence of amorphous carbon connecting the edges of crystallites [28], while the π peak is attributed to planar zigzag in the CFs is linked to the presence of aliphatic carbon atoms from PAN [29]. In comparison to the CFs, the CNTs in **Figure 4.2c**, showed two narrow peaks, indicating that the CNTs are more graphitic than the CFs. The two fitted peaks were attributed to CNTs with different crystalline sizes, as observed from the TEM image (see **Supporting Information, Figure S1 in Appendix A**). The deconvolution of the CNT@CF network (**Figure 4.2d**) revealed that it comprises two components cantered around 2 = 25.5° and 2 = 26.6°, respectively, matching the (002) plane reflections of the CFs and CNTs. A peak attributed to different CNT crystalline sizes was also observed around 2 = 24°. The TEM with high magnification (insert of **Figure 4.1b**) of the CNT@CF network reveals this disparity in crystalline sizes of CNTs. Up on doping the CNT@CF with nitrogen (**Figure 4.2e**), only two peaks were found as a result of the CFs and CNTs components. In addition, the narrower (002) peak of hybrid materials compared to reference materials suggests that growing CNTs on top of CFs improves the crystallinity of the hybrid materials [30]. The deconvolution data shown in (**Supporting Information, Table S1 in Appendix A**) comprises of peak centre, FWHM, height, and integral areas.

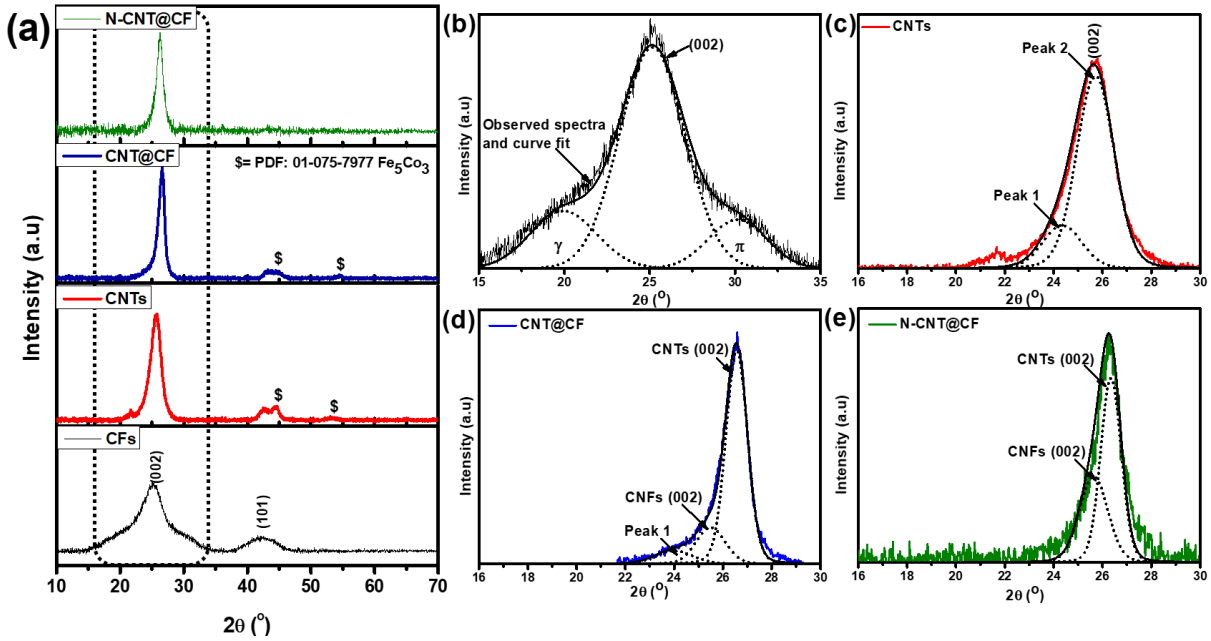


Figure 4.2: P-XRD patterns of (a) CFs, CNTs, CNT@CF network and N-CNT@CF network, and (b, c, d, e) deconvoluted (002) diffraction peak of all materials**.**

The structural information of carbon materials was analysed using Raman spectroscopy. The unevenness in the shape of the D and G bands means that the spectrum contains several peak components. The spectrum was deconvoluted to separate the D and G bands by fitting the sum of Lorentzian G, D_1, D_2, and D_4 bands, as well as the Gaussian D_3 band. The Gaussian curve was chosen for the D_3 band because it provided a better match with the experimental results. This spectral fitting approach was also employed by Sadezky *et al*. [31] and Amaral *et al*. [32]. The curve fitting findings are summarized in **(Supporting Information Table S2 in Appendix A)**. **Figure 4.3(a-d)** shows the Raman spectra of all samples, which shows five unique bands at 1233, 1353, 1543, 1587 and 1623 cm^{-1}, which correspond to the D_4, D_1, D_3, G and D_2 bands, respectively. The D_1 band around 1350 cm^{-1}, shows the presence of A_{1g} breathing vibration mode from the presence of surface defects or disorders and the G band around 1580 cm^{-1}, demonstrate the E_{2g} vibration which is attributed to the sp^2 hybridized carbon atoms with graphite crystal structure [33]. The D_4 (1200 cm^{-1}), D_3 (1500 cm^{-1}) and D_2 (1620 cm^{-1}) bands

result from the disordered graphitic lattice (A_{1g} symmetry), amorphous carbon and disordered graphitic lattice (surface graphene layers, E_{2g}-symmetry), respectively [34-36].

To compare the degree of graphitization of the materials, the R-coefficient ($R= I_{D1}/I_G$) was used. It should be noted that there are differences in reporting the R-coefficient among researchers working on Raman spectroscopy of carbon-based materials. Some researchers tend to use the integral area under the curves to report the (I_D/I_G) ratio, while others prefer to use the height/intensity of the bands [37]. In our situation, the use of the integral area under the curves was used because all carbon materials had multiple disordered carbon signals. The $(I_{D1}/I_G)_A$ ratio of all the samples had a ratio that varied between 3.85 and 1.72. The low R-values for the CNTs (I_{D1}/I_G = 1.72) and the CNT@CF network (I_{D1}/I_G = 1.79) suggest the presence of more sp^2 hybridized carbon clusters in the samples and growing CNTs on top of CFs increases the graphitization degree of the CFs (I_{D1}/I_G = 3.85) network. This supports the XRD results.

In addition, when the N-CNTs were grown on top of the CFs network (I_{D1}/I_G = 2.66), an intense D_1 band as compared to the G band was observed. The presence of surface defects forming in the carbon structure after nitrogen incorporation is responsible for the increased intensity of the D_1 band. In addition, relative to all samples, a small flattened D_3 band was observed. The N-CNT@CF network is fairly graphitic, particularly when compared to the reference CFs, but nitrogen doping causes surface defects in the material, resulting in a high I_{D1}/I_G ratio, as shown in **Figure 4.3d**. Furthermore, the I_{D1}/I_{D2} ratio is useful to assess the presence of defects in carbon materials, with the I_{D1}/I_{D2} ratios for vacancy-type and boundary defects in graphene being approximately 7 and 3.5, respectively [38]. The I_{D1}/I_{D2} ratios of the CNT@CF and N-CNT@CF networks were determined to be 4.02 and 5.88, respectively. In the N-CNT@CF network, incorporation of nitrogen introduced vacancy-type defects, as shown in **Scheme 4.2**. One of the advantages of vacancy-type defects is the high volume of micropores/mesopores in

the material, which enhances the surface area and hence improves the electric double-layer capacitance (EDLC) [39].

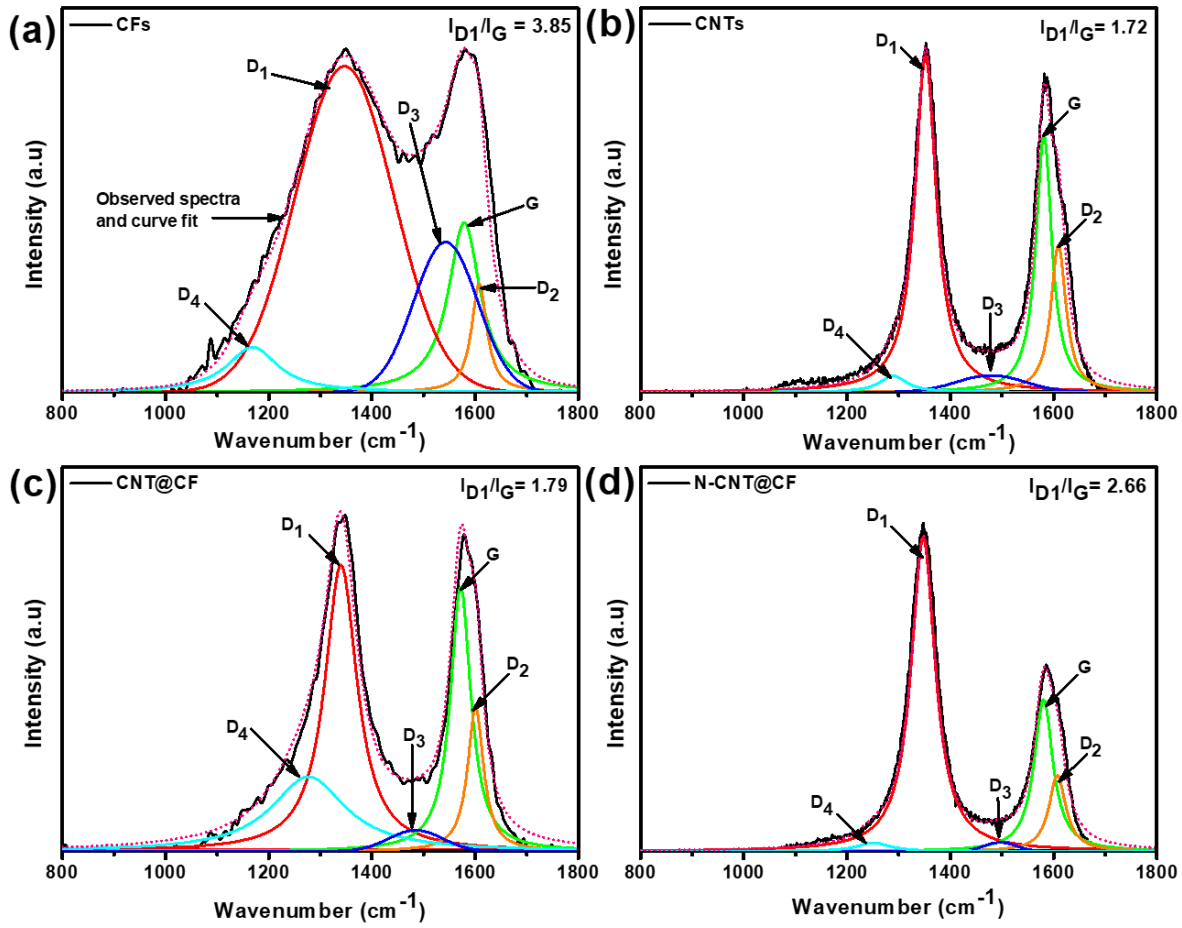


Figure 4.3: Raman spectra of (a) CFs, (b) CNTs, (c) CNT@CF network and (d) N-CNT@CF network**.**

The N_2 adsorption–desorption analysis was used to investigate the porosity of the CNT@CF and N-CNT@CF networks. **Figure 4.4(a & b)** illustrate the N_2 adsorption–desorption isotherms and pore size distribution curves of the CNT@CF and the N-CNT@CF networks, respectively. Type IV isotherms with type H3 hysteresis loops are found in all the hybrid networks, suggesting that they are mesoporous [40, 41].

The surface areas of the CNT@CF and the N-CNT@CF networks sown in **Table 4.1** were found to be 114 and 204 m^2/g, respectively. Due to formation defects when N-doped CNTs are

grown on the CFs network, the specific surface area of the N-CNT@CF network increased significantly when compared to the un-doped CNT@CF network. This is in agreement with the high I_{D1}/I_G ratio calculated for the N-CNT@CF network (**Figure 4.3d)**. Using the t-plot model, the surface microspores (0.1-1.9 nm) for both CNT@CF and N-CNT@CF networks were determined to be 27.35 and 33.31 m^2/g, respectively. The overall percentage of micropores fell from 24% to 16% when N-doped CNTs were grown on the surface of CFs networks. This suggests that incorporating nitrogen on the carbon matric can change a microporous structure into a more mesoporous structure by creating surface defects. The Barrett-Joyner-Halenda (BJH) approach was also used to assess the pore size distribution (mesopores and macropores) of the CNT@CF and N-CNT@CF networks (**Figure 4.4b**). A continuous pore size distribution within the range of 5–100 nm is observed, which is nearly in direct proportion to pore diameter increase. The pore diameters of the hybrid networks ranged between 3.3 and 4.5 nm, according to the BJH technique, as shown in the insert of **Figure 4.4b**, consistent with the mesoporous characteristics. The mesopores allow for quick electrolyte ions adsorption and a short diffusion distance, which improves the charging/discharging characteristics of the hybrid materials [42].

Table 4.1: Surface parameters and elemental composition of hybrid materials.

Samples	**S_{BET} (m^2/g)**	**Micropore area (m^2/g)**	**Volume (cm^3/g)**	**Size (nm)**	**CHN analysis**			**XPS atom %**		
					C%	H%	N%	C%	O%	N%
CNT@CF	114	27.35	0.32	10.2	81.9	0.6	1.35	96.3	3.3	0.4
N-CNT@CF	204	31.31	0.38	10.9	78.2	0.7	2.87	88.2	5.6	5.8

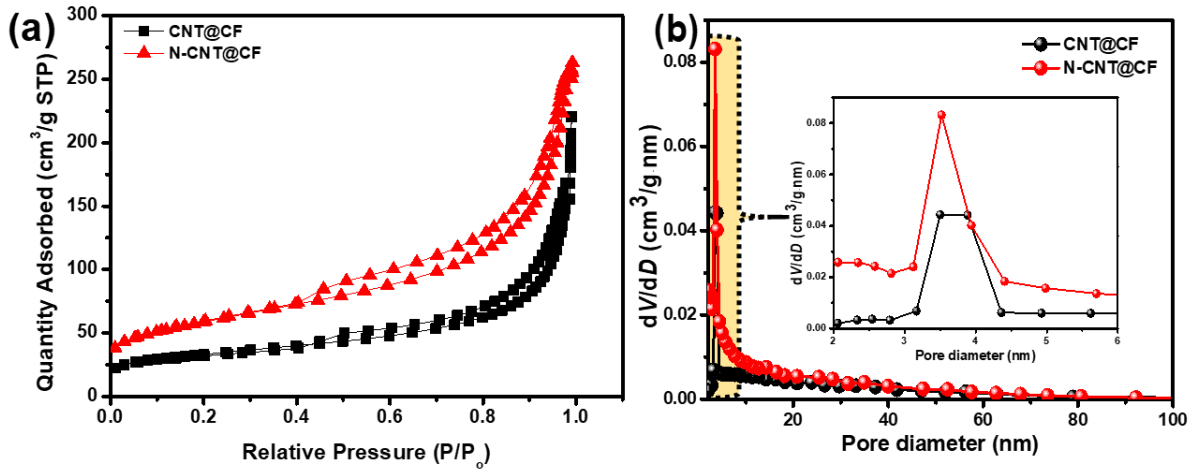


Figure 4.4: a) BET adsorption desorption curve and (b) pore size distribution curve of the CNT@CF network and the N-CNT@CF network (insert pore diameter between 2-6 nm).

The elemental composition and surface chemistry of the CNT@CF and N-CNT@CF networks were investigated using elemental analysis and X-ray photoelectron spectroscopy (XPS). Elemental analysis revealed a nitrogen percentage of ~2.87 wt. % in the N-CNT@CF networks, as shown in **Table 4.1**. XPS survey spectra shown in **Figure 4.5**, revealed that both hybrid materials have three peaks, cantered at 283.4, 400.1, and 532 eV, corresponding to C 1s, N 1s, and O 1s, respectively. The N 1s peak of N-CNTs@CF networks, is more intense compared to the CNTs@CF networks, indicating that nitrogen atoms were successfully incorporated in the carbon matrix. The overall C 1s, O 1s, and N 1s content were determined to be (96.3, 0.4, and 3.3 %) for the CNT@CF and (88.2, 5.8, and 5.6 %) for the N-CNT@CF networks, as shown in **Table 4.1**. The nitrogen content for the CNT@CF network is from the polyacrylonitrile (PAN) polymer used to prepare CFs [43, 44].

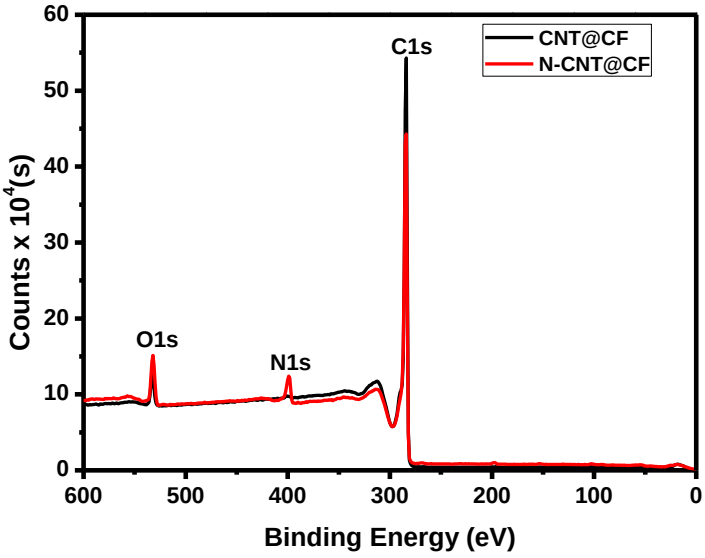


Figure 4.5: XPS survey spectra of CNT@CF network and N-CNT@CF network.

The chemical environments in hybrid materials were further examined by deconvolution of the C 1s, N 1s and O 1s, as illustrated in **Figure 4.6a-f**. The C 1s peak of hybrid materials was deconvoluted into three peaks, namely C–C (sp^3 carbon, 285.3 eV), C=C (286.5 eV) and C–OH/C–N (287.6 eV) as shown in **Figure 4.6a & b** [45]. The creation of surface defect-induced C–N bonding configurations with either sp^2 C–N and/or C=N bonding configurations is linked to the rise in the percentage (4.4%) of the C–OH/C–N peak found for the C 1s spectra of the N-CNT@CF [46, 47]. When the hybrid is doped with nitrogen, the fraction of carbon atoms reduces, implying that carbon atoms are being replaced by nitrogen atoms. The decrease of carbon is in support of the CHN analysis shown in **Table 4.2**. The peak analysis of the N 1s revealed the presence of three nitrogen atom bonding states: pyridinic-N (398.6 eV), pyrrolic-N (400.2 eV) and graphitic-N (401.2 eV), respectively [48, 49]. The structure of the N species is illustrated in **Scheme 4.2**. Pyridinic-N and pyrrolic-N are chemically active compounds that have been shown to cause structural disorders in graphene layers [42]. In comparison to the more inert graphitic-N equivalent, such functional groups and disorders are believed to boost the conductivity of the materials [50, 51]. The O 1s spectrum of the CNT@CF shown in **Figure**

4.6e was separated into two peaks O=C-O and C-O at 532.3 and 533.5eV, respectively. The N-CNT@CF network shown in **Figure 4.6f**, have an additional peak around 531.2 eV, which is assigned to C=O. The existence of a C=O bond indicates the existence of ester, carbonyl, or carboxyl groups caused by vacancy-type defects (dangling bonds) produced by nitrogen doping.

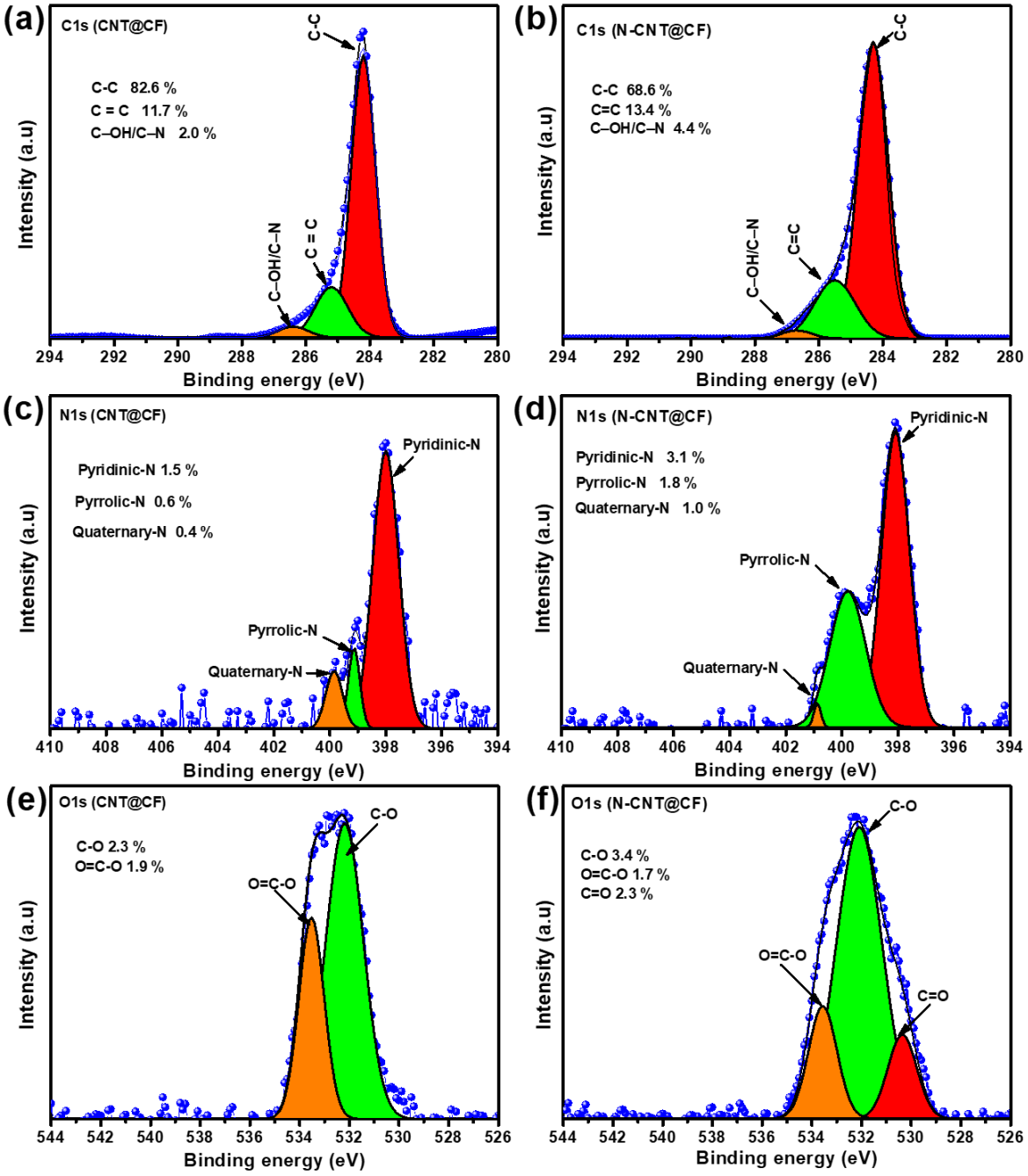
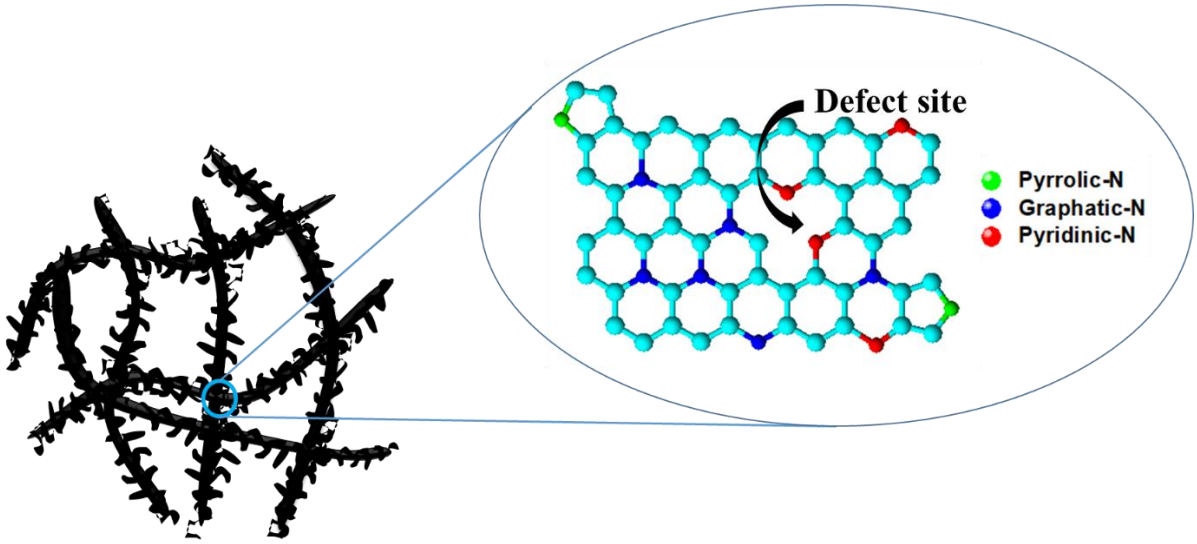


Figure 4.6: XPS spectra showing deconvoluted C1s, N1s and O1s of CNT@CF and N-CNT@CF networks.



Scheme 4. 2: N-configuration of N-CNT@CF network.

4.3.1 Electrochemical analysis

The electrochemical properties of all electrode materials were first evaluated using a three-electrode system in a 6 M KOH electrolyte. Nickel foam was used as the counter electrode and silver wire as a reference electrode. To study the charge storage capabilities of the materials, cyclic voltammetry (CV) was utilized at scan rates ranging from 5 to 100 mV s^{-1} and galvanostatic charge/discharge (GCD) was determined at various current densities (see **Figure S2 and S3 Supporting Information**). The voltammograms of all samples at 5 mV s^{-1} are shown in **Figure 4.7a.** The CV curves are close to rectangular, suggesting the EDLCs characteristics. The CV curves demonstrated that N-CNT@CF networks had superior current responsiveness. This strong current response suggests that the material might have high capacitance. As indicated by Raman in **Figure 4.3**, BET and XPS analyses in **Table 4.1**, the high specific capacitance of the N-CNT@CF networks may be attributed to the high surface area, vacancy-type defects and high N content.

The impedance behaviour (both resistive and capacitive behaviour) of the four electrode materials was evaluated using electrochemical impedance spectroscopy (EIS). Based on the

Nyquist plots obtained from EIS, all of the samples have a semicircle in the high-frequency region and a straight line in the low-frequency region. The x-intercept at the end of the semicircle represents the equivalent series resistance (ESR) of an electrode material, which indicates the contact resistance at the active materials and current collector interface, the entire ionic resistance of the electrolyte and the resistance of the electrode material itself. The ESR values of the CFs, CNTs, CNT@CF and N-CNT@CF were found to be, 0.42, 0.14, 0.32 and 0.21 Ω, respectively. The charge transfer resistance (R_{ct}) value for the N-CNT@CF network (2.22Ω) was smaller than that of the CNT@CF network (8.45 Ω), the CNTs (2.74Ω) and the CFs (15.55Ω) (see **Table S3 Supporting Information in Appendix A**). The smaller impedance of the N-CNT@CF is more beneficial for electrolyte ion diffusion and charge storage. In the low-frequency region, it is only the CNT@CF hybrid that gave the Warburg line at ~ 45^{o} (representing diffusion process) while the other electrodes show near straight lines parallel with the y-axis (representing capacitive behaviour). It is quite interesting to see how N-doping can transform the pristine CNT@CF networks from a diffusive process to a capacitive one with excellent impedimetric/conductive behaviour, in contrast to the general belief that N-doping generally leads to diffusion-controlled (pseudocapacitive) kinetics. This unique transformative is further interrogated and discussed in section 4.1.1.

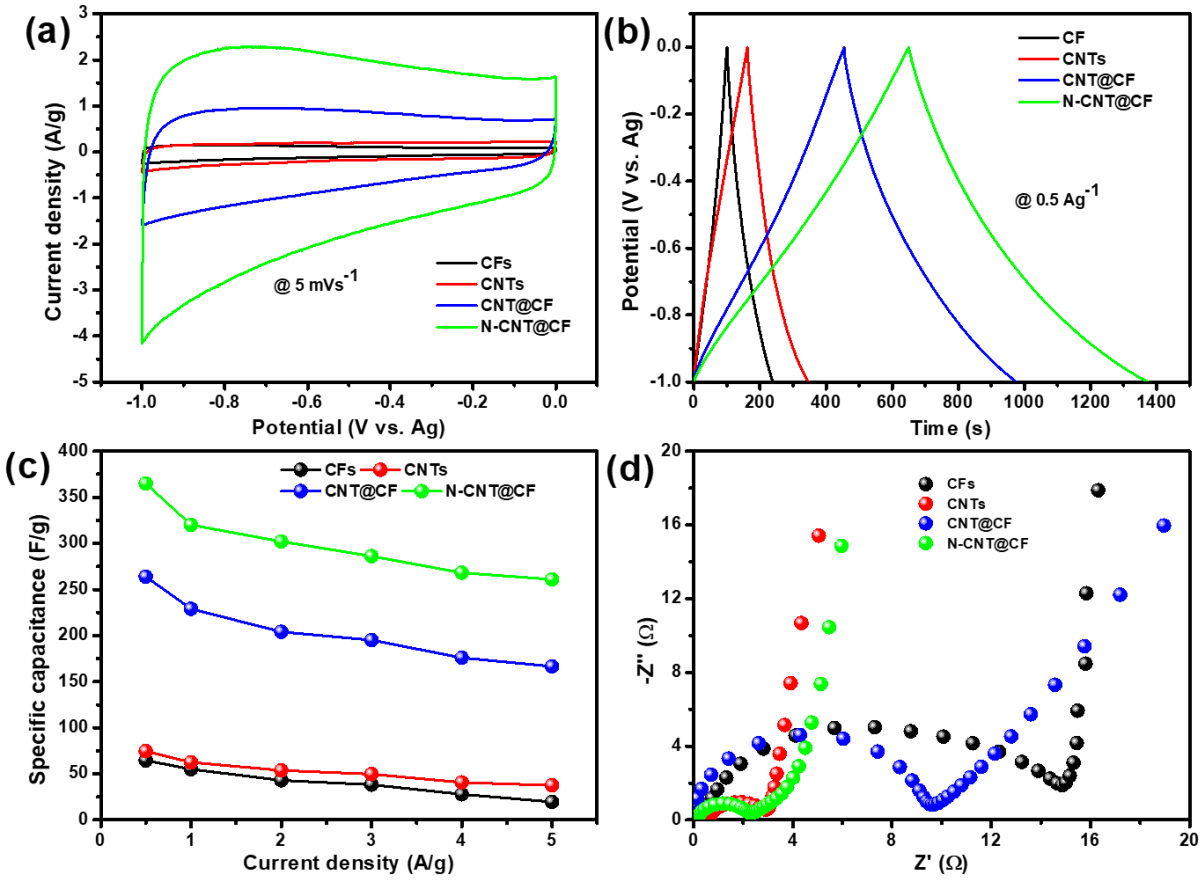


Figure 4.7: CV curves of (a) CFs, CNTs, CNT@CF and N-CNT@CF at 5 mVs^{-1} scan rates (b) GCD comparison of CFs, CNTs, CNT@CF and N-CNT@CF at 0.5 Ag^{-1}, (c) Comparison of specific capacitance of at different current densities, (d) EIS measurements of all electrode materials.

4.3.2 Surface-controlled and diffusion-controlled charge storage contributions

As seen from the above three-electrode results, the electrochemical properties of the material are influenced by incorporating nitrogen in the carbon matrix. In supercapacitors, incorporation of nitrogen in the carbon matrix has been shown to increase the capacitance of doped-carbon electrode material by generating pseudo-capacitance. Previous research reports have shown that the presence of nitrogen species on the edges of graphene sheets is essential for pseudo-capacitance [53, 54]. Seredych *et al*. [55] postulated a link between capacitance and surface functional groups, as well as the porosity of nitrogen-doped carbon materials, in an acidic electrolyte. In gravimetric capacitance experiments, Hulicova-Jurcakova and colleagues

looked at the link between the amount of basic groups, microporosity and the distribution of quaternary and pyridinic-N-oxide nitrogen species on the surface of micropores [56]. Similarly, researchers determined that the nitrogen groups pyridinic and pyrrolic (together with the quinone oxygen groups) have the greatest influence on capacitance. Other study groups identified pseudo-capacitive effects due to the existence of pyrrole and/or pyridine species after these studies [57, 58]. Based on the above-mentioned studies, since the materials possess nitrogen moieties in their carbon structure, diffusion-controlled processes are expected to contribute to charge storage in CNT@CF and N-CNT@CF networks. In this regard, Conway and co-workers quantitative analysed the surface and diffusion-controlled charge storage contribution from the CV curves [59] method is an important step for a better understanding of charge storage kinetics in such unique nanostructures. As a result, equations 4.8 and 4.9 were used to calculate the capacitive and pseudo-capacitive contributions from CV data at various scan rates (5-100 mV s^{-1}).

$$i = a\nu^{b} \tag{4.8}$$

$$\log j = b \log \nu + \log a \tag{4.9}$$

where j represents the current density, while a and b represent adjustable parameters which can easily be obtained from the plot of $\log j$ against $\log \nu$. A value of $b = 1$ indicates that a material is dominated by the surface-controlled, pure capacitive process; a value of $b = 0.5$ indicates that a material is dominated by diffusion-controlled (i.e., Faradaic) process; while b value greater than 0.5 but less than 1.0 suggests a mixed mechanism (i.e., both Faradaic and non-Faradaic processes in operation). The slope of log(i) *vs*. log(v) plots, as seen in the cathodic direction shown in **Figure 4.8a & b**, were used to calculate the *b*-values of both materials. Thus, the *b*-values equal to 1 were calculated for CNT@CF, while those of N-CNT@CF are between 0.5 and 1, indicative of mixed storage mechanisms. These findings back up the theory

that N-doping adds surface redox capabilities in carbon materials. The *b*-values in the anodic direction are shown in **(Figure S4a & b, Supporting Information in Appendix A)**.

The power-law equation may be divided into capacitive and Faradaic current responses using the same voltammetry technique, as shown by equations 4.10 and 4.11, respectively:

- Capacitive (adsorption-controlled) current response: $i \alpha v, \Rightarrow i = k_1 v$ (4.10)
- Faradaic (diffusion-controlled) current response: $i \alpha v^{1/2}, \Rightarrow i = k_2 v^{1/2}$ (4.11)

Thus, the total current response at a given potential (V) will be as given in equation 4.12:

$$i = k_1 v + k_2 v^{1/2} \quad (4.12)$$

$$\Rightarrow \quad i/v^{1/2} = k_1 v^{1/2} + k_2 \quad (4.13)$$

where k_1 and k_2 are constants that describe the capacitive and Faradaic current contributions, respectively. Thus, by plotting the relationship between $i/v^{1/2}$ against $v^{1/2}$, the values of k_1 and k_2 can be obtained (see **Figure S4 (c & d), Supporting Information in Appendix A)**. As shown in **Figure 4.8(c & e)**, the capacitive current contributions may be shown and distinguished from the Faradaic contributions by calculating the k_1 value at various voltages and scan rates. **Figure 4.8(d & f)** also shows the surface-controlled and diffusion-controlled percentages in relation to the various scan rates. For all scan rates, the CNT@CF networks had higher surface-controlled percentages than the N-CNT@CF networks. This demonstrates that nitrogen doping introduces surface defects and nitrogen functional groups, which boosts the pseudocapacitance and the overall electrochemical performance of the material. These findings support previous research on the role of nitrogen species in pseudo-capacitance improvement.

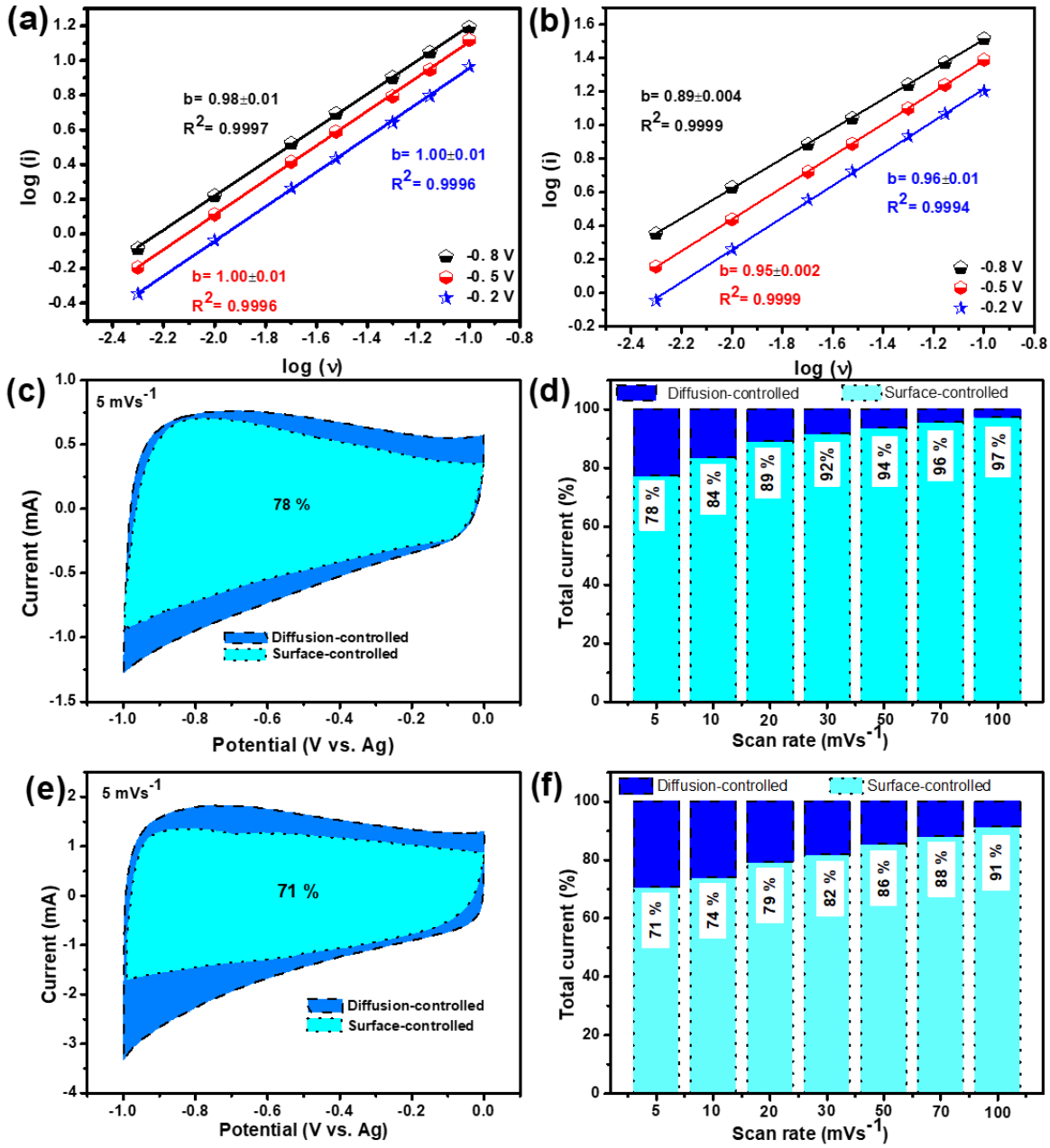


Figure 4.8: Log peak current *vs* log scan rate for (a) CNT@CF and (b) N-CNT@CF obtained at the cathodic directions; Typical charge storage contributions from capacitive and diffusive processes from cyclic voltammetry at 5 mV s^{-1} for (c) CNT@CF and (e) N-CNTs/CF; Comparative histograms of the percentage charge storage contributions from capacitive and diffusive processes from 5-100 mV s^{-1} for (d) CNT@CF and (f) N-CNTs/CF**.**

To further investigate the electrochemical performance of CFs, CNTs, CNT@CF, and N-CNT@CF materials, CV, GCD and EIS techniques were used in a two-electrode. The CV experiments were performed with the same 6 M KOH electrolyte in the potential range of 0 to

1 V at a scan rate of 50 mV s^{-1}. The CV curves of all carbon materials are shown in **Figure 4.9(a)** and they are all quasi-rectangular in shape, which is very close to the ideal behaviour of EDLCs. Furthermore, the CV curves of N-CNT@CF shown in **Figure 4.9b** retained their rectangular shape at various scan speeds, indicating a strong charge storing process.

The rate capability and cycle stability were investigated using the GCD technique. **Figure 4.9(c)** shows the GCD curves of all materials at a current density of 0.5 A g^{-1}. The charge-discharge curves of all materials are linear, which demonstrate the EDLC nature of the electrode materials. The specific capacitance was calculated using GCD curves according to equation 4.1 [60], which indicates the specific capacitance values as a function of current density. It can be shown that as the current density increased, the specific capacitance decreased (**Figure 4.9d**). When the current density is 0.5 A g^{-1}, the specific capacitance of N-CNT@CF electrode materials is 155 F g^{-1} and 137 F g^{-1} remained when the current density was increased to 5 A g^{-1}. On the other hand, when the current density is 0.5 A g^{-1}, the specific capacitance of CNT@CF is 67 F g^{-1} and when the current density increases to 5 A g^{-1} the capacitance dropped to 56 F g^{-1}. The high specific capacitance for the N-CNT@CF is attributed to the hierarchical structure, high surface area, high nitrogen content and defects created as a result of nitrogen doping. The high specific capacitance of N-CNT@CF material was also compared with other carbon composites electrodes previously reported (see **Table 4.2)**.

Table 4.2: Comparison of the capacitance of the present N-CNT@CF hybrid network with previously reported carbon composites electrode materials using 6 M KOH electrolyte.

Materials	**Electrolyte**	**Specific capacitance (F g $^{-1}$)**	**References**
CNT@m-C	6 M KOH	60	[61]
MWCNTs and graphene sheet	6 M KOH	91	[62]
G/SWCNT	6 M KOH	99	[63]
Activated carbon wrapped CNT buckypaper	6 M KOH	100	[64]
PAN/pitch base CNFs	6 M KOH	131	[65]
N-CNT@CF	6 M KOH	156	**This work**

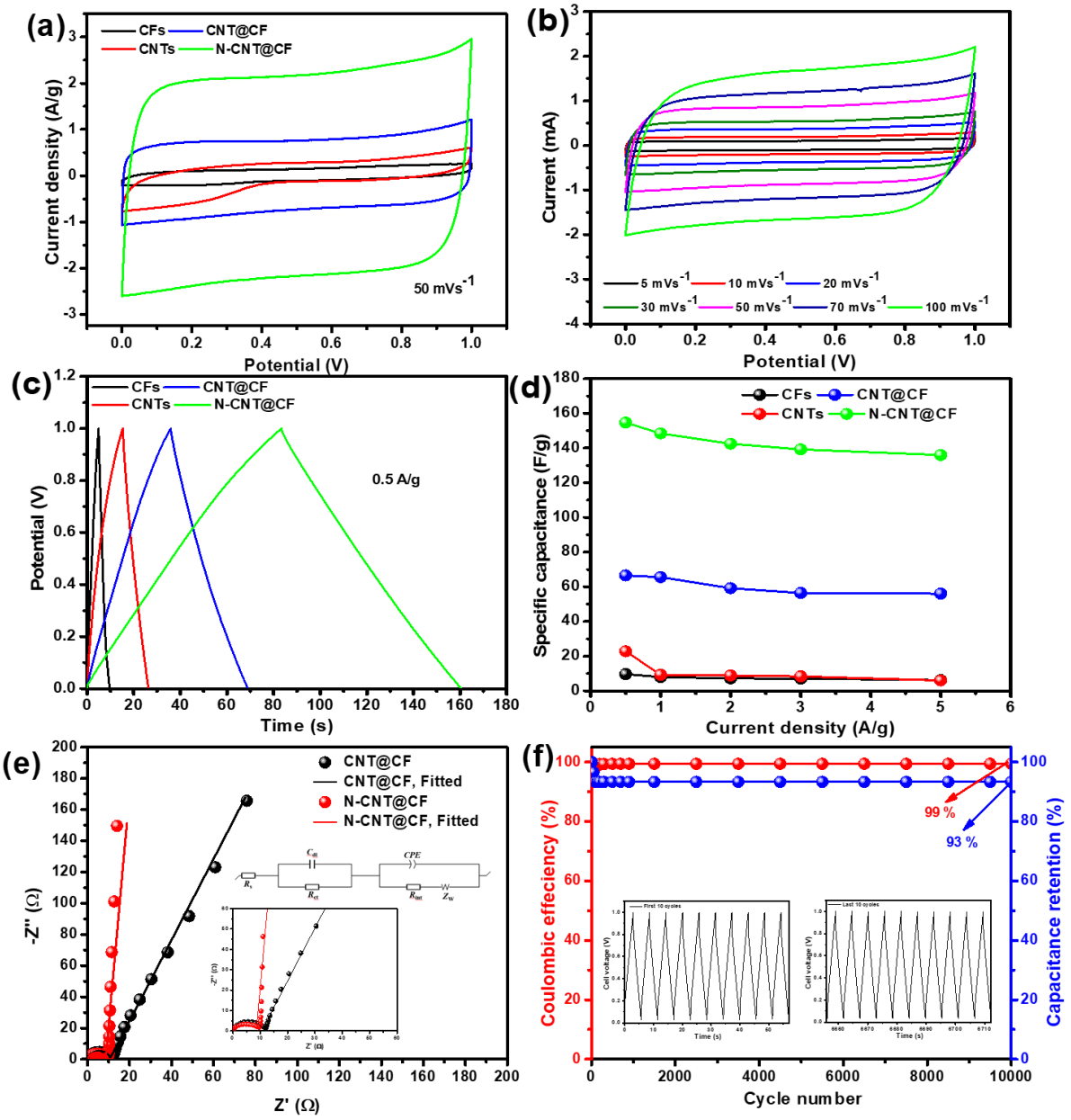


Figure 4.9: CV curves of (a) CFs, CNTs, CNT@CF and N-CNT@CF at 50 mV s^{-1} scan rates (b): CV curves of N-CNT@CF at different scan rates, (c) GCD comparison of CFs, CNTs, CNT@CF and N-CNT@CF at 0.5 A g^{-1}; (d) Comparison of specific capacitance of at different current densities, (e) EIS measurements of CNT@CF and N-CNT@CF electrodes and (f) coulombic efficiency and capacitance retention of N-CNT@CF.

Figure 4.9e shows the EIS measurements of the CNT@CF and N-CNT@CF hybrid materials with an electrochemical equivalent circuit (EEC, **Figure 4.9e** inset). The Nyquist plots are modelled with the combination RC/Randles circuit comprising of the solution resistance (R_s),

the charge-transfer resistance (R_{ct}), the internal resistance (R_{int}) resulting from IR drop, the double-layer capacitance (C_{dl}) and constant phase element (CPE) due to the porosity of the electrode materials. In addition, it should be noted that the EIS measurement of CNT@CF material showed Warburg diffusion region (Z_w) which describes the resistance to ion diffusion. This diffusion resistance for CNT@CF hybrid material may be due to the low ion diffusion barrier due to less conductivity compared to the N-CNT@CF hybrid materials.

The impedance of the CPE (Z_{CPE}) is a power-law relationship, based on equation 4.14 [66, 67]:

$$Z_{CPE} = [Q\ (j\omega)^a]^{-1} \quad (4.14)$$

where Q represent the frequency-independent constant associated with the electrode/electrolyte interface, $j = \sqrt{-1}$, ω represents the radial frequency, while the exponent a is the slope of the log Z *vs.* log *f*, the values of which $-1 \leq a \leq 1$: When $a = 0$, the CPE is a pure resistor; $a = 1$, the CPE is a pure capacitor; $a = -1$ the CPE is an inductor; while $a = 0.5$ the CPE is equivalent to the Warburg impedance (Z_w). From **Table 3**, the value of $n = 0.77$ indicates a mixed storage capacitor for the N-CNT/CF-based symmetric supercapacitor, in contrast with the $n = 0.96$ for the CNT@CF-based device indicating a predominantly surface-controlled capacitor. The R_s value for each of the device is the same since similar electrolyte and current collector materials are used. The R_{ct} value is slightly higher for the N-CNT@CF (~ 10.4 Ω) than the CNT@CF-based system (~ 8.4 Ω), indicating that the latter is more electron-conducting than the former. Interestingly, the R_{int} value is more than twice for the CNT@CF-based system (~ 95 Ω) than for the N-CNT@CF-based system (~ 41 Ω). Considering that R_{int} is due to the IR drop (also known as ohmic polarization or ohmic drop) and associated with the rate at which the electrolyte ions diffuse between the electrodes, it is perhaps not surprising that the diffusion-controlled system (N-CNT@CF-based EDLC) gave much smaller R_{int} value than the surface-controlled system (CNT@CF-based EDLC).

The symmetric system was also subjected to a cycling stability test, which included continuous charging-discharging for up to 10,000 cycles at a current density of 10 A g^{-1}, as shown in **Figure 4.9f**. After 10,000 cycles, the coulombic performance was 99 % and the capacitance retention was 93 %. In addition, the capacitance retention of 93 %, is higher than many other carbon-based materials, such as NPCM1.0 (91.4 %) [69] and CNF-12 (69 %) [70]. Excellent long-term cycling performance reveals the outstanding chemical stability and re-usage of the N-CNT@CF hybrid material.

Table 4.3: EIS parameters for the electrode materials for two-electrode (symmetric) systems.

EIS parameters	**Electrode material for the symmetric supercapacitor**			
	CNT@CF		**N-CNT@CF**	
	Before cycling (zeroth cycle)	After cycling (10,000th cycle)	Before cycling (zeroth cycle)	After cycling (10,000th cycle)
R_s / Ω	0.27 ± 0.46	0.37 ± 0.14	0.14 ± 0.37	0.37 ± 0.17
ESR (R_{ct}) / Ω	17.73 ± 0.81	8.42 ±0.44	8.50 ± 0.44	10.37 ± 0.45
C_{dl} / µF	18.76 ± 18.71	10.14 ± 2.79	10.15 ± 0.44	6.69 ± 1.53
R_{int} / Ω	58.29 ± 2.48	95.15 ± 7.79	18.87 ± 0.64	41.44 ± 3.56
CPE /mF.s^(*a*-1)	15.74 ± 1.88	3.42 ± 0.02	3.40 ± 0.02	7.95 ± 0.05
n	0.93	0.96	0.92	0.77
Z_w / Ω s^-1/2	-	-	-	21.33 ± 0.52

The Ragone plot assesses the device performance in terms of energy and power density. The Ragone plot of CNT@CF and N-CNT@CF hybrid materials is shown in **Figure 4.10a**. The specific energy density of the devices were determined to be 2.3 and 5.5 Wh kg^{-1} for CNT@CF and N-CNT@CF, respectively, with corresponding specific power densities of 247 and 254 W kg^{-1} at a specific current of 0.5 A g^{-1}. The high energy and power density of N-CNT@CF are attributed to the synergistic effect of high graphitization degree, high nitrogen content and high

surface area of N-CNT@CF hybrid material. The maximum power density of our assembled full cell for N-CNT@CF is 41. 7 kW kg^{-1}, based on the formulae used by Melchoir *et. al*.[23]. Furthermore, as shown in **Figure 4.10b**, a 1.6 V red LED was easily operated by three N-CNT@CF//N-CNT@CF cells connected in series and lasted for about 3 minutes after charging to 3.0 V for 30 seconds, demonstrating the practical application of the symmetric system.

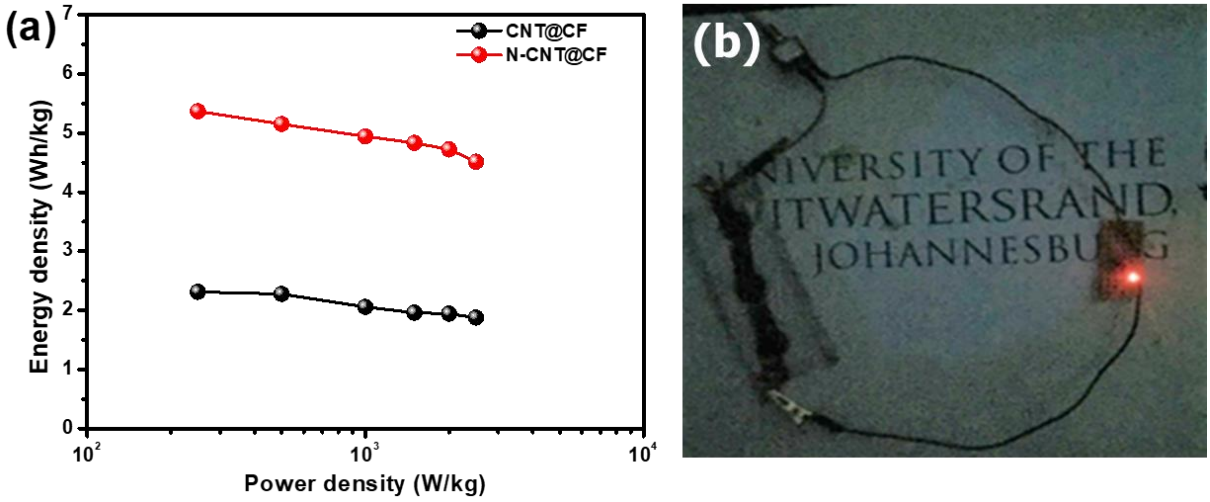


Figure 4.10: (a) Ragone plot and (b) image of 1.6 V red LED bulb lit up by N-CNT@CF supercapacitor.

4.4 Summary

In conclusion, two techniques were used to fabricate a binder-free hierarchical 3D N-CNT@CF nanostructure: electrospinning and chemical vapour deposition. The presence of CNTs, as well as N-doped CNTs in the CFs network, enhanced the electronic conductivity of the CF. The fabricated N-CNT@CF hybrid material showed exceptional electrochemical performance, including a high reversible specific capacity, remarkable rate capability, and extended cycle stability. The symmetric cell, on the other hand, has a specific energy density of 5.5 Wh kg^{-1} at a power density of 254 W kg^{-1} and a practical demonstration with an LED bulb demonstrates that it has a lot of potential in energy storage/management for compact and lightweight devices. Furthermore, the unique hierarchical porous structure of N-CNT@CF can be used to support

metal electro-catalyst to achieve enhanced energy density and power density in pseudo-capacitor applications.

4.5 References

[1] Ozoemena, K.I. and Chen, S. eds., 2016. Nanomaterials in advanced batteries and supercapacitors (p-567). Switzerland: Springer International Publishing.

[2] Wu, J., Xu, L., Zhou, W., Jiang, F., Liu, P., Zhang, H., Jiang, Q. and Xu, J., 2020. Fishnet-Like, Nitrogen-Doped Carbon Films Directly Anchored on Carbon Cloths as Binder-Free Electrodes for High-Performance Supercapacitor. *Global Challenges*, **4**, p.1900086.

[3] Zhai, Y., Dou, Y., Zhao, D., Fulvio, P.F., Mayes, R.T. and Dai, S., 2011. Carbon materials for chemical capacitive energy storage. *Advanced Materials*, **23**, pp.4828-4850.

[4] Wang, F., Wu, X., Yuan, X., Liu, Z., Zhang, Y., Fu, L., Zhu, Y., Zhou, Q., Wu, Y. and Huang, W., 2017. Latest advances in supercapacitors: from new electrode materials to novel device designs. *Chemical Society Reviews*, **46**, pp.6816-6854.

[5] Jiang, X., Setodoi, S., Fukumoto, S., Imae, I., Komaguchi, K., Yano, J., Mizota, H. and Harima, Y., 2014. An easy one-step electrosynthesis of graphene/polyaniline composites and electrochemical capacitor. *Carbon*, **67**, pp.662-672.

[6] Yang, M., Cheng, B., Song, H. and Chen, X., 2010. Preparation and electrochemical performance of polyaniline-based carbon nanotubes as electrode material for supercapacitor. *Electrochimica Acta*, **55**, pp.7021-7027.

[7] E. Stojanovska, E. and Kilic, A., 2019. Carbon nanofibers as thick electrodes for aqueous supercapacitors. *Journal of Energy Storage*, **26**, p.100981.

[8] Cai, P., Zou, K., Deng, X., Wang, B., Zou, G., Hou, H. and Ji, X., 2020. Defect rich hierarchical porous carbon for high power supercapacitors. *Frontiers in Chemistry*, **8**, p.43.

[9] Abbas, Q., Raza, R., Shabbir, I. and Olabi, A.G., 2019. Heteroatom doped high porosity carbon nanomaterials as electrodes for energy storage in electrochemical capacitors: A review. *Journal of Science: Advanced Materials and Devices*, **4**, pp.341-352.

[10] Shin, W.H., Jeong, H.M., Kim, B.G., Kang, J.K. and Choi, J.W., 2012. Nitrogen-doped multiwall carbon nanotubes for lithium storage with extremely high capacity. *Nano Letters*, **12**, pp.2283-2288.

[11] Wu, Z.S., Ren, W., Xu, L., Li, F. and Cheng, H.M., 2011. Doped graphene sheets as anode materials with superhigh rate and large capacity for lithium ion batteries. *ACS Nano*, **5**, pp.5463-5471.

[12] Heimböckel, R., Hoffmann, F. and Fröba, M., 2019. Insights into the influence of the pore size and surface area of activated carbons on the energy storage of electric double layer capacitors with a new potentially universally applicable capacitor model. *Physical Chemistry Chemical Physics*, **21**, pp.3122-3133.

[13] Zhao, J., Lai, H., Lyu, Z., Jiang, Y., Xie, K., Wang, X., Wu, Q., Yang, L., Jin, Z., Ma, Y. and Liu, J., 2015. Hydrophilic hierarchical nitrogen-doped carbon nanocages for ultrahigh supercapacitive performance. *Advanced Materials*, **27**, pp.3541-3545.

[14] Chmiola, J., Yushin, G., Dash, R. and Gogotsi, Y., 2006. Effect of pore size and surface area of carbide derived carbons on specific capacitance. *Journal of Power Sources*, **158**, pp.765-772.

[15] Kim, T., Jung, G., Yoo, S., Suh, K.S. and Ruoff, R.S., 2013. Activated graphene-based carbons as supercapacitor electrodes with macro-and mesopores. *ACS Nano*, **7**, pp.6899-6905.

[16] Jiang, L., Yang, S., Song, W., Zhao, J., Lu, Z., Zhai, Q. and Wang, J., 2020. A simple and green preparation method of nitrogen-doped carbon nanocages for supercapacitor application. *ChemNanoMat*, **6**, pp.308-315.

[17] Wu, J., Pan, Z., Zhang, Y., Wang, B. and Peng, H., 2018. The recent progress of nitrogen-doped carbon nanomaterials for electrochemical batteries. *Journal of Materials Chemistry A*, **6**, pp.12932-12944.

[18] Zhao, G., Chen, C., Yu, D., Sun, L., Yang, C., Zhang, H., Sun, Y., Besenbacher, F. and Yu, M., 2018. One-step production of ONS co-doped three-dimensional hierarchical porous carbons for high-performance supercapacitors. *Nano Energy*, **47**, pp.547-555.

[19] Chen, L.F., Huang, Z.H., Liang, H.W., Yao, W.T., Yu, Z.Y. and Yu, S.H., 2013. Flexible all-solid-state high-power supercapacitor fabricated with nitrogen-doped carbon nanofiber electrode material derived from bacterial cellulose. *Energy & Environmental Science*, **6**, pp.3331-3338.

[20] Deng, Y., Xie, Y., Zou, K. and Ji, X., 2016. Review on recent advances in nitrogen-doped carbons: preparations and applications in supercapacitors. *Journal of Materials Chemistry A*, **4**, pp.1144-1173.

[21] Abbas, Q., Raza, R., Shabbir, I. and Olabi, A.G., 2019. Heteroatom doped high porosity carbon nanomaterials as electrodes for energy storage in electrochemical capacitors: A review. *Journal of Science: Advanced Materials and Devices*, **4**, pp.341-352.

[22] Agboola, B.O., Ozoemena, K.I., Nyokong, T., Fukuda, T. and Kobayashi, N., 2010. Tuning the physico-electrochemical properties of novel cobalt (II) octa [(3, 5-biscarboxylate)-phenoxy] phthalocyanine complex using phenylamine-functionalised SWCNTs. *Carbon*, **48**, pp.763-773.

[23] Melchior, S.A., Raju, K., Ike, I.S., Erasmus, R.M., Kabongo, G., Sigalas, I., Iyuke, S.E. and Ozoemena, K.I., 2018. High-voltage symmetric supercapacitor based on 2D titanium carbide (MXene, Ti_2CT_x)/carbon nanosphere composites in a neutral aqueous electrolyte. *Journal of The Electrochemical Society*, **165**, p.A501.

[24] Kshetri, T., Thanh, T.D., Singh, S.B., Kim, N.H. and Lee, J.H., 2018. Hierarchical material of carbon nanotubes grown on carbon nanofibers for high performance electrochemical capacitor. *Chemical Engineering Journal*, **345**, pp.39-47.

[25] Liao, X.Z., Serquis, A., Jia, Q.X., Peterson, D.E., Zhu, Y.T. and Xu, H.F., 2003. Effect of catalyst composition on carbon nanotube growth. *Applied Physics Letters*, **82**, pp.2694-2696.

[26] Chen, L., Chen, N., Wu, H., Li, W., Fang, Z., Xu, Z. and Qian, X., 2018. Flexible design of carbon nanotubes grown on carbon nanofibers by PECVD for enhanced Cr (VI) adsorption capacity. *Separation and Purification Technology*, **207**, pp.406-415.

[27] Zhou, Y., Jin, P., Zhou, Y. and Zhu, Y., 2018. High-performance symmetric supercapacitors based on carbon nanotube/graphite nanofiber nanocomposites. *Scientific Reports*, **8**, pp.1-7.

[28] Ramos, A., Cameán, I. and García, A.B., 2013. Graphitization thermal treatment of carbon nanofibers. *Carbon*, **59**, pp.2-32.

[29] Maitra, T., Sharma, S., Srivastava, A., Cho, Y.K., Madou, M. and Sharma, A., 2012. Improved graphitization and electrical conductivity of suspended carbon nanofibers derived from carbon nanotube/polyacrylonitrile composites by directed electrospinning. *Carbon*, **50**, pp.1753-1761.

[30] Singh, D.K., Iyer, P.K. and Giri, P.K., 2010. Diameter dependence of interwall separation and strain in multiwalled carbon nanotubes probed by X-ray diffraction and Raman scattering studies. *Diamond and Related Materials*, **19**, pp.1281-1288.

[31] Lapuerta, M., Rodríguez–Fernández, J. and Sánchez-Valdepeñas, J., 2020. Soot reactivity analysis and implications on diesel filter regeneration. *Progress in Energy and Combustion Science*, **78**, p.100833.

[32] Li, X., Ji, X., Qin, A. and He, C., 2015. The plasticized spinning and cyclization behaviors of functionalized carbon nanotube/polyacrylonitrile fibers. *RSC Advances*, **5**, pp.52226-52234.

[33] Yang, G., Li, L., Lee, W.B. and Ng, M.C., 2018. Structure of graphene and its disorders: A review. *Science and Technology of Advanced Materials*, **19**, pp.613-648.

[34] Sadezky, A., Muckenhuber, H., Grothe, H., Niessner, R. and Pöschl, U., 2005. Raman microspectroscopy of soot and related carbonaceous materials: spectral analysis and structural information. *Carbon*, **43**, pp.1731-1742.

[35] Amaral Junior, M.A.D., Matsushima, J.T., Rezende, M.C., Gonçalves, E.S., Marcuzzo, J.S. and Baldan, M.R., 2017. Production and characterization of activated carbon fiber from textile PAN fiber. *Journal of Aerospace Technology and Management*, **9**, pp.423-430.

[36] Xing, Z., Qi, Y., Tian, Z., Xu, J., Yuan, Y., Bommier, C., Lu, J., Tong, W., Jiang, D.E. and Ji, X., 2017. Identify the removable substructure in carbon activation. *Chemistry of Materials*, **29**, pp.7288-7295.

[37] Al-Jishi, R. and Dresselhaus, G., 1982. Lattice-dynamical model for graphite. *Physical Review B*, **26**, p.4514.

[38] Wang, Y., Alsmeyer, D.C. and McCreery, R.L., 1990. Raman spectroscopy of carbon materials: structural basis of observed spectra. *Chemistry of Materials*, **2**, pp.557-563.

[39] Jawhari, T., Roid, A. and Casado, J., 1995. Raman spectroscopic characterization of some commercially available carbon black materials. *Carbon*, **33**, pp.1561-1565.

[40] Ferrari, A.C. and Robertson, J., 2000. Interpretation of Raman spectra of disordered and amorphous carbon. *Physical Review B*, **61**, p.14095.

[41] Eckmann, A., Felten, A., Mishchenko, A., Britnell, L., Krupke, R., Novoselov, K.S. and Casiraghi, C., 2012. Probing the nature of defects in graphene by Raman spectroscopy. *Nano Letters*, **12**, pp.3925-3930.

[42] Liu, D., Ni, K., Ye, J., Xie, J., Zhu, Y. and Song, L., 2018. Tailoring the structure of carbon nanomaterials toward high-end energy applications. *Advanced Materials*, **30**, p.1802104.

[43] Zhao, J., Chen, J., Xu, S., Shao, M., Zhang, Q., Wei, F., Ma, J., Wei, M., Evans, D.G. and Duan, X., 2014. Hierarchical NiMn layered double hydroxide/carbon nanotubes architecture with superb energy density for flexible supercapacitors. *Advanced Functional Materials*, **24**, pp.2938-2946.

[44] Xu, Y., Zhang, C., Zhou, M., Fu, Q., Zhao, C., Wu, M. and Lei, Y., 2018. Highly nitrogen doped carbon nanofibers with superior rate capability and cyclability for potassium ion batteries. *Nature Communications*, **9**, pp.1-11.

[45] Li, J., Zhang, W., Zhang, X., Huo, L., Liang, J., Wu, L., Liu, Y., Gao, J., Pang, H. and Xue, H., 2020. Copolymer derived micro/meso-porous carbon nanofibers with vacancy-type defects for high-performance supercapacitors. *Journal of Materials Chemistry A*, **8**, pp.2463-2471.

[46] J Li, J., Zhang, W., Zhang, X., Huo, L., Liang, J., Wu, L., Liu, Y., Gao, J., Pang, H. and Xue, H., 2020. Copolymer derived micro/meso-porous carbon nanofibers with vacancy-type

defects for high-performance supercapacitors. *Journal of Materials Chemistry A*, **8**, pp.2463-2471.

[47] Zhu, J., Chen, C., Lu, Y., Ge, Y., Jiang, H., Fu, K. and Zhang, X., 2015. Nitrogen-doped carbon nanofibers derived from polyacrylonitrile for use as anode material in sodium-ion batteries. *Carbon*, **94**, pp.189-195.

[48] Zhang, H., Zhang, L., Chen, J., Su, H., Liu, F. and Yang, W., 2016. One-step synthesis of hierarchically porous carbons for high-performance electric double layer supercapacitors. *Journal of Power Sources*, **315**, pp.120-126.

[49] Dou, S., Huang, X., Ma, Z., Wu, J. and Wang, S., 2015. A simple approach to the synthesis of BCN graphene with high capacitance. *Nanotechnology*, **26**, p.045402.

[50] Mosiane, L.R., Matsoso, B.J., Makhongoana, A., Mutuma, B.K., Mongwe, T.H., Coville, N.J. and Maubane-Nkadimeng, M.S., 2019. Tuning the properties of CVD-grown multiwalled carbon nanotubes by ex situ co-doping with boron and nitrogen heteroatoms. *Journal of Nanoparticle Research*, **21**, pp.1-15.

[51] Gao, S., Chen, Y., Fan, H., Wei, X., Hu, C., Luo, H. and Qu, L., 2014. Large scale production of biomass-derived N-doped porous carbon spheres for oxygen reduction and supercapacitors. *Journal of Materials Chemistry A*, **2**, pp.3317-3324.

[52] Mutuma, B.K., Matsoso, B.J., Ranganathan, K., Keartland, J.M., Wamwangi, D. and Coville, N.J., 2017. Generation of radical species in CVD grown pristine and N-doped solid carbon spheres using H_2 and Ar as carrier gases. *RSC Advances*, **7**, pp.21187-21195.

[53] Li, Z., Xu, Z., Tan, X., Wang, H., Holt, C.M., Stephenson, T., Olsen, B.C. and Mitlin, D., 2013. Mesoporous nitrogen-rich carbons derived from protein for ultra-high capacity battery anodes and supercapacitors. *Energy & Environmental Science*, **6**, pp.871-878.

[54] Zheng, F., Yang, Y. and Chen, Q., 2014. High lithium anodic performance of highly nitrogen-doped porous carbon prepared from a metal-organic framework. *Nature Communications*, **5**, pp.1-10.

[55] Tan, J., Han, Y., He, L., Dong, Y., Xu, X., Liu, D., Yan, H., Yu, Q., Huang, C. and Mai, L., 2017. In situ nitrogen-doped mesoporous carbon nanofibers as flexible freestanding electrodes for high-performance supercapacitors. *Journal of Materials Chemistry A*, **5**, pp.23620-23627.

[56] Lota, G., Lota, K. and Frackowiak, E., 2007. Nanotubes based composites rich in nitrogen for supercapacitor application. *Electrochemistry Communications*, **9**, pp.1828-1832.

[57] Zhang, L.L., Zhao, X., Ji, H., Stoller, M.D., Lai, L., Murali, S., Mcdonnell, S., Cleveger, B., Wallace, R.M. and Ruoff, R.S., 2012. Nitrogen doping of graphene and its effect on quantum capacitance, and a new insight on the enhanced capacitance of n-doped carbon. *Energy & Environmental Science*, **5**, pp.9618-9625.

[58] Seredych, M., Hulicova-Jurcakova, D., Lu, G.Q. and Bandosz, T.J., 2008. Surface functional groups of carbons and the effects of their chemical character, density and accessibility to ions on electrochemical performance. *Carbon*, **46**, pp.1475-1488.

[59] Hulicova-Jurcakova, D., Seredych, M., Lu, G.Q. and Bandosz, T.J., 2009. Combined effect of nitrogen-and oxygen-containing functional groups of microporous activated carbon on its electrochemical performance in supercapacitors. *Advanced Functional Materials*, **19**, pp.438-447.

[60] Xu, B., Hou, S., Cao, G., Wu, F. and Yang, Y., 2012. Sustainable nitrogen-doped porous carbon with high surface areas prepared from gelatin for supercapacitors. *Journal of Materials Chemistry*, **22**, pp.19088-19093.

[61] Zhou, M., Pu, F., Wang, Z. and Guan, S., 2014. Nitrogen-doped porous carbons through KOH activation with superior performance in supercapacitors. *Carbon*, **68**, pp.185-194.

[62] Liu, T.C., Pell, W.G., Conway, B.E. and Roberson, S.L., 1998. Behavior of molybdenum nitrides as materials for electrochemical capacitors: comparison with ruthenium oxide. *Journal of the Electrochemical Society*, **145**, p.1882.

[63] Makgopa, K., Raju, K., Ejikeme, P.M. and Ozoemena, K.I., 2017. High-performance Mn3O4/onion-like carbon (OLC) nanohybrid pseudocapacitor: Unravelling the intrinsic properties of OLC against other carbon supports. *Carbon*, **117**, pp.20-32.

[64] Qian, X., Lv, Y., Li, W., Xia, Y. and Zhao, D., 2011. Multiwall carbon nanotube@ mesoporous carbon with core-shell configuration: a well-designed composite-structure toward electrochemical capacitor application. *Journal of Materials Chemistry*, **21**, pp.13025-13031.

[65] Lin, C.C. and Lin, Y.W., 2015. Synthesis of carbon nanotube/graphene composites by one-step chemical vapor deposition for electrodes of electrochemical capacitors. *Journal of Nanomaterials*, 2015.

[66] Zhao, M.Q., Zhang, Q., Huang, J.Q., Tian, G.L., Chen, T.C., Qian, W.Z. and Wei, F., 2013. Towards high purity graphene/single-walled carbon nanotube hybrids with improved electrochemical capacitive performance. *Carbon*, **54**, pp.403-411.

[67] H. Y. Chen, J. T. Di, Y. Jin, M. H. Chen, J. Tian, Q. W. Li. Active carbon wrapped carbon nanotube buckypaper for the electrode of electrochemical supercapacitors. *J. Power Sources*, 2013; **237**: 325–331.

[68] Kim, B.H., Yang, K.S., Kim, Y.A., Kim, Y.J., An, B. and Oshida, K., 2011. Solvent-induced porosity control of carbon nanofiber webs for supercapacitor. *Journal of Power Sources*, **196**, pp.10496-10501.

[69] Pillay, J. and Ozoemena, K.I., 2009. Layer-by-layer self-assembled nanostructured phthalocyaninatoiron (II)/SWCNT-poly (m-aminobenzenesulfonic acid) hybrid system on gold surface: Electron transfer dynamics and amplification of H_2O_2 response. *Electrochimica Acta*, **54**, pp.5053-5059.

[70] Ozoemena, K.I., Mathebula, N.S., Pillay, J., Toschi, G. and Verschoor, J.A., 2010. Electron transfer dynamics across self-assembled N-(2-mercaptoethyl) octadecanamide/mycolic acid layers: impedimetric insights into the structural integrity and interaction with anti-mycolic acid antibodies. *Physical Chemistry Chemical Physics*, **12**, pp.345-357.

[71] Mathis, T.S., Kurra, N., Wang, X., Pinto, D., Simon, P. and Gogotsi, Y., 2019. Energy storage data reporting in perspective—guidelines for interpreting the performance of electrochemical energy storage systems. *Advanced Energy Materials*, **9**, p.1902007.

[72] S Zhang, S., Tian, K., Cheng, B.H. and Jiang, H., 2017. Preparation of N-doped supercapacitor materials by integrated salt templating and silicon hard templating by pyrolysis of biomass wastes. *ACS Sustainable Chemistry & Engineering*, **5**, pp.6682-6691.

[73] Li, J., Song, X., Zhang, W., Xu, H., Guo, T., Zhang, X., Gao, J., Pang, H. and Xue, H., 2020. Microporous Carbon Nanofibers Derived from Poly (acrylonitrile-co-acrylic acid) for High-Performance Supercapacitors. *Chemistry–A European Journal*, **26**, pp.3326-3334.

CHAPTER 5

Nitrogen-doped carbon nanotube-carbon fibre networks as anode materials for nickel-metal organic frameworks-derived carbon hybrid supercapacitors[2]

5.1 Introduction

With the ever-increasing worldwide energy demand and the start of the fourth Industrial revolution (4IR), developing environmentally clean, cost-effective and viable energy storage devices has become increasingly relevant [1]. Electrochemical energy storage (EES) systems that make use of both properties of batteries and supercapacitors are needed to power the next-generation energy-hungry applications, such as an electric vehicle (EV), portable electronics and emergency opening systems in buses and planes [2, 3].

Based on their energy storage mechanism, EES can be divided into three categories [4]: (i) electric double-layer capacitive (EDLC), (ii) pseudocapacitive and (iii) battery-type charge storage. In summary, an EDLC uses only carbon-based electrode materials and stores charge at the electrode/electrolyte interface *via* adsorption of electrolyte ions [5]. Pseudocapacitors on the other hand make use of transition metal oxides or conducting polymers as electrode materials and store charge *via* Faradaic (oxidation and reduction processes) [6] and exhibit symmetric redox peaks (i.e., peak-to-peak separation, ΔE_p, being essentially zero voltage). Battery-type energy storage (BTES), on the other hand, is characterized by a bulk redox mechanism, exhibits asymmetric redox peaks (i.e., ΔE_p is greater than zero voltage) and is reported to be completely controlled by the Faradaic process [4], a claim with which this study

[2] A substantial part of this chapter has been published in a peer-reviewed journal: **Mofokeng, T.P**., Ipadeola, A.K., Tetana, Z.N. and Ozoemena, K.I., 2020. Defect-Engineered Nanostructured Ni/MOF-Derived Carbons for an Efficient Aqueous Battery-Type Energy Storage Device. ACS omega, 5(32), pp.20461-20472.

disagrees with; it is not entirely Faradaic (to be discussed later). The fourth classification, battery-supercapacitor hybrid or hybrid energy storage system (HESS), or *supercapattery or supercabattery,* is gaining a lot of attention in the literature and describes an energy storage device that combines the qualities of an EDLC and battery material.

Battery-type cathode materials, particularly Ni-based materials, are high-voltage materials as compared to carbon-based materials utilized in EDLCs. Some authors continue to refer to Ni-based battery electrodes as pseudocapacitive and calculate energy storage in capacitance (Farad) rather than capacity (mAh). Researchers in the field of electrochemical energy storage have expressed concern about this misinterpretation [4, 7-9], as it makes it almost impossible to compare the electrochemical data in the literature. Another issue raised is the assumption that charge storage in BTES is solely a diffusion-controlled (Faradaic) process, with the capacitive process making no substantial influence on the storage mechanism [4]. As a result, it is crucial to determine if any Ni-based electrode (which is well-known for being a battery-type electrode) is often operated by a pure diffusion process with negligible surface-controlled contributions. This knowledge gap in the battery-type energy storage properties of Ni-based materials encouraged us to investigate the electrochemistry of nickel-based metal-organic-frameworks (MOF) electrode materials.

Due to their inherent tuneable pore diameters, highly accessible surface areas, active metal sites, and ordered crystallinity, MOFs have continued to gain considerable scientific attention. [10, 11]. Due to their excellent properties, MOFs are suitable for different applications, including supercapacitors [12, 13]. Carbonization of MOFs is a good way to make porous carbon materials with uniform pore size distributions, high surface area and enhanced electrical conductivity [14]. MOF-derived carbons (MOFDC) are hence significant electrodes for supercapacitor applications [15, 16].

Herein, a microwave-assisted synthesis technique was used to synthesize Ni-MOF as a sacrificial template yield nanostructured Ni supported MOFDC (Ni/MOFDC). The chemical etching was done to yield AT-Ni/MOFDC with unique physio-chemical properties that will improve the electrochemical performance of HESS. Chemical etching confers defect-rich properties on Ni/MOFDC, together with the production of oxygen vacancies that double its energy storage capacity [17]. Most importantly, the BTES mechanism is seen to be a mixed Faradaic/non-Faradaic process rather than a pure Faradaic process, contrary to recent literature [4].

5.2 Experimental section

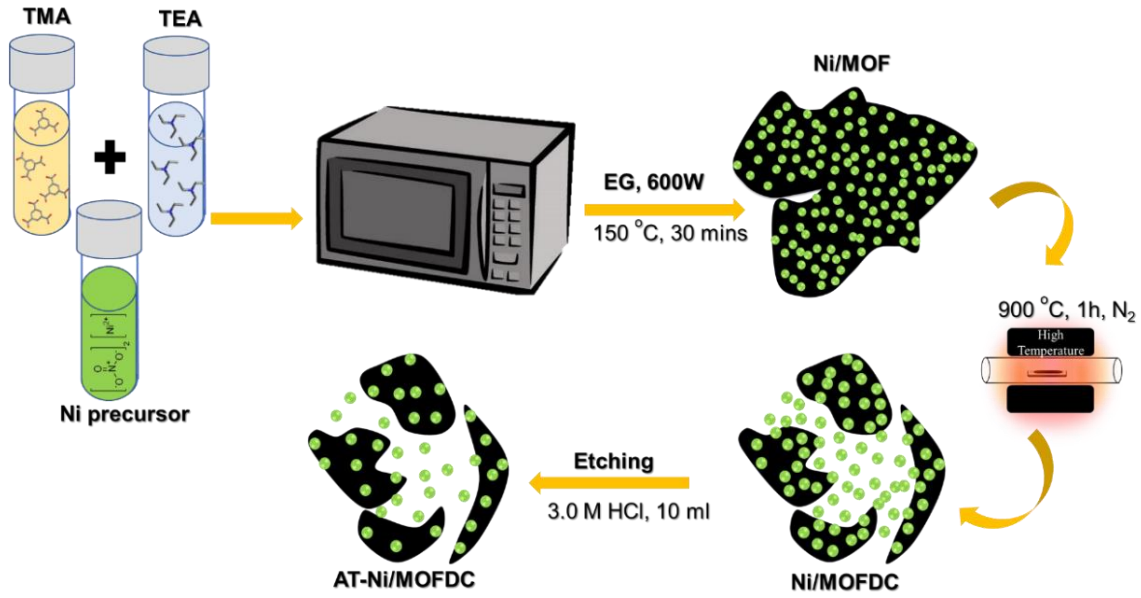
5.2.1 Materials

Nickel nitrate hexahydrate ($Ni(NO_3)_2.6H_2O$, 98 %), triethylamine (TEA, $N(CH_2CH_3)_3$, ≥ 99.5 %), trimeric acid (TMA, $C_9H_6O_6$, 99.9 %), ethylene glycol (EG, $C_2H_6O_2$, 99.8 %) and ethanol (C_2H_6O, 99 %) were purchased from Sigma Aldrich. No additional purifications were performed on any of the compounds or solvents used.

5.2.2 Synthesis of Ni-MOF, Ni/MOFDC and AT-Ni/MOFDC

A microwave-assisted solvothermal approach, with minor modifications, was used to synthesize nickel-based metal-organic framework (Ni-MOF) [1]. Typically, 1.6811 g (8.0 mmol) of TMA, 10 mL (1.2 mol) of TEA and 1.1632 g (4.0 mmol) of $Ni(NO_3)_2{\cdot}6H_2O$ were dissolved in 50 mL (0.9 mol) of EG in a beaker. The mixture was ultrasonicated for 1 hour to ensure homogeneity. The mixture was then microwave irradiated (MW) for 30 minutes at 600 W and 150 °C before cooling to ambient temperature. A deep green Ni-MOF crystal was collected, centrifuged three times using ethanol to remove impurities and then dried for 12 hours in a vacuum oven at 80 °C. The Ni-MOF powder was poured into a quartz boat, placed in a quartz tube and annealed in an electric furnace for 3 hours at 900 °C under N_2 flow at a

rate of 5 °C min^{-1}, resulting in nickel nanoparticles supported MOF-derived carbon (Ni/MOFDC). The Ni/MOFDC was split into two parts: one was chemically etched with 3.0 M HCl (10 mL), yielding AT-Ni/MOFDC and the other was not (i.e., Ni/MOFDC).



Scheme 5.1: Schematic illustrations of the synthesis of the Ni-MOF, Ni/MOFDC and AT-Ni/MOFDC.

5.2.3 Characterization

The materials were thoroughly characterized using Fourier transform infrared spectroscopy (FTIR, BRUKER TENSOR 27), Raman spectroscopy (BRUKER SENTERRA), Powder X-ray diffraction (XRD, BRUKER D2 diffractometer equipped with Cu Kα radiation (λ = 1.54178 Å)), X-Ray photoelectron spectroscopy (AXIS SUPRA XPS equipped with an Al Kα radiation source (1486.6 eV)), transmission electron microscopy (FEI Tecnai T12 Sprint TEM), scanning electron microscopy (FEI Nova Nanolab 600 SEM), coupled with Energy-dispersive X-ray spectroscopy (EDX) and Brunauer-Emmett-Teller (BET, Micrometric Tristar 3000) to determine the presence of functional groups, bond vibrations, crystalline structures, chemical environments, morphological properties, surface area and pore sizes, respectively.

5.2.4 Electrochemical characterization

5.2.4.1 Fabrication and testing of single electrode materials

A Bio-Logic SP300 electrochemical workstation with EC-Lab software was used to perform the electrochemical measurements. The active materials Ni/MOFDC and AT-Ni/MOFDC were crushed using pestle and mortar and dispersed separately in ethanol and stirred for 2 hours to generate separate slurries. The working electrodes were then prepared by coating the slurries onto a carbon paper current collector, which were then dried in a vacuum oven overnight. For both electrodes, the mass loadings ranged from 1.5 to 2.3 mg. The counter electrode used was Ni foam, the reference electrode was silver metal and the electrolyte was 3.0 M KOH solution. The energy storage properties of the materials were investigated using cyclic voltammetry (CV), galvanostatic charge-discharge (GCD) and electrochemical impedance spectroscopy (EIS). The EIS experiments were carried out with a 10 mV amplitude AC voltage in the frequency range of 0.1 Hz to 100 kHz.

5.2.4.2 Fabrication of the N-CNT@CF//AT-Ni/MOFDC hybrid device

The assembly of the hybrid device was carried out with the AT-Ni/MOFDC as a cathode while N-CNT@CF as an anode, with 3.0 M KOH as the electrolyte. The mass ratio of the cathode to anode materials (obtained from 3-electrode experiments) was calculated using the conventional approach for charge-balancing, equation 5.1.

$$q^{+}=q^{-} \tag{5.1}$$

where q^{+} and q^{-} are the charges at the cathode and anode, respectively. The optimal mass ratio was obtained using equation 5.2.

$$\frac{m^{+}}{m^{-}}=\frac{c^{-}}{c^{+}}+\frac{\Delta V^{-}}{\Delta V^{+}} \tag{5.2}$$

where m^{+}, ΔV^{+} and c^{+} are the mass, potential window and specific capacity of the cathode, while m^{-}, ΔV^{-} and c^{-} are the mass, potential window and specific capacity of the anode,

respectively. Voltammetric specific capacity (C_S), power density (P_S) and energy density (E_S) are following the formulae in equations 5.3–5.6 [6]:

$$C_s = \frac{\oint IdV}{3.6mS} \ (\text{mAh g}^{-1}) \tag{5.3}$$

$$C_s = \frac{I.\Delta t}{3.6\ m} \ (\text{mAh g}^{-1}) \tag{5.4}$$

where $\oint I.dV$ (A·V) is the voltammetric charge, which is an area under the curve of the CV. S (V s^{-1}) is the scan rate, I (A) is the discharging current, Δt is the discharge time and m (g) represents the active mass of the electrodes.

Specific energy (E_S, Wh kg^{-1}) and specific power (P_S, W kg^{-1}) are calculated from the discharge curves using the conventional formulae for the battery and battery-type energy storage:

$$E_S = \frac{I.V.\Delta t}{m} \ \left(\text{Whk g}^{-1}\right) \tag{5.5}$$

$$P_S = \frac{E_S}{\Delta t} \ \left(\text{W kg}^{-1}\right) \tag{5.6}$$

where E_S (Wh kg^{-1}) represents the specific energy, I (A) defines the discharging current, V (V) is the voltage, m (kg) is the total mass of the two electrode materials, P_S (W kg^{-1}) is the specific power, while t (h) is the time of discharge.

5.3 Results and discussion

5.3.1 Physical characterization

The FTIR spectrum of the as-synthesized Ni-MOF shows the functional groups present in the sacrificial template (see **supporting information, Figure S1a in Appendix B**). The following functional groups confirming the formation of Ni-MOF were observed: -OH stretching (3320 cm^{-1}), C-H stretching (2925 cm^{-1}), C-H bending (2865 cm^{-1}), CO stretching vibration (1726 cm^{-1}), COO^- symmetric vibrations (1568 cm^{-1}), C-C stretching (1427 cm^{-1}), COO- asymmetric

vibrations (1365 cm^{-1}), C-H out-of-plane (1047 cm^{-1}), C-H in-plane (869 cm^{-1}), CO bending vibrations (704 cm^{-1}) and Ni-O coordinate bond (548 cm^{-1}) [18-22]. After carbonization and chemical etching, the FTIR spectra (see **Figure S1b in the supporting information in Appendix B**) show similar moieties in the Ni/MOFDC and AT-MOFDC, which are C-H stretching (3100.0 cm^{-1}), C-H bending (2946.2 cm^{-2}), carboxylic acid O-H (2363.4 – 2680.0 cm^{-1}), C≡N (2168.8 cm^{-1}), C=C (2025.5 cm^{-1}) and Ni-O (548 cm^{-1}), respectively. These findings indicate that the MOF frameworks were broken down at high temperatures.

The bond vibrations of Ni/MOFDC and AT-Ni/MOFDC are seen in the Raman spectra displayed in **Figure 5.1a**. In the Ni/MOFDC, the bond vibrations of Ni-OH (487 cm^{-1}) and prominent MOFDC vibration modes D-band (1350 cm^{-1}), G-band (1599 cm^{-1}) and 2D-band (2450 cm^{-1}) [23]. The Ni-OH became smooth after chemical etching (AT-Ni/MOFDC), with minor changes in the D-band (1345 cm^{-1}) and G-band (1589 cm^{-1}), but the 2D (2450 cm^{-1}) remained in the same place. These findings suggest that the chemically etched sample had some defects as a result of the removal of the passive $Ni(OH)_2$ layer. Since $Ni(OH)_2$ has been reported to exhibit substantial interfacial resistance to electron transport, it is essential to remove the passive $Ni(OH)_2$ layer [24, 25]. The spectral fitting of all Ni/MOFDC and AT-Ni/MOFDC materials was used to confirm the defects caused by chemical etching. Both materials revealed five distinct bands at 1229, 1343, 1489, 1575 and 1610 cm^{-1}, which correspond to the D_4, D_1, D_3, G, and D_2 bands, respectively. Following the procedure used previously [26, 27], the I_{D1}/I_G values of the Ni/MOFDC and AT-Ni/MOFDC composites were determined as 1.8 and 2.1, respectively. The increased I_{D1}/I_G value of AT-Ni/MOFDC indicates that major defects have developed in its arrays.

Powder X-ray diffraction spectroscopy was used to investigate the crystalline structures of as-synthesised Ni-MOF, Ni/MOFDC and AT-Ni/MOFDC (**Figure 5.1b**). The as-synthesized Ni/MOF gives two distinct diffraction patterns at 9.7º and 22.2º corresponding to Miller indices

of Ni-MOF (100) and Ni-MOF (101), respectively [25]. Similar diffraction patterns have previously been identified for Ni-based MOFs and these characteristic peaks are a direct indicator for the full synthesis of the as-synthesized Ni-MOF [29-31]. The frameworks of the as-synthesised Ni-MOF disintegrated during high-temperature annealing, yielding nickel nanoparticles-supported MOF-derived carbon (Ni/MOFDC) with different diffraction patterns observed at 26.3º, 44.9º, 52.1º, 76.7º, 93.1º and 98.5º, attributable hexagonal graphitic carbon, MOFDC (002), Ni(111), Ni(200), Ni(220), Ni(311) and Ni(222), respectively [32]. The hexagonal graphitic carbon peak became more prominent and Ni diffraction patterns widened after chemical etching of the Ni/MOFDC to give the AT-Ni/MOFDC, implying the formation of defects in the chemically etched composite and the removal of the passive $Ni(OH)_2$ layer. This observation supports the Raman data shown in **Figure 5.1a**.

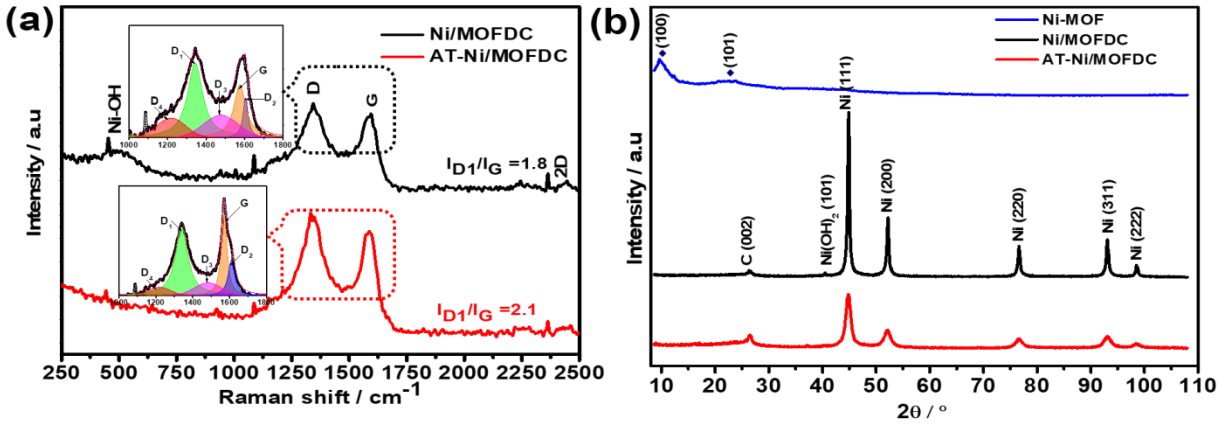


Figure 5.1: (a) Raman spectra of Ni/MOFDC and AT-Ni/MOFDC (the insert show typical deconvoluted Raman signal of carbon) and (b) XRD of the Ni-MOF, Ni/MOFDC and AT-Ni/MOFDC.

The XPS (**Figure 5.2**) was used to analyse the chemical composition of the composites before and after chemical etching, revealing that the composites are primarily composed of Ni, C and O and that their deconvolutions clarify their chemical environment. The Ni 2p of the Ni/MOFDC shown in **Figure 5.2a** was separated into double peaks of metallic Ni and $Ni(OH)_2$ resulting in four distinct peaks at binding energies: 878.5 eV ($Ni(OH)_2$ $2p_{1/2}$ satellite), 872.8

eV (Ni $2p_{1/2}$), 860.7 eV ($Ni(OH)_2$ $2p_{3/2}$ satellite) and 855.1 eV (Ni $2P_{3/2}$) [33]. The AT-Ni/MOFDC shown in **Figure 5.2b** was also fitted to four distinct peaks at 876.0 eV (Ni $2p_{1/2}$ shake-up satellite), 869.7 eV (Ni $2p_{1/2}$), 856.8 eV (Ni $2p_{3/2}$ shake-up satellite) and 853.2 eV (Ni $2p_{3/2}$), respectively [34, 35]. The differences of Ni 2p in the MOF-derived carbons verify the presence of additional $Ni(OH)_2$ ($3p_{1/2}$ and $3p_{3/2}$) satellites in the Ni/MOFDC, while the shift in these spectra in the chemically etched sample shows the removal of the passive $Ni(OH)_2$ satellite and its substitution with metallic Ni ($3p_{1/2}$ and $3p_{3/2}$) shake-up satellites. In addition, minor Ni ($3p_{1/2}$ and $3p_{3/2}$) shifts for the AT-Ni/MOFDC to lower binding energies confirm the development of mainly metallic Ni nanoparticles, owing to the induction of oxygen vacancies (O_V) and strong interaction between the Ni and C leading to increased electron density for the Ni, compared to the Ni/MOFDC possessing additional $Ni(OH)_2$ satellites [36]. The C 1s of the Ni/MOFDC (**Figure 5.2c**) were fitted by different peaks at binding energies of 287 eV (O=C-N), 285 eV (C-O), 284.6 eV (C sp^2/sp^3) [37] and 282.2 eV for metallic carbide (Ni-C) [38, 39]. After carbonization of the Ni-MOF sacrificial template, the metallic Ni nanoparticles are thought to stay in the core of the carbon lattice, preventing their exposure. **Figure 5.2d** reveals comparable C 1s deconvolution for the AT-Ni/MOFDC, except the metallic carbide continuum at 282.2 eV, which has flattened. This explains why chemical etching causes defects and strains in both the Ni and C lattices, as well as the removal of the passive $Ni(OH)_2$ [40]. The Ni/MOFDC deconvoluted O 1s (**Figure 5.2e**) reveals two distinct spectra at 532.8 eV (surface oxygen, O_S) and 530.5 eV (lattice oxygen, O_L), which can be attributed to the surface covering of OH on Ni metals and the Ni-O bond in the sample. These results confirmed the formation of passive $Ni(OH)_2$ on the metallic Ni [41].

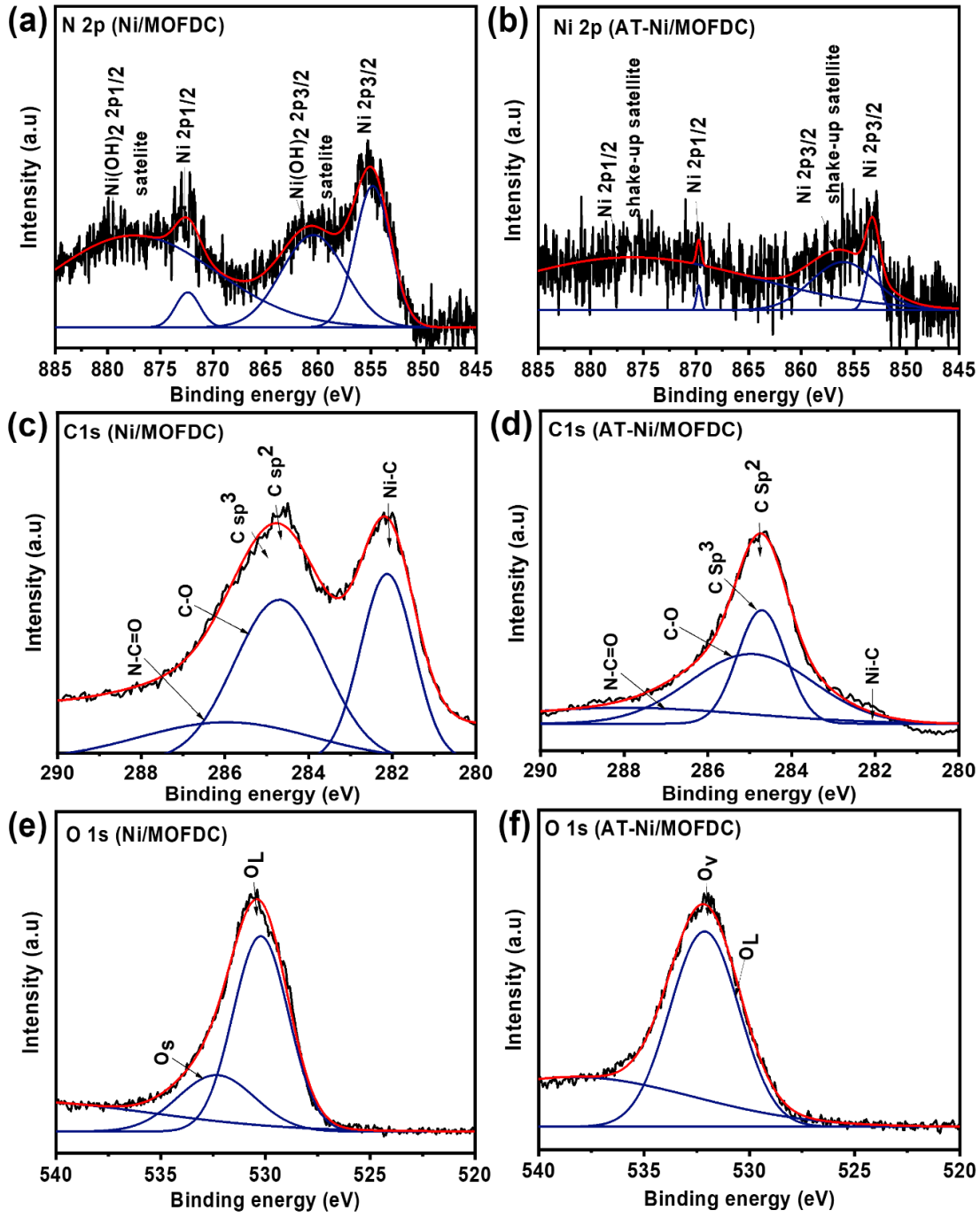


Figure 5.2: Deconvolved XPS scan of the electrocatalysts (a, b) Ni 2p, (c,d) C 1s and (e, f) O 1s.

Figure 5.2f depicts the deconvolved O 1s for the AT-Ni/MOFDC, which reveals just a single peak at 531.9 eV (oxygen vacancy, O_V) and a shoulder at 530.5 eV (O_L), however, the surface coverage of OH became smooth, similar to the previous study [40]. These findings show that chemical etching not only removes the passive $Ni(OH)_2$ but also creates enriched oxygen

vacancies in the AT-Ni/MOFDC material. This finding supports previous reports that etching causes oxygen deficiency in transition metal oxides and hydroxides [41-43].

Figure 5.3 depicts TEM micrographs of Ni/MOFDC, and AT-Ni/MOFDC. The TEM micrograph of the as-synthesized Ni-MOF is shown in (**Supporting information**, **Figure S2 in Appendix B**), depicts interconnected pores distributed over the surface. After annealing at a high temperature (900 ^{o}C), the frameworks disintegrated to form the Ni/MOFDC as shown in **Figure 5.3a**, where Ni and passive $Ni(OH)_2$ layers are tightly packed on the MOFDC with some aggregation. The AT-Ni/MOFDC (**Figure 5.3b**) resulted from the chemical etching of the annealed product, in which the passive $Ni(OH)_2$ layer was removed, leaving more active metal Ni nanoparticles supported MOFDC with well-dispersed nanoparticles. **Figure 5.3(c, d)** shows the Ni nanoparticle size distributions in the Ni/MOFDC and AT-Ni/MOFDC composites, with mean particle sizes of 13.7 and 11.6 nm, respectively. These findings show that chemical etching not only removes the $Ni(OH)_2$ passive layer but also slightly decreases Ni nanoparticle sizes and raises surface area, providing more adsorption sites for the OH^- ions with a simple redox reaction, which is beneficial in energy storage applications.

The SEM images of the as-prepared Ni/MOFDC and AT-Ni/MOFDC composites are shown in **Figure S3(a**, **b)** in the **Supporting Information in Appendix B**. EDX was used to describe the qualitative elemental analysis. The following elements Ni, C, O, N and Au can be seen in the EDX spectra of both Ni/MOFDC (**Supporting Information, Figure S3c in Appendix B**) and AT-Ni/MOFDC (**Supporting Information, Figure S3d in Appendix B**). The presence of Au results from the coating of the samples to avoid charging. Also, the HCl employed for chemical etching can be linked to Cl absorption in the AT-Ni/MOFDC.

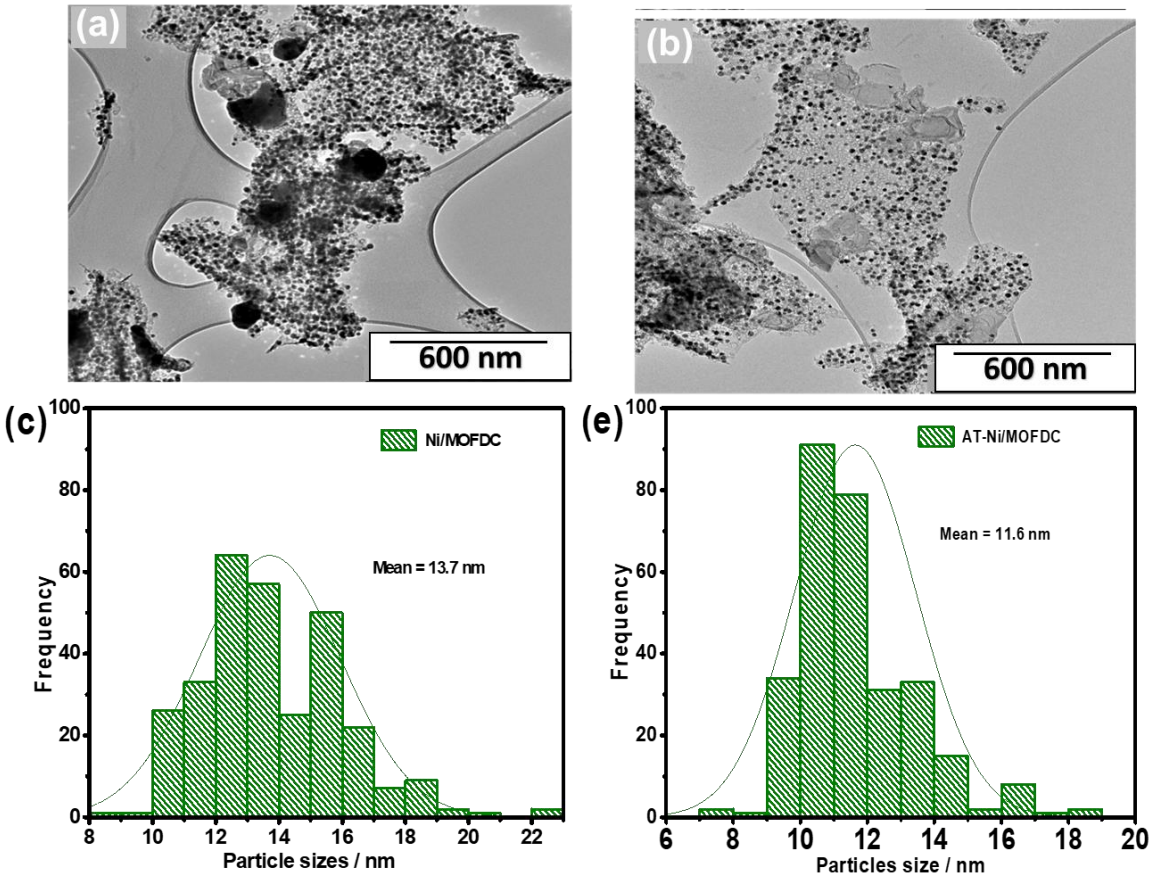


Figure 5.3: TEM micrograms of (a) Ni/MOFDC, (b) AT-Ni/MOFDC and corresponding nanoparticles size distribution of (c) Ni/MOFDC and (d) AT-Ni/MOFDC.

The BET analysis was used to verify the surface area, pore sizes and pore volumes of the as-prepared Ni-MOF, Ni/MOFDC and AT-Ni/MOFDC composites (see **Table 5.1**). The Ni-MOF as-prepared has the largest pore size but the smallest pore volume and surface area. The structures decomposed into Ni/MOFDC after carbonization, with decreased pore size but expanded pore volume and surface area. Chemical etching improved the pore size, pore volume and surface area of AT-Ni/MOFDC material.

Table 5.1: Brunauer-Emmett-Teller (BET) analysis of the as-prepared Ni-MOF and the composites.

Samples	Pore size / nm	Pore volume / $cm^3\ g^{-1}$	S_{BET} / $m^2\ g^{-1}$
Ni-MOF	7.1670	0.0490	85.0948
Ni/MOFDC	2.9493	0.1049	148.9240
AT-Ni/MOFDC	3.4873	0.1240	153.0463

5.3.2 Electrochemical measurements

5.3.2.1 Three-electrode system

The electrochemical performance of the Ni/MOFDC and AT-Ni/MOFDC electrodes were first evaluated in a three-electrode system using a 3.0 M KOH electrolyte. The CV curves shown in **Figure 5.4a** for both the Ni/MOFDC and AT-Ni/MOFDC display a pair of redox couple at 5 mV s^{-1}, showing the battery-like behaviour (Faradaic redox reactions). The reaction mechanism is mostly based on one-electron transfer between the divalent and trivalent nickel (Ni^{2+}/Ni^{3+}) in β-type crystals, with the intercalation and de-intercalation of OH^- ions (equation 5.7), which is consistent with previous reports for Ni-based electrodes [44].

$$\beta\text{-}Ni(OH)_2 \underset{Discharge}{\overset{Charge}{\rightleftharpoons}} \beta\text{-}NiOOH \quad (5.7)$$

For the AT-Ni/MOFDC that contains mainly the metallic nickel (Ni^0), the metal first undergoes a reduction reaction to form the nickel hydroxide $Ni(OH)_2$. This redox behaviour is similar to previous reports [45-47]. The AT-Ni/MOFDC has a larger area under the CV curve than the Ni/MOFDC, indicating that the etched Ni-based material would have a higher specific capacity (Cs) than the pristine counterpart.

Furthermore, the Ni/MOFDC and AT-Ni/MOFDC GCD curves (**Figure 5.4b**) were examined to determine their charge-storage properties. The AT-Ni/MOFDC had a longer discharging time at the same current density, which supports the CV curves. The gravimetric capacity of both electrode materials is determined from the CV curves in **Figure 5.4c**. According to equation 5.3, the Ni/MOFDC and AT-Ni/MOFDC electrodes have cyclic gravimetric capacities of 92 and 199 mAh g^{-1} at 5 mV s^{-1}, respectively. The higher C_s value of the AT-Ni/MOFDC is due to its fine-tuned physico-chemical properties, which include defect formation (Raman analysis, **Figure 5.1a**), enriched oxygen vacancy and removal of passive $Ni(OH)_2$ (XPS analysis, **Figure 5.2**), reduced mean Ni nanoparticle size (TEM analysis, **Figure 5.3d**) and improved surface area (BET analysis, **Table 5.1**). The redox peaks in both Ni/MOFDC and AT-Ni/MOFDC increases with increasing scan rate (see **Supporting Information**, **Figure S4a, b in Appendix B**) which a typical electrochemical signature of Ni-based electrodes [48]. The easy diffusion of the OH^- ions is confirmed by the rise in the peaks of anodic and cathodic current responses [18]. The GCD of electrode materials at various current densities is depicted in (**Supporting Information, Figure S4c, d in Appendix B**). The GCD curves of the AT-Ni/MOFDC (**Figure S4d**) are asymmetrical, which is characteristic of battery-type nanostructured Ni-based electrode materials.

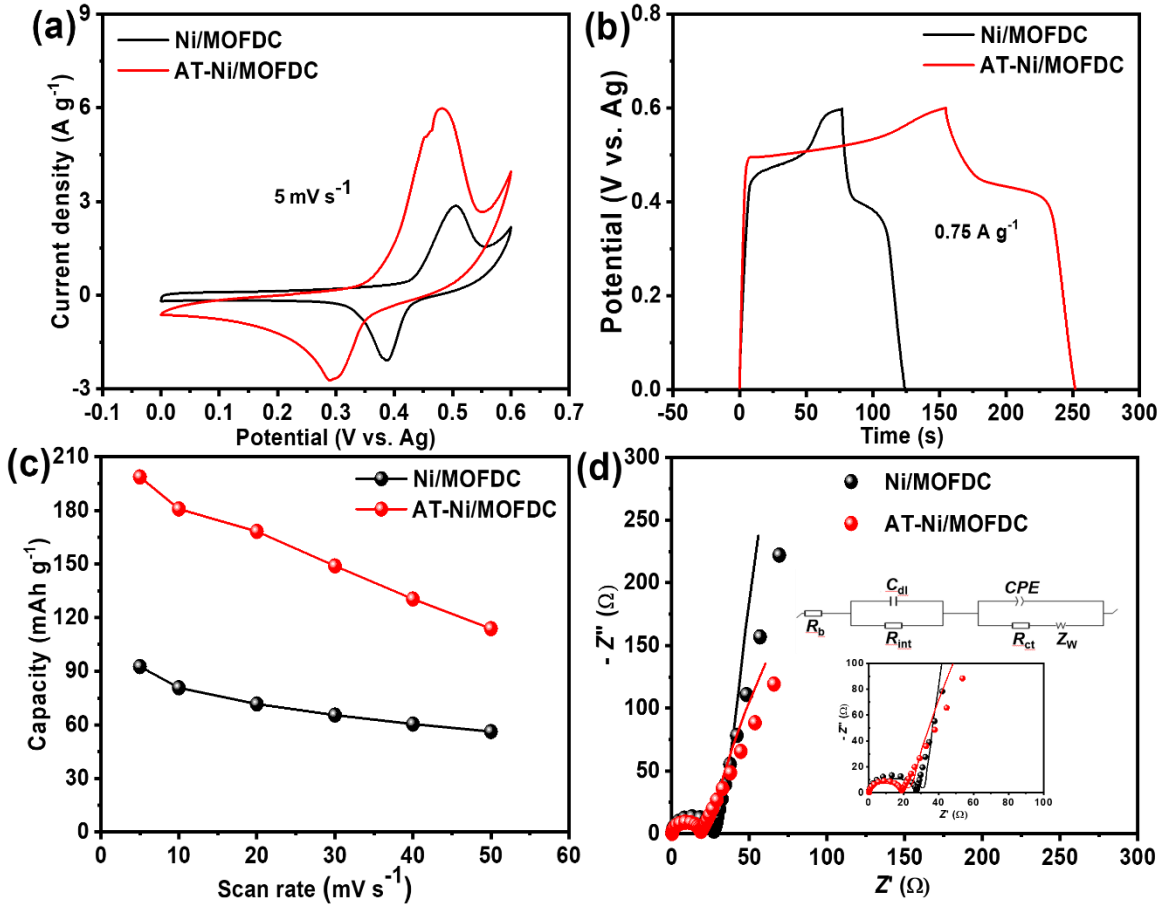


Figure 5.4: (a) CV curves, (b) GCD curves, (c) gravimetric specific capacity and (d) Nyquist plots of the Ni/MOFDC and AT-Ni/MOFDC for the three-electrode system.

EIS is a useful technique for determining the impedance of different electrode materials [49-55]. The EIS measurement of the Ni/MOFDC and AT-Ni/MOFDC with an electrical equivalent circuit is shown in **Figure 5.4d**. The Nyquist plot is represented by a combined RC/Randles circuit that includes the solution resistance (R_s), interfacial resistance (R_{int}) due to IR drop, charge-transfer resistance (R_{ct}) due to electron transport, the double-layer capacitance (C_{dl}), constant phase element (CPE) due to the inhomogeneity of the electrode surface and Warburg diffusion region (Z_w) describing the resistance to ion diffusion. The impedance of the CPE (Z_{CPE}) is a power-law relationship, equation 5.8 [51-55]:

$$Z_{CPE} = [Q\ (j\omega)^{a}]^{-1} \qquad (5.8)$$

where Q is the frequency-independent constant associated with the electrode/electrolyte interface, $j = \sqrt{-1}$, ω represents the radial frequency, the exponent a is the slope of the Log Z *vs.* Log F, the values of which are $-1 \leq a \leq 1$: When $a = 0$, the CPE is a pure resistor; $a = 1$, the CPE is a pure capacitor; $a = -1$ the *CPE* is an inductor; while $a = 0.5$ the CPE is equivalent to the Warburg impedance (Z_w). The Nyquist plots show a larger semicircle diameter for the Ni/MOFDC, suggesting fewer Faradaic reactions near the surface of the active material. Furthermore, the AT-Ni/MOFDC has a smaller semicircle, which indicates low charge transfer resistance. It is worth noting that the semi-circle of AT-Ni/MOFDC material is accompanied by a well-defined 45° line region, which is the hallmark of genuine battery-type energy storage [4].

The Ni/MOFDC and AT-Ni/MOFDC series resistance ($R_s + R_{int} + R_{ct}$) values are 126 and 39, respectively, based on **Table 5.2**. Based on these findings, it is apparent that the AT-Ni/MOFDC has a lower series resistance value, indicating that it has higher conductivity, thanks to its exposed porous carbon and defect of the more active metallic Ni, whereas the increased series resistance of the Ni/MOFDC may be traced to the presence of passive $Ni(OH)_2$. The interfacial resistance of passive Ni hydroxides to electron transport has previously been recorded [56]. For the Ni/MOFDC and AT-Ni/MOFDC, Z_w values of 26.76 and 16.28 $s^{-1/2}$ were observed, respectively. The values of "*a*" (i.e., 0.88 and 0.76 which are less than 1.0 for an ideal capacitor, showing a mixture of EDLC and pseudocapacitive behaviour). As a result of the AT-Ni/MOFDC showed high specific capacity, increased OH^- ions diffusion and increased electrochemical conductivity in the three-electrode system, therefore, only the chemically etched material (AT-Ni/MOFDC) was used in a subsequent two-electrode system.

Table 5.2: EIS parameters for the electrode materials for three-electrode systems.

EIS parameters	Electrode materials	
	Ni/MOFDC	**AT-Ni/MOFDC**
R_s / Ω	0.30 ± 0.01	0.30 ± 0.01
R_{int} / Ω	26.81 ± 1.10	18.16 ± 1.00
C_{dl} / μF	4.75 ± 1.01	7.25 ± 1.23
R_{ct} / Ω	100.20 ± 0.50	13.63 ± 0.09
CPE / mF.s^(*a*-1)	6.66 ± 1.41	110.80 ± 11.99
a	0.88	0.76
Z_w / Ω s^-1/2	29.76 ± 0.01	16.28 ± 0.01

The charge storage mechanism was determined using Trasatti and Dunn differentiation techniques as described in section 2.5 in Chapter two. The log(i) *vs.*log(*v*) graphs in **Figure 5.5(a &b)** reveal that the *b* values are larger than 0.5 (i.e., 0.56 and 0.61 for Ni/MOFDC and 0.59 and 0.77 for AT-Ni/MOFDC) indicating that both electrode materials (Ni/MOFDC and AT-Ni/MOFDC) exhibit mixed storage mechanism. At a scan rate of 5 mV s^{-1}, **Figure 5.5c** depicts the voltage profile for the surface-controlled (capacitive) current in contrast to the diffusion-controlled current. The histogram (**Figure 5.5d**), which compares the percentage contributions of Faradaic and non-Faradaic processes, shows that battery-type storage dominates at low scan rates while EDLC-type storage dominates at high scan rates, indicating that the AT-Ni/MOFDC electrode material has unique high-energy and high-power characteristics. In contrast to the literature, the energy storage mechanism of Ni-based battery-type electrode material is a combined Faradaic/capacitive process. The cycle stability of Ni-based electrode materials illustrated in (**Figure S5, Supporting Information in Appendix B)**, demonstrate that the electrodes are robust after 2,000 cycles.

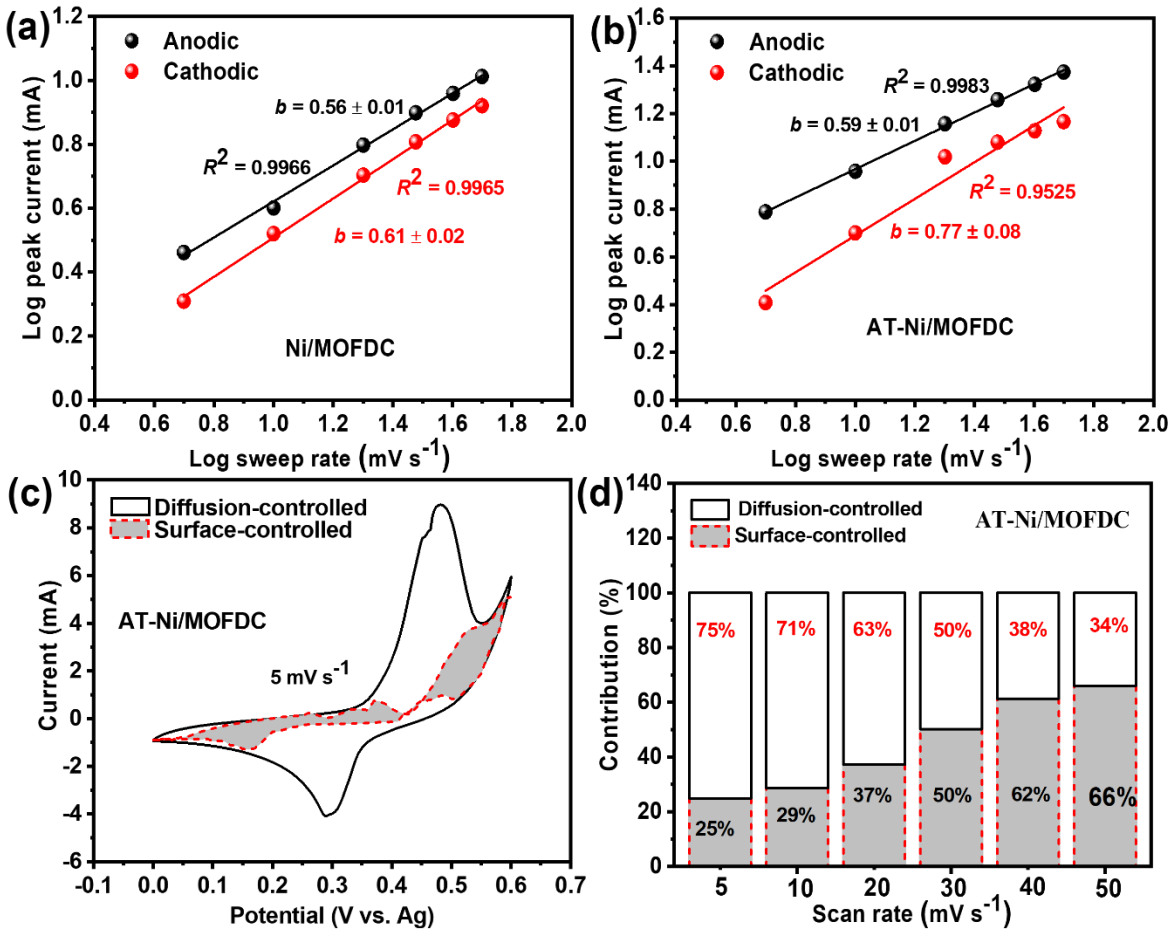


Figure 5.5: (a) Log peak current vs log scan rate for Ni/MOF, (b) Log peak current vs Log scan rate for AT-Ni/MOF, (c) Comparison of the capacitive and diffusion-controlled contributions fraction for the AT-Ni/MOFDC at 5 mV s^{-1} and (d) histograms of the percentage contributions at 5–50 mV s^{-1}.

5.3.2.2 Electrochemical study of hybrid device (N-CNT@CF//AT-Ni/MOFDC)

To better understand the battery-type electrode potential of the AT-Ni/MOFDC a hybrid supercapacitor (HSC) was assembled. The AT-Ni/MOFDC and N-CNT@CF as the positive and negative electrodes were used to fabricate a simple HSC system in a 3.0 M KOH electrolyte. The potential windows of the N-CNT@CF and AT-Ni/MOFDC electrodes at 20 mV s^{-1} scan rate are shown in **Figure 5.6a**. CV measurements at various voltage windows were used to check the stable electrochemical window of the HSC (see **Supporting Information, Figure S6 in Appendix B**). The HSC uses two electrodes with varying potentials to increase the working voltage of its device, resulting in a higher energy density [57]. The electrochemical

performance of HSC devices was investigated further at a potential range of 0–1.6 V, with CV and GCD tests carried out at various scan rates and current densities. The CV curves (**Figure 5.6b**) of the HSC exhibits a quasi-rectangular shape, which is characteristic of pseudocapacitance behaviour. The GCD curves of HSC devices at various current densities are shown in **Figure 5.6c**; all GCD symmetrical curves can reach a high potential of 1.6 V, indicating the high coulomb efficiency of the device [58]. The gravimetric and volumetric capacity of the HSC device at different current densities are plotted in **Figure 5.6d**. At a current density of 0.5 A g^{-1}, the HSC device exhibits high gravimetric and volumetric capacities of 10 F g^{-1} and 37 F cm^{-3}, while at a current density of 5 A g^{-1} the capacities are 5 F g^{-1} and 18 F cm^{-3}, which is equivalent to 50 % of the initial capacity.

For any electrochemical energy storage system, cycling stability is very important. **Figure 5.6a** shows the coulombic efficiency and capacitive retention of the N-CNT@CF//AT-Ni/MOFDC device tested at a 5 A g^{-1} in the voltage window of 0.0 to 1.6 V. After being subjected to 2000 charge/discharge cycles, the HSC device also exhibited excellent cycle stability with capacitance retention as high as 94 % and a high coulombic efficiency of ~ 100%.

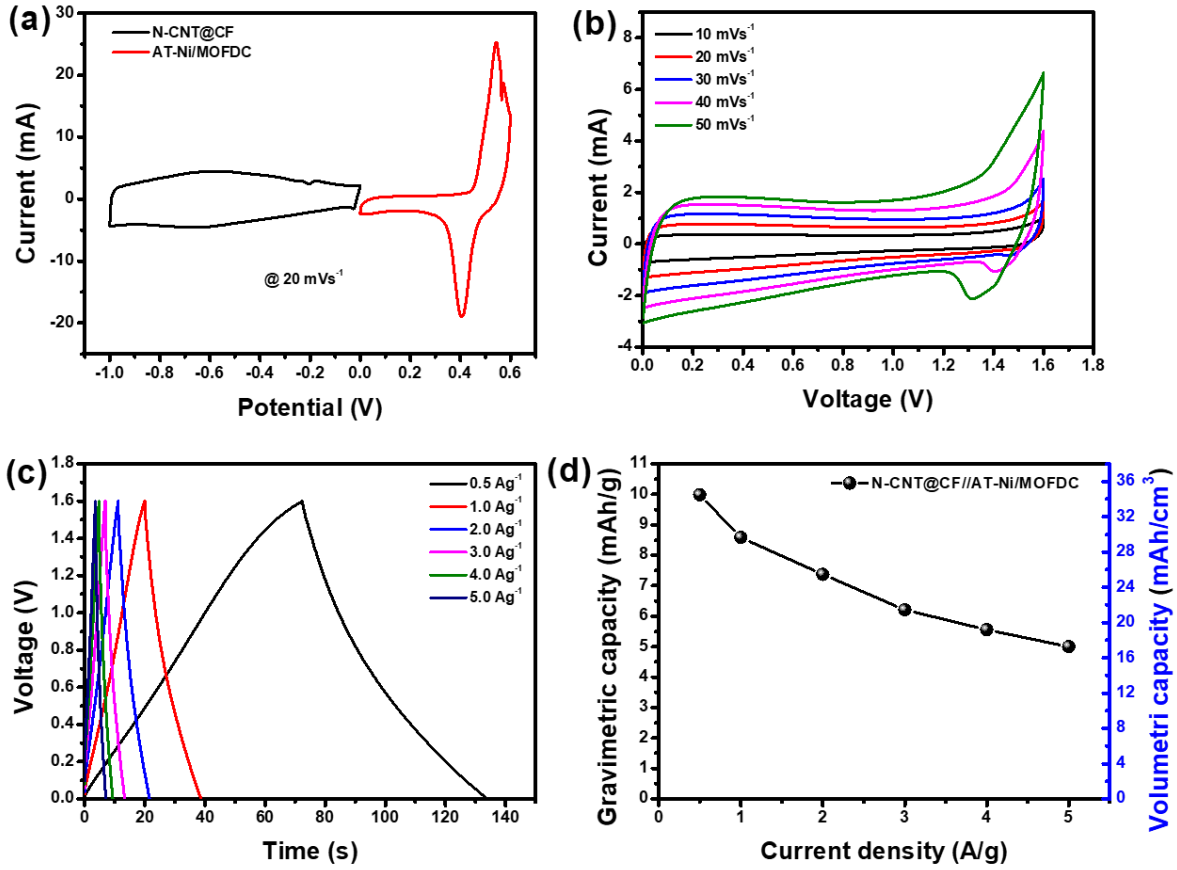


Figure 5.6: (a) CV curves of N-CNT@CF and AT-Ni/MOFDC, (b) CV curves of N-CNT@CF//AT-Ni/MOFDC at different scan rates, (c) typical GCD curves of N-CNT@CF//AT-Ni/MOFDC at different current densities and (d) capacity versus current density plot.

EIS can be used to comprehend interfacial electrochemistry and describe the cycling stability of materials. **Figure 5.7b** shows the Nyquist plots collected before and after 2,000 cycles. The EIS parameters before and after 2,000 cycles (modelled with the simple Randles electrical equivalent circuit, EEC, **Figure 5.7b inset**) comprises the (i) bulk resistance (R_s) due to the combined resistances arising from the current collectors, electrodes, electrolyte and separator, (ii) the charge-transfer resistance (R_{ct}) due to electron transport, (iii) interfacial resistance (R_{int}) due to IR drop and (iv) the CPE due to the inhomogeneous or irregular structure or morphology of the electrode surfaces, as previously explained. The modelled parameters are summarized in **Table 5.3.** Before and after cycling, the R_s and R_{ct} values were essentially the same,

indicating that the HSC's electrochemical efficiency was stable. Furthermore, the CPE "*a*" values remain constant at 0.62 (before and after the 2,000th cycle), indicating that the electrode materials retain their mixed pseudocapacitance mechanism. In general, the EIS data shows that the structure of the EEI layer, where electrochemistry takes place, does not change over time, confirming the satisfactory stability (capacity retention of 94 % after 2,000 cycles) shown in **Figure 5.7a**.

Table 5.3: EIS parameters for N-CNT@CF//AT-Ni/MOFDC hybrid device before and after the 2,000th cycle.

EIS parameters	**N-CNT@CF//AT-Ni/MOFDC device**	
	Before 2,000 cycles	**After 2,000 cycles**
R_s **/Ω**	9.73 ± 0.49	9.12 ± 0.49
R_{ct} **/Ω**	13.67 ± 1.22	13.73 ± 0.63
***CPE* /mF. s^(a-1)**	1.18 ± 0.95	1.27 ± 1.01
R_{int} **/Ω**	388.4 ± 206	386.5 ± 209.1
a	0.62	0.62
f_o **/Hz**	2.35	3.49
τ **/s**	0.43	0.29
Phase angle	-60^o	-60^o

Through analysing the knee frequency (f_o/Hz) before and after long-term cycling, changes in the EEI layer may be compared to the power density of the device [54]. The presence of a high f_o value indicates that the HSC has a high-power density. The HSC has a lower f_o value before cycling (around 2.35 Hz, τ, 0.43 s of response time) than after the 2,000th cycle (around 3.49 Hz, τ, 0.29 s response time). This small improvement in response times also confirms the stability of the electrode materials. The Bode plots (**Figure 5.7c**) show the phase angles of the

N-CNT@CF//AT-Ni/MOFDC HSC before (-61°) and after 2,000 cycles (-61°), confirming the diffusion processes.

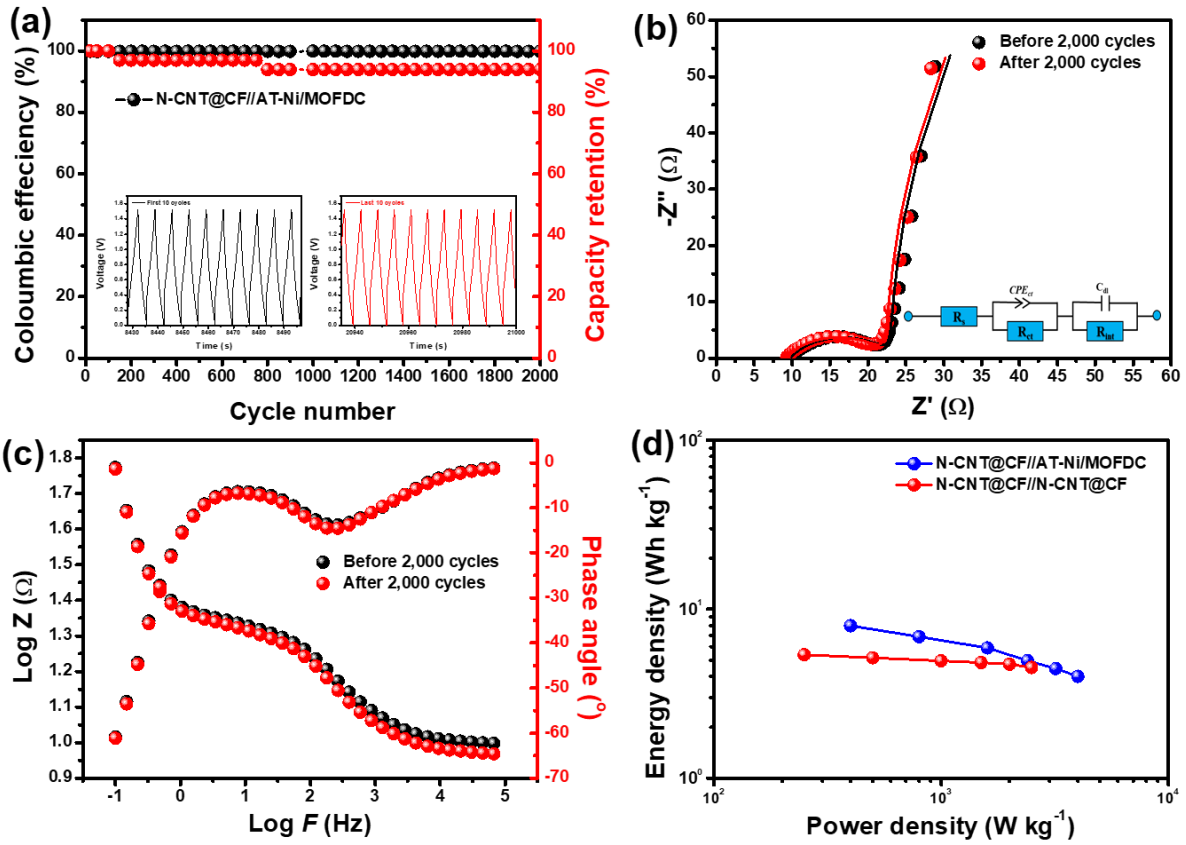


Figure 5.7: Electrochemical performance of the N-CNT@CF//AT-Ni/MOFDC hybrid device: (a) typical cycling performance at 5 A g^{-1}, (b) Nyquist plots obtained before and after 2,000 charge-discharge cycles, (c) Bode plots before and after 2,000 cycles of the N-CNT@CF//AT-Ni/MOFDC device and (d) comparative Ragone plot of this work with a symmetric N-CNT@CF//N-CNT@CF.

The specific energy vs. specific power density (Ragone plot) of the HSC device analysed in this Chapter is compared to the symmetric capacitor stated in Chapter four of this thesis. The N-CNT@CF//AT-Ni/MOFDC device exhibits a higher energy density (8 Wh kg^{-1}) and power density (400 W kg^{-1}). Furthermore, the high energy and power density are far higher than the symmetrical supercapacitor mentioned in Chapter 4, confirming the fundamental assumption that hybrid supercapacitors have a higher energy and power density than symmetric devices.

5.4 Summary

Microwave-assisted solvothermal synthesis was used to successfully synthesize Ni-MOF which was explored as a sacrificial template to prepare Ni/MOFDC composite and subsequently etched with acid, to yield the AT-Ni/MOFDC. In comparison to the untreated analogue (Ni/MOFDC), the AT-Ni/MOFDC exhibits superior physico-chemical and electrochemical properties. AT-Ni/MOFDC has better battery-type energy storage in a three-electrode configuration, with lower series resistance and higher specific capacity. Faradaic and non-Faradaic processes have been shown to control the energy-storage process of AT-Ni/MOFDC. At a current density of 0.5 A g^{-1}, the assembled N-CNT@CF//AT-Ni/MOFDC hybrid unit has a specific capacity of 10 mAh g^{-1}. In comparison to the symmetric device (N-CNT@CF/N-CNT@CF), the HSC device has a higher energy density (8 Wh kg^{-1}) and a power density (400 W kg^{-1}), as well as excellent cycling performance (94 % capacity retention after 2,000 cycles). This research opens up a new avenue for investigating the MOF sacrificial template for developing high-performance BTES electrode materials with mesoporous carbon support.

5.5 References

[1] Jiao, Y., Pei, J., Chen, D., Yan, C., Hu, Y., Zhang, Q. and Chen, G., 2017. Mixed-metallic MOF based electrode materials for high performance hybrid supercapacitors. *Journal of Materials Chemistry A*, **5**, pp.1094-1102.

[2] Naoi, K., Naoi, W., Aoyagi, S., Miyamoto, J.I. and Kamino, T., 2013. New generation "nanohybrid supercapacitor". *Accounts of Chemical Research*, **46**, pp.1075-1083.

[3] Simon, P. and Gogotsi, Y., 2010. Materials for electrochemical capacitors. *Nanoscience and Technology: A Collection of Reviews from Nature Journals*, pp.320-329.

[4] Mathis, T.S., Kurra, N., Wang, X., Pinto, D., Simon, P. and Gogotsi, Y., 2019. Energy storage data reporting in perspective—guidelines for interpreting the performance of electrochemical energy storage systems. *Advanced Energy Materials*, **9**, p.1902007.

[5] Sharma, P. and Bhatti, T.S., 2010. A review on electrochemical double-layer capacitors. *Energy Conversion and Management*, **51**, pp.2901-2912.

[6] Makgopa, K., Ejikeme, P.M., Jafta, C.J., Raju, K., Zeiger, M., Presser, V. and Ozoemena, K.I., 2015. A high-rate aqueous symmetric pseudocapacitor based on highly graphitized onion-like carbon/birnessite-type manganese oxide nanohybrids. *Journal of Materials Chemistry A*, **3**, pp.3480-3490.

[7] Rong, H., Chen, T., Shi, R., Zhang, Y. and Wang, Z., 2018. Hierarchical $NiCo_2O_4$@ $NiCo_2S_4$ nanocomposite on Ni foam as an electrode for hybrid supercapacitors. *ACS Omega*, **3**, pp.5634-5642.

[8] Makkar, P., Chandel, M., Patra, M.K. and Ghosh, N.N., 2019. A "one-pot" route for the synthesis of snowflake-like Dendritic CoNi alloy-reduced graphene oxide-

based multifunctional nanocomposites: An efficient magnetically separable versatile catalyst and electrode material for high-performance supercapacitors. *ACS Omega*, **4**, pp.20672-20689.

[9] Shinde, N.M., Shinde, P.V., Yun, J.M., Gunturu, K.C., Mane, R.S., O'Dwyer, C. and Kim, K.H., 2020. NiF_2 nanorod arrays for supercapattery applications. *ACS Omega*, **5**, pp.9768-9774.

[10] Wu, Z., Zhu, Y. and Ji, X., 2014. $NiCo_2O_4$-based materials for electrochemical supercapacitors. *Journal of Materials Chemistry A*, **2**, pp.14759-14772.

[11] Xiao, Y., Wei, W., Zhang, M., Jiao, S., Shi, Y. and Ding, S., 2019. Facile surface properties engineering of high-quality graphene: toward advanced Ni-MOF heterostructures for high-performance supercapacitor electrode. *ACS Applied Energy Materials*, **2**, pp.2169-2177.

[12] Kitagawa, S., 2014. Metal–organic frameworks (MOFs). *Chemical Society Reviews*, **43**, pp.5415-5418.

[13] Choi, K.M., Jeong, H.M., Park, J.H., Zhang, Y.B., Kang, J.K. and Yaghi, O.M., 2014. Supercapacitors of nanocrystalline metal–organic frameworks. *ACS Nano*, **8**, pp.7451-7457.

[14] Lin, X.M., Niu, J.L., Lin, J., Wei, L.M., Hu, L., Zhang, G. and Cai, Y.P., 2016. Lithium-ion-battery anode materials with improved capacity from a metal–organic framework. *Inorganic Chemistry*, **55**, pp.8244-8247.

[15] Chaikittisilp, W., Ariga, K. and Yamauchi, Y., 2013. A new family of carbon materials: synthesis of MOF-derived nanoporous carbons and their promising applications. *Journal of Materials Chemistry A*, **1**, pp.14-19.

[16] Salunkhe, R.R., Kamachi, Y., Torad, N.L., Hwang, S.M., Sun, Z., Dou, S.X., Kim, J.H. and Yamauchi, Y., 2014. Fabrication of symmetric supercapacitors based

on MOF-derived nanoporous carbons. *Journal of Materials Chemistry A*, **2**, pp.19848-19854.

[17] Jiao, Y., Qu, C., Zhao, B., Liang, Z., Chang, H., Kumar, S., Zou, R., Liu, M. and Walton, K.S., 2019. High-performance electrodes for a hybrid supercapacitor derived from a metal–organic framework/graphene composite. *ACS Applied Energy Materials*, **2**, pp.5029-5038.

[18] Ipadeola, A.K., Barik, R., Ray, S.C. and Ozoemena, K.I., 2019. Bimetallic Pd/SnO_2 nanoparticles on metal organic framework (MOF)-derived carbon as electrocatalysts for ethanol oxidation. *Electrocatalysis*, **10**, pp.366-380.

[19] Salunkhe, R.R., Tang, J., Kamachi, Y., Nakato, T., Kim, J.H. and Yamauchi, Y., 2015. Asymmetric supercapacitors using 3D nanoporous carbon and cobalt oxide electrodes synthesized from a single metal–organic framework. *ACS Nano*, **9**, pp.6288-6296.

[20] Zhang, H., Xiao, R., Song, M., Shen, D. and Liu, J., 2014. Hydrogen production from bio-oil by chemical looping reforming. *Journal of Thermal Analysis and Calorimetry*, **115**, pp.1921-1927.

[21] Rios-Ramos, A., Rivera-Maldonado, C., Garcia-Acosta, G.I., Lozano-Paulino, C.M., Fierro-Mercado, P.M., Fuentes-Cobas, L., and Roque-Malherbe, R.M., 2012. Synthesis, structure, adsorption space and magnetic properties of Ni-oxalate porous molecular magnet. *Journal of Materials Science and Engineering. A*, **2012**.

[22] Yang, J., Xiong, P., Zheng, C., Qiu, H. and Wei, M., 2014. Metal–organic frameworks: a new promising class of materials for a high performance supercapacitor electrode. *Journal of Materials Chemistry A*, **2**, pp.16640-16644.

[23] Wu, Z., Huang, X.L., Wang, Z.L., Xu, J.J., Wang, H.G. and Zhang, X.B., 2014. Electrostatic induced stretch growth of homogeneous β-Ni $(OH)_2$ on graphene with enhanced high-rate cycling for supercapacitors. *Scientific Reports*, **4**, pp.1-8.

[24] Cui, K. and Wardle, B.L., 2019. Breakdown of native oxide enables multifunctional, free-form carbon nanotube–metal hierarchical architectures. *ACS Applied Materials & Interfaces*, **11**, pp.35212-35220.

[25] Huang, Y., Yang, H., Xiong, T., Adekoya, D., Qiu, W., Wang, Z., Zhang, S. and Balogun, M.S., 2020. Adsorption energy engineering of nickel oxide hybrid nanosheets for high areal capacity flexible lithium-ion batteries. *Energy Storage Materials*, **25**, pp.41-51.

[26] Hou, L., Chen, Z., Zhao, Z., Sun, X., Zhang, J. and Yuan, C., 2018. Universal $FeCl_3$-activating strategy for green and scalable fabrication of sustainable biomass-derived hierarchical porous nitrogen-doped carbons for electrochemical supercapacitors. *ACS Applied Energy Materials*, **2**, pp.548-557.

[27] Liu, Y., Sun, Z., Sun, X., Lin, Y., Tan, K., Sun, J., Liang, L., Hou, L. and Yuan, C., 2020. Construction of Hierarchical Nanotubes Assembled from Ultrathin V_3S_4@C Nanosheets towards Alkali-Ion Batteries with Ion-Dependent Electrochemical Mechanisms. *Angewandte Chemie International Edition*, **59**, pp.2473-2482.

[28] Du, P., Dong, Y., Liu, C., Wei, W., Liu, D. and Liu, P., 2018. Fabrication of hierarchical porous nickel based metal-organic framework (Ni-MOF) constructed with nanosheets as novel pseudocapacitive material for asymmetric supercapacitor. *Journal of Colloid and Interface Science*, **518**, pp.57-68.

[29] Chen, Y., Ni, D., Yang, X., Liu, C., Yin, J. and Cai, K., 2018. Microwave-assisted synthesis of honeycomblike hierarchical spherical Zn-doped Ni-MOF as a high-performance battery-type supercapacitor electrode material. *Electrochimica Acta*, **278**, pp.114-123.

[30] Wei, T., Zhang, M., Wu, P., Tang, Y.J., Li, S.L., Shen, F.C., Wang, X.L., Zhou, X.P. and Lan, Y.Q., 2017. POM-based metal-organic framework/reduced graphene oxide nanocomposites with hybrid behavior of battery-supercapacitor for superior lithium storage. *Nano Energy*, **34**, pp.205-214.

[31] Venna, S.R., Jasinski, J.B. and Carreon, M.A., 2010. Structural evolution of zeolitic imidazolate framework-8. *Journal of the American Chemical Society*, **132**, pp.18030-18033.

[32] Zou, F., Chen, Y.M., Liu, K., Yu, Z., Liang, W., Bhaway, S.M., Gao, M. and Zhu, Y., 2016. Metal organic frameworks derived hierarchical hollow NiO/Ni/graphene composites for lithium and sodium storage. *ACS Nano*, **10**, pp.377-386.

[33] Jiang, H., Guo, Y., Wang, T., Zhu, P.L., Yu, S., Yu, Y., Fu, X.Z., Sun, R. and Wong, C.P., 2015. Electrochemical fabrication of $Ni(OH)_2$/Ni 3D porous composite films as integrated capacitive electrodes. *RSC Advances*, **5**, pp.12931-12936.

[34] Hengne, A.M., Samal, A.K., Enakonda, L.R., Harb, M., Gevers, L.E., Anjum, D.H., Hedhili, M.N., Saih, Y., Huang, K.W. and Basset, J.M., 2018. Ni–Sn-supported ZrO_2 catalysts modified by indium for selective CO_2 hydrogenation to methanol. *ACS Omega*, **3**, pp.3688-3701.

[35] Wu, J.B., Li, Z.G., Huang, X.H. and Lin, Y., 2013. Porous Co_3O_4/NiO core/shell nanowire array with enhanced catalytic activity for methanol electro-oxidation. *Journal of Power Sources*, **224**, pp.1-5.

[36] Wang, J., Zhao, Q., Hou, H., Wu, Y., Yu, W., Ji, X. and Shao, L., 2017. Nickel nanoparticles supported on nitrogen-doped honeycomb-like carbon frameworks for effective methanol oxidation. *RSC Advances*, **7**, pp.14152-14158.

[37] Li, A., Song, H., Bian, Z., Shi, L., Chen, X. and Zhou, J., 2017. ZnO nanosheet/squeezebox-like porous carbon composites synthesized by in situ pyrolysis of a mixed-ligand metal–organic framework. *Journal of Materials Chemistry A*, **5**, pp.5934-5942.

[38] Georgiev, D.G., Baird, R.J., Newaz, G., Auner, G., Witte, R. and Herfurth, H., 2004. An XPS study of laser-fabricated polyimide/titanium interfaces. *Applied Surface Science*, **236**, pp.71-76.

[39] Liu, M.C., Hu, Y.M., An, W.Y., Kong, L.B. and Kang, L., 2017. Liquid phase synthesis of dendritic nickel carbide alloy with high conductivity for advanced energy storage. *Journal of Energy Chemistry*, **26**, pp.750-756.

[40] Wong, K.M., Fang, Y., Devaux, A., Wen, L., Huang, J., De Cola, L. and Lei, Y., 2011. Assorted analytical and spectroscopic techniques for the optimization of the defect-related properties in size-controlled ZnO nanowires. *Nanoscale*, **3**, pp.4830-4839.

[41] Feng, S., Wang, T., Liu, B., Hu, C., Li, L., Zhao, Z.J. and Gong, J., 2020. Enriched surface oxygen vacancies of photoanodes by photoetching with enhanced charge separation. *Angewandte Chemie International Edition*, **59**, pp.2044-2048.

[42] Minato, T., Kawai, M. and Kim, Y., 2012. Creation of single oxygen vacancy on titanium dioxide surface. *Journal of Materials Research*, **27**, p.2237.

[43] Yang, Y., Chen, J., Liu, X., Qiu, M., Liu, L. and Gao, F., 2019. Oxygen vacancy-mediated WO_3 nanosheets by etched {200} facets and the efficient visible-light photocatalytic oxygen evolution. *New Journal of Chemistry*, **43**, pp.16391-16395.

[44] Hall, D.S., Bock, C. and MacDougall, B.R., 2014. An oxalate method for measuring the surface area of nickel electrodes. *Journal of The Electrochemical Society*, **161**, p.H787.

[45] Augustyn, V., Simon, P. and Dunn, B., 2014. Pseudocapacitive oxide materials for high-rate electrochemical energy storage. *Energy & Environmental Science*, **7**, pp.1597-1614.

[46] Wang, Y., Song, Y. and Xia, Y., 2016. Electrochemical capacitors: mechanism, materials, systems, characterization and applications. *Chemical Society Reviews*, **45**, pp.5925-5950.

[47] Shao, Y., El-Kady, M.F., Sun, J., Li, Y., Zhang, Q., Zhu, M., Wang, H., Dunn, B. and Kaner, R.B., 2018. Design and mechanisms of asymmetric supercapacitors. *Chemical Reviews*, **118**, pp.9233-9280.

[48] Alhebshi, N.A., Rakhi, R.B. and Alshareef, H.N., 2013. Conformal coating of $Ni(OH)_2$ nanoflakes on carbon fibers by chemical bath deposition for efficient supercapacitor electrodes. *Journal of Materials Chemistry A*, **1**, pp.14897-14903.

[49] Yan, Y., Gu, P., Zheng, S., Zheng, M., Pang, H. and Xue, H., 2016. Facile synthesis of an accordion-like Ni-MOF superstructure for high-performance flexible supercapacitors. *Journal of Materials Chemistry A*, **4**, pp.19078-19085.

[50] Adekunle, A.S. and Ozoemena, K.I., 2008. Electron transfer behaviour of single-walled carbon nanotubes electro-decorated with nickel and nickel oxide layers. *Electrochimica Acta*, **53**, pp.5774-5782.

[51] Pillay, J. and Ozoemena, K.I., 2009. Layer-by-layer self-assembled nanostructured phthalocyaninatoiron (II)/SWCNT-poly (m-aminobenzenesulfonic acid) hybrid system on gold surface: Electron transfer dynamics and amplification of H_2O_2 response. *Electrochimica Acta*, **54**, pp.5053-5059.

[52] Agboola, B.O. and Ozoemena, K.I., 2008. Self-assembly and heterogeneous electron transfer properties of metallo-octacarboxyphthalocyanine complexes on gold electrode. *Physical Chemistry Chemical Physics*, **10**, pp.2399-2408.

[53] Ozoemena, K.I., Mathebula, N.S., Pillay, J., Toschi, G. and Verschoor, J.A., 2010. Electron transfer dynamics across self-assembled N-(2-mercaptoethyl) octadecanamide/mycolic acid layers: impedimetric insights into the structural integrity and interaction with anti-mycolic acid antibodies. *Physical Chemistry Chemical Physics*, **12**, pp.345-357.

[54] Chidembo, A.T., Ozoemena, K.I., Agboola, B.O., Gupta, V., Wildgoose, G.G. and Compton, R.G., 2010. Nickel (II) tetra-aminophthalocyanine modified MWCNTs as potential nanocomposite materials for the development of supercapacitors. *Energy & Environmental Science*, **3**, pp.228-236.

[55] Lekitima, J.N., Ozoemena, K.I., Jafta, C.J., Kobayashi, N., Song, Y., Tong, D., Chen, S. and Oyama, M., 2013. High-performance aqueous asymmetric electrochemical capacitors based on graphene oxide/cobalt (ii)-tetrapyrazinoporphyrazine hybrids. *Journal of Materials Chemistry A*, **1**, pp.2821-2826.

[56] Druska, P., Strehblow, H.H. and Golledge, S., 1996. A surface analytical examination of passive layers on CuNi alloys: Part I. Alkaline solution. *Corrosion Science*, **38**, pp.835-851.

[57] Zhang, X., Zhang, Z., Sun, S., Sun, Q. and Liu, X., 2018. Hierarchical 3D $NiFe_2O_4$@ MnO_2 core–shell nanosheet arrays on Ni foam for high-performance asymmetric supercapacitors. *Dalton Transactions*, **47**, pp.2266-2273.

[58] Qu, C., Zhang, L., Meng, W., Liang, Z., Zhu, B., Dang, D., Dai, S., Zhao, B., Tabassum, H., Gao, S. and Zhang, H., 2018. MOF-derived α-NiS nanorods on graphene as an electrode for high-energy-density supercapacitors. *Journal of Materials Chemistry A*, **6**, pp.4003-4012.

CHAPTER 6

Nitrogen-doped carbon nanotube-carbon fibre networks as an anode material for nanowire-like sodium manganese oxide-based asymmetric supercapacitors

6.1 Introduction

In recent decades, the global economy and the global population, has grown rapidly, resulting in an increase in energy demand. As a result of increased global energy usage, global energy depletion could pose a threat to human society in the immediate future. Fossil fuels have been widely used as a primary source of energy in our modern world; nevertheless, fossil fuel supplies are small and will eventually be depleted [1]. As a result, research into creating clean, effective and sustainable alternative energy such as solar, tidal and wind has been launched worldwide to replace fossil fuels. Energy storage is a vital intermediate phase between these energy resources and diverse energy storage applications [1].

As one of the energy storage devices, supercapacitors (SCs) have emerged as the most promising candidate for energy storage devices due to their high-power density (>10 kW/kg) and remarkable cycle life (>10^5 cycles), which makes them promising candidates for energy storage devices such as portable devices, hybrid electric cars, optical telecommunication systems and other renewable energy storage applications [2-4]. However, the poor energy density of SCs relative to traditional batteries limits their commercialization.

Efforts to improve the energy density of SCs have been made in the last decade, including the use of various transition metal oxides. Since the energy density is proportional to the specific capacitance (F g^{-1}) and the square of the operating voltage, energy density can be improved in

two ways: electrode material characteristics and electrolyte selection. When it comes to electrolytes, supercapacitors in aqueous electrolytes could generate substantially more power density than those in non-aqueous electrolytes due to the higher ionic conductivity of aqueous electrolytes. Furthermore, aqueous electrolytes are environmentally friendly because they do not need an anhydrous environment for cell assembly [5]. Nevertheless, aqueous electrolytes are usually unstable over a voltage window of 1.23 V, however, asymmetric aqueous supercapacitors, which make use of the different potential windows of two electrodes and the high oxygen and/or hydrogen over-potentials of the electrodes, could widen the maximum operating voltage of aqueous electrolytes. Asymmetric aqueous supercapacitors, such as activated carbon MnO_2@C-BD//NPC [6], rGO//$Na_{0.21}MnO_2$ [7], AC//$NaMnO_2$ [8], have been explored.

Activated carbons and transition metal oxides such as RuO_2 and MnO_2 have commonly been used as anode and cathode materials, with most transition metal oxides and conducting polymers exhibiting pseudocapacitance. Lithium-ion hybrid electrochemical supercapacitors (LICs), on the other hand, have recently been the focus of research [9]. However, the intercalation or de-intercalation of Li^+ ions in Li-ion batteries (LIBs) results in high energy density electrodes, but with low power density, making LIBs unsuitable for high-power applications [10]. LIC is an alternative device to increase the power density which shows higher power density than LIBs and higher energy density than SCs. However, due to the limited earth abundance and high cost of lithium, sustainable resources should be prioritized. Therefore, since sodium is abundant and has lower costs than lithium, sodium-ion (Na-ion) batteries were developed as an alternative [11]. Nevertheless, researchers are currently working on Na-ion hybrid supercapacitors (NIC), however, it should be noted that the field is still in its infancy. As far as our knowledge is concerned, the only materials found for NIC are V_2O_5/CNT, $NiCo_2O_4$, $Na_2Ti_3O_7$@CNT, Na-TNT and $NaMnO_2$ polymorphs [12-17].

Under high charge/discharge rates, electrochemical active materials should have high reversible capacitance, excellent cycle stability, structural flexibility and fast cation diffusion [7]. Manganese dominates energy storage devices as a flexible transition metal with several stable oxidation states (Mn^{2+}, Mn^{3+}, Mn^{4+}) as well as diverse crystal structures and morphology [18]. Manganese dioxide (MnO_2) can be used alone or in conjunction with other transition metals as a cathode material for batteries and SCs. For example, Kim *et al*. [19], recently reported novel composite layered−tunnel $Na_{0.5}Mn_{0.5}Co_{0.48}Mg_{0.02}O_2$ cathode material. In this study, the NIC exhibited a maximum energy density of 35 Wh kg^{-1} and good stability retaining 72% of its initial energy density after 3000 cycles. In another study, Clément and co-workers presented an in-depth investigation of the effect of Mg doping on the electrochemical performance and structural stability of $Na_{2/3}MnO_2$ with a P2 layer stacking by comparing three compositions: $Na_{2/3}Mn_{1-y}Mg_yO_2$ (y = 0.0, 0.05, 0.1). In this study, it was shown that Mg substitution leads to smoother electrochemistry, with fewer distinct electrochemical processes, improved rate performance and better capacity retention [20]. Here, we report a simple hydrothermal route to synthesize the $Na_{0.44}MnO_2$ (NMO) for Na-ion asymmetric capacitor in different aqueous electrolytes (1M Na_2SO_4, 3M NaOH and 3M KOH). The motivation of this study inferred from the pioneering work done by Li and co-workers on aqueous electrolyte battery demonstrating reversible insertion/desertion of Li/Na in metal oxides [21]. NMO is regarded as one of the promising cathode materials owing to its high capacity and good cycle life. Moreover, it can also be used in both aqueous and non-aqueous systems, with aqueous electrolyte systems offering benefits in terms of safety, environmental friendliness and cost. Since ion-size compatibility with pore-size, charge transfer resistance and electrolyte ionic mobility are major driving parameters for better performance, a thorough understanding of electrode/electrolyte interaction and charge storage kinetics is needed.

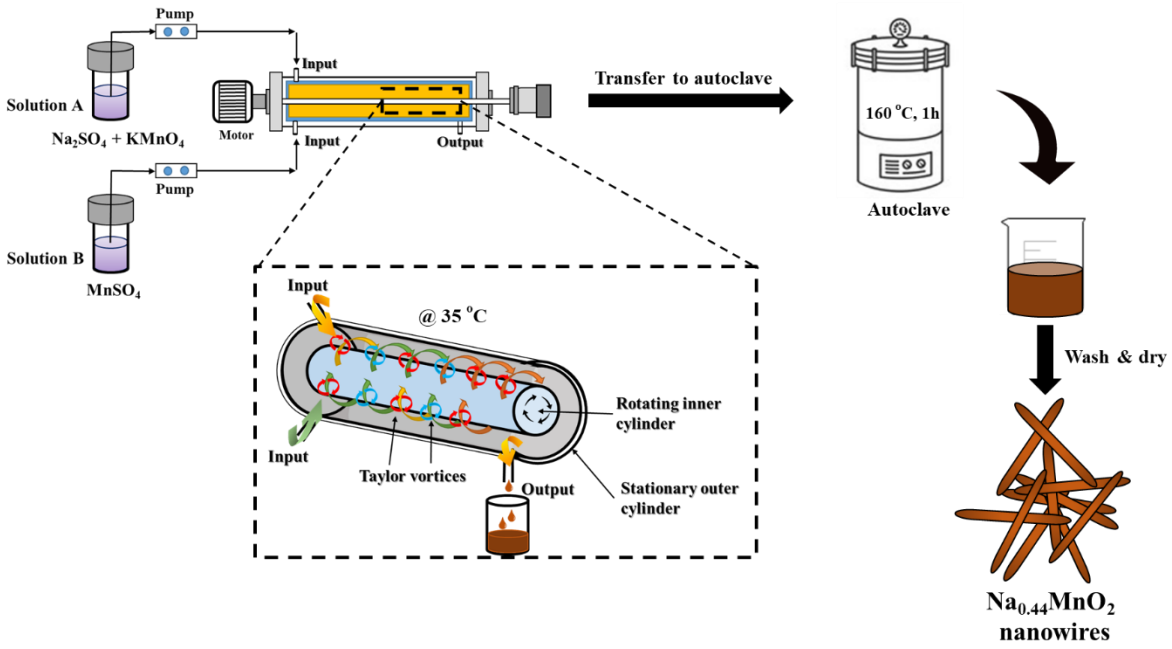
6.2 Experimental section

6.2.1 Materials

Potassium permanganate ($KMnO_4$, ≥ 99.5 %), sodium sulphate (Na_2SO_4, ≥ 99 %) and manganese sulfate ($MnSO_4 \cdot H_2O$, ≥ 99 %) were purchased from Sigma Aldrich (South Africa) and used as received.

6.2.2 Preparation of $Na_{0.44}MnO_2$

The two-step synthetic techniques: Couette-Taylor flow reactor and hydrothermal method were used to synthesize the sodium manganese oxide material [2]. The stoichiometric ratios of $KMnO_4$, Na_2SO_4 and $MnSO_4$ were first calculated. Typically, 0.1054 g of $KMnO_4$ was dissolved in ultrapure water (30 mL), followed by the addition of Na_2SO_4 to the above solution A. The Na_2SO_4 and $KMnO_4$ mole concentration ratio was 15:1. Subsequently, 0.1690 g of $MnSO_4$ was dissolved in distilled water (20 mL) to form solution B. Solutions A and B were then fed into the Laminar Continuous Taylor Flow Reactor (LCTR). In the LCTR, the two solutions were subjected to Taylor-Couette flow, which allows for vigorous homogeneous micro and macro mixing at 35 °C, resulting in a faster reaction, dense and uniform product particle. The resultant dark brown solution was then poured into a 60 mL Teflon-lined autoclave and kept for 1 hour at 160 °C. After the autoclave had naturally cooled to room temperature, the product was filtered out, washed five times with deionized water/ethanol and dried at 80 °C for 12 hours (see **Scheme 6.1**).



Scheme 6.1: Schematic illustrations of the synthesis of the $Na_{0.44}MnO_2$.

6.2.3 Characterization

The materials were thoroughly characterized using powder X-ray diffraction (XRD, BRUKER D2 diffractometer equipped with Cu Kα radiation (λ = 1.54178 Å)), X-ray photoelectron spectroscopy (Thermo ESCAlab 250Xi XPS equipped with an Al Kα radiation source (1486.7eV), transmission electron microscopy (FEI Tecnai T12 Sprint TEM), scanning electron microscopy (JEOL JSM-7500F) field emission scanning electron microscope (FE-SEM) equipped with energy dispersive X-ray spectroscopy (EDX)) and Brunauer-Emmett-Teller (BET, Micrometric Tristar 3000) to determine the crystalline structure, chemical environments, morphological properties, surface area and pore sizes, respectively. The bulk density (ρ, g cm^{-3}) of the active material in the electrode was calculated by equation 6.1 [22]:

$$\rho = \frac{1}{V_t + (\frac{1}{\rho_T})} \quad (6.1)$$

where, V_t is the total pore volume (cm^3 g^{-1}) and ρ_T is the true density of the materials.

6.2.4 Electrochemical measurements

The electrochemical behaviour of the samples was carried out in a Biologic-SP300 workstation in a two-electrode and three-electrode setup using 1 M Na_2SO_4, 3M NaOH and 3M KOH as electrolytes. To make a homogeneous slurry in N-methyl-pyrrolidinone (NMP), the active materials were mixed with acetylene black and polytetrafluoroethylene (PTFE) binder in a 90:5:5 ratio, which was taken and drop-casted onto a carbon paper current collector. The fabricated electrodes dried for 12 h at 80 °C in a vacuum oven. EIS measurements were carried out at frequencies ranging from 100 kHz to 0.1 Hz. In a three-electrode and two-electrode configuration, the specific gravimetric and volumetric capacitance (C_s, F g^{-1}, C_{Vol}) were calculated under the CV and GCD curve using equation 6.3 & 6.8 and 6.4 & 6.9. Specific energy (E, Wh kg^{-1}) and specific power (P, W kg^{-1}) were measured with GCD curves shown in equation 6.10 and 6.11, respectively, under the two-electrode setup (full-cell).

6.3 Results and discussion

6.3.1 Physical characterization

The morphology of $Na_{0.44}MnO_2$ was characterized by scanning electron microscopy coupled with energy dispersive spectrometric (SEM-EDS) and transmission electron microscopy (TEM). As shown in the SEM image in **Figure 6.1a** and the TEM image in **Figure 6.1b**, the sample exhibits a relatively uniform nanowire structure with an average diameter of about 100 nm and a length of few micrometres (see bar graph in **Supporting Information, Figure S1 in Appendix C**). It can be seen from EDS mapping in **Figure 6.1c** that the sample contains four major elements of Na, Mn, and O and the distribution of these elements are uniform in the sample. Also, the EDS spectra in **Figure 6.1d** shows some traces of C, Si, S and K, which are from the coating, starting materials and quartz boat.

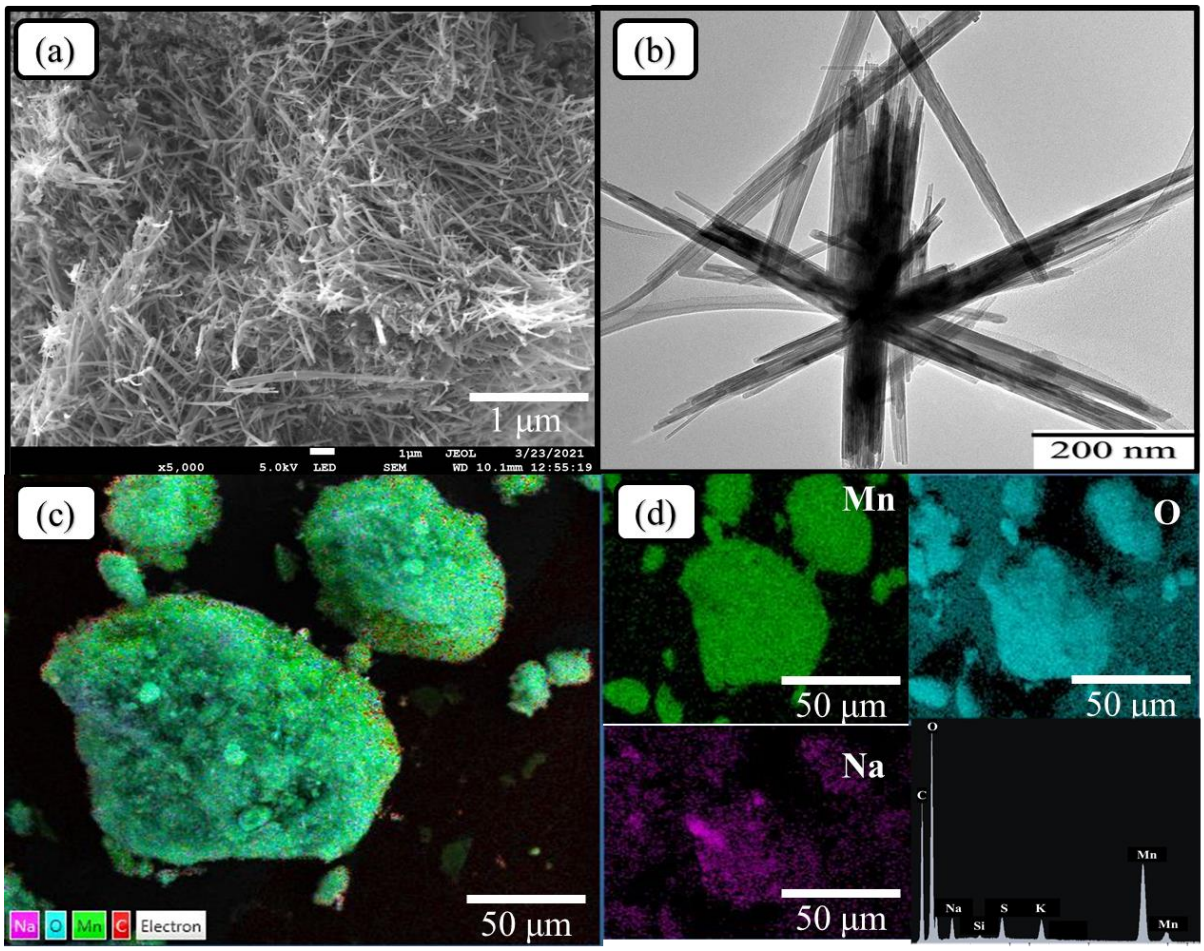


Figure 6.1: (a) SEM image of $Na_{0.44}MnO_2$, (b) TEM image of $Na_{0.44}MnO_2$, (c) EDS mapping images of $Na_{0.44}MnO_2$ and (d) elemental mapping of Mn, O and Na together with the corresponding EDS spectrum.

Figure 6.2a shows the XRD pattern of the $Na_{0.44}MnO_2$ nanowires. All of the reflection peaks in the pattern are similar to the orthorhombic $Na_{0.44}MnO_2$ phase (*Pbam*, JCPDS no 27-0750) [17, 23, 24]. The ratio of Na/Mn in the raw materials has been shown to have a significant impact on the phase purity of $Na_{0.44}MnO_2$. There were traces of MnO_2 and Na_2SO_4 impurities in the diffraction pattern, suggesting that some portions of the precursors did not react completely during the synthetic process.

X-ray photoelectron spectroscopy (XPS) was used to check the surface compositions and oxidation states of $Na_{0.44}MnO_2$ nanowires and the results are shown in **Figure 6.2(b-f)**. The XPS spectra show the existence of Na, Mn, O and C atoms. The Na 1s had a peak at about

1070 eV. The Mn 2p peak split spin-orbit components which were Mn $2p_{3/2}$ at about 641 eV and Mn $2p_{1/2}$ at about 653 eV, respectively. Both the Mn $2p_{3/2}$ and Mn $2p_{1/2}$ peaks were deconvoluted into two peaks corresponding to the co-existence of Mn^{4+} and Mn^{3+} valence state at 644.1 and 641.3 eV, respectively, in good agreement with previous reports [25]. In addition, the peak corresponding to the Mn^{3+} state has a higher peak intensity and a larger area under the curve than the peak corresponding to the Mn^{4+} state, suggesting $Na_{0.44}MnO_2$ would have a higher Na^+ ion diffusion coefficient and electronic conductivity, as well as enhanced electrochemical performance [26]. The presence of oxygen species in $Na_{0.44}MnO_2$ is indicated by the feature peaks of O 1s (**Figure 6.2e**) located at 529.3, 530.8, 531.8 and 533.1 eV [26]. The specific surface area, pore size and pore volume were determined using N_2 absorption–desorption measurements (**Table 6.1**). The surface areas and pore volume of the as-prepared $Na_{0.44}MnO_2$ nanowires were found to 27.63 $m^2\ g^{-1}$ and 0.16 $cm^3\ g^{-1}$, respectively.

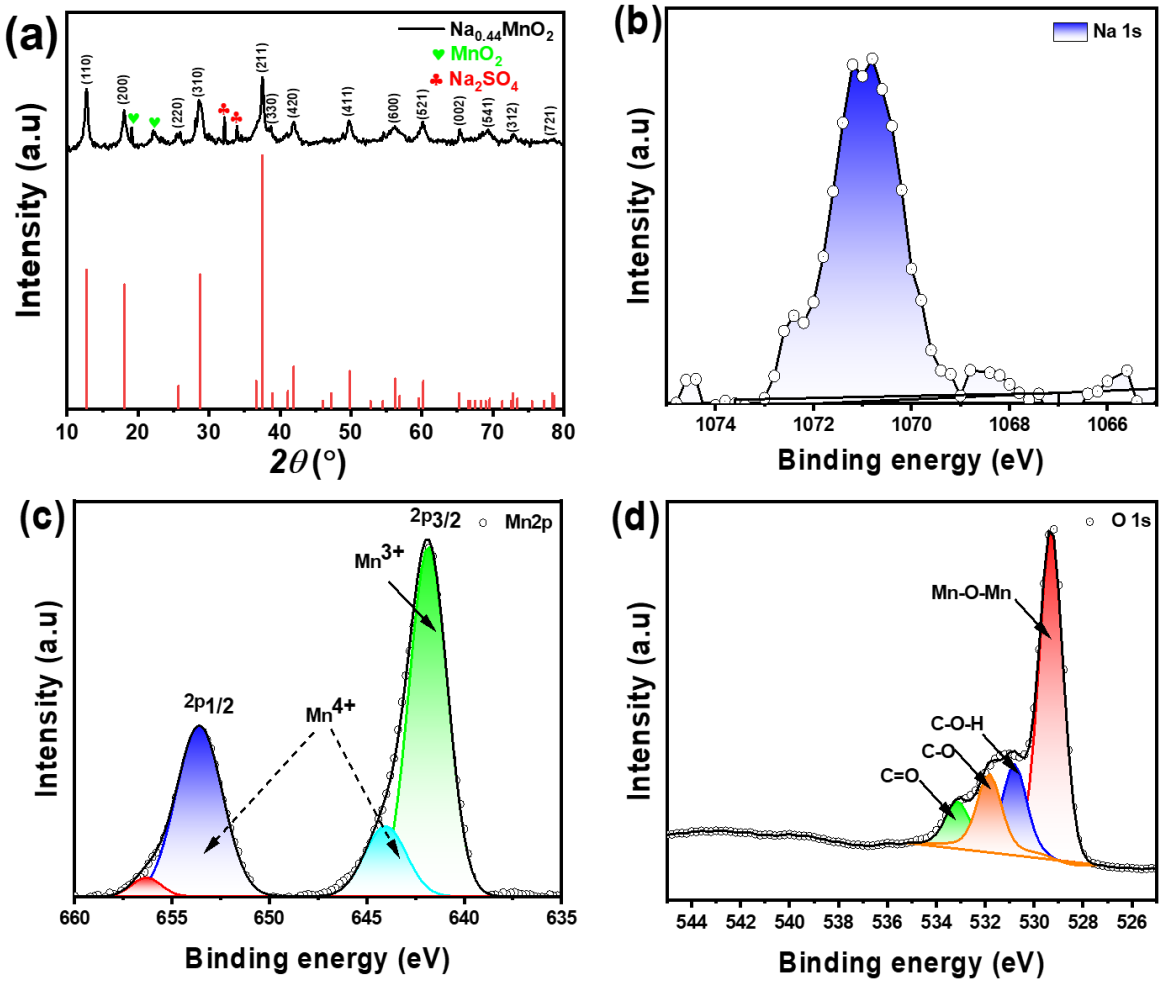


Figure 6.2: (a) X-ray diffraction (XRD) pattern of $Na_{0.44}MnO_2$, (b) X-ray photoelectron spectroscopy (XPS) analysis, (b) narrow scan of Na, (c) Mn 2p and (d) O 1s.

Table 6.1: Brunauer-Emmett-Teller (BET) analysis of the as-prepared $Na_{0.44}MnO_2$.

Samples	Pore size /nm	Pore volume /cm^3 g^{-1}	S_{BET} / m^2 g^{-1}
$Na_{0.44}MnO_2$	22.4493	0.145889	27.6327

6.3.2 Electrochemical measurements

6.3.2.1 Three-electrode system

The electrochemical performance of $Na_{0.44}MnO_2$ as an electrode for SCs was investigated by a three-electrode system in 1M Na_2SO_4, 3M NaOH and 3M KOH electrolytes. **Figure 6.3(a-c)**

illustrates the respective cyclic voltammograms at 50 to 5 mV s^{-1} scan rates. The voltage ranges are 0.0-1.0 V, 0.0-0.6 V and -0.4-0.6 V, respectively. This shows that the potential windows are different for all the electrolytes studied. It is seen from **Figure 6.3(a-c)** that the current response increases with the scan rate. As shown in **Figure 6.3a**, the CV curves of $Na_{0.44}MnO_2$ in 1M Na_2SO_4 electrolyte have a nearly rectangular shape at various scan rates ranging from 5 mV s^{-1} to 50 mV s^{-1}, suggesting good capacitive behaviour. This infers that the charge storage was primarily due to the EDLC type, which involves the adsorption-desorption of ions at the electrode/electrolyte interface. In 3M NaOH electrolyte, however, the behaviour of $Na_{0.44}MnO_2$ deviates slightly from the ideal rectangular shape, with two small redox couples, indicating intercalation pseudocapacitance properties of the $Na_{0.44}MnO_2$ cathode material [27]. Furthermore, in 3M KOH, similar intercalation pseudocapacitance properties of the $Na_{0.44}MnO_2$ were observed. A similar type of redox peaks has been reported for MnO_2 [28, 29] and Na_xMnO_2 [27]. The possible charge storage mechanism of $Na_{0.44}MnO_2$ in 3 M NaOH and 3 M KOH electrolyte is shown in equation 6.2.

$$Na_XMnO_2 + xM^+ + xe^- \leftrightarrow NaMnO_2 \quad (6.2)$$

$M^+ = Na^+$ or K^+

where x represents the mole fraction of inserted sodium or potassium ions. The gravimetric specific capacitance (C_s in F g^{-1}) and volumetric specific capacitance (C_s in F cm^{-3}) of the electrode/electrolyte systems are calculated from the CV curve using these equations 6.3 and 6.4:

$$C_s = \frac{\oint IdV}{2mS} \ (F\ g^{-1}) \quad (6.3)$$

$$C_{Vol} = C_s \times \rho \ (F\ cm^{-3}) \quad (6.4)$$

where C_S is the gravimetric capacitance of the electrode, C_{Vol} is the volumetric capacitance of the electrode, $\oint I.dV$ (A·V) represent the voltammetric charge, which is an area under the curve of the CV. S (V s^{-1}) represent the scan rate, m (g) represents the active mass of the electrodes and ρ is the density of the electrode.

At 5 mV s^{-1}, the maximum capacitance measured was (99 F g^{-1}; 608 F cm^{-3}) for the $Na_{0.44}MnO_2$/KOH system, followed by both $Na_{0.44}MnO_2$/Na_2SO_4 and $Na_{0.44}MnO_2$/NaOH systems with a comparable capacitance of (~26 F g^{-1}; ~162 F cm^{-3}). The difference in capacitance values in different systems can be attributed to the difference in ion permeability into the active matrix [30]. The different rate of accessibility of ions into the matrix depends on the ionic radius, ionic mobility and molar ionic conductivity [31]. Though the size of K^+ ions is larger compared to Na^+ ions, the specific gravimetric and volumetric capacitance are found to be higher in KOH than that in both Na_2SO_4 and NaOH. This can be attributed to the higher conductivity of 3M KOH. According to the report by Senthilkumar *et al*. [32], the ionic solvation radius of OH^-, NO^{-3}, Cl^- and SO_2^{-4} in water are 3.00, 3.35, 3.32, and 3.79 Å, respectively. As a result, in terms of ionic conductivity and ionic diffusion rate, the aqueous electrolyte based on NaOH and KOH has distinct advantages, hence, the high capacitance was achieved for the $Na_{0.44}MnO_2$/KOH system. The lower capacitance in the $Na_{0.44}MnO_2$/Na_2SO_4 system, on the other hand, is due to the higher radius of hydrated Na^+ ions (3.59 Å), neutral pH, lower ionic mobility and low molar ionic conductivity of Na^+ ions compared to K^+ ions. With an increase in scan rate, the specific capacitance values for all systems are found to decrease (**Figure 6.3d**). This is because, at higher scan rates, ions have less access to the interior surface of the material.

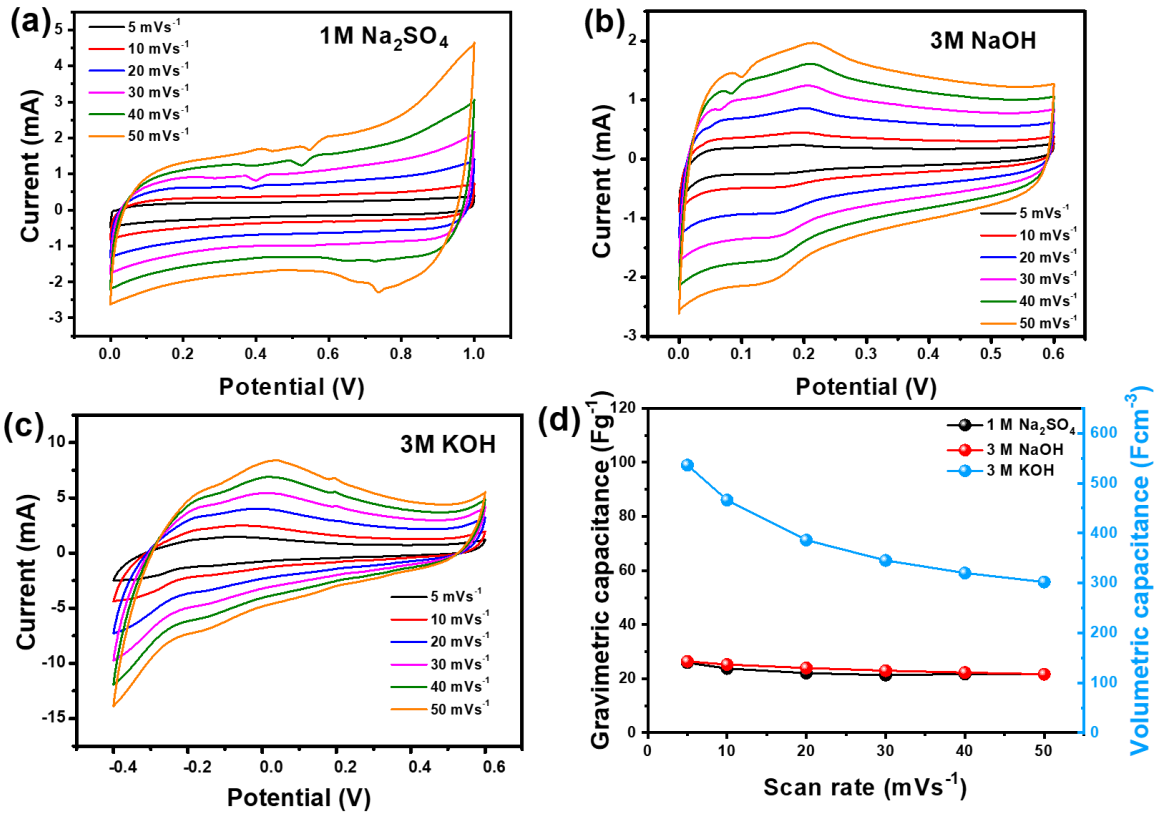


Figure 6.3: The CV curves of $Na_{0.44}MnO_2$ in (a) 1M Na_2SO_4, (b) 3M NaOH and (c) 3M KOH medium at scan rate ranging from 5 to 50 mV s^{-1}, (d) Specific gravimetric and volumetric capacitance versus scan rate of $Na_{0.44}MnO_2$ under different aqueous electrolytes**.**

Figure 6.5(a-c) shows the charge-discharge curves for various $Na_{0.44}MnO_2$/aqueous electrolyte systems at various current densities. As it can be seen in **Figure 6.5a**, the linear and symmetric charge-discharge profile without an obvious potential drop is observed for $Na_{0.44}MnO_2/Na_2SO_4$ system, again verifying the EDLC character. Interestingly, the GCD plots at various current densities of $Na_{0.44}MnO_2$ in both NaOH and KOH electrolytes in **Figure 6.5b** and **Figure 6.5c** all show distorted triangular-shaped patterns with obvious deviation from the linear GCD curves, further confirming intercalation pseudocapacitance. The calculated gravimetric and volumetric capacities of the three systems are shown in **Figure 6.5d**. The calculated gravimetric specific capacitances are 23.4, 41.5 and 108.4 F g^{-1} corresponding to specific volumetric capacities of 143.7, 254.6 and 665.6 F cm^{-3}, for 1M Na_2SO_4, 3M NaOH, and 3M KOH respectively, at 0.5 A g^{-1}. The difference in specific capacitance of $Na_{0.44}MnO_2$ at

different electrolytes is due to the different ionic sizes, electrolyte conductivity and different charge storage mechanism. This can be demonstrated based on the pH and ionic solvation radius of the electrolytes. Based on the Pourbaix diagram, Mn^{2+} ions are only involved in redox reactions in alkali aqueous (3M NaOH and 3M KOH) electrolytes and not in neutral aqueous electrolytes such as Na_2SO_4 and $NaNO_3$ [32]. Thus, the observed Faradaic electrochemical response of $Na_{0.44}MnO_2$ in both NaOH and KOH electrolytes are mainly due to electron transfer between Mn^{3+} and Mn^{2+} ions.

On the other hand, OH^- (3.00 Å) ions have a small ionic solvation radius relative to SO_2^{-4} (3.79 Å) ions. As a result, the OH^- ions can quickly diffuse through the electrode nanopores, resulting in a greater number of ions lodged on the surface and hence, a higher specific capacitance [33, 34]. In other words, ions with a smaller ionic radius have higher ionic conductivity in aqueous solutions, therefore, increasing the number of ions that can interact with the active electrode material. As a result, more active sites are created in the electrode material. Also, the overall, electrochemical efficiency has been enhanced by lowering the ionic solvation radius of electrolytes anions and increasing the pH of the electrolytes.

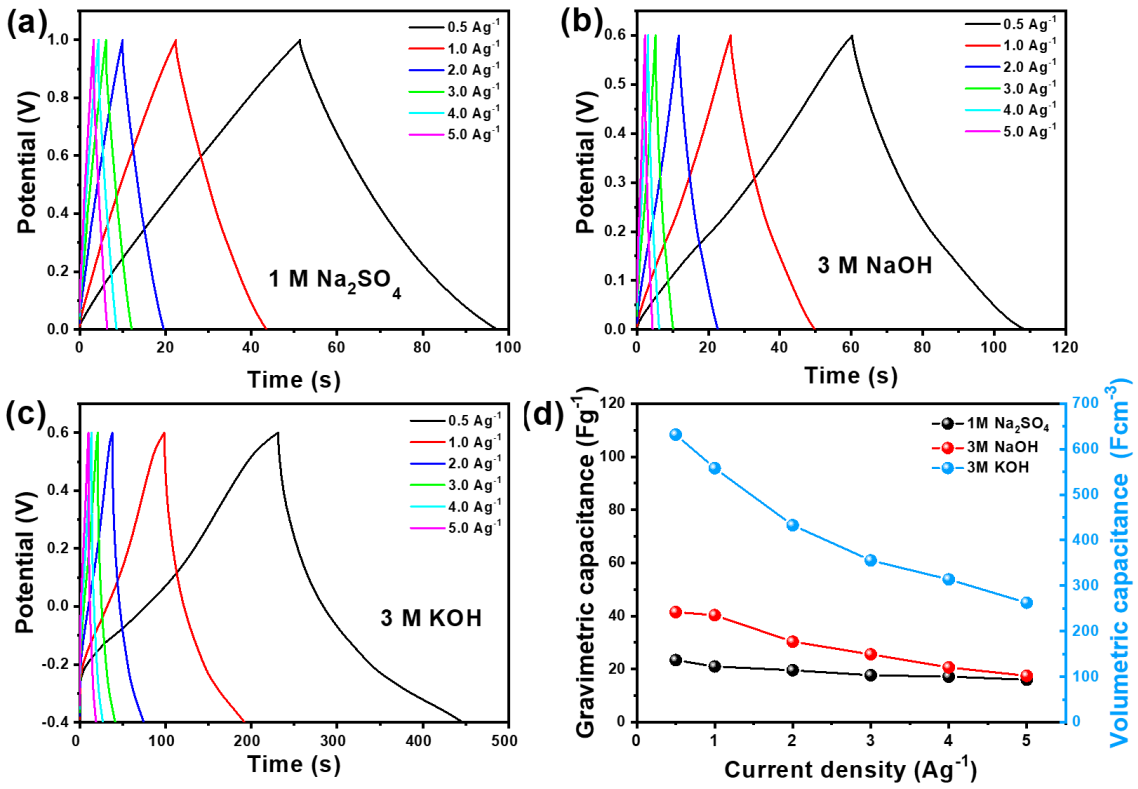


Figure 6.4: The GCD curves of $Na_{0.44}MnO_2$ in (a) 1M Na_2SO_4, (b) 3M NaOH and (c) 3M KOH medium at current densities ranging from 0.5 to 5 A g^{-1}, (d) Specific gravimetric and volumetric capacitance versus scan rate of $Na_{0.44}MnO_2$ under different aqueous electrolytes.

EIS is a useful instrument for determining the electrochemical properties of various materials. **Figure 6.5a** shows the EIS measurements of the $Na_{0.44}MnO_2$ in three different electrolytes. The Nyquist plot is modelled using a combined RC/Randles circuit that includes the solution/electrolyte (R_s), the resistance of the electrode surface (R_{cs}) caused by the resistance of the SEI to transport of the Na^+ and K^+, interfacial resistance (R_{int}) due to IR drop, charge-transfer resistance (R_{ct}) due to electron transport, double-layer capacitance (C_{dl}), constant phase element (CPE_{ct}) due to electrode surface inhomogeneity and the double-layer capacitance (C_{dl}). The EIS data were fitted using the equivalent circuit as shown in the insert in **Figure 6.5a** and the results are shown in **Table 6.1**, where χ^2 is the deviation indicator. The impedance of the CPE (Z_{CPE}) is a power-law relationship, equation 6.5 [35-37]:

$$Z_{CPE} = [Q\ (j\omega)^{a}]^{-1} \quad (6.5)$$

where Q is the frequency-independent constant associated with the electrode/electrolyte interface, $j = \sqrt{-1}$, ω represents the radial frequency, the exponent a is the slope of the log Z *vs.* log F, the values of which are $-1 \leq a \leq 1$: When $a = 0$, the CPE is a pure resistor; $a = 1$, the CPE is a pure capacitor; $a = -1$ the CPE is an inductor; while $a = 0.5$ the CPE is equivalent to the Warburg impedance (Z_w). The Nyquist plots for $Na_{0.44}MnO_2$ in Na_2SO_4 and NaOH electrolytes show a larger semicircle diameter, suggesting decreased faradic reactions at the active material's surface. Furthermore, the semicircle of $Na_{0.44}MnO_2$ in KOH is smaller, suggesting low charge transfer resistance.

According to **Table 6.2**, the series resistance ($R_s + R_{cs} + R_{int} + R_{ct}$) values of the $Na_{0.44}MnO_2$ in 1M Na_2SO_4, 3M NaOH and 3M KOH are 661, 629 and 216, respectively. Based on these findings, it can be shown that the $Na_{0.44}MnO_2$ in KOH has a lower series resistance value, indicating that it has better conductivity. Furthermore, $Na_{0.44}MnO_2$ in Na_2SO_4 and NaOH electrolytes has a more vertical line in the low-frequency region than in KOH electrolyte, indicating strong capacitive behaviour with little diffusion restriction of $Na_{0.44}MnO_2$ charge storage. In the high-frequency region, the diameter of the quasi-semicircle reflects the charge transfer resistance at the electrode/electrolyte interface [38]. As shown from the insert of **Figure 6.5a** that the R_{ct} of $Na_{0.44}MnO_2$ in KOH (1.60 Ω) is smaller than that of $Na_{0.44}MnO_2$ in Na_2SO_4 (7.65 Ω) and NaOH (5.43 Ω), owing to the high conductivity and fast ion diffusion of KOH electrolyte ions. **Figure 6.5b-d** shows the Bode plot of –phase angle *vs* log (*f*/Hz) for the three electrolytes. $Na_{0.44}MnO_2$ phase angles in Na_2SO_4 and NaOH electrolytes approached –80°, confirming capacitive behaviour, while $Na_{0.44}MnO_2$ phase angles in KOH approached –50°, confirming pseudocapacitance. Furthermore, the obtained "*a*" values (**Table 6.2**) are less than 1.0 for an ideal capacitor, suggesting a mixture of EDLC and pseudocapacitive behaviour.

Table 6.2: EIS fitting results of $Na_{0.44}MnO_2$ in three electrolytes.

Electrolytes	1M Na_2SO_4	3M NaOH	3M KOH
R_s (Ω)	2.63 ± 0.67	1.78 ± 2.68	0.08 ± 0.41
R_{cs} (Ω)	2.95 ± 9.21	3.14 ± 8.56	202.5 ± 98.96
R_{ct} (Ω)	7.65 ± 7.47	5.43 ± 7.18	1.60 ± 1.92
R_{int} (Ω)	648.7 ± 391.7	618.2 ± 628.3	11.53 ± 44.37
***CPE_{sc}* (F. s^(a-1))**	1.68 ± 0.03	0.35 ± 0.99	0.02 ± 0.03
***CPE_{ct}* (F. s^(a-1))**	0.01 ± 0.04	0.02 ± 0.06	88.14 ± 1.56
C_{dl} (F)	0.02 ± 1.31	0.02 ± 3.41	0.02 ± 0.09
a	0.80	0.64	0.60
χ^2	0.0035	0.029	1.05
Phase angle	-75^o	-75^o	-48^o

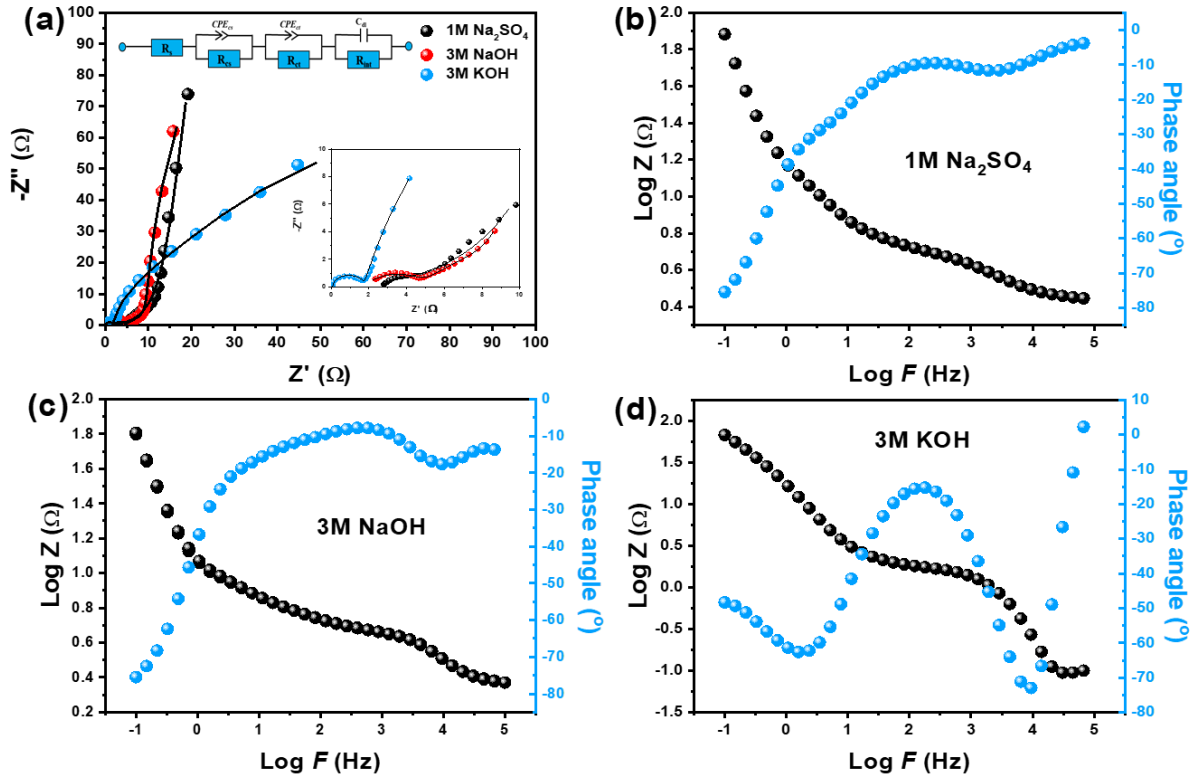


Figure 6.5: Presents (a) Nyquist plots and (b-d) Bode plots of $Na_{0.44}MnO_2$ in 1M Na_2SO_4, 3M NaOH and 3M KOH. The inset of (a) shows the magnified high-frequency region of Nyquist plots and the electrical circuit used in the fitting of the impedance data.

The charge storage mechanism was also determined using Trasatti and Dunn differentiation techniques as described in section 2.5 in Chapter 2. As shown in **Figure 6.6b, d & f** the log *I* *vs* log *v* plots show that the b values are greater than 0.5 at different potentials (i.e., 0.88, 1.03, and 1.18 for Na_2SO_4, 0.92, 0.96 and 1.14 for NaOH and 0.79, 0.85 and 0.74 for KOH electrolyte) indicating that $Na_{0.44}MnO_2$ in all electrolytes exhibit mixed Faradaic-capacitive mechanism. In addition, at a scan rate of 20 mV s^{-1}, typical voltage profiles for capacitive current with the total current is shown in (**Figure 6.6a, c and e**). While comparing the percentage contributions of Faradaic and non-Faradaic processes (see **supporting information Figure S3 (a-c) in Appendix C**), it is important to see that the EDLC storage mechanism (non-Faradaic process/surface-controlled) dominates the from the lowest scan rate (5 mV s^{-1}) for $Na_{0.44}MnO_2$ in both Na_2SO_4 and NaOH electrolytes. However, at 5 mV s^{-1} scan rate for

$Na_{0.44}MnO_2$ in KOH electrolyte, pseudocapacitive-type storage (Faradaic process/diffusion-controlled) dominated. These results are in good agreement with the CV, GCD and EIS data.

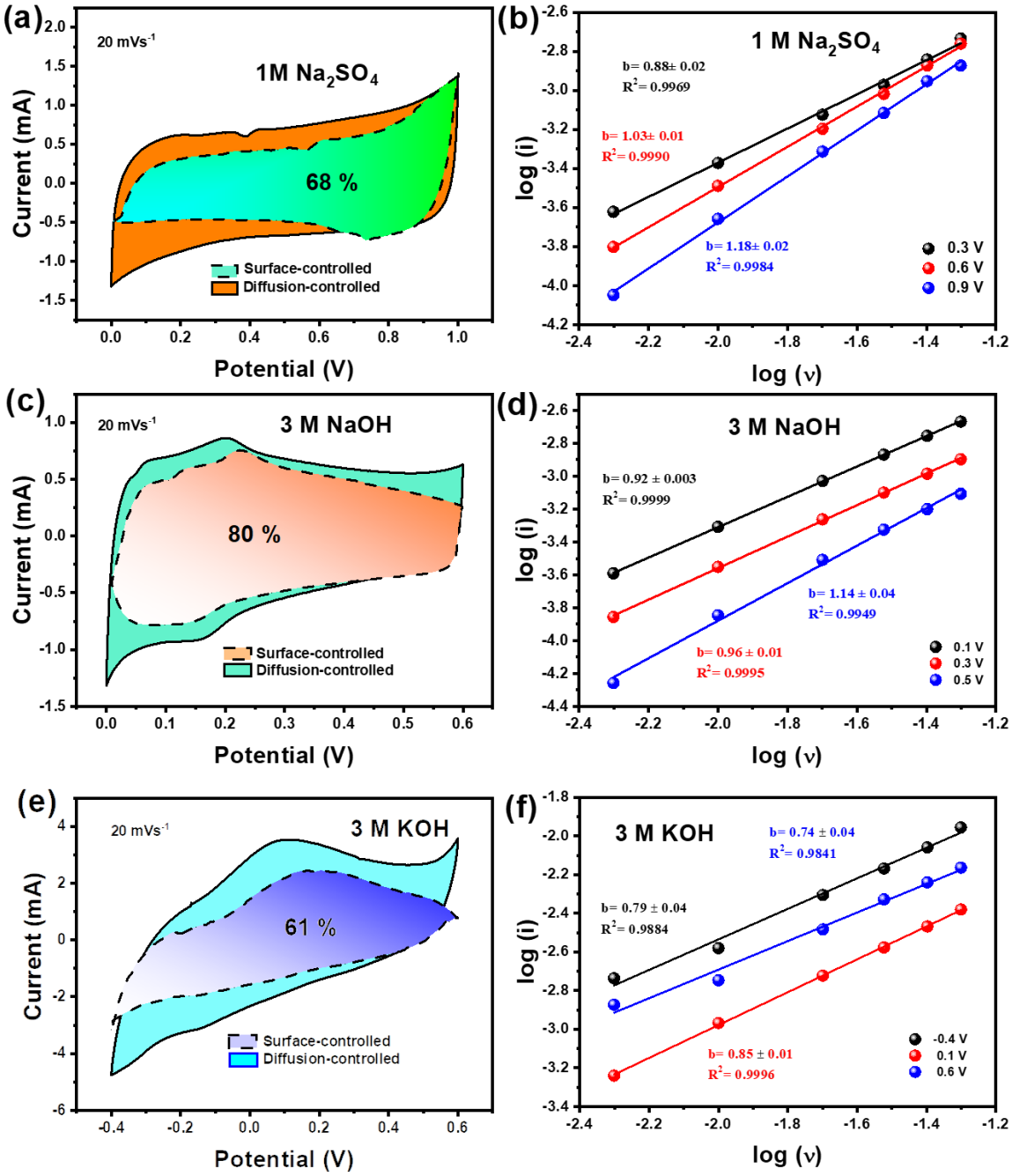


Figure 6.6: (a, c & e) Comparison of the capacitive and diffusion-controlled contributions fraction for $Na_{0.44}MnO_2$ at 20 mV s^{-1} in different electrolytes, (b, d & f) log peak current *vs.* log scan rate for $Na_{0.44}MnO_2$ in different electrolytes.

6.3.2.2 Asymmetric N-CNTs@CF//$Na_{0.44}MnO_2$ supercapacitor characteristics

In comparison to $Na_{0.44}MnO_2$ in 1M Na_2SO_4 and $Na_{0.44}MnO_2$ in 3M NaOH electrolytes, $Na_{0.44}MnO_2$ in 3M KOH delivered more capacitance (108.5 F g^{-1}; 665.6 F cm^{-3}) in cyclic voltammetry and charge-discharge studies. As a result, an asymmetric full cell (N-CNTs@CF//$Na_{0.44}MnO_2$) was fabricated using the $Na_{0.44}MnO_2$ and nitrogen-doped carbon nanotube-carbon nanofiber hybrid material (N-CNTs@CF) as the positive and negative electrodes, respectively. **Figure 6.7a** shows the CV curves of $Na_{0.44}MnO_2$ and N-CNTs@CF in a three-electrode system recorded at a scan rate of 20 mV s^{-1}. The EDLC behaviour of N-CNTs@CF due to the adsorption-desorption of electrolyte cations (K^+) is confirmed by the rectangular shape CV curve. The far negative working potential (-1.0 V) of N-CNTs@CF in aqueous electrolyte makes this material promising for use as a negative electrode material for asymmetric supercapacitors. It is well known that the positive and negative charge should be balanced for the fabrication of the full cell. For charge-balancing, the mass ratio of the cathode to the anode materials (obtained from 3-electrode experiments) was determined using the conventional method, equation 6.6:

$$q^+ = q^- \tag{6.6}$$

where q^+ and q^- are the charges at the cathode and anode, respectively. The optimal mass ratio was obtained using equation 6.7:

$$\frac{m^+}{m^-} = \frac{C^-}{C^+} + \frac{\Delta V^-}{\Delta V^+} \tag{6.7}$$

where m^+, V^+ and C^+ denote the mass, potential window and specific capacitance of the cathode, respectively and m^-, V^- and C^- denote the mass, potential window and specific capacitance of the anode, respectively. Gravimetric and volumetric specific capacitance (C_s & C_{vol}), were calculated based on the following formulae in equations 6.8–6.9:

$$C_s = \frac{I \times \Delta t}{m \times \Delta V} \ (F\ g^{-1}) \quad (6.8)$$

$$C_{Vol} = C_s \times \rho \ (F\ cm^{-3}) \quad (6.9)$$

where C_s is the gravimetric capacitance, C_{vol} is the volumetric capacitance, I (in ampere) is the discharge current, Δt (in second) is the discharge time, m (in g) is the mass of both electrodes, ΔV is the potential window during the discharge process after the IR drop, ρ is the density of the electrode materials. The corresponding gravimetric energy density (E_s) and power density (P_s) were obtained from equations 6.10 and 6.11, respectively.

$$E_s = \frac{0.5 C_s \times \Delta V^2}{3.6} \ (Wh\ kg^{-1}) \quad (6.10)$$

$$P_s = \frac{E_s \times 3600}{\Delta t} \ (W\ kg^{-1}) \quad (6.11)$$

The CV curves were used to maximize the potential window (**Figure 6.7a**). In 3M KOH electrolyte, the overall working potential of the asymmetric cell is 1.8 V, which is higher than that of our earlier work based on N-CNTs@CF-based symmetric supercapacitor (1.0 V) [40]. **Figure 6.7b** shows the CV measurements for the asymmetric full cell (N-CNTs@CF//$Na_{0.44}MnO_2$) at different scan rates. The presence of redox peaks in the CV curves confirms the presence of pseudocapacitance in the positive electrode. The charge storage mechanism at the negative electrode (N-CNTs@CF) is aided by the adsorption-desorption of electrolyte cations (K^+) and the creation of an electrical double layer. The possible electrochemical charge storage reactions on the positive electrode are due to a diffusion-controlled reversible redox reaction facilitated by the electron transfer between Mn^{3+} and Mn^{2+} ions. Below is the proposed mechanism for the negative electrode based on similar reports [32, 41].

$$\text{N-CNTs@CF} + x\text{K}^+ \; xe^- \leftrightarrow \text{N-CNTs@CF}(xe^-) \| \; x\text{K}^+ \qquad (6.12)$$

(where ‖ indicates double layer).

The galvanostatic charge-discharge curves of the asymmetric capacitor were recorded at different current densities, as shown in **Figure 6.7c**. The mirror-like form of GCD curves shows good electrochemical reversibility of the cell. In addition, the non-linear GCD curves are observed, which supports the CV data. **Figure 6.7d** shows the discharge gravimetric and volumetric capacitance at various current densities (0.5 to 5 A g^{-1}) with 47 F g^{-1} and 86 F cm^{-3} at 0.5 A g^{-1}, demonstrating 72 % capacity retention even at a high rate of 5 A g^{-1}.

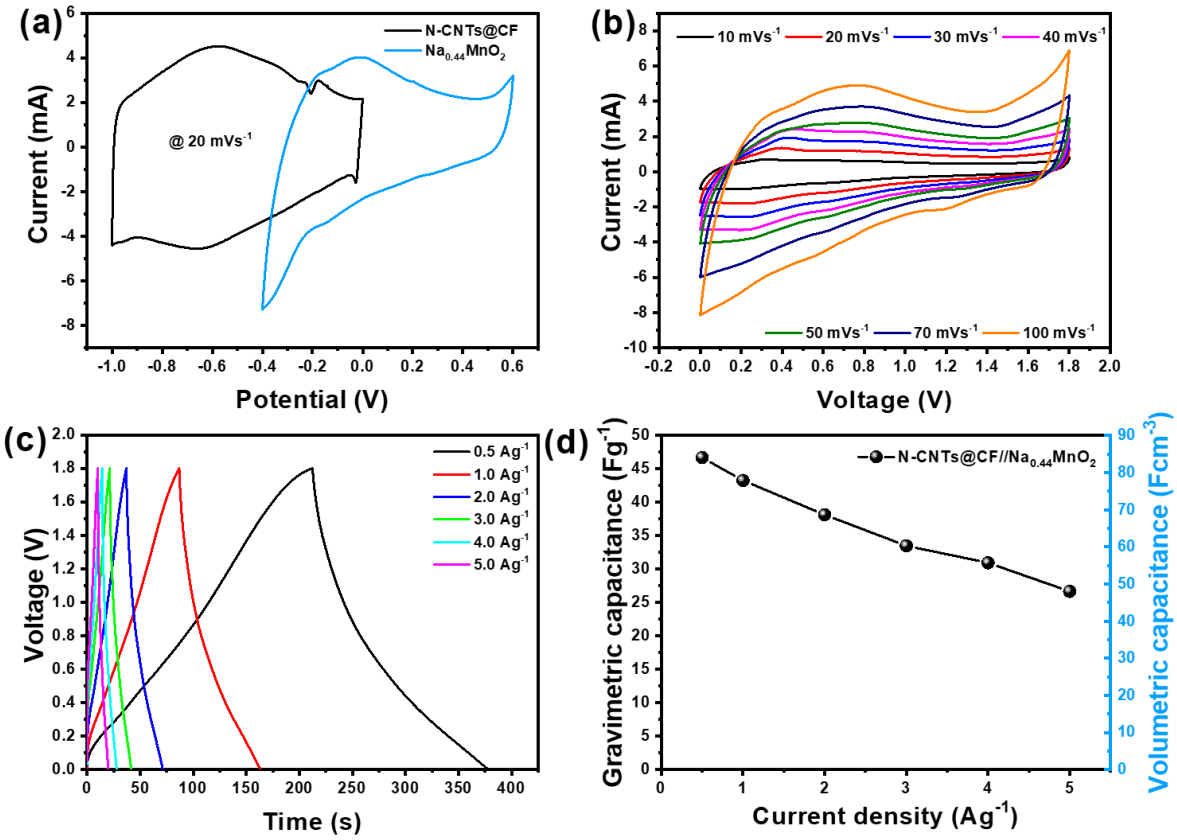


Figure 6.7: (a) CV curves of N-CNT@CF and $Na_{0.44}MnO_2$, (b) CV curves of N-CNT@CF//$Na_{0.44}MnO_2$ at different scan rates, (c) typical GCD curves of N-

CNT@CF//$Na_{0.44}MnO_2$ at different current densities and (d) capacitance versus current density plot**.**

The cycle life of the full cell was studied for up to 5,000 cycles. At a current density of 5 A g^{-1}, coloumbic efficiency and capacity retention of the asymmetric cell were measured for 5,000 charge-discharge cycles (see **Figure 6.8a**). The asymmetric cell has a higher coulombic efficiency (>97 %), and its capacitance is stable, with over 70 % of its initial capacitance retained after 5,000 cycles. **Figure 6.8b** compares the Nyquist plots obtained before and after 5,000 cycles. The EIS parameters before and after 5,000 cycles (modelled with the simple Randles electrical equivalent circuit, EEC, **Figure 8b** inset) include: (i) bulk resistance (R_s) due to the combined resistances arising from the current collectors, electrodes, electrolyte and separator, (ii) charge-transfer resistance (R_{ct}) due to electron transport, (iii) interfacial resistance (R_{int}) due to IR drop and (iv) the CPE due to inhomogeneous or irregular structure or morphology of the electrode surfaces. The modelled parameters are summarized in **Table 6.3**. After the 5,000th cycle, the R_s and R_{ct} values decreased slightly (from 3.02 and 9.13 to 0.08 and 8.35, respectively), suggesting that the EEI layer was slightly activated, resulting in increased conductivity. The "*a*" values from CPE increased from 0.56 (before cycling) to 0.81 (after 5,000 cycles), indicating that the electrode materials retain their mixed pseudocapacitance mechanism. Changes in the EEI layer can also be calculated from the power capability asymmetric device before and after long-term cycling by examining the knee frequency (f_o/Hz) [42]. The presence of a high f_o value indicates that the asymmetric device has a high-power density. The asymmetric device showed a lower f_o value before cycling (ca. 25.12 Hz, response time, τ, 39.8 ms) than after the 5,000th cycle (ca. 37.28 Hz, 26.8 ms). The activation of the EEI layer of the electrode materials is also confirmed by this slight difference in response times. The Bode plots (**Figure 6.8c**) show the phase angles of the N-CNT@CF/$Na_{0.44}MnO_2$ asymmetric cell before (-65^o) and after 5,000 cycles (-66^o), confirming

the enhanced ion diffusion process. In general, the EIS data shows that the structure of the EEI layer, where electrochemistry takes place, changed slightly after long-term cycling, confirming the satisfactory stability (capacity retention of 72 % after 5,000 cycles) shown in **Figure 6.8a**.

Table 6.3: EIS parameters for N-CNT@CF//$Na_{0.44}MnO_2$ asymmetric cell before and after the 5,000th cycle.

EIS parameters	**N-CNTs@CF//$Na_{0.44}MnO_2$ device**	
	Before 5,000 cycles	**After 5,000 cycles**
R_s **/ Ω**	3.02 ± 0.58	0.80 ± 0.50
R_{ct} **/ Ω**	9.13 ± 1.83	8.35 ± 0.78
***CPE* / mF. s^(a-1)**	1.87 ± 3.12	0.92 ± 1.18
a	0.60	0.67
***CPE* / mF. s^(a-1)**	0.02 ± 1.53	9.08 ± 0.72
f_o **/ Hz**	25.12	37.28
τ **/ ms**	39.81	26.82
Phase angle	65°	66°
χ^2	0.00918	0.03408

The Ragone plots derived from charge-discharge curves at different current densities are compared in **Figure 6.8d**. At a power density of 450 W kg^{-1}, the asymmetric device provides an energy density of 21 W h kg^{-1} and 12 W h kg^{-1} also at a high-power density of 4500 W kg^{-1}. The power and energy density of the asymmetric N-CNT@CF//$Na_{0.44}MnO_2$ C capacitor is comparatively higher than symmetric (N-CNT@CF//N-CNT@CF) [40]. Furthermore, the energy density of the asymmetric device is significantly higher than the previously reported AC//$NaMnO_2$ [8], AC//$NaNiPO_4$ [32] and AC//$NaNi_{1/3}Co_{1/3}Mn_{1/3}PO_4$ [43] hybrid capacitors,

corroborating the synergistic influence of N-CNT@CF and $Na_{0.44}MnO_2$ in the performance of the asymmetric device. However, the energy density is low compared with recent reports of $NaMnO_{2-x}$/NF//AC/NF [44] and Na_xMnO_2//N-rgo [45]. Overall, $Na_{0.44}MnO_2$ is a promising electrode material for energy storage applications due to its electrochemical reversibility, high specific capacitance and excellent cycle life.

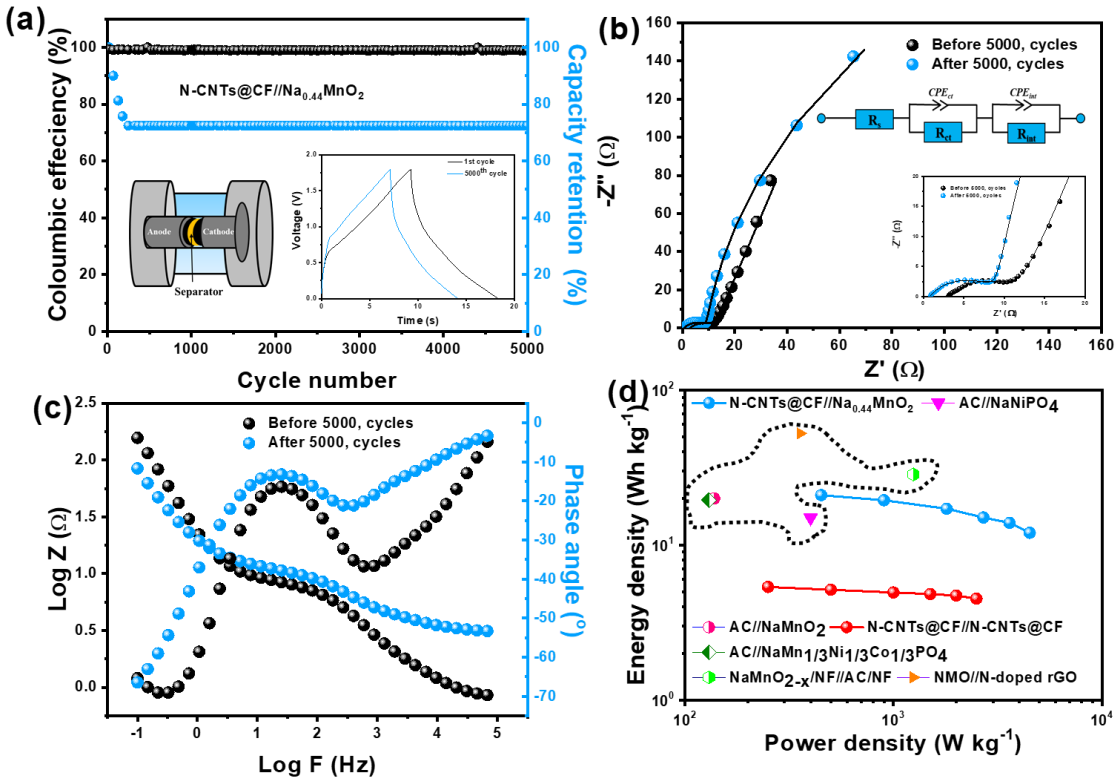


Figure 6.8: Electrochemical performance of the N-CNT@CF//$Na_{0.44}MnO_2$ asymmetric device: (a) cycling stability and coulombic efficiency of N-CNT@CF//$Na_{0.44}MnO_2$ asymmetric device at 5 A g^{-1}, (b) Nyquist plots obtained before and after 5,000 charge-discharge cycles, (c) Bode plots before and after 5,000 cycles of the N-CNT@CF//$Na_{0.44}MnO_2$ device and (e) comparative Ragone plot of this work with recent literature**.**

6.4 Summary

In conclusion, the hydrothermal method was used to successfully synthesize $Na_{0.44}MnO_2$ cathode material. Nanowire-like morphology was revealed in SEM and TEM micrographs, with an average diameter of about 100 nm. XRD was used to identify the formation of

crystalline $Na_{0.44}MnO_2$ material. XPS verified the existence of Na, Mn and O elements. The specific surface area and pore size distributions were determined using N_2 absorption–desorption measurements. The charge storage mechanism was proposed after investigating the electrochemical performance of the $Na_{0.44}MnO_2$ in various aqueous electrolytes (1M Na_2SO_4, 3M NaOH and 3M KOH). Due to intercalation/de-intercalation like behaviour in 3 M KOH electrolyte and reversible redox reaction of Mn, the $Na_{0.44}MnO_2$ delivered a maximum capacitance of 108 F g^{-1}. An asymmetric full cell (N-CNT@CF//$Na_{0.44}MnO_2$) was fabricated and it delivered a high gravimetric and volumetric specific capacitance (47 F g^{-1}, 86 F cm^{-3}), the energy density of (21 W h kg^{-1}) and power density of (450 W kg^{-1}) at 0.5 A g^{-1}.

6.5 References

[1] Shi, F., Li, L., Wang, X.L., Gu, C.D. and Tu, J.P., 2014. Metal oxide/hydroxide-based materials for supercapacitors. *RSC Advances*, **4**, pp.41910-41921.

[2] Kouchachvili, L., Yaïci, W. and Entchev, E., 2018. Hybrid battery/supercapacitor energy storage system for the electric vehicles. *Journal of Power Sources*, **374**, pp.237-248.

[3] Pu, X., Hu, W. and Wang, Z.L., 2018. Toward wearable self-charging power systems: the integration of energy-harvesting and storage devices. *Small*, **14**, p.1702817.

[4] Banerjee, S., De, B., Sinha, P., Cherusseri, J. and Kar, K.K., 2020. Applications of supercapacitors. In Handbook of Nanocomposite Supercapacitor Materials I (pp. 341-350). Springer, Cham.

[5] Wang, G., Fu, L., Zhao, N., Yang, L., Wu, Y. and Wu, H., 2007. An aqueous rechargeable lithium battery with good cycling performance. *Angewandte Chemie*, **119**, pp.299-301.

[6] An, C., Li, W., Wang, M., Deng, Q. and Wang, Y., 2018. High energy density aqueous asymmetric supercapacitors based on MnO_2@C branch dendrite nanoarchitectures. *Electrochimica Acta*, **283**, pp.603-610.

[7] Karikalan, N., Karuppiah, C., Chen, S.M., Velmurugan, M. and Gnanaprakasam, P., 2017. Three-dimensional fibrous network of $Na_{0.21}MnO_2$ for aqueous sodium-ion hybrid supercapacitors. *Chemistry–A European Journal*, **23**, pp.2379-2386.

[8] Qu, Q.T., Shi, Y., Tian, S., Chen, Y.H., Wu, Y.P. and Holze, R., 2009. A new cheap asymmetric aqueous supercapacitor: activated carbon//$NaMnO_2$. *Journal of Power Sources*, **194**, pp.1222-1225.

[9] Aravindan, V., Gnanaraj, J., Lee, Y.S. and Madhavi, S., 2014. Insertion-type electrodes for nonaqueous Li-ion capacitors. *Chemical Reviews*, **114**, pp.11619-11635.

[10] Yang, Z., Choi, D., Kerisit, S., Rosso, K.M., Wang, D., Zhang, J., Graff, G. and Liu, J., 2009. Nanostructures and lithium electrochemical reactivity of lithium titanites and titanium oxides: A review. *Journal of Power Sources*, **192**, pp.588-598.

[11] Palomares, V., Casas-Cabanas, M., Castillo-Martínez, E., Han, M.H. and Rojo, T., 2013. Update on Na-based battery materials. A growing research path. *Energy & Environmental Science*, **6**, pp.2312-2337.

[12] Chen, Z., Augustyn, V., Jia, X., Xiao, Q., Dunn, B. and Lu, Y., 2012. High-performance sodium-ion pseudocapacitors based on hierarchically porous nanowire composites. *ACS Nano*, **6**, pp.4319-4327

[13] Tomboc, G.M. and Kim, H., 2019. Derivation of both EDLC and pseudocapacitance characteristics based on synergistic mixture of $NiCo_2O_4$ and hollow carbon nanofiber: an efficient electrode towards high energy density supercapacitor. *Electrochimica Acta*, **318**, pp.392-404.

[14] Dong, S., Shen, L., Li, H., Pang, G., Dou, H. and Zhang, X., 2016. Flexible sodium-ion pseudocapacitors based on 3D $Na_2Ti_3O_7$ nanosheet arrays/carbon textiles anodes. *Advanced Functional Materials*, **26**, pp.3703-3710.

[15] Jiang, Y., Tan, S., Wei, Q., Dong, J., Li, Q., Xiong, F., Sheng, J., An, Q. and Mai, L., 2018. Pseudocapacitive layered birnessite sodium manganese dioxide for high-rate non-aqueous sodium ion capacitors. *Journal of Materials Chemistry A*, **6**, pp.12259-12266.

[16] Xia, H., Zhu, X., Liu, J., Liu, Q., Lan, S., Zhang, Q., Liu, X., Seo, J.K., Chen, T., Gu, L. and Meng, Y.S., 2018. A monoclinic polymorph of sodium birnessite for ultrafast and ultrastable sodium ion storage. *Nature Communications*, **9**, pp.1-10.

[17] Chen, Z., Yuan, T., Pu, X., Yang, H., Ai, X., Xia, Y. and Cao, Y., 2018. Symmetric sodium-ion capacitor based on $Na_{0.44}MnO_2$ nanorods for low-cost and high-performance energy storage. *ACS Applied Materials & Interfaces*, **10**, pp.11689-11698.

[18] Wei, W., Cui, X., Chen, W. and Ivey, D.G., 2011. Manganese oxide-based materials as electrochemical supercapacitor electrodes. *Chemical Society Reviews*, **40**, pp.1697-1721.

[19] Kim, H.J., Ramasamy, H.V., Jeong, G.H., Aravindan, V. and Lee, Y.S., 2020. Deciphering the Structure–Property Relationship of Na–Mn–Co–Mg–O as a Novel High-Capacity Layered–Tunnel Hybrid Cathode and Its Application in Sodium-Ion Capacitors. *ACS Applied Materials & Interfaces*, **12**, pp.10268-10279.

[20] Clément, R.J., Billaud, J., Armstrong, A.R., Singh, G., Rojo, T., Bruce, P.G. and Grey, C.P., 2016. Structurally stable Mg-doped P2-$Na_{2/3}Mn_{1-y}Mg_yO_2$ sodium-ion battery cathodes with high rate performance: insights from electrochemical, NMR and diffraction studies. *Energy & Environmental Science*, **9**, pp.3240-3251.

[21] Li, W., Dahn, J.R. and Wainwright, D.S., 1994. Rechargeable lithium batteries with aqueous electrolytes. *Science*, **264**, pp.1115-1118.

[22] Li, H., Qi, C., Tao, Y., Liu, H., Wang, D.W., Li, F., Yang, Q.H. and Cheng, H.M., 2019. Quantifying the volumetric performance metrics of supercapacitors. *Advanced Energy Materials*, **9**, p.1900079.

[23] Liu, Q., Hu, Z., Chen, M., Gu, Q., Dou, Y., Sun, Z., Chou, S. and Dou, S.X., 2017. Multiangular rod-shaped $Na_{0.44}MnO_2$ as cathode materials with high rate and long life for sodium-ion batteries. *ACS Applied Materials & Interfaces*, **9**, pp.3644-3652.

[24] Dall'Asta, V., Buchholz, D., Chagas, L.G., Dou, X., Ferrara, C., Quartarone, E., Tealdi, C. and Passerini, S., 2017. Aqueous processing of $Na_{0.44}MnO_2$ cathode material for the

development of greener Na-ion batteries. *ACS Applied Materials & Interfaces*, **9**, pp.34891-34899.

[25] Li, J., Yu, J., Amiinu, I.S., Zhang, J., Sheng, J., Kou, Z., Wang, Z., Yu, Q., Mai, L. and Mu, S., 2017. Na–Mn–O@ C yolk–shell nanorods as an ultrahigh electrochemical performance anode for lithium ion batteries. *Journal of Materials Chemistry A*, **5**, pp.18509-18517.

[26] Cai, Y., Huang, S.Z., She, F.S., Liu, J., Zhang, R.L., Huang, Z.H., Wang, F.Y. and Wang, H.E., 2016. Facile synthesis of well-shaped spinel $LiNi_{0.5}Mn_{1.5}O_4$ nanoparticles as cathode materials for lithium ion batteries. *RSC Advances*, **6**, pp.2785-2792.

[27] Mai, L., Li, H., Zhao, Y., Xu, L., Xu, X., Luo, Y., Zhang, Z., Ke, W., Niu, C. and Zhang, Q., 2013. Fast ionic diffusion-enabled nanoflake electrode by spontaneous electrochemical pre-intercalation for high-performance supercapacitor. *Scientific Reports*, **3**, pp.1-8.

[28] Pang, S.C. and Anderson, M.A., 2000. Novel electrode materials for electrochemical capacitors: Part II. Material characterization of sol-gel-derived and electrodeposited manganese dioxide thin films. *Journal of Materials Research*, **15**, pp.2096-2106.

[29] Chu, Y.H., Hu, C.C. and Chang, K.H., 2012. Electrochemical quartz crystal microbalance study of amorphous MnO_2 prepared by anodic deposition. *Electrochimica Acta*, **61**, pp.124-131.

[30] Misnon, I.I., Abd Aziz, R., Zain, N.K.M., Vidhyadharan, B., Krishnan, S.G. and Jose, R., 2014. High performance MnO_2 nanoflower electrode and the relationship between solvated ion size and specific capacitance in highly conductive electrolytes. *Materials Research Bulletin*, **57**, pp.221-230.

[31] Nightingale Jr, E.R., 1959. Phenomenological theory of ion solvation. Effective radii of hydrated ions. *Journal of Physical Chemistry*, **63**, pp.1381-1387.

[32] Senthilkumar, B., Sankar, K.V., Vasylechko, L., Lee, Y.S. and Selvan, R.K., 2014. Synthesis and electrochemical performances of maricite-$NaMPO_4$ (M= Ni, Co, Mn) electrodes for hybrid supercapacitors. *RSC Advances*, **4**, pp.53192-53200.

[33] Hu, C.C. and Wang, C.C., 2004. Effects of electrolytes and electrochemical pre-treatments on the capacitive characteristics of activated carbon fabrics for supercapacitors. *Journal of Power Sources*, **125**, pp.299-308.

[34] Cheng, F., He, C., Shu, D., Chen, H., Zhang, J., Tang, S. and Finlow, D.E., 2011. Preparation of nanocrystalline VN by the melamine reduction of V_2O_5 xerogel and its supercapacitive behavior. *Materials Chemistry and Physics*, **131**, pp.268-273.

[35] Pillay, J. and Ozoemena, K.I., 2009. Layer-by-layer self-assembled nanostructured phthalocyaninatoiron (II)/SWCNT-poly (m-aminobenzenesulfonic acid) hybrid system on gold surface: Electron transfer dynamics and amplification of H_2O_2 response. *Electrochimica Acta*, **54**, pp.5053-5059.

[36] Agboola, B.O. and Ozoemena, K.I., 2008. Self-assembly and heterogeneous electron transfer properties of metallo-octacarboxyphthalocyanine complexes on gold electrode. *Physical Chemistry Chemical Physics*, **10**, pp.2399-2408.

[37] Ozoemena, K.I., Mathebula, N.S., Pillay, J., Toschi, G. and Verschoor, J.A., 2010. Electron transfer dynamics across self-assembled N-(2-mercaptoethyl) octadecanamide/mycolic acid layers: impedimetric insights into the structural integrity and interaction with anti-mycolic acid antibodies. *Physical Chemistry Chemical Physics*, **12**, pp.345-357.

[38] Xi, S., Zhu, Y., Yang, Y., Jiang, S. and Tang, Z., 2017. Facile synthesis of free-standing NiO/MnO_2 core-shell nanoflakes on carbon cloth for flexible supercapacitors. *Nanoscale Research Letters*, **12**, pp.1-10.

[39] Raju, K., Han, H., Velusamy, D.B., Jiang, Q., Yang, H., Nkosi, F.P., Palaniyandy, N., Makgopa, K., Bo, Z. and Ozoemena, K.I., 2019. Rational design of 2D manganese phosphate hydrate nanosheets as pseudocapacitive electrodes. *ACS Energy Letters*, **5**, pp.23-30.

[40] Mofokeng, T.P., Ipadeola, A.K., Tetana, Z.N. and Ozoemena, K.I., 2020. Defect-Engineered Nanostructured Ni/MOF-Derived Carbons for an Efficient Aqueous Battery-Type Energy Storage Device. *ACS Omega*, **5**, pp.20461-20472.

[41] Zhao, Y., Lai, Q.Y., Hao, Y.J. and Ji, X.Y., 2009. Study of electrochemical performance for AC/$(Ni_{1/3}Co_{1/3}Mn_{1/3})(OH)_2$. *Journal of Alloys and Compounds*, **471**, pp.466-469.

[42] Chidembo, A.T., Ozoemena, K.I., Agboola, B.O., Gupta, V., Wildgoose, G.G. and Compton, R.G., 2010. Nickel (II) tetra-aminophthalocyanine modified MWCNTs as potential nanocomposite materials for the development of supercapacitors. *Energy & Environmental Science*, **3**, pp.228-236.

[43] Minakshi, M., Meyrick, D. and Appadoo, D., 2013. Maricite ($NaMn_{1/3}Ni_{1/3}Co_{1/3}PO_4$)//activated carbon: hybrid capacitor. *Energy & Fuels*, **27**, pp.3516-3522.

[44] Xu, S., Wan, T., Zhou, K.B., Zhu, G.M., He, Z.Q., Huang, H.B., Zhou, T., Mao, W.Q., Wu, J.J., Gong, S.K. and Qiao, Y.X., 2020. $NaMnO_{2-x}$ thin nanosheets assembled microspheres as electrode for aqueous asymmetric supercapacitor. *Materials Research Express*, **7**, p.035508.

[45] Yang, Z., Vinodh, R., Balakrishnan, B., Rajmohan, R. and Kim, H.J., 2020. Rational design of asymmetric aqueous supercapacitor based on Na_xMnO_2 and N-doped reduced graphene oxide. *Journal of Energy Storage*, **28**, p.101293.

CHAPTER 7

"Water-In-Salt" electrolyte-based high-voltage (3.0 V) $Na_{0.44}MnO_2$ asymmetric capacitor

7.1 Introduction

With the ever-increasing demand for environmentally friendly and sustainable energy storage devices, rechargeable batteries and supercapacitors have received extensive attention for use in portable electronic devices (PED), electrical vehicles (EV) and grid-scale energy storage systems (ESSs) [1]. However, the energy and power demands of the above-mentioned applications cannot be met by batteries or supercapacitors alone, because rechargeable batteries offer high energy density but low power density, whereas capacitors offer high power density but low energy density. Therefore, to alleviate such limitations, it is best to combine these two devices in a hybrid system and have synergy from both devices.

Recently, the use of high energy density battery materials, especially lithium-ion batteries (LIB) and high-power density supercapacitors have been explored in hybrid systems [2]. Commercial LIB currently offers a higher energy density (150-210 Wh kg^{-1}) than supercapacitors (5 Wh kg^{-1}) but at the expense of low power density (~ 1 kW kg^{-1}) and long charge/discharge time [3-5]. At the same time, LIB cycle life is limited to approximately 1000 cycles [6]. In addition, at high current densities, the use of lithium intercalated materials such as $LiMn_2O_4$ as a cathode and activated carbon (AC) as an anode has been reported to have difficulties with the intercalation and deintercalation of Li^+ ions [7]. As a consequence, the energy density of the AC//$LiMn_2O_4$ asymmetric capacitor decreases very rapidly with increasing current density.

On the other hand, the rapid growth of lithium consumption leads to continuously increasing demand for lithium and the inherent limitations of lithium supply and demand are difficult to resolve, given the disproportionate distribution of lithium resources. Therefore, an alternative to lithium must be considered, especially for large-scale energy storage applications in the foreseeable future [8, 9]. The sodium-ion battery (NIB), which has a reaction pattern comparable with that of the LIB, is one of the promising alternatives because of its low cost and the abundance of sodium resources [10]. In addition, the use of Na-based materials instead of Li-based materials allows the use of aluminium as an anode current collector, which provide a cheaper alternative to the use of copper current collectors [11].

Furthermore, due to the similarities between LIBs and NIBs, NIB equivalents of LIB cathode materials, including oxides and phosphates, have been extensively studied [12, 13]. Among these, Mn-containing compounds such as sodium manganese oxides e.g., ($Na_{0.67}MnO_2$, $Na_{0.44}MnO_2$) and other Na-compounds ($Na_xMn_yB_zO_2$, B-transition metal) are widely researched for rechargeable NIBs as cathode materials [14]. This is because sodium manganese oxide compounds are known to be cost-effective, non-toxic and have a high theoretical capacity [15]. Among various cathode materials for NIBs, $Na_{0.44}MnO_2$ (NMO) has been identified as a highly promising cathode material, due to its large theoretical capacity (~ 121 mAh g^{-1}) and good stability, even in aqueous electrolytes [16, 17]. The microsphere $Na_{0.44}MnO_2$ as a cathode material can afford fast Na-ion transportation and accommodate the structural strain from multiple phase changes during the process of Na ions intercalation/deintercalation [7]. Furthermore, the electrochemical performance of the $Na_{0.44}MnO_2$ cathode for NIBs can be greatly improved by changing its morphology (shape and size) and regulating surface activity [18].

Nevertheless, owing to their ultra-high-power density and excellent cycling stability, supercapacitors are considered the front-runner for next-generation EES devices. However, their practical application is constrained by their relatively low energy density and hence, it would be exciting to transplant the high specific energy of LIB to supercapacitors. According to the equation $E=1/2CV^2$, the energy density of supercapacitors can be improved by either increasing the specific capacitance (C) or voltage window (V). Besides, designing novel micro/nanostructured electrode materials to increase specific capacitance, several studies have focused on extending the voltage window of supercapacitors [19]. As the key component of supercapacitors, electrolyte plays a dominant role in the electrochemical performance and in determining the cost and safety of the overall device [20].

Supercapacitors can be assembled using different types of electrolytes such as aqueous (acidic, neutral, base), organic electrolytes, ionic liquids, gel-electrolytes and solid-state electrolytes (without any solvent). Among these, organic and ionic liquid electrolytes exhibit appealing applications in supercapacitors due to their wider electrochemical window ($\geq$ 2V) [21]. However, these electrolytes contain large amounts of expensive yet flammable solvents with certain levels of toxicity, which makes the device assembly conditions relatively harsh. Consequently, aqueous electrolytes have been established as promising alternative candidates for supercapacitors. They are several distinct merits of aqueous electrolyte supercapacitors, there are safe, low cost, have high electronic conductivity and mild assembly environment. [22]. Nevertheless, the electrochemical stability voltage window of aqueous electrolytes is as small as 1.23 V, which, due to the presence of hydrogen and oxygen evolution reactions, severely limits the optimum choice of cathode and anode materials in asymmetric supercapacitors [23].

Distinguished from traditional aqueous electrolytes, high concentrated 'water-in-salt' (WIS) electrolytes in which the dissolved salts far exceed the water molecules (salt/solvent ratio > 1 by volume or weight) have been reported to expand the stable voltage window up to 3.0 V [23]. These rather stable super-concentrated WIS electrolytes have been successfully applied to enable high-voltage aqueous LIBs and NIBs [24, 25]. In this work, we report on an asymmetric 'water-in-salt' (WIS) aqueous supercapacitor using nitrogen-doped reduced graphene oxide (N-rGO) as an anode and sodium manganese oxide ($Na_{0.44}MnO_2$) as a cathode.

The rate performance of aqueous batteries is limited by the low conductivity and the high viscosity of the WIS electrolytes because of the strong electrostatic cation-anion attractions. If WIS electrolytes are used, this strong ion coupling will significantly impair the rate performance of supercapacitors, especially during fast charge/discharge rates. To alleviate such concerns, we introduced a co-solvent-in-salt system by blending acetonitrile with a WIS electrolyte (17m $(NaClO_4)_{1.7}/(H_2O)_{5.5}$) to make an acetonitrile/water in the salt electrolyte $(NaClO_4)_{1.7}/(H_2O)_{5.5}(ACN)_2$ (AWIS)). Acetonitrile was used as a co-solvent to compete with water molecules to coordinate with Na^+ ions, to reduce some of the water molecules coordinated with Na^+ ions.

7.2 Materials

Graphite powder ($<20\ \mu$m), potassium permanganate ($KMnO_4$, 99%), sulfuric acid (H_2SO_4, 98%), phosphoric acid (H_3PO_4, 85%), hydrogen peroxide (H_2O_2, 30%) and barium chloride dihydrate ($BaCl_2{\cdot}2H_2O$, 96%) were purchased from Sigma Aldrich, South Africa and used as is without any further purification. A 10 % hydrochloric acid solution was prepared by diluting a purchased HCl (36%, Sigma Aldrich, South Africa) solution with distilled water.

7.2.1 Preparation of graphene oxide (GO)

Graphene oxide was synthesized using the improved Hummers' method [26]. In brief graphite powder (3 g) and $KMnO_4$ (18 g) was carefully added into an ice-cold (0 °C) H_2SO_4 and H_3PO_4 (360 mL: 40 mL) acid mixture while stirring. This reaction mixture was stirred for 12 h at 50 °C and terminated by adding 3 mL of H_2O_2 followed by 400 mL of ice-cold distilled water. The brown gel was centrifuge washed at 15000 rpm with 10% HCl to remove all the sulphate ions (tested using $BaCl_2 \cdot 2H_2O$) and with distilled water until a pH of ~7. The obtained gel was ultra-sonicated for an hour and vacuum freeze-dried at ~ -80 °C for a week.

7.2.2 Preparation of N-doped reduced graphene oxide (N-rGO)

N-rGO was synthesized by a modified method reported by Yang *et al*. [27] with GO as raw material and urea as a reducing-doping agent. In a typical process for preparing N-rGO, graphene oxide (451.1 mg) was dispersed in 100 mL distilled water by ultrasonication. Afterwards, 1.3533 g of urea was dissolved in the above suspension and then place in a refluxing set-up at a temperature of 90 °C. After refluxing for 6 hours, the resulting product was separated by filtration and dried in an oven at 80 °C for 24 hours. The resulting black powder was then annealed at 350 °C for 1 h in a tubular furnace at the heating rate of 1 °C/min. The obtained black powder was rinsed with excess distilled water and dried at 80 °C overnight in an oven. The obtained N-doped reduced graphene oxide was named N-rGO.

7.2.3 Electrochemical measurements

The electrochemical behaviour of the samples was carried out in a Biologic-SP300 workstation in a two-electrode and three-electrode setup using WIS and AWIS as electrolytes. To make a homogeneous slurry in N-methyl-pyrrolidinone (NMP), the active materials were mixed with acetylene black and polytetrafluoroethylene (PTFE) binder in a 90:5:5 ratio, which was taken and drop-casted onto a carbon paper current collector. The fabricated electrodes were dried for

12 h at 80 °C in a vacuum oven. EIS measurements were carried out at frequencies ranging from 100 kHz to 0.1 Hz. In a three-electrode and two-electrode configuration, the specific gravimetric (C_s, F g^{-1}) were calculated under the GCD curve using equation 7.3 in section 7.4.1.1. Specific energy (E, Wh kg^{-1}) and specific power (P, W kg^{-1}) were measured with GCD curves using equation 7.5 and 7.6 in section 7.4.1.1, respectively, under the two-electrode setup (full-cell).

7.3 Physical characterization

The phase characteristics of the GO and N-rGO powders were determined by powder X-ray diffraction (Bruker D2 phaser diffractometer) in the scan range $5° \leq 2\theta \leq 90°$ with a 0.02° measurement step, using a Cu-Kα (λ = 0.154 nm) radiation source. Raman measurements were conducted on a Horiba LabRAM Raman spectrometer equipped with an Olympus BX41 microscope attachment. The morphology of the samples was established using a transmission electron microscope (FEI Spirit T12 instrument at 120 keV).

7.4 Results and discussion

The results and the discussion below are for only N-rGO negative electrode. The positive electrode $Na_{0.44}MnO_2$ was discussed in CHAPTER 6.

The X-ray diffraction patterns for GO and N-rGO are illustrated in **Figure 7.1**. GO has distinct peaks located at 2θ= 12.2° and 42.9° attributed to (001) and (100) planes, respectively. The narrow (001) peak corresponds to an interlayer spacing of 0.73 nm, which is higher than that of graphite (0.34 nm) due to the incorporated oxygen functionalities on the graphite sheets [26]. After reduction with urea, the (001) plane disappears and the graphitic (002) plane emerges at 2θ= 24.4° producing an interlayer spacing of 0.36 nm. This value is lower than that of GO because of the decreased oxygen moieties, as a result of reduction; and slightly higher than that of graphite due to structural defects produced by N-doping in the graphitic structure. The broad

peak centred at 2θ= 43.7° is associated with the overlap of the (100) and (101) planes of graphite [28]. The broadness of the diffraction peaks in N-rGO suggests a low ordering along the stacking direction which can also suggest that N-rGO consists of free-standing sheets [29]. The crystallite stack height and in-plane crystallite size (L_c and L_a) were low in N-rGO as compared to GO, which serves as further confirmation of the removal of oxygen functionalities. Only a slight difference in the number of stacked sheets (N_c) is observed suggesting that the number of stacked sheets in GO and N-rGO is between 3 and 4 (**Table 7.1**).

Table 7.1: Crystallographic parameters for GO and N-rGO.

	(002) or (001) Plane (2θ (°))	**L_c (nm)**	**d_{002} (nm)**	**N_c**	**(100) Plane (2θ (°))**	**L_a (nm)**
GO	12.2	2.7	0.73	3.7	42.9	16.7
N-rGO	24.4	1.2	0.36	3.2	43.7	5.0

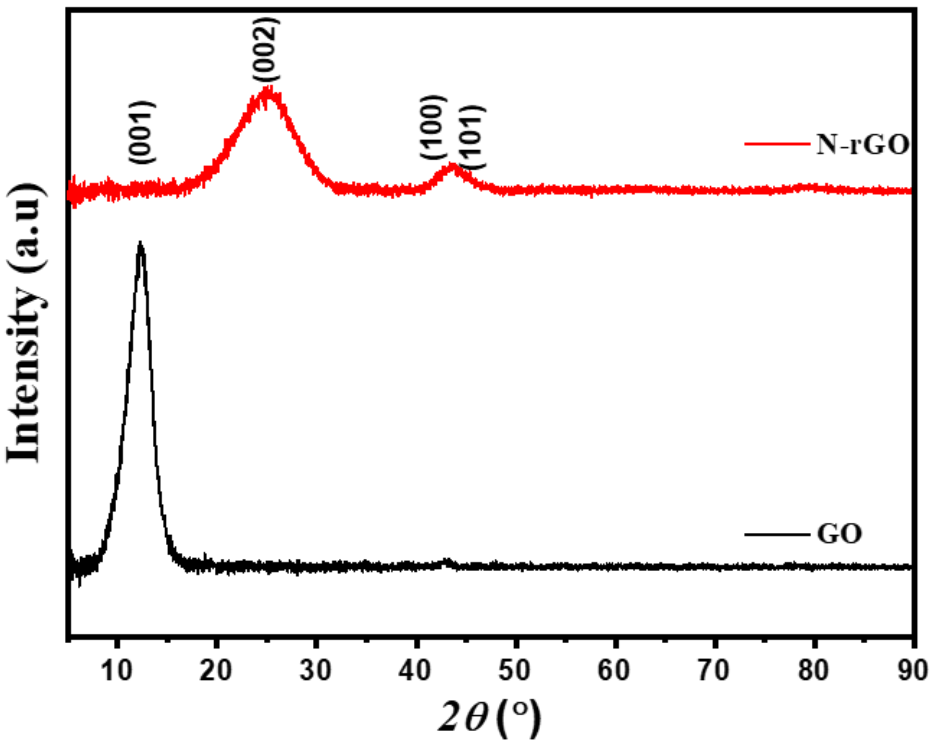


Figure 7.1: XRD spectrum of GO and N-rGO.

The Raman spectra of GO (**Figure 7.2a**) shows a prominent G band at 1590.3 cm^{-1} which is induced by the first-order Raman scattering processes of the in-plane vibrational modes of the sp^2 carbon in the graphene basal planes and a disorder-induced D band at 1358.2 cm^{-1} [30, 31]. Three additional bands, D_1, 2D and D+D', were observed at 1148.4 cm^{-1}, 2709.7 cm^{-1} and 2939.9 cm^{-1}, respectively. The D_1 band is ascribed to disorder in the graphitic lattice, sp^2–sp^3 bonds or the presence of polyene-like structures [32]. The 2D band is a result of the double resonance process which include intervalley scattering by two in-plane transverse optical (TO) phonons near the κ point of the Brillouin zone [30]. The D+D' band is a second-order peak derived from the combination of the D and G band [33]. N-rGO, the G band is slightly shifted to a higher wavenumber (1593.1 cm^{-1}) and the D, 2D and D+D' bands to lower wavenumbers (1349.4 cm^{-1}, 2691.5 cm^{-1} and 2936.2 cm^{-1}, respectively). The shifts in wavenumbers may be

associated with the strain produced in the carbon structure during reduction. An overtone of the 2D band, 2D', at 3173.7 cm^{-1} is also observed for N-rGO.

The intensity (or area) ratio of the D and G band provides information regarding the degree of disorder in the carbon structure [30], while the 2D to G intensity ratio gives an estimation of the number of graphene layers [34]. An increase in the degree of disorder is observed from GO to N-rGO due to the combined effects of the incorporation of N species which produced more structural defects in the carbon structure. This is further supported by the increase in the intensity ratio of the D+D' and 2D bands [33]. The I_{2D}/I_G ratio of both GO and N-rGO was lower than 1 (0.20 and 0.13) suggesting a multi-layered graphene structure.

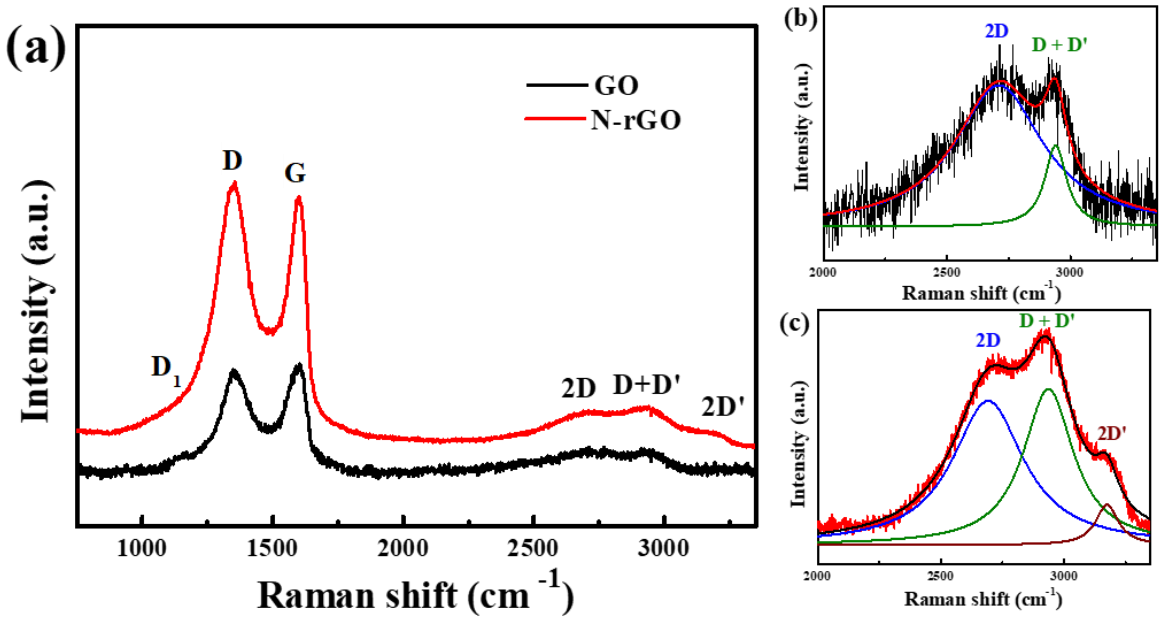


Figure 7.2: (a) Raman spectrum of GO and N-rGO (b) deconvoluted 2D peaks of GO and (c) deconvoluted 2D peaks of N-rGO.

Table 7.2: Raman parameters for GO and N-rGO.

	D Band		G Band		2D Band		
	Centre (cm^{-1})	**Area**	**Centre (cm^{-1})**	**Area**	**Centre (cm^{-1})**	**I_D/I_G**	**I_{2D}/I_G**
GO	1358.2	306244.2	1590.3	180577	2709.7	1.70	0.20
N-rGO	1349.6	800589.5	1593.1	323623.4	2691.5	2.47	0.13

X-ray photoelectron spectroscopy (XPS), was used to confirm the surface compositions of N-rGO and the results are illustrated in **Figure 7.3a**. The C 1s (**Figure 7.3b**) shows the C-C sp^2 band at 284.2 eV, C-C sp^3 band at 284.7 eV, C-O band at 285.8 eV, C=O band at 288.0 eV and O-C=O band at 288.7 eV, respectively. **Figure 7.3c** shows the oxygen region ((C-O) at 531.7 eV and (C=O) at 533.1 eV) existence in N-rGO. The N 1s peak can be split into two individual peaks (as shown in **Figure 7.3d**) located at 398.1 eV, 400.5 eV and 403.4 eV associated with pyridinic, pyrrolic and oxidized nitrogen, respectively. The introduction of nitrogen atoms into the honeycomb-like lattice is accompanied by structure defects such as vacancies, bonding disorders, and noncyclized structures, resulting in high structural disorder [35]. Furthermore, due to the high electronegativity and smaller covalent radius of nitrogen, doping would have a major impact on the graphene structure and electrical properties, which would increase the capacitance of N-rGO [36].

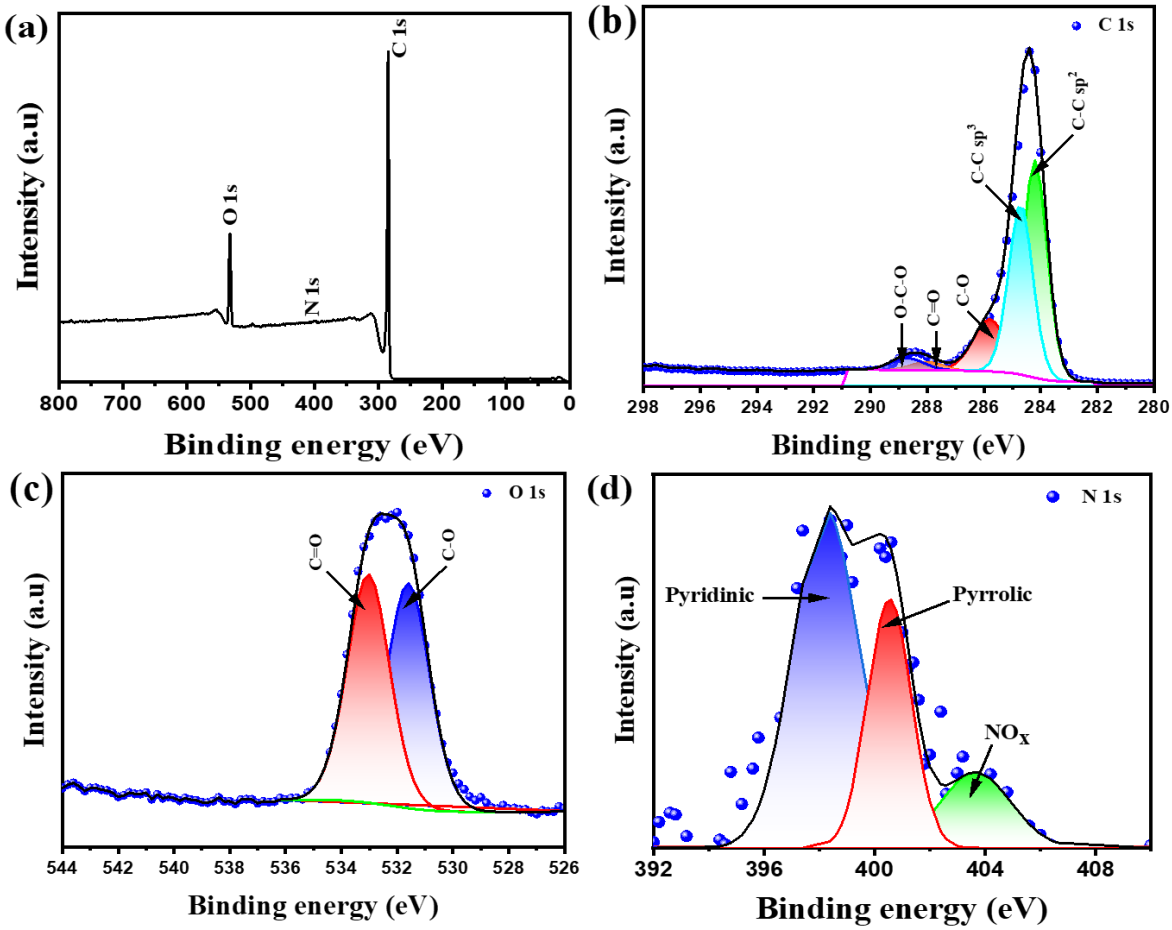


Figure 7.3: (a) XPS survey spectra of the N-rGO, (b) high resolution C 1s XPS spectra, (c) high resolution O 1s XPS spectra, (d) high resolution N 1s XPS spectra.

The TEM micrographs in **Figure 7.4** show the sheet-like structures of GO and N-rGO with a few micrometres in size. The wrinkles in the GO are due to the sp^2 to sp^3 transformations in the carbon electronic structure that took place during oxidation [37]. The N-rGO sheets show little to no wrinkling because of the restoration of some of the sp^2 carbon configurations. TEM further supports the multi-layered graphene structure suggested by Raman analysis.

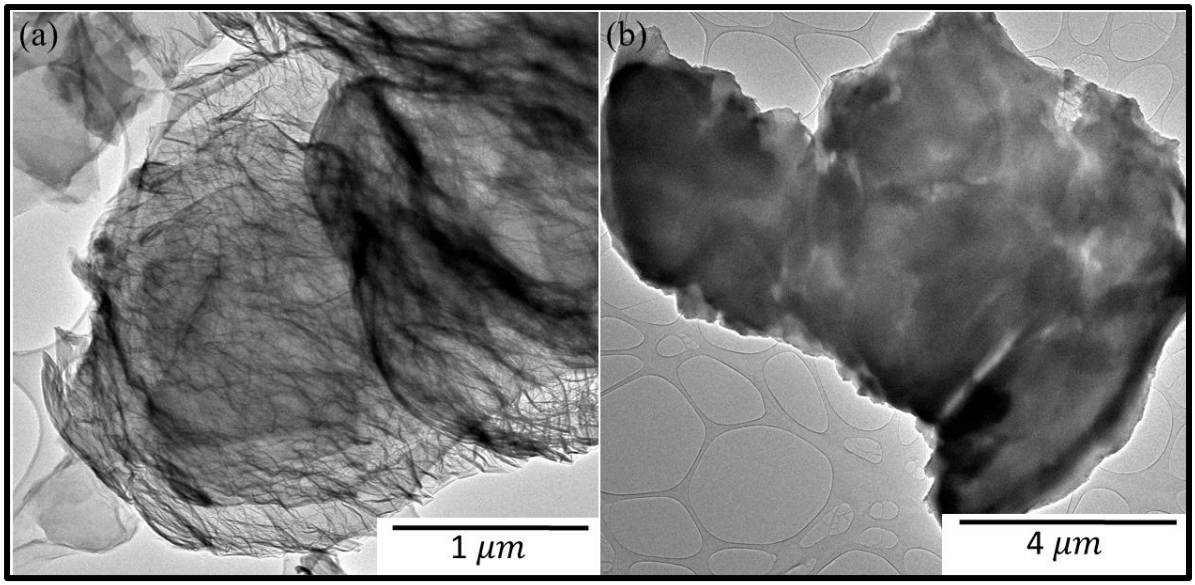


Figure 7.4: TEM images of (a) GO and (b) N-rGO.

7.4.1 Electrochemical characterization

The sodium storage properties of $Na_{0.44}MnO_2$ nanowires were initially tested in a three-electrode system using WIS and AWIS electrolytes. **Figure 7.5** shows the cyclic voltammograms (CV), galvanostatic charge/discharge (GCD), electrochemical impedance spectroscopy (EIS) and specific capacity (C_s) of $Na_{0.44}MnO_2$ electrode material. As shown in **Figure 7.5a**, the CV curves at 40 mV s^{-1} display an ideal pseudocapacitive behaviour with redox couples, indicative of surface Faradaic reactions due to physical intercalation/de-intercalation of Na^+ ions [38]. The narrow redox peak separation indicates the excellent electrochemical reversibility of the $Na_{0.44}MnO_2$ electrode and the separation widens with the gradual increase of scan rate (see **Supporting Information**, **Figure S1 (b & e) in Appendix D**). The result also shows that $Na_{0.44}MnO_2$ in AWIS electrolyte has better electrochemical performance (high current response and slightly wider voltage window) as compared to the WIS electrolyte. The extended voltage window of the AWIS electrolyte is attributed to the acetonitrile suppressing salt precipitation capability [39]. **Figure 7.5b** shows GCD curves with non-linear triangular shapes in both electrolytes, which further reveal the pseudocapacitive

behaviour of $Na_{0.44}MnO_2$. The GCD of $Na_{0.44}MnO_2$ in AWIS show higher discharge time and a higher charging potential maximum, which is in good agreement with the CV data. In addition, the symmetric GCD plots at high current densities (see **Supporting Information**, **Figure S1 (c & f) in Appendix D**) demonstrate the excellent reversibility and coulombic efficiency of the $Na_{0.44}MnO_2$ electrode material.

Furthermore, EIS was carried out to investigate the electrochemical properties of $Na_{0.44}MnO_2$ in both electrolytes. The Nyquist plots were fitted to circuit components, such as the solution resistance (R_s), charge-transfer resistance (R_{ct}), interfacial resistance (R_{int}), Warburg impedance (W), constant phase element (CPE) and electric double-layer capacitance (C_{dl}). At the low-frequency range, the Nyquist plots of $Na_{0.44}MnO_2$ in two electrolytes showed the R_s values of 0.21 and 0.73, respectively. The high R_s value of AWIS is attributed to the high viscosity of the electrolyte due to the addition of ACN. In addition, at the high-frequency range, the smaller semicircle of the AWIS electrolyte as compared to the WIS electrolyte revealed lower charge transfer resistance as shown in **Table 7.3** and the inset of **Figure 7.5c**. Based on equation 7.3, the C_s values of $Na_{0.44}MnO_2$ in WIS and AWIS electrolytes at different current densities (0.5 A g^{-1} to 5 A g^{-1}) were calculated and at 0.5 A g^{-1} was found to be 74 and 78 F g^{-1} respectively, showing that the introduction of ACN into the electrolyte can enhance the specific capacity. The high capacity in AWIS is attributed to the excellent ion transport from the electrolyte to the active material surface.

Table 7.3: EIS fitting results of $Na_{0.44}MnO_2$ in WIS and AWIS electrolytes.

Electrolytes	WIS	AWIS
R_s (Ω)	0.21 ± 0.10	0.73 ± 0.02
R_{ct} (Ω)	4.36 ± 0.35	4.15 ± 0.24
R_{int} (Ω)	109.63 ± 3.48	79.98 ± 3.03
***CPE_{ct}* (F. s^(a-1))**	17.44 ± 1.00	4.14 ± 0.78
C_{dl} (F)	0.008 ± 0.001	24.31 ± 5.52
a	0.50	0.58

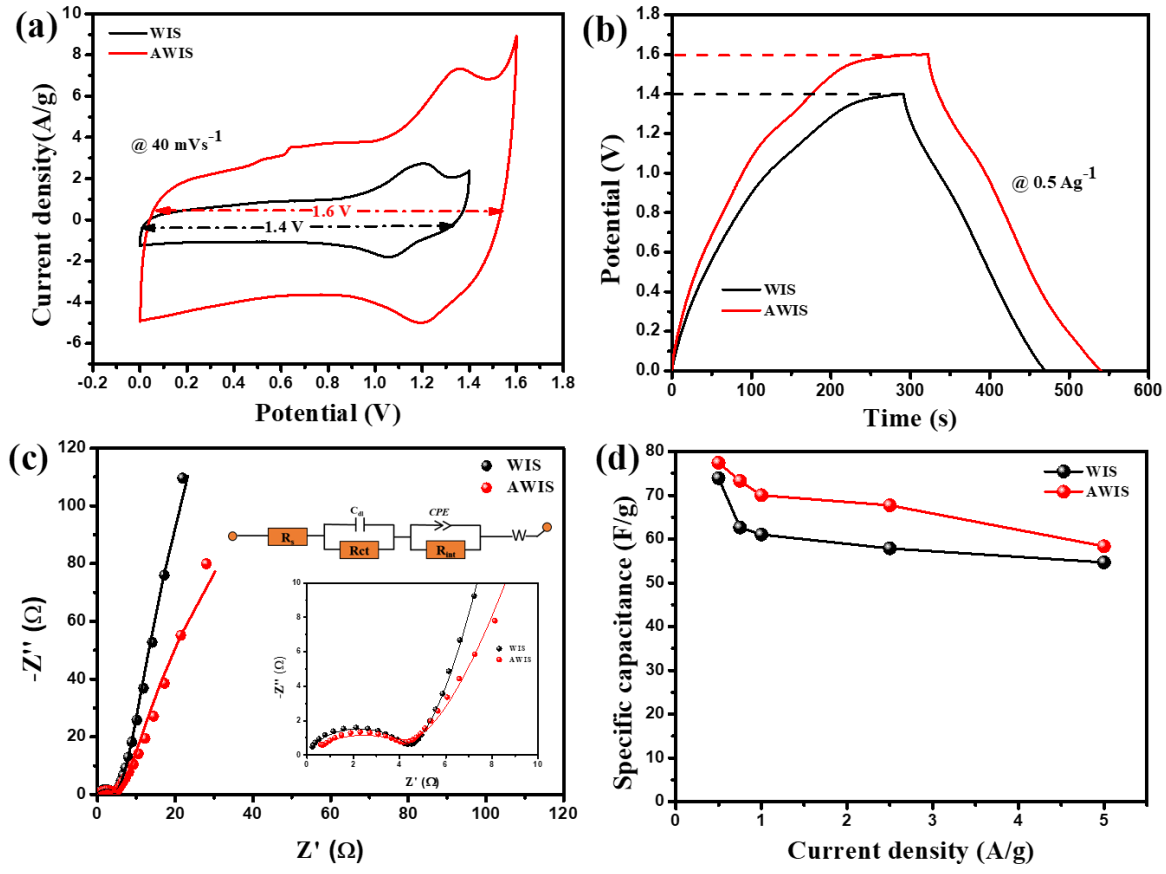


Figure 7.5: Half-cell electrochemical characterization of $Na_{0.44}MnO_2$ cathode material (a) CV plots of $Na_{0.44}MnO_2$ in different electrolytes collected at scan rates of 40 mV s^{-1}, (b) galvanostatic charging-discharging plots collected at the current density of 0.5 A g^{-1}, (c) EIS

measurements of $Na_{0.44}MnO_2$ electrode in different electrolytes (insert Randle circuit) and (d) variation of specific capacitance as a function of current density.

The electrochemical performance of N-rGO was carried out using the same electrolytes in a three-electrode system. **Figure 7.6a** demonstrates N-rGO has an excellent EDLCs characterization in both electrolytes. The GCD curves shown in **Figure 7.6b** also exhibit a symmetric triangular shape with a slightly higher discharge time in the AWIS electrolyte. These results show that N-rGO is more capacitive in AWIS than WIS electrolyte. To further investigate the influence of ACN as a co-solvent on electronic transport of the N-rGO, EIS was recorded out in both WIS and AWIS aqueous electrolytes. As shown in **Figure 7.6c**, the bulk solution resistance R_s and the charge transfer resistance R_{ct} can be obtained from the Nyquist plot, where the high-frequency semicircle intercepts the real axis at R_s and (R_s + R_{ct}) respectively. For N-rGO in AWIS electrolyte, a small semicircle in the high-frequency region and a straight line in the low-frequency region with a small intercept can be found. Compared with WIS electrolyte, R_s for the N-rGO in both electrolytes remained close to 0.5 Ω, however, R_{ct} after the introduction of ACN co-solvent decreases abruptly from 5.23 to 3.38 Ω. The EIS results suggest that the introduction of ACN as a co-solvent helps reduce the internal resistance and increase the electrons transfer and electrolyte ions transport rate in the diffusion layer, which enhanced the specific capacitance. **Table 7.4** below shows the EIS parameters after fitting.

Table 7.4: EIS fitting results of N-rGO in WIS and AWIS electrolytes.

Electrolytes	WIS	AWIS
$\mathbf{R_s}$ **(Ω)**	0.52 ± 0.67	0.062 ± 1.06
$\mathbf{R_{cs}}$ **(Ω)**	1.61 ± 7.05	1.12 ± 2.63
$\mathbf{R_{ct}}$ **(Ω)**	5.23 ± 39.17	3.38 ± 0.91
$\mathbf{R_{int}}$ **(Ω)**	633030 ± 391.7	99.76 ± 233.4
$\boldsymbol{CPE_{sc}}$ **(F. s^(a-1))**	0.09 ± 0.11	0.02 ± 0.11
$\boldsymbol{CPE_{ct}}$ **(F. s^(a-1))**	0.65 ± 3.99	23.74 ± 0.16
$\mathbf{C_{dl}}$ **(F)**	0.02 ± 1.11	0.11 ± 0.05
a	0.86	1.00
$\boldsymbol{\chi^2}$	0.098	0.104

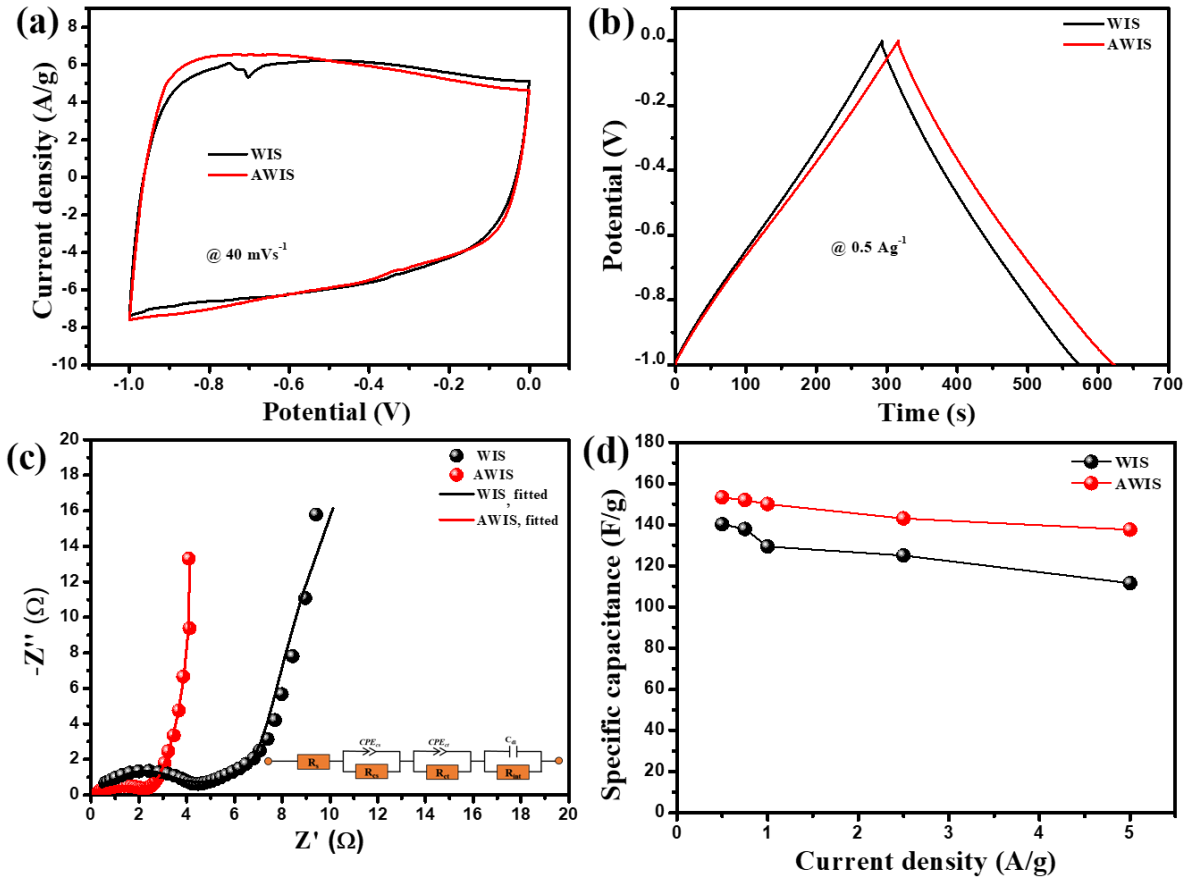


Figure 7.6: Half-cell electrochemical characterization of N-rGO anode material (a) CV plots of N-rGO in different electrolytes collected at scan rates of 40 mV s^{-1}, (b) galvanostatic charging-discharging plots collected at the current density of 0.5 A g^{-1}, (c) EIS measurements of N-rGO electrode in different electrolytes and (d) variation of specific capacitance as a function of current density.

Figure 7.6d shows the specific capacitance at different current densities. The capacitance values of N-rGO in both electrolytes decrease with increasing current density. The capacitance of the N-rGO in AWIS electrolyte remains essentially the same (*cf*. 153 F g^{-1} at 0.5 A g^{-1} versus 138 F g^{-1} at 5 A g^{-1}, which is about 10% capacitance loss). This ability of the N-rGO in AWIS electrolyte to maintain high capacitance even at high current density is indicative of excellent capacity retention and high-power performance. The appreciable electrochemical performance of N-rGO justifies its selection for anode material in an ASC.

7.4.1.1 N-rGO//$Na_{0.44}MnO_2$ asymmetric supercapacitor characteristics

An aqueous asymmetric supercapacitor (ASC) device consisting of $Na_{0.44}MnO_2$ and N-rGO as the positive and negative electrode was assembled in a two-electrode system (full-cell) to test the electrochemical performance of N-rGO//$Na_{0.44}MnO_2$ in AWIS electrolyte. The mass ratio of electroactive material for the positive and negative electrode was calculated according to the charge balance relation shown in equations 7.1 and 7.2:

$$q^+ = q^- \tag{7.1}$$

where q^+ and q^- are the charges at the cathode and anode, respectively. The optimal mass ratio, equation 7.2 was obtained using equation 7.1:

$$\frac{m^+}{m^-} = \frac{C^-}{C^+} + \frac{\Delta V^-}{\Delta V^+} \tag{7.2}$$

where m^+, V^+ and C^+ denote the mass, potential window and specific capacitance of the cathode, respectively and m^-, V^- and C^- denote the mass, potential window and specific capacitance of the anode, respectively. Gravimetric specific capacitance (C_s), were calculated based on the following formulae in equation 7.3:

$$C_s = \frac{I \times \Delta t}{m \times \Delta V} \ (F\ g^{-1}) \tag{7.3}$$

where C_s is the gravimetric capacitance, I (in ampere) is the discharge current, Δt (in second) is the discharge time, m (in g) is the mass of both electrodes, ΔV is the potential window. The corresponding gravimetric energy density (E_s) and power density (P_s) were obtained from equations 7.4 and 7.5, respectively.

$$E_s = \frac{0.5 C_s \times \Delta V^2}{3.6} \ (Wh\ kg^{-1}) \tag{7.4}$$

$$P_s = \frac{E_s \times 3600}{\Delta t} \ (W\ kg^{-1}) \qquad (7.5)$$

The electrochemical calculations were carried out based on the total mass of the electrode materials in the ASC. **Figure 7.7a** shows the typical CV plots of the individual electrodes (N-rGO and $Na_{0.44}MnO_2$) recorded at a scan rate of 40 mV s^{-1} in the potential windows of −1 to 0.0 V and 0.0 to1.6 V, respectively. The rectangular-shaped CV curve of the N-rGO electrode showed an electric double layer capacitance, whereas the distorted CV curve of $Na_{0.44}MnO_2$ reveals a pseudocapacitance behaviour in addition to the double layer effect of MnO_2. Since N-rGO and $Na_{0.44}MnO_2$ can store electric charges in the potential windows of −1.0 V and 1.6 V, respectively, the ASC built from these electrodes can be expected to work from 0 to 2.6 V, however, due to the use of water-in-salt electrolyte, the maximum voltage window was 3.0 V (see **Supporting Information**, **Figure S2a in Appendix D**). **Figure 7.7b** shows the CV curves of the ASC cell plotted at scan rates of 10, 20, 40, 60, 80 and 100 mV s^{-1} in the voltage window of 0–3.0 V. All the CV plots are similar in shape, maintaining a pair of cathodic and anodic peaks. In addition, these redox peaks are shifted away from each other as the scan rates increases. This is indicative of the pseudo-capacitive nature of an ASC and dominates the double layer contribution of N-rGO enormously, which is very clear from the large area of corresponding CV plots. The GCD curves of the ASC are plotted in **Figure 7.7c** at current densities of 0.75, 1, 1.5, 2.5 and 5 A g^{-1}, within the voltage window of 0–3.0 V. Additionally, the nonlinear GCD plots support the fast and reversible redox peaks recorded in the CV plots. **Figure 7.7d** show estimated specific capacitances at different current densities. The highest value of specific capacitance, i.e., 61 F g^{-1}, was achieved at a current density of 0.75 A g^{-1} with a reduction to 25 F g^{-1} at a current density of 5 A g^{-1}. The decrease in capacitance is attributed to the low utilization efficiency of active materials under high discharge currents.

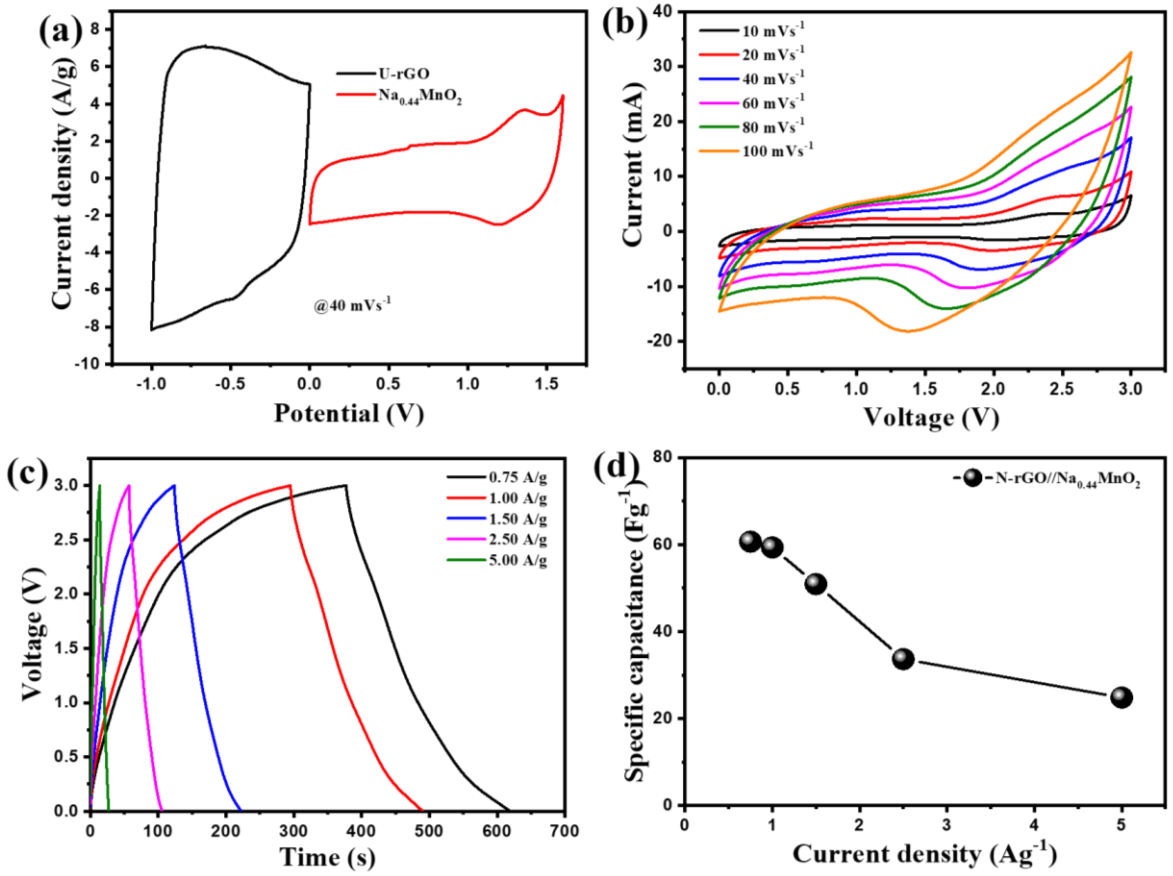


Figure 7.7: Electrochemical properties of the assembled ASC N-rGO//$Na_{0.44}MnO_2$ with AWIS as electrolyte (a) CV plots of negative electrode prepared using nitrogen-doped graphene oxide and positive electrode prepared using $Na_{0.44}MnO_2$ at a scan rate of 40 mV s^{-1} in AWIS electrolyte, (b) CV plots of ASC cell recorded at different scan rates, (c) GCD plots recorded at different current densities and (d) specific capacitance of at different current densities.

The capacity retention and coulombic efficiency of the ASC are shown in **Figure 7.8a**. The first and last ten cycles of the GCD curves is shown in the inset of **Figure 7.8a**. The cyclic stability determines the use of an ASC device in the industry. Here, the designed ASC was subjected to 1,900 GCD cycles at a current density of 5 A g^{-1}. It was found that ASC retains its specific capacitance by 68 % with improving coulombic efficiency ($\eta = td/tc \times 100$), higher than the initial cycles (94–98%). The EIS parameters before and after 1,900 cycles (modelled with the simple Randles electrical equivalent circuit, EEC, insert in **Figure 7.8b**) include: (i) bulk resistance (R_s) due to the combined resistances arising from the current collectors,

electrodes, electrolyte and separator, (ii) charge-transfer resistance (R_{ct}) due to electron transport, (iii) interfacial resistance (R_{int}) due to IR drop and (iv), (CPE) due to inhomogeneous or irregular structure or morphology of the electrode surfaces and (C_{dl}) due to double-layer capacitance. The modelled parameters are summarized in **Table 7.5**. After the 1,900th cycle, the R_s and R_{ct} values increased from 0.21 and 3.90 to 2.58 and 7.63, respectively, suggesting that there was a formation of solid electrolyte interface (SEI) and recrystallization of the electrolyte (see **Supporting Information**, **Figure S4b in Appendix D)**, resulting in a decrease electrolyte ion mobility. The "*a*" values from CPE increased from 0.83 (before cycling) to 0.87 (after 1,900 cycles), indicating that the electrode materials retain their mixed pseudocapacitance. Changes in the EEI layer can also be calculated from the power capability of an asymmetric device before and after long-term cycling by examining the knee frequency (f_o/Hz) [40]. The presence of a high f_o value indicates that the ASC device has a high-power density. The ASC device showed a higher f_o value before cycling (ca. 82.08 Hz, response time, τ, 12.18 ms) than after the 1,900th cycle (ca. 16.92 Hz, 59.10 ms). The SEI layer of the electrodes is also confirmed by this huge difference in response times. The Bode plots shown in **Figure 7.8c**, illustrate the phase angles of the N-rGO//$Na_{0.44}MnO_2$ ASC device before (-71^o) and after 1,900 cycles (-79^o), confirming the poor ion diffusion process.

Table 7.5: EIS parameters for N-rGO//$Na_{0.44}MnO_2$ asymmetric cell before and after the 1,900th cycles.

EIS parameters	**N-rGO//$Na_{0.44}MnO_2$ device**	
	Before 1,900 cycles	**After 1,900 cycles**
R_s / Ω	0.21 ± 0.04	2.58 ± 0.37
R_{ct} / Ω	3.90 ± 0.40	7.63 ± 0.45
C_{dl}/*uF*	7.60 ± 4.84	12.65 ± 3.88
R_{int} / Ω	98.36 ± 14.05	59.72 ± 39.00
a	0.83	0.87
CPE / mF. s^(a-1)	14.55 ± 0.33	29.18 ± 1.84
f_o / Hz	82.08	16.92
τ / ms	12.18	59.10
Phase angle	-71°	-79°

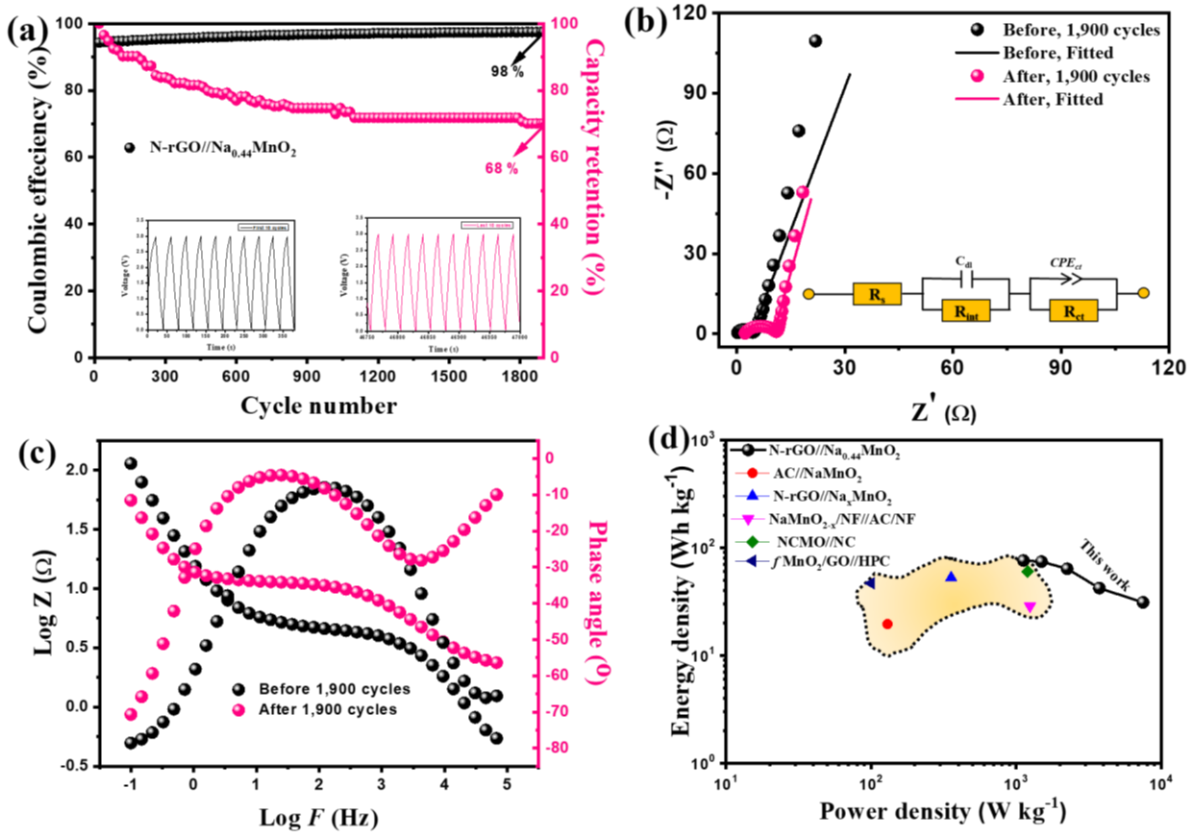


Figure 7.8: (a) Coulombic efficiency and capacity retention for 1,900 GCD cycles carried out at a current density of 5 A g^{-1}, (b) EIS measurement before and after 1,900 cycles, (c) Bode plots before and after 1,900 cycles of the N-rGO//$Na_{0.44}MnO_2$ device and (d) Ragone plot of the supercapacitor (energy density *vs*. power density).

The Ragone plot of the N-rGO//$Na_{0.44}MnO_2$ ASC device is shown in **Figure 7.8d** and the values of E_s and P_s are calculated from the GCD curves at different current densities according to equation 7.4 and 7.5. The energy density of the N-rGO//$Na_{0.44}MnO_2$ ASC device can reach up to 75.8 W h kg^{-1} at a power density of 1125 W kg^{-1} and remains 31 W h kg^{-1} at a power density of 7500 W kg^{-1}. This is a good energy density compared to other MnO_2-based asymmetric supercapacitors reported in literatures, such as AC//$NaMnO_2$ [7], N-rGO//Na_xMnO_2 [27], $NaMnO_{2-x}$/NF//AC/NF [41], NCMO//NC [42] and MnO_2/GO//HPC [43]. The excellent specific capacitance, cyclic stability performance and columbic efficiency of the ASC is attributed to the defects in N-rGO and well-crystallized $Na_{0.44}MnO_2$ nanowires. The $Na_{0.44}MnO_2$ nanowires provide a large ion accessible surface for electrolyte ions diffusion and

insertion–desertion. Moreover, the assembled $Na_{0.44}MnO_2$ and highly conductive N-rGO facilitate the electronic charge transport between poorly conducting $Na_{0.44}MnO_2$ and the current collector.

7.5 Summary

In this work, an asymmetric supercapacitor device operable in a "water-in-salt" electrolyte is developed, using $Na_{0.44}MnO_2$ nanowires and N-rGO as positive and negative electrodes, respectively. The N-rGO//$Na_{0.44}MnO_2$ ASC device can be operated reversibly in a wide potential between 0 and 3 V in AWIS aqueous electrolyte and exhibits a maximum specific capacitance of 61 F g^{-1}. The energy density of 75.8 Wh kg^{-1} at a power density of 1125 W kg^{-1} was obtained and still remains 31 Wh kg^{-1} at a power density of 7500 W kg^{-1}. Meanwhile, such asymmetric supercapacitor device also exhibits superior long cycle life along with ~68% specific capacitance retained after 1,900 cycles. These findings show how to build an asymmetric supercapacitor simply and effectively to meet the growing need for energy storage devices with high energy and power density.

7.6 References

[1] Lukatskaya, M.R., Feldblyum, J.I., Mackanic, D.G., Lissel, F., Michels, D.L., Cui, Y. and Bao, Z., 2018. Concentrated mixed cation acetate "water-in-salt" solutions as green and low-cost high voltage electrolytes for aqueous batteries. *Energy & Environmental Science*, **11**, pp.2876-2883.

[2] Chen, Z., Yuan, T., Pu, X., Yang, H., Ai, X., Xia, Y. and Cao, Y., 2018. Symmetric sodium-ion capacitor based on $Na_{0.44}MnO_2$ nanorods for low-cost and high-performance energy storage. *ACS Applied Materials & Interfaces*, **10**, pp.11689-11698.

[3] Lee, W.S.V., Peng, E., Li, M., Huang, X. and Xue, J.M., 2016. Rational design of stable 4 V lithium ion capacitor. *Nano Energy*, **27**, pp.202-212.

[4] Gao, Q., Demarconnay, L., Raymundo-Piñero, E. and Béguin, F., 2012. Exploring the large voltage range of carbon/carbon supercapacitors in aqueous lithium sulfate electrolyte. *Energy & Environmental Science*, **5**, pp.9611-9617.

[5] Li, K., Wang, X., Li, S., Urbankowski, P., Li, J., Xu, Y. and Gogotsi, Y., 2020. An ultrafast conducting polymer@MXene positive electrode with high volumetric capacitance for advanced asymmetric supercapacitors. *Small*, **16**, p.1906851.

[6] Zhang, T., Zhang, F., Zhang, L., Lu, Y., Zhang, Y., Yang, X., Ma, Y. and Huang, Y., 2015. High energy density Li-ion capacitor assembled with all graphene-based electrodes. *Carbon*, **92**, pp.106-118.

[7] Qu, Q.T., Shi, Y., Tian, S., Chen, Y.H., Wu, Y.P. and Holze, R., 2009. A new cheap asymmetric aqueous supercapacitor: Activated carbon//$NaMnO_2$. *Journal of Power Sources*, **194**, pp.1222-1225.

[8] Yang, S., Zhang, F., Ding, H., He, P. and Zhou, H., 2018. Lithium metal extraction from seawater. *Joule*, **2**, pp.1648-1651.

[9] Choubey, P.K., Chung, K.S., Kim, M.S., Lee, J.C. and Srivastava, R.R., 2017. Advance review on the exploitation of the prominent energy-storage element Lithium. Part II: From sea water and spent lithium ion batteries (LIBs). *Minerals Engineering*, **110**, pp.104-121.

[10] Zhao, C., Liu, L., Qi, X., Lu, Y., Wu, F., Zhao, J., Yu, Y., Hu, Y.S. and Chen, L., 2018. Solid-state sodium batteries. *Advanced Energy Materials*, **8**, p.1703012.

[11] Ferrara, C., Tealdi, C., Dall'Asta, V., Buchholz, D., Chagas, L.G., Quartarone, E., Berbenni, V. and Passerini, S., 2018. High-Performance $Na_{0.44}MnO_2$ Slabs for sodium-Ion batteries obtained through urea-based solution combustion synthesis. *Batteries*, **4**, p.8.

[12] Palomares, V., Serras, P., Villaluenga, I., Hueso, K.B., Carretero-González, J. and Rojo, T., 2012. Na-ion batteries, recent advances and present challenges to become low cost energy storage systems. *Energy & Environmental Science*, **5**, pp.5884-5901.

[13] Ong, S.P., Chevrier, V.L., Hautier, G., Jain, A., Moore, C., Kim, S., Ma, X. and Ceder, G., 2011. Voltage, stability and diffusion barrier differences between sodium-ion and lithium-ion intercalation materials. *Energy & Environmental Science*, **4**, pp.3680-3688.

[14] Kim, H., Kim, H., Ding, Z., Lee, M.H., Lim, K., Yoon, G. and Kang, K., 2016. Recent progress in electrode materials for sodium-ion batteries. *Advanced Energy Materials*, **6**, p.1600943.

[15] Xiang, X., Zhang, K. and Chen, J., 2015. Recent advances and prospects of cathode materials for sodium-ion batteries. *Advanced Materials*, **27**, pp.5343-5364.

[16] Li, Z., Young, D., Xiang, K., Carter, W.C. and Chiang, Y.M., 2013. Towards high power high energy aqueous sodium-ion batteries: the $NaTi_2(PO_4)_3/Na_{0.44}MnO_2$ system. *Advanced Energy Materials*, **3**, pp.290-294.

[17] Hung, T.F., Lan, W.H., Yeh, Y.W., Chang, W.S., Yang, C.C. and Lin, J.C., 2016. Hydrothermal synthesis of sodium titanium phosphate nanoparticles as efficient anode materials for aqueous sodium-ion batteries. *ACS Sustainable Chemistry & Engineering*, **4**, pp.7074-7079.

[18] He, X., Wang, J., Qiu, B., Paillard, E., Ma, C., Cao, X., Liu, H., Stan, M.C., Liu, H., Gallash, T. and Meng, Y.S., 2016. Durable high-rate capability $Na_{0.44}MnO_2$ cathode material for sodium-ion batteries. *Nano Energy*, **27**, pp.602-610.

[19] Ghidiu, M., Lukatskaya, M.R., Zhao, M.Q., Gogotsi, Y. and Barsoum, M.W., 2014. Conductive two-dimensional titanium carbide 'clay' with high volumetric capacitance. *Nature*, **516**, pp.78-81.

[20] Dou, Q., Lei, S., Wang, D.W., Zhang, Q., Xiao, D., Guo, H., Wang, A., Yang, H., Li, Y., Shi, S. and Yan, X., 2018. Safe and high-rate supercapacitors based on an "acetonitrile/water in salt" hybrid electrolyte. *Energy & Environmental Science*, **11**, pp.3212-3219.

[21] Dou, Q., Liu, L., Yang, B., Lang, J. and Yan, X., 2017. Silica-grafted ionic liquids for revealing the respective charging behaviors of cations and anions in supercapacitors. *Nature Communications*, **8**, pp.1-9.

[22] Huang, J., Guo, Z., Ma, Y., Bin, D., Wang, Y. and Xia, Y., 2019. Recent progress of rechargeable batteries using mild aqueous electrolytes. *Small Methods*, **3**, p.1800272.

[23] Wang, Y., Meng, X., Sun, J., Liu, Y. and Hou, L., 2020. Recent progress in "Water-in-salt" electrolytes toward non-lithium based rechargeable batteries. *Frontiers in Chemistry*, **8**.

[24] Yamada, Y., Usui, K., Sodeyama, K., Ko, S., Tateyama, Y. and Yamada, A., 2016. Hydrate-melt electrolytes for high-energy-density aqueous batteries. *Nature Energy*, **1**, pp.1-9.

[25] Zhang, M., Li, Y. and Shen, Z., 2019. "Water-in-salt" electrolyte enhanced high voltage aqueous supercapacitor with all-pseudocapacitive metal-oxide electrodes. *Journal of Power Sources*, **414**, pp.479-485.

[26] Marcano, D.C., Kosynkin, D.V., Berlin, J.M., Sinitskii, A., Sun, Z., Slesarev, A., Alemany, L.B., Lu, W. and Tour, J.M., 2010. Improved synthesis of graphene oxide. *ACS Nano*, **4**, pp.4806-4814.

[27] Yang, Z., Vinodh, R., Balakrishnan, B., Rajmohan, R. and Kim, H.J., 2020. Rational design of asymmetric aqueous supercapacitor based on Na_XMnO_2 and N-doped reduced graphene oxide. *Journal of Energy Storage*, **28**, p.101293.

[28] Hou, L., Chen, Z., Zhao, Z., Sun, X., Zhang, J. and Yuan, C., 2018. Universal $FeCl_3$-activating strategy for green and scalable fabrication of sustainable biomass-derived hierarchical porous nitrogen-doped carbons for electrochemical supercapacitors. *ACS Applied Energy Materials*, **2**, pp.548-557.

[29] Díez, N., Śliwak, A., Gryglewicz, S., Grzyb, B. and Gryglewicz, G., 2015. Enhanced reduction of graphene oxide by high-pressure hydrothermal treatment. *RSC Advances*, **5**, pp.81831-81837.

[30] Ferrari, A.C. and Robertson, J., 2000. Interpretation of Raman spectra of disordered and amorphous carbon. *Physical Review B*, **61**, p.14095.

[31] Oliveira, A.E.F., Braga, G.B., Tarley, C.R.T. and Pereira, A.C., 2018. Thermally reduced graphene oxide: synthesis, studies and characterization. *Journal of Materials Science*, **53**, pp.12005-12015.

[32] Tsaneva, V.N., Kwapinski, W., Teng, X. and Glowacki, B.A., 2014. Assessment of the structural evolution of carbons from microwave plasma natural gas reforming and biomass pyrolysis using Raman spectroscopy. *Carbon*, **80**, pp.617-628.

[33] Johra, F.T., Lee, J.W. and Jung, W.G., 2014. Facile and safe graphene preparation on solution based platform. *Journal of Industrial and Engineering Chemistry*, **20**, pp.2883-2887.

[34] Shen, Y. and Lua, A.C., 2013. A facile method for the large-scale continuous synthesis of graphene sheets using a novel catalyst. *Scientific Reports*, **3**, pp.1-6.

[35] Xing, Z., Ju, Z., Zhao, Y., Wan, J., Zhu, Y., Qiang, Y. and Qian, Y., 2016. One-pot hydrothermal synthesis of Nitrogen-doped graphene as high-performance anode materials for lithium ion batteries. *Scientific Reports*, **6**, pp.1-10.

[36] Wang, X., Sun, G., Routh, P., Kim, D.H., Huang, W. and Chen, P., 2014. Heteroatom-doped graphene materials: syntheses, properties and applications. *Chemical Society Reviews*, **43**, pp.7067-7098.

[37] Shen, X., Lin, X., Yousefi, N., Jia, J. and Kim, J.K., 2014. Wrinkling in graphene sheets and graphene oxide papers. *Carbon*, **66**, pp.84-92.

[38] Noh, J., Yoon, C.M., Kim, Y.K. and Jang, J., 2017. High performance asymmetric supercapacitor twisted from carbon fibre/MnO_2 and carbon fibre/MoO_3. *Carbon*, **116**, pp.470-478.

[39] Sun, Y., Wang, Y., Liu, L., Liu, B., Zhang, Q., Wu, D., Zhang, H. and Yan, X., 2020. Towards the understanding of acetonitrile suppressing salt precipitation mechanism in a water-in-salt electrolyte for low-temperature supercapacitors. *Journal of Materials Chemistry A*, **8**, pp.17998-18006.

[40] Chidembo, A.T., Ozoemena, K.I., Agboola, B.O., Gupta, V., Wildgoose, G.G. and Compton, R.G., 2010. Nickel (II) tetra-aminophthalocyanine modified MWCNTs as potential nanocomposite materials for the development of supercapacitors. *Energy & Environmental Science*, **3**, pp.228-236.

[41] Xu, S., Wan, T., Zhou, K.B., Zhu, G.M., He, Z.Q., Huang, H.B., Zhou, T., Mao, W.Q., Wu, J.J., Gong, S.K. and Qiao, Y.X., 2020. $NaMnO_{2-x}$ thin nanosheets assembled microspheres as electrode for aqueous asymmetric supercapacitor. *Materials Research Express*, **7**, p.035508.

[42] Wei, X., Peng, H., Li, Y., Yang, Y., Xiao, S., Peng, L., Zhang, Y. and Xiao, P., 2018. In situ growth of ZIF-67-derived nanoporous carbon@$K_{0.5}Mn_2O_4$ for high-performance 2.4 V aqueous asymmetric supercapacitors. *ChemSusChem*, **11**, pp.3167-3174.

[43] Zhao, Y., Ran, W., He, J., Huang, Y., Liu, Z., Liu, W., Tang, Y., Zhang, L., Gao, D. and Gao, F., 2015. High-performance asymmetric supercapacitors based on multilayer MnO_2/graphene oxide nanoflakes and hierarchical porous carbon with enhanced cycling stability. *Small*, **11**, pp.1310-1319.

CHAPTER 8

Conclusions and recommendations

8.1 Conclusions

This research investigated the synthesis and characterization of a 3D hierarchical nitrogen-doped carbon nanotubes-carbon nanofiber hybrid as an improved electrode material for symmetric and asymmetric supercapacitors. The research focused on using 3D N-CNT@CT EDLCs in conjunction with battery-type (AT-Ni/MOFDC) and pseudocapacitive ($Na_{0.44}MnO_2$) materials to strengthen the performance of hybrid supercapacitors. The work included: (i) nitrogen-doping CNT@CF hybrid network for enhanced symmetric supercapacitor performance in an aqueous electrolyte; (ii) synthesizing and characterizing AT-Ni/MOFDC cathode material for hybrid asymmetric capacitors and (iii) synthesizing and characterizing $Na_{0.44}MnO_2$ cathode material for asymmetric capacitors. X-ray powder diffraction (XRD), Raman spectroscopy, scanning electron microscopy (SEM), transmission electron microscopy (TEM), Brunauer-Emmett-Teller (BET) analysis and X-ray photoelectron spectroscopy (XPS) were used to investigate the structural, morphological, porosity and compositional properties of the as-synthesised materials. For all the materials, electrochemical tests such as cyclic voltammetry (CV), galvanostatic charge-discharge (GCD), electrochemical impedance spectroscopy (EIS) and cycle stability test were evaluated using aqueous electrolytes. The results show that when the 3D N-CNT@CT electrodes were assembled into a symmetric cell and operated in an aqueous electrolyte (6 M KOH) a relatively high energy density of 5.5 Wh kg^{-1} and a power density of 254 W kg^{-1} were obtained. In addition, a demonstration for its

practical application, using LED bulb indicates the great potential application in energy storage/management for small and lightweight electronics.

We also have successfully fabricated AT-Ni/MOFDC battery-type electrode material. In a three-electrode configuration, the AT-Ni/MOFDC exhibits superior electrochemical properties in terms of lowered series resistance and high specific capacity as compared to the untreated analogue (Ni/MOFDC). Furthermore, it was demonstrated that the Faradaic and non-Faradaic processes control the energy-storage mechanism of this novel Ni-based electrode material, which is something that is often misrepresented in the literature. The electrochemical properties of the N-CNT@CF//AT-Ni/MOFDC hybrid capacitor was also studied using cyclic voltammetry (CV), galvanostatic charge-discharge and impedance measurements. Results showed that the N-CNT@CT//AT-Ni/MOFDC hybrid supercapacitor has a greater capacitance, rate capability and cycling stability as compared to the N-CNT@CT//N-CNT@CT symmetric cell.

The two-step synthetic techniques: Couette-Taylor flow reactor and hydrothermal method were used to successfully synthesize $Na_{0.44}MnO_2$ cathode material. The electrochemical properties of the material were investigated using a three-electrode device in 1M Na_2SO_4, 3M NaOH and 3M KOH electrolytes. Due to high conductivity and intercalation/de-intercalation like behaviour in 3 M KOH electrolyte, the $Na_{0.44}MnO_2$ delivered a maximum capacitance of 108 F g^{-1}. An asymmetric full cell (N-CNT@CF//$Na_{0.44}MnO_2$) was also fabricated using 3M KOH as electrolyte and demonstrated better electrochemical performance compared to its counterparts. In addition, the cell delivered a high gravimetric and volumetric specific capacitance (47 F g^{-1}, 86 F cm^{-3}), the energy density of (21 W h kg^{-1}) and power density of (450 W kg^{-1}) at 0.5 A g^{-1}.

Finally, an asymmetric supercapacitor device operated in a “water-in-salt” electrolyte was developed, using $Na_{0.44}MnO_2$ nanowires and N-rGO as positive and negative electrodes, respectively. The N-rGO//$Na_{0.44}MnO_2$ ASC device was operated in a wide potential between 0 and 3 V in AWIS aqueous electrolyte and exhibits a maximum specific capacitance of 61 F g^{-1}. The energy density of 75.8 Wh kg^{-1} at a power density of 1125 W kg^{-1} was obtained and still remains 31 Wh kg^{-1} at a power density of 7500 W kg^{-1}. These findings demonstrate that asymmetric supercapacitors can effectively be used to meet the growing need for energy storage devices with high energy and power density.

In summary, carbon nanomaterials with a porous structure and high electrical conductivity are of great interest for a wide range of applications. Designing and fabricating various carbon materials by combining different carbon nanomaterials to produce a hierarchical composite structure with superior properties is an excellent way to learn more about carbon materials. Such composite structures will be very useful for multidisciplinary applications such as energy storage devices, energy conversion devices, and capacitive deionization of water and so on, implying the potential for more research in this area to solve many environmental issues.

8.2 Recommendations for future work

Additional research is necessary to further explore the properties of the investigated materials to improve them. These future studies should include:

- Investigation of the effect of different nitrogen concertation on electrochemical properties of N-CNT@CT.
- Study of the AT/NiMOFDC cathode material with other anode materials in an asymmetric configuration to further enlarge the energy and power densities.
- Characterize the WIS and AWIS electrolytes using FTIR and Raman spectroscopy.

- Power LID bulb using N-rGO//$Na_{0.44}MnO_2$ ASC device.

APPENDIX A

Supporting information for Chapter 4.

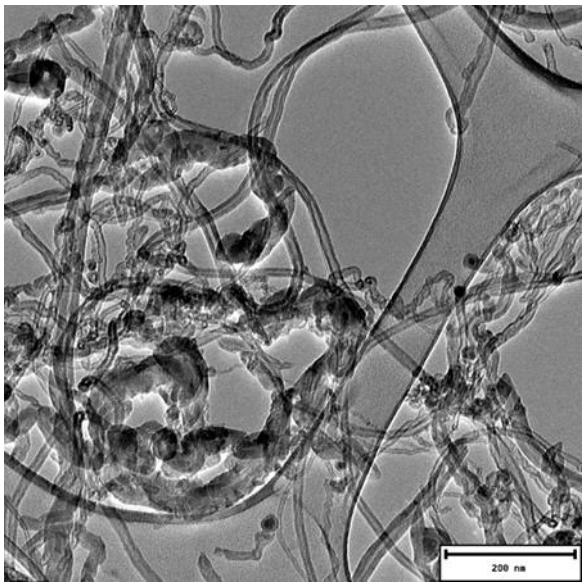


Figure S1: TEM image of reference CNTs**.**

Table S1: Gaussian and Voigt spectral fitting parameters of the CFs, CNTs, CNT@CF, N-CNT@CF samples.

Samples	Centre	Height	FWHM	Area
CFs				
ϒ	20.0	4.70	4.56	22.8
CFs (002)	25.1	18.4	4.45	87.2
π	30.4	3.8	4.01	16.2
CNTs				
Peak 1	24.4	20.4	1.89	43
Peak 2	25.8	90.6	1.73	174.9
CNT@CF				
Peak 1	24.0	7.2	1.82	14.6
CFs (002)	25.5	20.1	1.41	31.4
CNTs (002)	26.6	117.4	1.05	136.9
N-CNT@CF				
CFs (002)	25.6	2.5	1.37	3.9
CNTs (002)	26.3	5.4	0.99	6.0

Table S2: Lorentzian and Gaussian fitted parameters of the G, D_1, D_3, D_4 and D_3 bands for the CFs, CNTs, CNT@CF, N-CNT@CF samples.

Bands	Position (cm^{-1})	Area	FWHM
CFs			
D_4	1169	2654.8	119.5
D_1	1347	24227.1	223.5
D_3	1543	7289.4	146
G	1579	6299.6	75.7
D_2	1608	1919.7	36.1
CNTs			
D_4	1289	5152.8	63.6
D_1	1352	13393.7	50
D_3	1478	8792.1	157.1
G	1581	7797.2	37.4
D_2	1609	25603.1	35.5
CNT@CF			
D_4	1277	8000.9	175.1
D_1	1340	84545.3	76.3
D_3	1485	1078.9	123.1
G	1572	47289.9	48.2
D_2	1601	3303.8	37.5
N-CNT@CF			
D_4	1171	9565.7	110.6
D_1	1347	193773	60
D_3	1523	15440.2	108
G	1583	72916.4	44
D_2	1611	21405.2	34.7

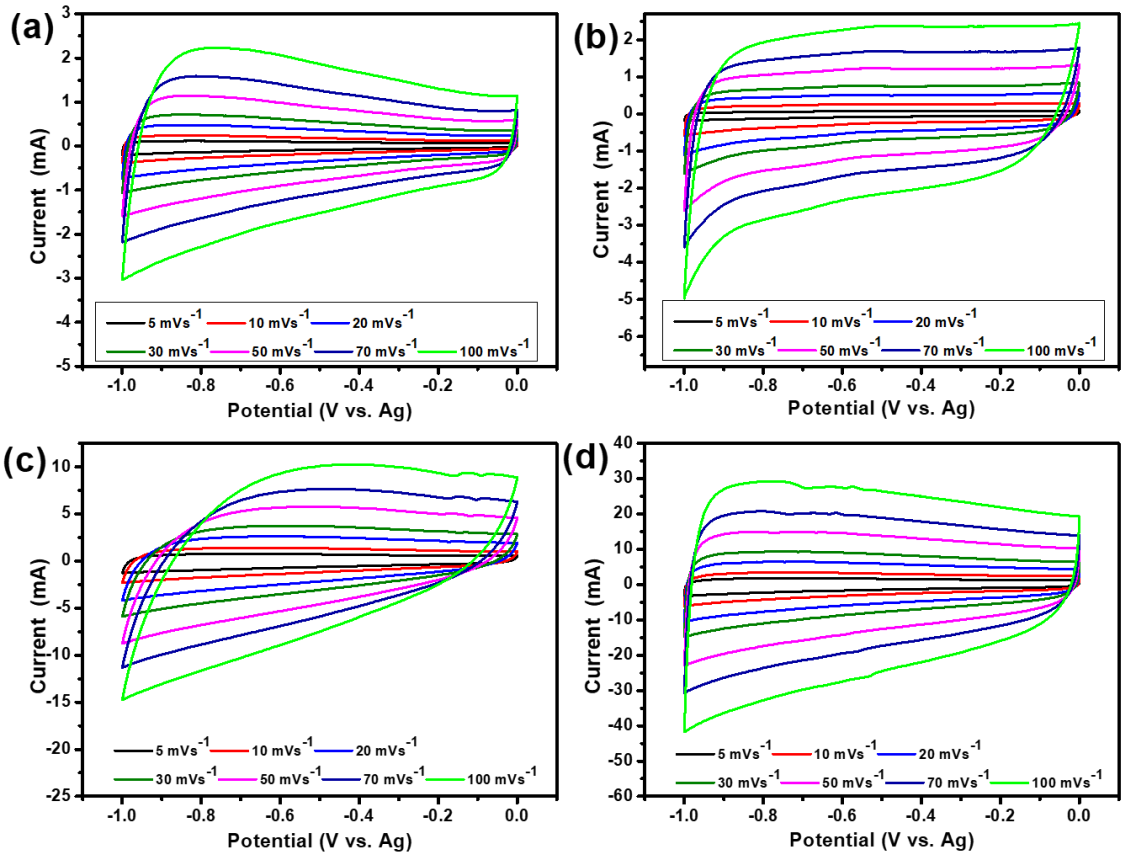


Figure S2: CV curves of (a) CFs, (b) CNTs, (c) CNT@CF and (d) N-CNT@CF network.

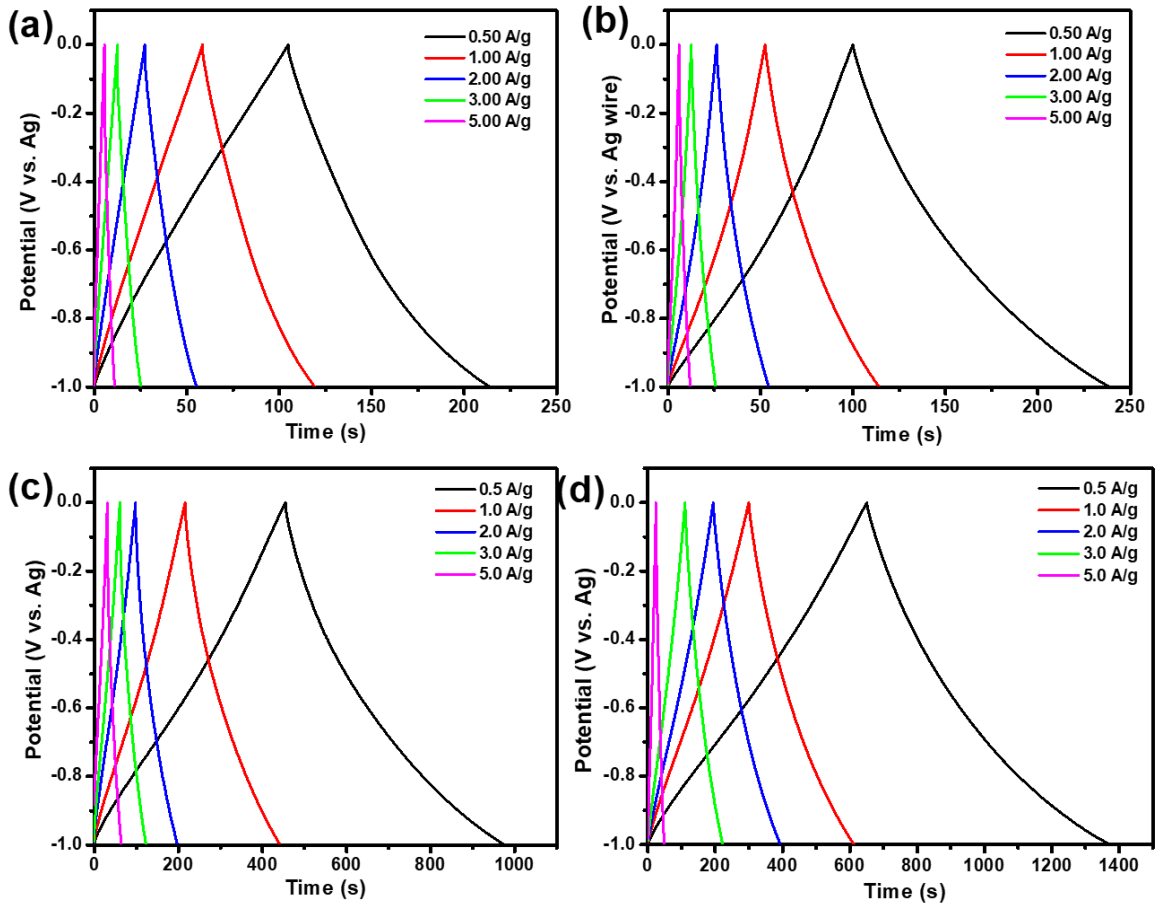


Figure S3: GCD curves of (a) CFs, (b) CNTs, (c) CNT@CF and (d) N-CNT@CF network.

Table S3: EIS parameters for the electrode materials for three-electrode systems

EIS parameters	Electrode materials			
	CFs	CNTs	CNT@CF	N-CNT@CF
R_s / Ω	0.42 ± 0.45	0.14 ± 0.43	0.32 ± 1.00	0.21 ± 0.76
ESR/R_{ct} / Ω	15.44 ± 1.00	2.74 ±0.45	8.45 ± 1.00	2.22 ± 0.54
C_{dl} / µF	5.56 ± 0.22	0.66 ± 0.84	9.28 ± 0.94	0.98 ± 0.92
R_{int} / Ω	18.02 ± 5.35	11.26 ± 21.81	41.05 ± 0.55	14.05 ± 0.85
CPE / mF.s^(***a***-1)	77.47 ± 83.56	10.12 ± 90.94	6.63 ± 0.62	16.39 ± 0.82
a	0.83	0.93	0.62	0.98
Z_w / Ω s^-1/2	-	-	94.41 ± 0.11	-

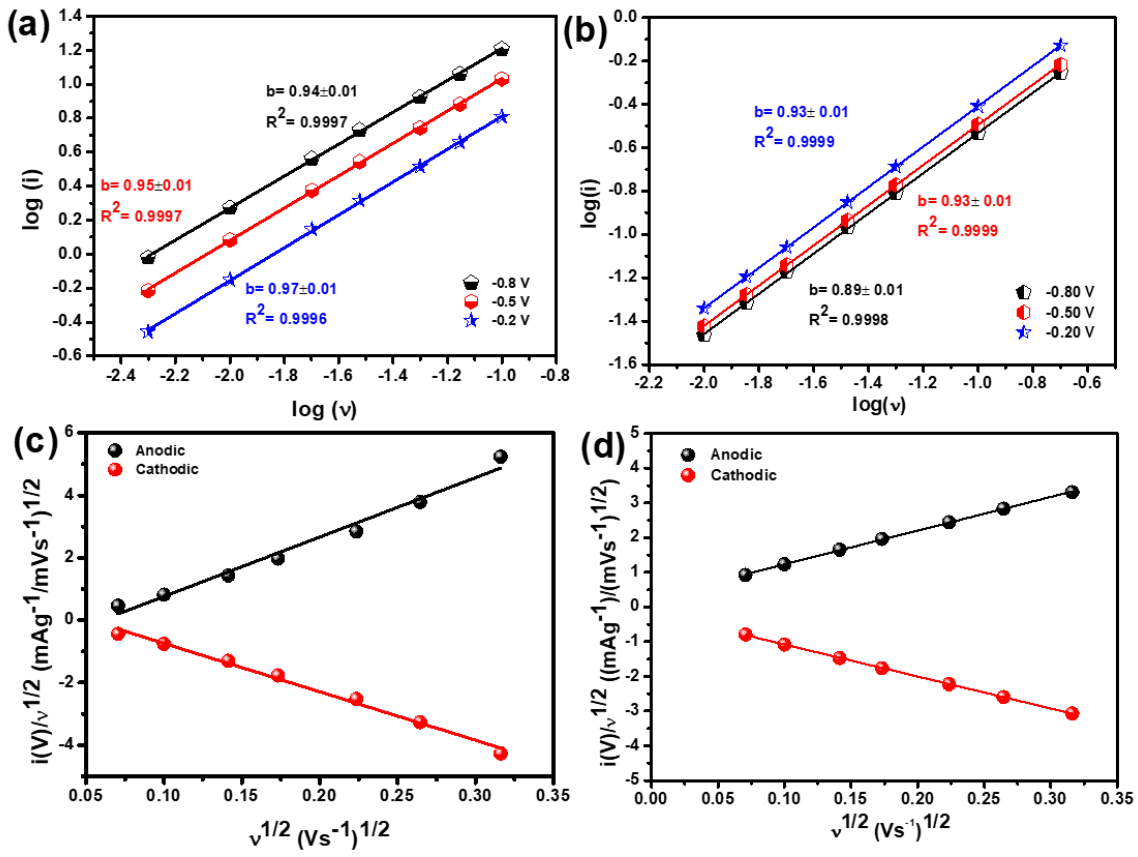


Figure S4: (a) Log peak current vs log scan rate for CNT@CF network anodic, (b) Log peak current vs log scan rate for N-CNT@CF network anodic, (c) $i/v^{1/2}$ vs. $v^{1/2}$ for CNT@CF network and (d) $i/v^{1/2}$ vs. $v^{1/2}$ N-CNT@CF network.

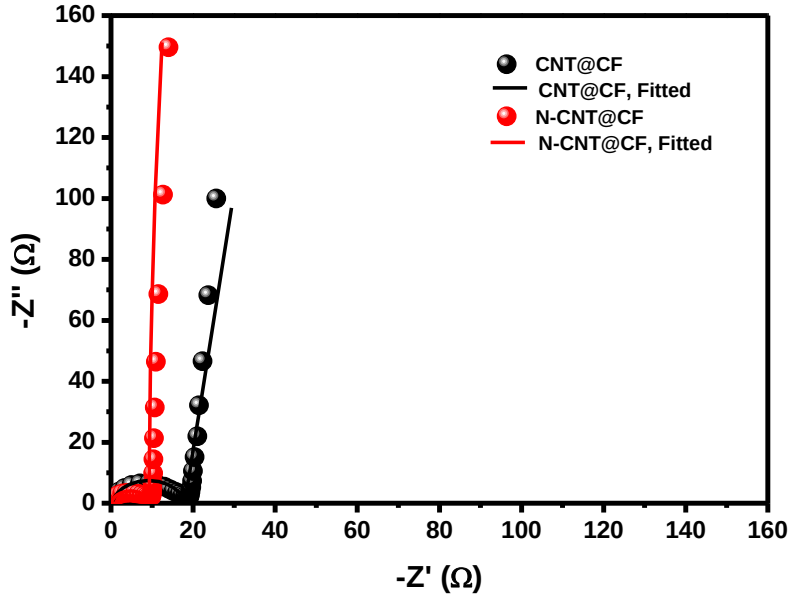


Figure S4: EIS measurements of CNT@CF and N-CNT@CF electrodes, before 10,000 cycles.

APPENDIX B

Supporting information for Chapter five.

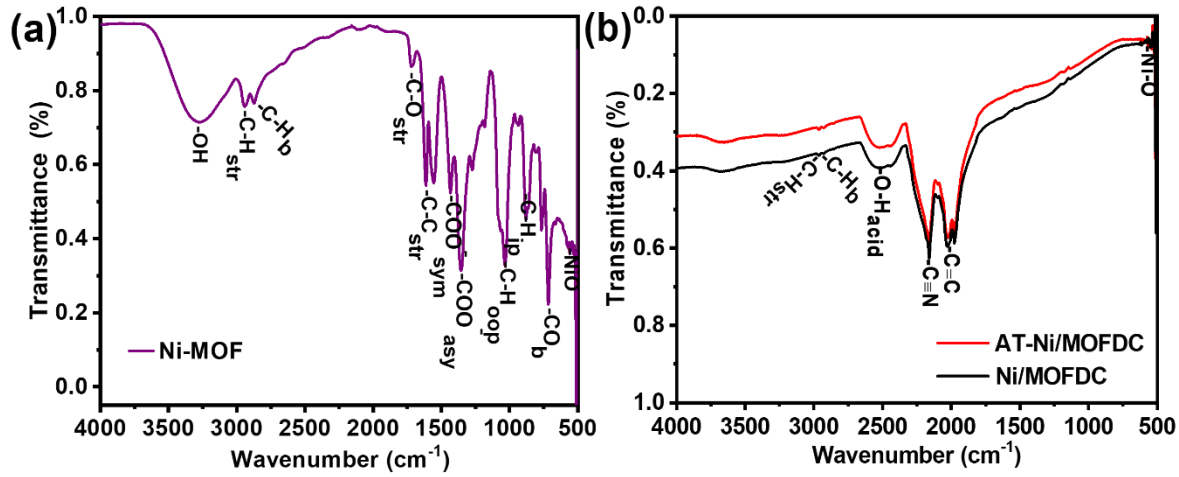


Figure S1: FTIR spectra (a) Ni-MOF, (b) Ni/MOFDC, and AT-Ni/MOFDC

The FTIR spectrum of the as-synthesized Ni-MOF (**Figure S1a**) shows the functional groups present in the formation of the sacrificial template. Absorption of the following functional groups: -OH stretching (3320 cm^{-1}), C-H stretching (2925 cm^{-1}), C-H bending (2865 cm^{-1}), C-H in-plane (869 cm^{-1}), C-H out-of-plane (1047 cm^{-1}), C-C stretching (1427 cm^{-1}), COO- symmetric vibrations (1568 cm^{-1}), COO- asymmetric vibrations (1365 cm^{-1}), CO bending vibrations (704 cm^{-1}), CO stretching vibration (1726 cm^{-1}) and Ni-O coordinate bond (548 cm^{-1}) confirm the formation of the as-synthesized Ni-MOF. After carbonization and/or chemically etching, the FTIR spectra (**Figure S1b**) show the same functional groups in the Ni/MOFDC and AT-MOFDC, which are Ni-O (548 cm^{-1}), C=C (2025.5 cm^{-1}), C≡N (2168.8 cm^{-1}), carboxylic acid O-H (2363.4 – 2680.0 cm^{-1}), C-H bending (2946.2 cm^{-1}) and C-H stretching (3100. 0 cm^{-1}), respectively. These results show that the frameworks of the MOF were broken down at high temperatures.

Table S1: Lorentzian and Gaussian fitted parameters of the G, D_1, D_2, D_3 and D_4 bands for the Ni/MOFDC and AT-Ni/MOFDC materials.

Bands	Position (cm^{-1})	Area	FWHM
Ni/MOFDC			
D_4	1219	2944.7	175.8
D_1	1344	8874.1	94.0
D_3	1478	4022.9	210.5
G	1575	4974.4	74.9
D_2	1605	1582.5	31.8
AT-Ni/MOFDC			
D_4	1229	508.5	105.9
D_1	1341	13522.4	97.2
D_3	1489	1294.8	101
G	1571	6341.3	37.2
D_2	1610	2630.9	41.4

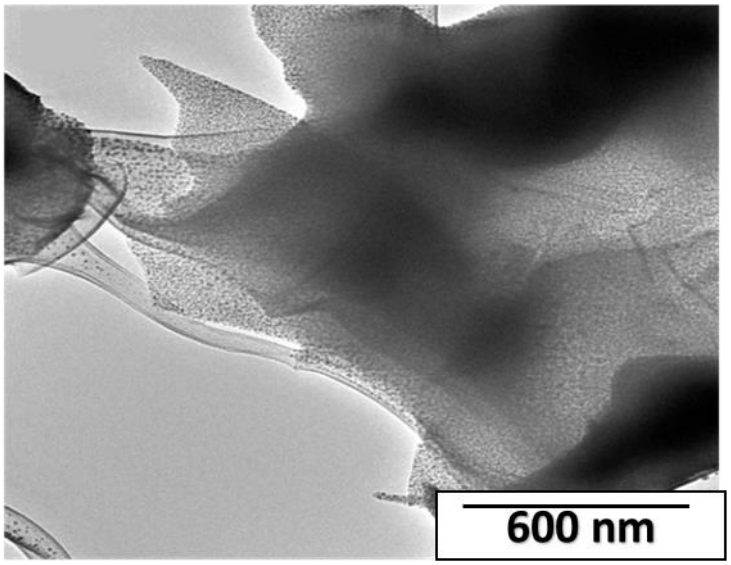


Figure S2: Typical TEM micrograph of as-prepared Ni-MOF in this work shows interconnecting pores distributed over the surface.

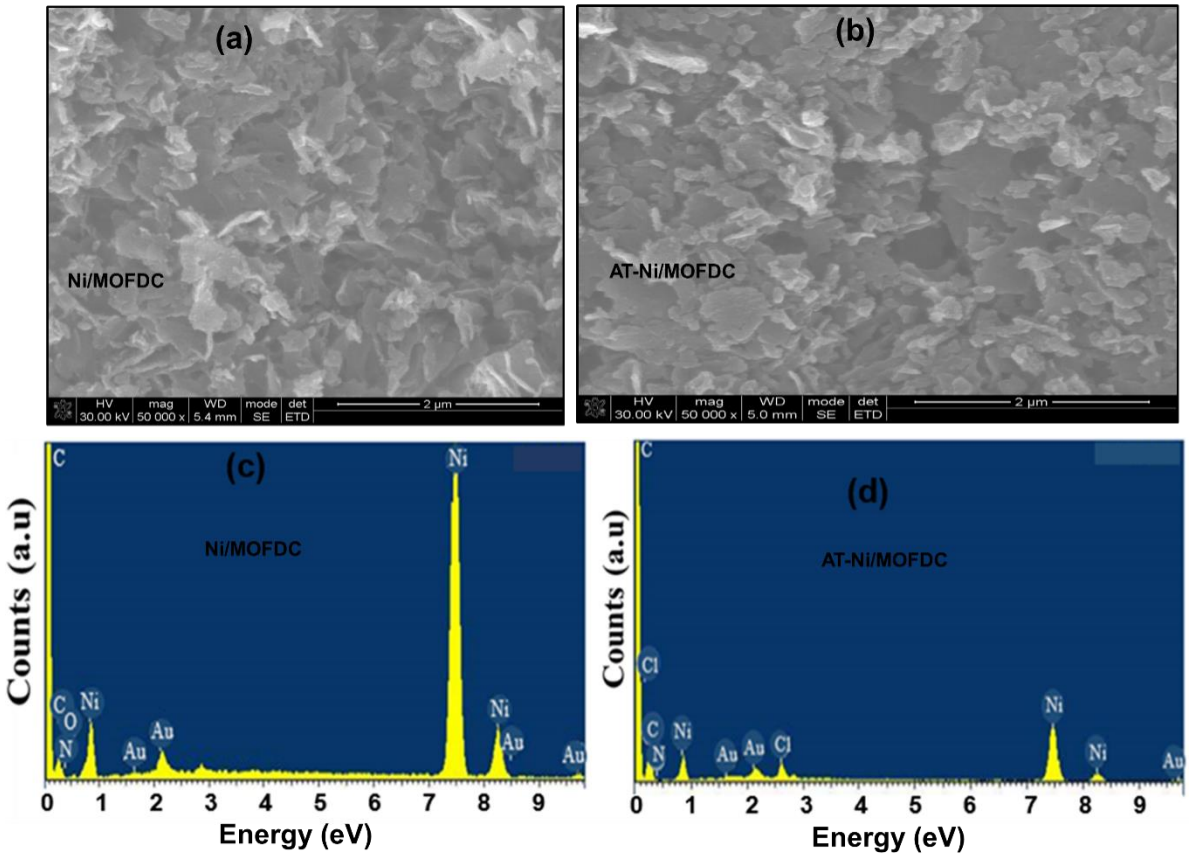


Figure S3: SEM images of the (a) Ni/MOFDC, (b) AT-Ni/MOFDC, EDS spectra of the (c) Ni/MOFDC, and (d) AT-Ni/MOFDC.

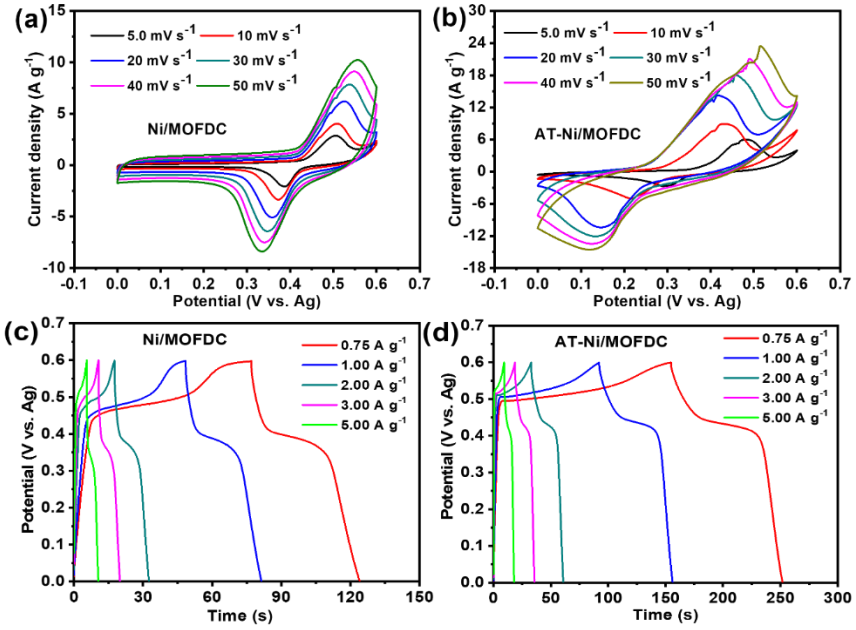


Figure S4: (a, b) CV curves of Ni/MOFDC and AT-Ni/MOFDC at different scan rates, and (c, d) GCD curves of Ni/MOFDC and AT-Ni/MOFDC at different current densities.

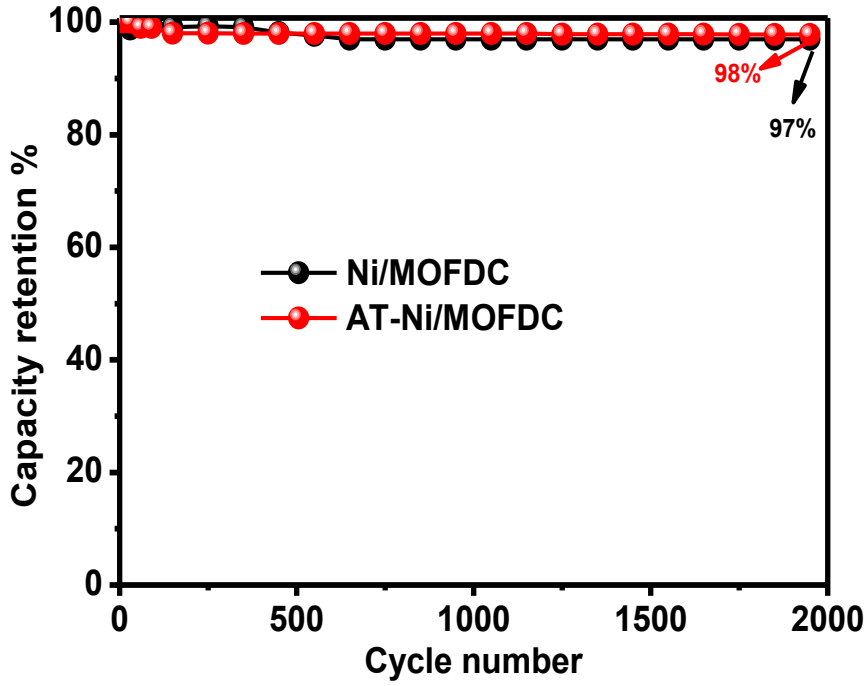


Figure S5: Cycling performance of Ni-based electrodes.

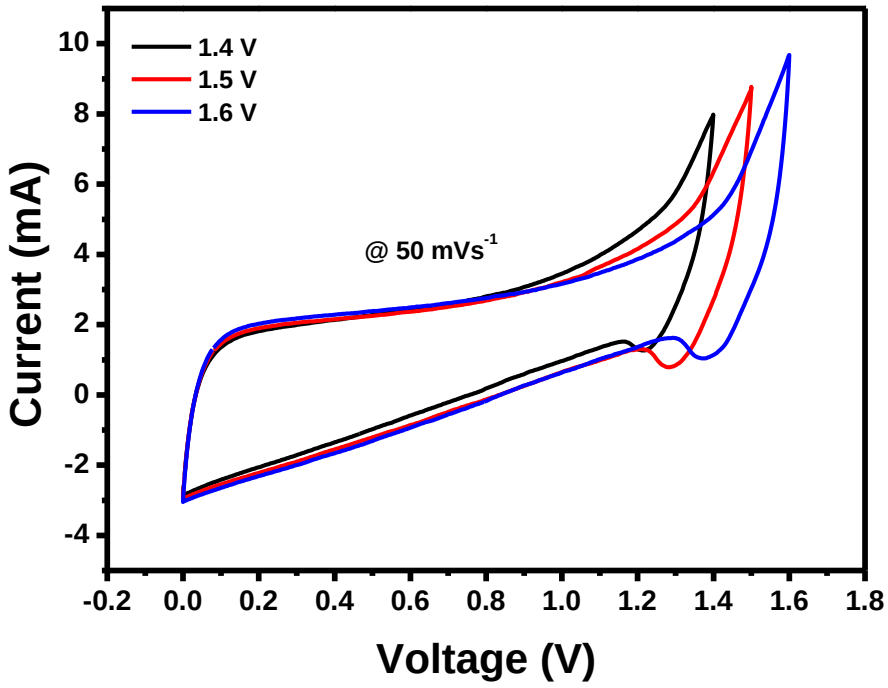


Figure S6: Electrochemical stable window for N-CNT@CF//AT-Ni/MOFDC.

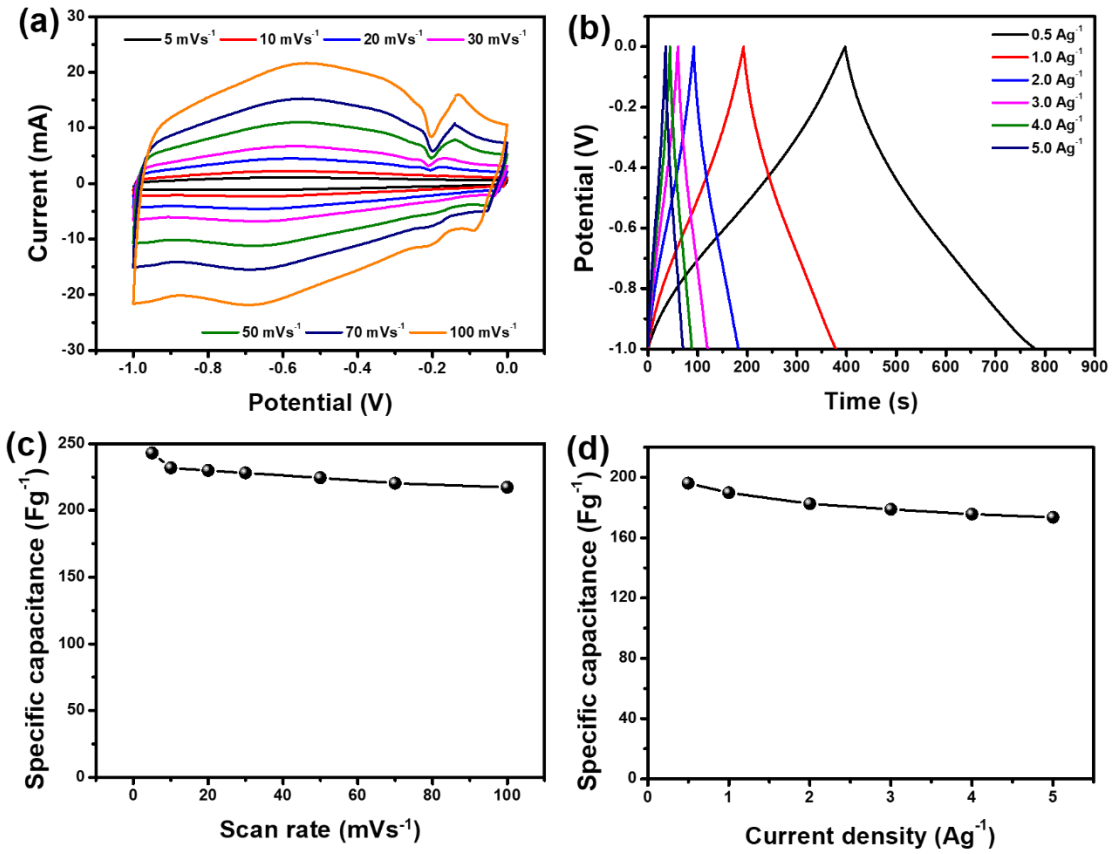


Figure S7: (a) CV curves of N-CNT@CF, (b) GCD curves of N-CNT@CF, (c) specific capacitance from CV, and (d) specific capacitance from GCD in 3M KOH.

APPENDIX C
Supporting information for Chapter six.

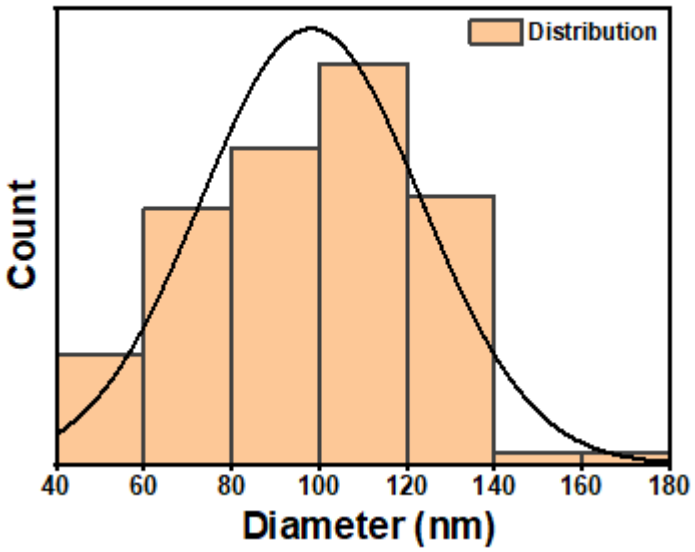


Figure S1: Size distribution bar graph..

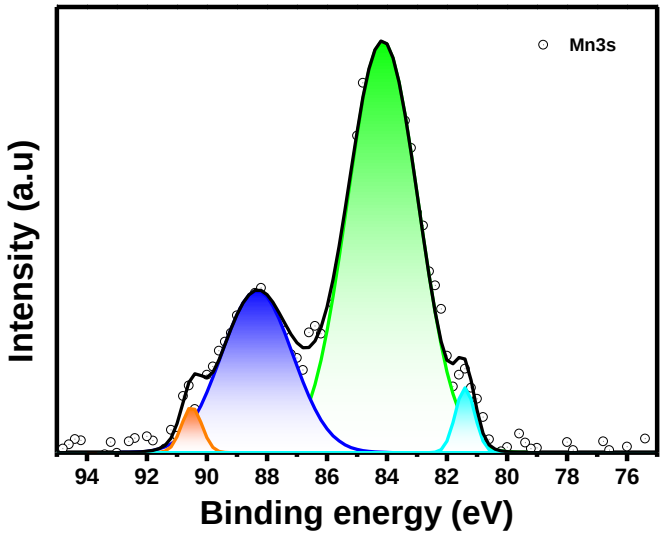


Figure S2: X-ray photoelectron spectroscopy (XPS) analysis, narrow scan of Mn3s.

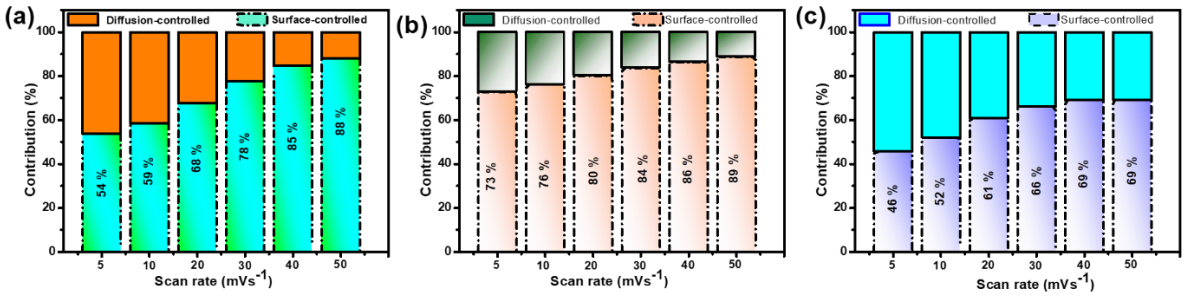


Figure S3: Histograms of the percentage contributions from 5-50 mVs^{-1} in (a) 1M Na_2SO_4, 3M NaOH, and (c) 3M KOH.

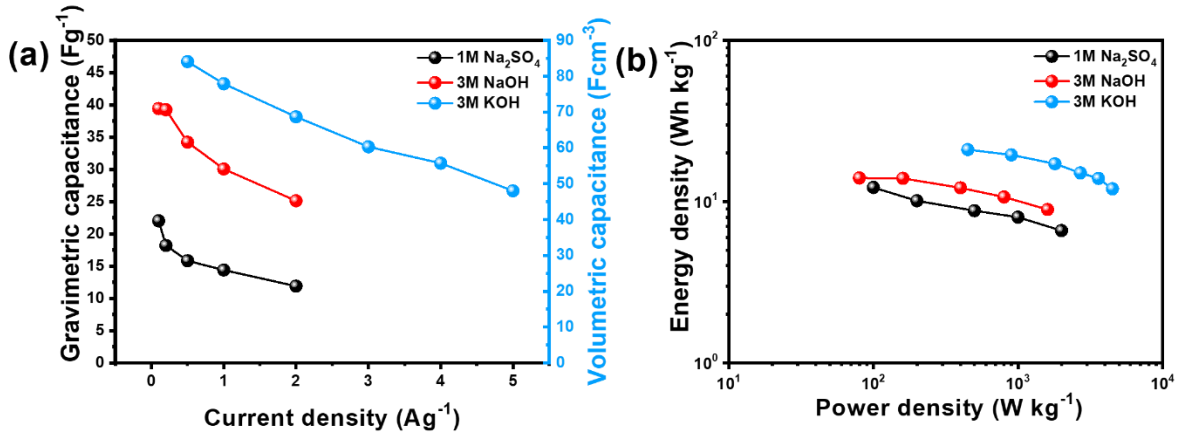


Figure S4: Capacitance and Ragone plot of asymmetric capacitors on N-CNT@CF//$Na_{0.44}MnO_2$ in 1M Na_2SO_4, 3M NaOH, and (c) 3M KOH.

APPENDIX D

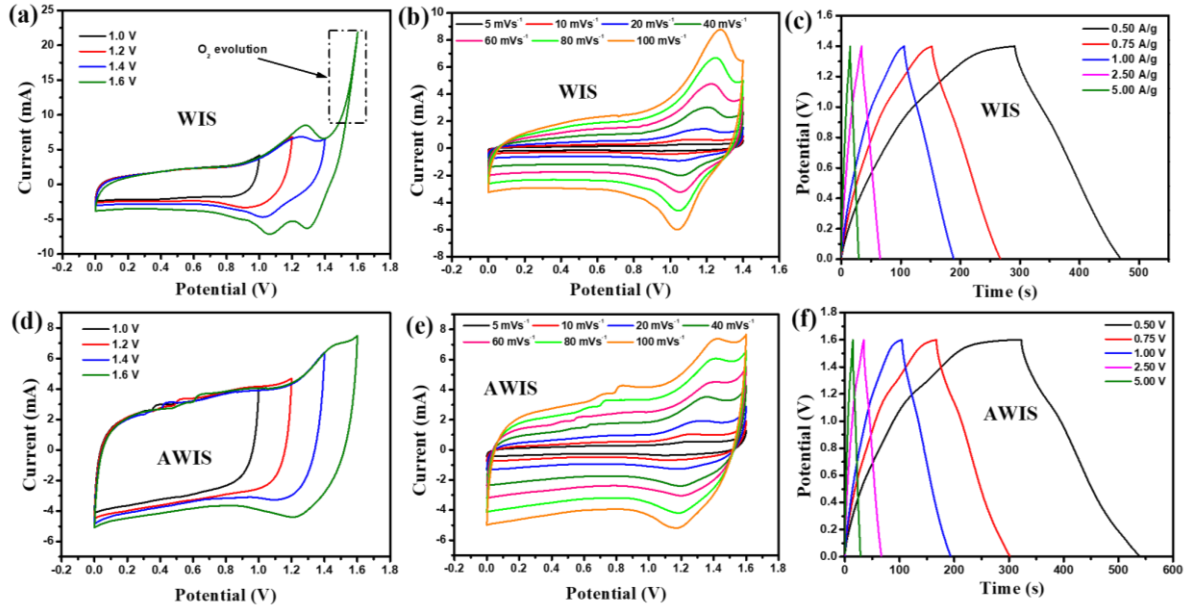


Figure S1: (a, d) Electrochemical stable window, (b, e) CV at various scan rates and (c, f) GCD at various current densities of $Na_{0.44}MnO_2$ in WIS and AWIS electrolytes.

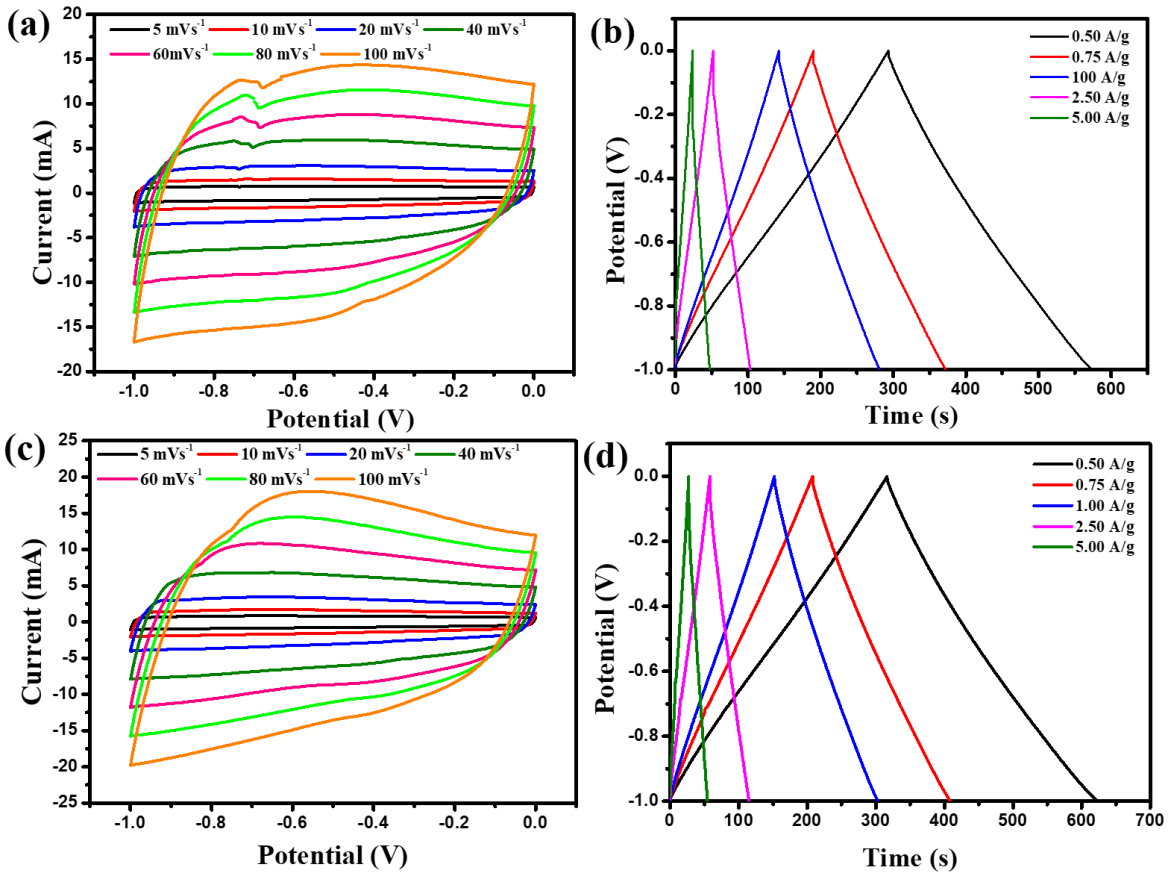


Figure S2: (a, c) CV at various scan rates and (b, d) GCD at various current densities of Na-rGO in WIS and AWIS electrolytes.

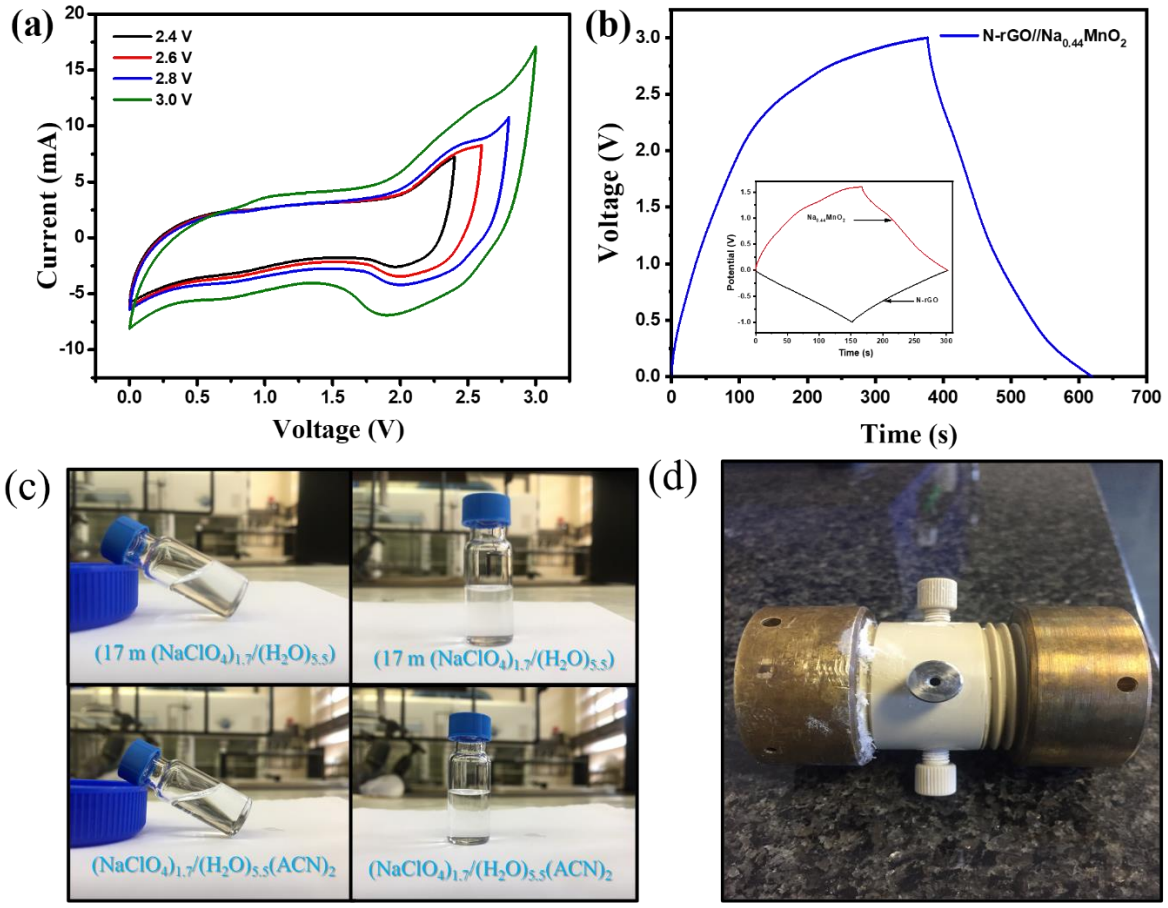


Figure S3: (a) electrochemical window of ASC device, (b) GCD of ASC device (insert GCD of N-rGO and $Na_{0.44}MnO_2$), (c) images of WIS and AWIS electrolytes and (d) T-type Swagelok after 1,900 cycles (re-crystallization of the electrolyte).